October 2023

Knowledge Integration in Domain-Informed Machine Learning and Multi-scale Modeling of Nonlinear Dynamics in Complex Systems

Phat K. Huynh
University of South Florida

Knowledge Integration in Domain-Informed Machine Learning and Multi-scale Modeling of Nonlinear Dynamics in Complex Systems

by

Phat K. Huynh

A dissertation submitted in partial fulfillment
of the requirements for the degree of
Doctor of Philosophy
Department of Industrial and Management Systems Engineering
College of Engineering
University of South Florida

Major Professor: Trung (Tim) Quoc Le, Ph.D.
Om Prakash Yadav, Ph.D.
Hadi Charkhgard, Ph.D.
Susana Lai-Yuen, Ph.D.
Mingyang Li, Ph.D.
Arman Sargolzaei, Ph.D.

Date of Approval:
October 27, 2023

Keywords: data-driven sensor-based modeling, multi-resolution systems modeling, complex system dynamics, multi-modal health sensing data analysis, multi-physics integration

Dedication

I would like to dedicate this dissertation to the many mentors and colleagues who have made this journey a rich and fulfilling one. Foremost among these is my advisor, Dr. Trung (Tim) Quoc Le. Your guidance and wisdom have been an intellectual compass that guided me through the complex maze of research. Your mentorship went beyond academic guidance, as you fostered a sense of responsibility, ethics, and a thirst for continual learning, qualities that I will carry forward into my future academic and professional endeavors.

Next, I would like to extend heartfelt thanks to the Department Chair, Dr. Tapas K. Das, and my committee members: Dr. Om Prakash Yadav, Dr. Hadi Charkhgard, Dr. Susana Lai-Yuen, Dr. Mingyang Li, and Dr. Arman Sargolzaei. Your insightful feedback and encouragement were instrumental in the shaping and completion of this work. Additionally, I would like to extend my sincere appreciation to Dr. Changhyun Kwon, Dr. Alex Savachkin, and Dr. Hadi Charkhgard for their valuable contributions to my academic journey. Their insightful instruction during my coursework played a critical role in shaping my understanding and interests in machine learning, optimization models and stochastic models.

Last but not least, this work is also dedicated to my family. To my grandparents, whose love and belief in my abilities have been my constant source of strength; my parents, whose unwavering support and guidance have always led me in the right direction; my little sister, who adds a unique brightness to our lives; and to my beautiful fiancé, who has been a pillar of support and understanding throughout this journey. This achievement is as much yours as it is mine.

Table of Contents

List of Tables

List of Figures

Abstract

Nonlinear dynamical systems have been extensively used to model various phenomena in the changing world around us, especially in science and engineering fields. Thanks to breakthrough advancements in sensing technologies, an increasingly high volume of multi-modal sensor data has been collected, which enables us gain better insights into complex systems dynamics and build sophisticated data-driven machine-learning-based dynamic models without having the access to the underlying governing equations. However, integrating domain-specific knowledge in machine learning algorithms remains pivotal for various reasons: it promises enhanced predictive accuracy, better model interpretability, and increased generalizability. This dissertation delves into three core research questions, each highlighting a unique facet of domain-informed machine learning's application in complex, dynamic systems.

The first research question probes the methodology and efficacy of incorporating prior domain knowledge into machine learning models. Traditional data-driven machine learning approaches, while powerful, often overlook the vast body of existing domain expertise. Our research showcases the novel approaches, methodologies, and architectures that allow seamless integration of this domain knowledge. Our results indicate that with appropriate incorporation techniques, machine learning models can achieve significantly improved accuracy, offer richer interpretability, and display superior generalization capabilities across varied datasets.

Addressing the second question, we venture into the intricacies of dynamic models designed to handle multi-scale and multi-physics interactions with high noise robustness. With many real-world systems governed by processes occurring at different temporal and spatial scales,

and often influenced by diverse physical phenomena, there's a pressing need for models that capture this complexity. Our study offers advancements in state-of-the-art dynamic models, emphasizing their adaptability and robustness, particularly in noisy environments. Through rigorous testing and validation, we demonstrate how these refined models present a more comprehensive representation of intricate systems, mitigating inaccuracies arising from scale mismatches, multi-physics interplays, and data noise.

The third leg of our investigation ties domain knowledge to the realm of control in complex systems. Control strategies for intricate systems can gain substantially from domain-specific insights, ensuring not just system stability but also optimality in performance. We present frameworks and methodologies to fuse domain knowledge into control design, leading to strategies that are more attuned to the intrinsic characteristics of the systems they govern. Real-world applications, from industrial automation to ecological system management, highlight the profound benefits of these enriched control approaches.

In summation, this dissertation underscores the indispensable role of domain knowledge in shaping the next generation of machine learning models and dynamic systems control. Through focused research on each of our three foundational questions, we hope to chart a path forward for scholars and practitioners aiming to harness the full potential of domain-informed machine learning in understanding and managing complex systems.

Chapter 1: Introduction

In the realm of modern computational research, the blend of domain knowledge with emerging technologies like machine learning (ML) presents unique opportunities and challenges. With the vastness of data available today, harnessing this information to create models, make predictions, or even influence complex systems has become a central academic and industrial endeavor. ML has undeniably paved the way for these advances, allowing researchers to transcend traditional modeling limits. However, the path is not devoid of challenges, and to truly realize the potential of these computational methods, a fusion with domain knowledge seems not only beneficial but essential. Complex systems, characterized by their intricate interactions, nonlinear dynamics, and multi-scale behaviors, stand as a testament to the challenges ahead. Addressing their complexities requires a synthesis of knowledge from the specific domain they belong to and advanced computational techniques. Control of these systems further amplifies the need for domain-specific insights to ensure stability, efficiency, and optimality. The purpose of this dissertation is to explore the confluence of domain knowledge, ML, and the modeling and control of nonlinear dynamics in complex systems. As we embark on this exploration, a proper understanding of the historical and current landscape of each of these facets is paramount.

1.1 Background and Research Motivations

1.1.1 Evolution and Significance of Domain-Informed Machine Learning

The evolution of ML over the late 20th century saw a discernible shift towards increasingly data-driven approaches. As the digital era advanced, the sheer volume, velocity, and variety of data available grew exponentially, calling for methodologies capable of harnessing this deluge [1].

Traditional ML, founded on algorithms like support vector machines, decision trees, and ensemble methods, had for years been the standard-bearers of the field, offering solutions that often required domain expertise for feature engineering and model fine-tuning [2-4]. However, the burgeoning datasets and escalating computational capacities culminated in a renewed emphasis on neural networks, a concept that had been explored in earlier decades but gained newfound significance due to these technological advancements [5]. Deep learning, a subset of neural networks characterized by its multi-layered architectures, emerged as the leading edge of this transformation [6]. Convolutional Neural Networks (CNNs) [7], a class of deep models, revolutionized image recognition and classification tasks, dramatically outperforming preceding techniques by automatically extracting hierarchical features from raw pixel data. Similarly, Recurrent Neural Networks (RNNs) and their advanced variants, like Long Short-Term Memory (LSTM) networks, set new benchmarks in sequence-based tasks, from natural language processing to time series forecasting [8, 9]. The allure of data-driven methods was not only their performance but also the promise of automatic feature extraction, where models could, in principle, discern relevant features from raw data without explicit human guidance. This reduced the reliance on domain-specific feature engineering, though not without its own challenges and caveats. As datasets grew in complexity, so did concerns over overfitting, model interpretability, and ethical considerations related to biases in training data [10, 11].

As ML models, particularly deep learning architectures, grew in complexity and capability, they began to weave their way into critical domains such as healthcare diagnostics, finance, and autonomous systems. The performance of these models was unparalleled, but this prowess often came at the cost of transparency, giving rise to what was frequently referred to as “black-box” models [12] . In critical domains, a mere predictive output without insight into the underlying

decision-making process was insufficient and, in many cases, ethically and legally untenable. Thus, there arose a pressing need to open this black box, to shine a light on the inner workings of these intricate models, and to understand the rationale behind their predictions. Fortunately, the ML community has responded with vigor. The pursuit of explainability and interpretability in ML took center stage, leading to a paradigm shift from purely performance-oriented models to those that balanced accuracy with understanding [10]. Methods like LIME (Local Interpretable Model-agnostic Explanations) [13] and SHAP (SHapley Additive exPlanations) [14] emerged, offering insights into model decisions by approximating complex models with simpler, interpretable ones or assigning importance values to features based on their contribution to predictions. Simultaneously, a growing body of research began to focus on inherently interpretable models—those designed from the ground up to be transparent. This included techniques like decision trees, rule lists, or sparse linear models, which provided clear and straightforward decision boundaries [15]. While these models sometimes sacrificed the raw performance of their deeper counterparts, they were invaluable in contexts where understanding the “why” was as vital as the decision itself.

As ML flourished into various sectors, it became clear that while its data-driven nature was groundbreaking, it lacked finesse when facing intricate domain-specific challenges. The convergence between empirical ML models and domain knowledge gave rise to domain-informed ML, a methodology that seeks to intertwine ML with established domain principles for enhanced precision and interpretability. At the heart of domain-informed ML lies the concept of leveraging existing knowledge within a specific domain. Rather than solely relying on vast datasets, models are "guided" and constrained by well-understood and accepted domain rules, frameworks, or theories. Particularly, the fusion of domain knowledge into ML can manifest in myriad ways, whether through probability distributions that set prior expectations, logical rules which guide

decision boundaries, ingrained physical laws and equations for constraining predictions, or structured graphs that encode domain relationships [16-18]. For instance, in the medical realm, probabilistic graphical models can integrate biological pathways to inform diagnostic predictions, ensuring alignment with known medical science [19]. Likewise, in computer vision tasks, incorporating geometric and physical knowledge about the world can initialize neural network weights or guide data augmentation processes, boosting model generalization especially in data-scarce scenarios [20]. This integration aids in producing more accurate, generalizable, and interpretable outcomes, especially where data might be scarce or noisy.

In addition, a quintessential manifestation of domain-informed ML is physics-informed ML. It marries the discipline of physics with ML, epitomized by models such as Physics-informed Neural Networks (PINNs). In these networks, known physical laws and equations, like the Navier-Stokes equations in fluid dynamics, are incorporated into the ML model, essentially grounding the model's predictions in the laws of physics. Such an approach ensures that outcomes adhere to both the observed data and the foundational tenets of physics, offering an added layer of reliability [21]. The overarching connection between domain-informed and physics-informed ML is that both aim to bring an added layer of domain-specific expertise to the ML paradigm. Where physics-informed ML focuses specifically on integrating physical laws, domain-informed ML embraces a broader spectrum, incorporating knowledge from varied fields such as biology, economics, or sociology.

1.1.2 Complex Systems: Characteristics and Challenges

A complex system is a system that consists of many interrelated components which may interact with each other. Examples of complex systems are weather and climate [22], organisms [23], the human body systems (e.g., cardiovascular system [24, 25], the human brain [26, 27]), infrastructure (e.g., power grid [28], transportation systems [29]). At their core, these systems are

a combination of many interconnected components or agents, each operating based on its set of rules. However, the emergent behaviors observed at the macro-level often transcend the mere summation of individual interactions, leading to phenomena that are far from intuitive [30]. Historically, these systems, with their complicated structures and dynamics, have both attracted and baffled researchers. Traditional linear theories and modeling approaches, where systems are broken down into simpler units for study, often fail when confronted with the sophisticated and unpredictable nature of complex systems [31]. It becomes evident that while the underlying interactions might be simple or even well-understood, their collective outcome often breeds unexpected complexities and challenges, necessitating novel paradigms of understanding.

Complex systems, while varied in nature and application, share a set of defining attributes that distinguish them from simpler linear systems [32]. One of the hallmarks is nonlinearity, where the system's response is disproportionately amplified or suppressed relative to changes in inputs, defying straightforward extrapolation [32]. Emergence, another defining trait, encapsulates the idea that the collective behaviors and properties of the system arise spontaneously from the interactions of its components, without any centralized coordination [33]. This leads to outcomes that are often unpredictable, a phenomenon accentuated by feedback loops prevalent in these systems. Feedback mechanisms, be they positive or negative, can either reinforce or regulate the system's behaviors, often leading to unexpected and rapid shifts in system states [33]. Additionally, complex systems often exhibit high levels of adaptability, continuously evolving in response to external stimuli and internal dynamics, thereby manifesting resilience and robustness against disturbances [34, 35]. The inherent heterogeneity and diversity of components, coupled with the dense web of interactions, further complicate the dynamics, making any modeling approach to

study them limited in scope and depth [36, 37]. These prototypical attributes underscore the challenges in modeling, analyzing, and predicting the behaviors of complex systems.

Modeling and understanding the intricacies of complex systems present multifaceted challenges that extend beyond conventional scientific paradigms [38, 39]. One primary challenge lies in the sheer scale and granularity of these systems, often comprising a vast number of interconnected components operating at multiple temporal and spatial scales [40, 41]. The dynamic interplay between components is not always deterministic; stochasticity can introduce variability and uncertainty into system behaviors, demanding probabilistic or statistical approaches to grasp their dynamics [42, 43]. Moreover, the computational cost associated with simulating such intricate systems can be prohibitively high, particularly when considering longer time scales or larger spatial domains [44]. Another significant obstacle stems from the incomplete or imprecise information available about the system's components, which can lead to models that are overly simplified or fail to capture essential dynamics [31]. Furthermore, the adaptability and evolutionary nature of complex systems can alter their characteristics over time, rendering static models ineffective and emphasizing the need for adaptive, evolving models [45, 46]. Lastly, the emergent properties, which are cornerstone features of complex systems, pose inherent challenges since they cannot be easily deduced from the properties of individual components alone [47, 48]. This quality of emergence demands integrative, universal approaches that can capture the collective dynamics and behaviors arising from the interactions among individual elements [49].

1.1.3 Nonlinear Dynamical Systems for Modeling Complex Systems

Dynamical systems, a foundational concept in the study of processes that evolve over time, offer a structured way to represent and analyze the nonlinearities of complex systems. While linear dynamical systems can be understood through superposition and have solutions that can be

analytically determined, nonlinear dynamical systems, by contrast, can exhibit a plethora of behaviors that are far richer and, in many cases, unexpected [50]. Mathematically, a nonlinear dynamical system can be described by differential equations of the form:

$$\frac{d}{dt}\boldsymbol{x}(t) = \boldsymbol{f}\big(\boldsymbol{x}(t), t, \boldsymbol{u}(t), \boldsymbol{\beta}(t)\big) + \boldsymbol{d} \tag{1.1}$$

In this equation, $\boldsymbol{x}(t)$ is the state vector representing the system's variables, t denotes time, $\boldsymbol{u}(t)$ is an external input or control, $\boldsymbol{\beta}(t)$ captures varying parameters over time, and $\boldsymbol{d}$ is an external disturbance or noise. The function $\boldsymbol{f}$ is a nonlinear function that encapsulates the dynamic relationships among these variables and parameters. The inherent nonlinearity in $\boldsymbol{f}$ is what induces to the various behaviors seen in complex systems.

Nonlinear dynamical systems are replete with behaviors that are absent or simplified in their linear counterparts. A defining trait of nonlinear systems is the rich variety of patterns and dynamics they can exhibit, many of which cannot be readily predicted just from the system's governing equations. One such phenomenon is bifurcation, where a minor change in a system parameter can lead to an abrupt and significant change in the system's long-term behavior [51]. This can manifest as a transition from stable to oscillatory behavior, or vice versa, and it underpins the principle that in nonlinear systems, small causes can sometimes lead to large effects. Limit cycles represent another distinctive behavior, where a system's state evolves over time in a repetitive or periodic fashion, eventually returning to its original position and repeating the cycle, creating closed trajectories in its phase space [51]. Chaotic behavior, on the other hand, is characterized by its sensitivity to initial conditions—often referred to as the "butterfly effect". Though the system's behavior might appear random, it is deterministic and bound within a certain region of the phase space known as a strange attractor [52]. The presence of such attractors means that while the exact future state of a chaotic system is practically unpredictable due to its sensitivity

to initial conditions, its behavior is confined within a certain structure. Moreover, multiple stable states or attractors can coexist in some nonlinear systems, leading to multistability that is sensitive to initial conditions or external perturbations [53]. Such multistability has been observed in numerous real-world systems, from electronic circuits to biological processes, and underscores the challenge of predicting system behavior without comprehensive knowledge of initial conditions.

Dynamical systems theory has found profound applications in predicting, optimizing, and controlling various systems. Firstly, in forecasting future states, dynamical systems provide tools for both ensemble and statistical predictions. Ensemble predictions involve running multiple simulations with slightly varied initial conditions to create a collection of potential outcomes, offering a probabilistic forecast of the system's future states [54]. In contrast, statistical predictions are based on analyzing past behavior to infer future trajectories, a method particularly embraced in meteorology and climate science [55]. Secondly, dynamical systems play a pivotal role in system optimization and design. By understanding the underlying dynamics, one can engineer systems that perform efficiently under specific constraints or environmental conditions, as observed in applications ranging from aerospace engineering to biological systems [55]. Lastly, optimal system control, rooted in the principles of dynamical systems, aims to drive a system to a desired state by applying appropriate inputs or interventions. The optimal system control has led to innovations in areas like robotics, economics, and, notably, healthcare, where treatment regimens act as control mechanisms to achieve patient outcomes [56, 57].

1.1.4 Multi-Scale Modeling for Complex Systems

In the vast realm of nonlinear systems, one consistent challenge arises from the intrinsic multi-scale nature of many phenomena. Complex systems, as discussed earlier, can display behaviors at several different scales, both in time and space. The intricate interactions between

these scales amplify the complexities associated with analyzing and controlling such systems. Multi-scale modeling has emerged as a pivotal approach to address these intricacies by simultaneously capturing phenomena at multiple resolutions [58]. For instance, in biological systems, interactions span from molecular and cellular levels to tissues, organs, and eventually the whole organism, with each scale governed by its own set of principles and interactions [59]. The primary challenge in multi-scale modeling lies in appropriately coupling models designed for specific scales. It's not merely about juxtaposing models of different scales, but about ensuring their coherent integration such that information flows effectively across scales, maintaining accuracy and computational feasibility [60]. This becomes particularly crucial when considering the nonlinear behaviors detailed in the previous paragraph. For instance, a minor perturbation on a smaller scale, as seen in bifurcation scenarios, can lead to significant consequences on larger scales. Thus, multi-scale modeling is not a luxury but a necessity, offering the potential to elucidate the details of complex systems and providing a complete approach mono-scale models might miss.

While multi-scale modeling offers promising avenues for understanding and predicting the behavior of complex systems, it brings forth its own array of challenges. First, the intricate coupling of different scales can result in a vast computational burden, making simulations resource-intensive and often prohibitive [61]. This is particularly exacerbated when nonlinearities from one scale permeate and influence another, demanding a higher fidelity in simulations. Another challenge lies in the seamless integration of models across scales. Given that models designed for different scales might be based on disparate principles or methodologies, merging them coherently while maintaining their individual accuracy poses a significant hurdle [62]. Despite these challenges, the opportunities presented by multi-scale modeling are enormous. By effectively bridging scales, one can derive insights that are otherwise obscured when analyzing

scales in isolation. For instance, understanding the molecular mechanisms behind material deformation can lead to breakthroughs in macro-level material design [62]. Furthermore, the advent of advanced computational techniques and the integration of ML with domain-specific knowledge, as elucidated in previous sections, offer exciting prospects for overcoming some of the computational challenges inherent to multi-scale modeling [63]. Leveraging domain-informed ML approaches can expedite simulations by efficiently approximating behaviors at certain scales, allowing for faster yet accurate model predictions [64]. As we venture deeper into the realms of complex systems, the union of multi-scale modeling with advanced computational strategies will be instrumental in unlocking a plethora of scientific and engineering breakthroughs.

1.2 Broader Impacts of the Work

The evolution and advancements of machine learning, coupled with the intricate nature of complex systems, represent two converging pathways of contemporary scientific exploration. The challenges brought about by the congenital characteristics of complex systems - emergence, adaptation, nonlinearity, interconnectedness, and self-organization - necessitate a reevaluation and redesign of traditional modeling and analytical methods. The merging horizon where machine learning meets complex systems thus becomes a pivotal intersection for innovation. This study is situated at this very crossroads, and its significance can be appreciated through several key aspects:

- The first is *enhancing predictive accuracy and interpretability*. At the core of our research is the integration of domain knowledge into machine learning models. The goal is to leverage the strengths of empirical data-driven machine learning while embedding domain-specific expertise to boost the accuracy, generalizability, and interpretability of predictive models. This confluence is especially crucial for complex systems where inaccurate predictions can have cascading and potentially catastrophic consequences. Tackling the

predictive complexity arising from emergent and adaptive behavior becomes more feasible with models enhanced by domain knowledge.

- The second is *bridging scales in complex systems*. Complex systems often exhibit behaviors that span multiple scales, both temporal and spatial. By advancing state-of-the-art dynamic models to accommodate multi-scale and multi-physics interactions, this dissertation aims to offer a more holistic representation of systems, from microscopic interactions to macroscopic outcomes. This ensures robustness even in the face of noise and uncertainties inherent in such systems. Within this dissertation, our primary objective is to advance state-of-the-art dynamic models to encapsulate these multi-scale phenomena intrinsic to human pathophysiology. Such an approach becomes indispensable for ensuring robustness, especially considering the noise and uncertainties that are inherent in the dissertation of human pathophysiology.
- The third is *revolutionizing complex system control strategies*. Effective control strategies for complex systems are contingent upon a comprehensive understanding of their behavior. Through the systematic integration of domain-specific knowledge, our research will pave the way for more adaptive and responsive control strategies, enabling more efficient management and stabilization of these systems in dynamic environments. In this dissertation, we center our attention on the human body, treating it as a paramount example of a complex system. The inherent complexities of physiological interactions necessitate precise and informed therapeutic interventions and treatment regimens. Harnessing a comprehensive understanding of the body's multifaceted behavior, through the systematic integration of domain-specific knowledge, is essential. Our research aims to inform and revolutionize therapeutic strategies tailored specifically for the human body. This approach

will enable the development of more adaptive and individualized treatment regimes, assuring optimized health outcomes in the face of the dynamic nature of human physiology.

- The last is *fostering interdisciplinary collaboration and addressing societal implications*. Beyond the technical benefits, this dissertation serves as a platform for fostering interdisciplinary dialogue and collaboration. By integrating knowledge from physics, pathophysiology, engineering, and more into machine learning models, a more enriched and holistic understanding of complex phenomena can emerge. This synergy can propel breakthroughs that may remain elusive within siloed disciplinary boundaries. As machine learning models become more rooted in decision-making processes, especially in critical domains like healthcare and finance, ensuring their interpretability, fairness, and transparency becomes paramount. This dissertation, by emphasizing domain-informed machine learning and interpretable modeling, addresses these pressing concerns, leading the way towards more ethically sound applications.

1.3 Research Questions

Complex systems, irrespective of their nature or domain, exhibit intricate behaviors that often require multifaceted approaches for understanding and optimization. In guiding our exploration of these systems, we have formulated three specific research questions, aiming to address the overarching challenges these systems pose, as follows:

- *Research question 1* is how can prior domain knowledge be effectively incorporated into machine learning models to enhance their predictive accuracy, interpretability, and generalizability in understanding complex system dynamics?

This question seeks to understand the benefits and mechanisms of integrating well-established domain principles into machine learning. For instance, in the context of human

physiological processes, a model that is informed by medical and physiological principles might leverage vast data while being guided by our foundational understanding of human biology, potentially offering improved diagnostic or predictive tools.

- *Research question 2* is considering the inherent multi-scale nature of many complex systems, how can state-of-the-art dynamic models be advanced to accommodate multi-scale and multi-physics interactions, ensuring robustness in the presence of noise and uncertainties?

To fully capture the essence of complex systems, our models need to recognize and account for interactions at various scales. Taking human physiology as an example, this would involve understanding interactions ranging from molecular processes in cells to the coordinated efforts of entire organ systems, emphasizing the importance of multi-scale modeling in such contexts.

- *Research question 3* is how can domain-specific knowledge be systematically incorporated into the design and control strategies of complex systems for optimized outcomes?

A deep understanding of any complex system is instrumental when devising strategies for its control and optimization. By channeling domain-specific knowledge, we aim to enhance the performance and responsiveness of these strategies. For instance, in a healthcare setting, this could translate to more tailored therapeutic interventions leading to better patient outcomes.

1.4 Dissertation Overview

The unfolding complexities of various systems, exemplified by our focus on complex systems in general, demand an in-depth examination. This dissertation is structured to elucidate these intricacies, relying on a systematic approach. Below is an outline of the chapters that constitute this dissertation:

- *Chapter 2: Literature Review* delves deep into the existing body of knowledge, tracing the historical and recent developments in the domain of complex system dynamics, forecasting methods, and advanced computational techniques. It lays the foundation for the subsequent research by providing context and highlighting the gaps in the current understanding.
- *Chapter 3: Research Methodologies is* a detailed discussion on the various research methodologies employed throughout the dissertation. This chapter elaborates on the rationale, design, and implementation of the methods, ensuring the validity and reliability of the research findings.
- *Chapter 4: Probabilistic Domain-Knowledge Modeling of Disorder Pathogenesis for Dynamics Forecasting of Acute Onset* presents a novel approach to predict the dynamics of acute-onset disorders, integrating domain-specific knowledge within a probabilistic framework. The focus is on ensuring accurate forecasting of disorder evolution, providing vital insights into the pathogenesis processes.
- *Chapter 5: A Physics-informed Latent Variable Model of Corrosion Growth in Oil and Gas Pipelines* is an in-depth exploration of corrosion processes in oil and gas pipelines. By weaving together physics-based principles and latent variable modeling, this chapter offers a refined understanding of the corrosion growth mechanisms.
- *Chapter 6: A Noise-Robust Koopman Spectral Analysis of an Intermittent Dynamics Method for Complex Systems: A Case Study in Pathophysiological Processes of Obstructive Sleep Apnea* delves into the complexities of intermittent dynamics in pathophysiological processes. The focus is on the Koopman spectral analysis, enhanced for noise-robustness, illuminating the intricate behaviors of such systems.

- *Chapter 7: Detecting Transition to Turbulence in Intracranial Aneurysms by Optimized Dynamic Mode Decomposition* addresses the critical issue of detecting the onset of turbulence in intracranial aneurysms.
- *Chapter 8: Noise-Robust Optimal Sampling Strategy for Multi-scale Complex Systems Using Deep Reinforcement Learning* is A discussion on the challenges of modeling multi-scale complex systems and the proposed solution using a deep reinforcement learning-based approach.
- *Chapter 9: Adaptive Control Strategies in Therapeutic Intervention: A Multicentric Randomized Controlled Trial on Obstructive Sleep Apnea Management* is an innovative approach to treating sleep-disordered breathing, this chapter combines system control theory and longitudinal causal analysis. The research demonstrates the potential of considering therapeutic interventions as control inputs, yielding transformative insights into the broader cardiovascular implications of the disorder.
- *Chapter 10: Translational Research* delves into real-world applications of prior findings. It covers: (1) A novel platform for real-time COVID-19 diagnosis, combining magnetic respiratory sensing and machine learning, offering a reliable and cost-effective health response tool. (2) The use of multifractality in surface potential for cancer diagnosis, leveraging high-resolution imaging and multifractal analysis, presenting a game-changer in early cancer detection.
- *Chapter 11: Conclusions and Future Directions* offers a comprehensive summary of the key findings and their implications. Additionally, it provides a roadmap for future research, pointing to potential avenues of exploration and underscoring the significance of the research undertaken in this dissertation.

Chapter 2: Literature Review

With a comprehensive understanding established in Chapter 1 regarding the intricacies of complex systems, nonlinear dynamics, and multi-scale modeling, we now shift our focus towards a deeper exploration of the scholarly landscape surrounding these concepts. Chapter 2, the Literature Review, is structured to offer a methodical breakdown of the prevalent literature in the field. We commence with Section 2.1, which commences with the various strategies of integrating domain-specific knowledge into machine learning models, a theme central to our research questions. Moving forward, Section 2.2 emphasizes the intricate methodologies and advancements related to multi-scale modeling in complex systems, linking it with our earlier discussions on nonlinear dynamics. Section 2.3 then deepens the discourse, analyzing various control strategies tailored for these intricate systems, providing insights into the current best practices and challenges. Lastly, Section 2.4 critically examines the existing literature to highlight the gaps and uncharted territories, setting the stage for our subsequent investigations. Together, this chapter aims to offer a well-rounded survey of the past and present, allowing us to forge a path for future innovations in the study of complex systems.

2.1 Domain Knowledge Integration in Machine Learning

Domain knowledge, derived from centuries of scientific inquiries, experimentation, and observation, has been the foundation upon which we've built our understanding of the world. Every scientific discipline, from the microcosm of quantum physics to the vastness of astrophysics, from the intricacies of cellular biology to the complexities of socio-economic systems, is underpinned by a wealth of accumulated domain knowledge [65]. As the machine learning paradigm began its

ascendant trajectory in the late 20th century, it quickly became evident that its data-driven models, while powerful, often lacked the depth and nuance provided by this deep-seated domain knowledge. The raw, unbridled computational prowess of ML was impressive, but without the guiding hand of domain expertise, it was akin to a ship without a compass, capable but directionless [66]. There arose a pressing need to bridge the chasm between these two worlds. Domain knowledge, with its rich tapestry of theories, principles, and empirical findings, offered insights that data alone could never unveil. Its integration into machine learning was no longer seen as a mere enhancement but a critical component, essential to create models that were not just accurate but also meaningful, interpretable, and grounded in the realities and constraints of their respective domains [67, 68]. As the 21st century progressed, the ML community began to actively champion the union of algorithmic learning and domain expertise, heralding a new era where models were built upon the synergistic interplay of data and domain wisdom.

Integrating domain knowledge into machine learning has been both a challenge and an opportunity, manifesting in a variety of methodologies tailored to harness the strengths of traditional insights and modern algorithms. Constraint-based modeling offers a foundational approach, guiding the learning process through specific domain-driven constraints, often influencing the design of optimization tasks' objective functions or constraints to ensure solutions stay within plausible domains [69, 70]. Feature engineering, another pivotal method, directly incorporates domain insights into the feature design phase, enabling models to perform optimally even with less data [71]. In Bayesian contexts, priors derived from domain knowledge set initial expectations, guiding probabilistic models before data observations [72]. Hybrid models, like Physics-informed Neural Networks (PINNs), seamlessly merge traditional domain-specific modeling with the flexibility of ML algorithms, offering both robustness and expressiveness [21].

Furthermore, domain insights have found their way into algorithm design, introducing specific regularization terms or penalties to improve alignment with known domain-specific structures, thereby enhancing model reliability and generalization [73]. This intricate blend of domain wisdom and algorithmic prowess, as echoed in recent studies, not only deepens the interpretative potential of machine learning but also paves the way for models that are both computationally proficient and conceptually insightful.

The incorporation of domain knowledge into machine learning presents a myriad of advantages, substantiated by an expanding corpus of research. Firstly, domain knowledge alleviates issues of data scarcity, enabling models to draw upon established principles and insights when training data is limited, thus enhancing generalization capabilities [74]. This integration further bolsters interpretability, presenting models whose predictions are grounded in familiar theories and constructs, a trait that becomes invaluable especially in sectors where interpretability is paramount, such as medicine or finance [75]. By doing so, it bridges the chasm between machine learning specialists and domain experts, facilitating collaborative innovations [76]. However, integrating domain knowledge is not without challenges. The process of codifying often nuanced and context-dependent domain insights into rigid algorithmic constructs can be intricate, sometimes leading to oversimplifications that undermine model accuracy [77]. There's also the risk of model rigidity; over-reliance on domain knowledge can curtail a model's ability to discover novel patterns or relationships outside of established paradigms [78]. Furthermore, ensuring the correct and consistent translation of domain knowledge into machine learning models necessitates a deep understanding of both the domain in question and the intricacies of ML methodologies. The constant evolution of both domain knowledge and machine learning techniques requires

researchers to continually reevaluate and recalibrate their integration methods, an endeavor demanding both technical prowess and domain acumen.

The trajectory of machine learning intertwined with domain knowledge is poised for significant advancements in the coming years, driven by both technological innovation and emerging research paradigms. A prominent trend is the ascent of hybrid models that symbiotically leverage the strength of data-driven ML methods and domain expertise. Such models are anticipated to dominate fields where stakes are high and errors can have profound implications, including autonomous driving, energy management, and biomedicine [79, 80]. Furthermore, the push for more transparent and explainable AI will likely accentuate the importance of domain-centric ML models. Models grounded in domain principles inherently offer better avenues for interpretability, aligning well with regulatory and societal demands for accountable AI [80]. Moreover, evolving research in transfer learning and meta-learning is increasingly recognizing the role of domain knowledge in facilitating the transfer of insights across different, yet related, tasks, thus accelerating the learning process [81]. Simultaneously, advancements in unsupervised and semi-supervised learning techniques are revealing the potential of leveraging domain knowledge to guide learning even when labeled data is scant [82]. The continuous integration of machine learning with fields like cognitive science and neuroscience further suggests that future ML models might more closely emulate human-like learning, where prior knowledge plays a pivotal role in understanding novel situations [83]. However, it is imperative to strike a balance. While domain knowledge offers rich insights, machine learning's strength in uncovering hidden patterns should not be overshadowed. Future research must focus on optimizing this synergy, ensuring that domain insights amplify, rather than inhibit, the discovery potential of machine learning [84]. The confluence of domain expertise with advanced machine learning paradigms is not just an academic

pursuit but stands as a beacon for the next generation of intelligent systems that can deeply comprehend and adeptly navigate the intricacies of our complex world [6].

2.2 Multi-Scale and Nonlinear Modeling in Complex Systems

Understanding the dynamic behavior of systems across multiple scales has been a cornerstone of scientific pursuits since the early days of theoretical research. Beginning with Poincare's pioneering work on the three-body problem in celestial mechanics in the late 19th century, the complexities of nonlinear behaviors in natural systems were brought to light [85]. As the 20th century unfolded, particularly from the mid-century onwards, there was a substantial shift towards more advanced modeling techniques tailored to the nuances of complex systems. In fields as diverse as physics, biology, chemistry, and even socio-economic sciences, the inadequacy of linear models for certain phenomena became increasingly evident, especially when systems displayed behaviors vastly differing across scales. The challenge was not just about the vastness of scales but also about the unpredictability and interconnectedness of components within these scales. For example, in fluid dynamics, the Navier-Stokes equations highlighted the intricacies of turbulence and chaotic flow patterns, and how small-scale vortices could influence larger flow structures [86]. In the biological realm, the study of complex biochemical pathways and cellular interactions necessitated a departure from reductionist approaches, leading to the genesis of systems biology by the late 20th century [87]. It wasn't long before the advent of computer science and numerical simulations further catalyzed the evolution of modeling techniques. Lorenz's groundbreaking work in the 1960s on atmospheric predictability underscored the sensitivity of nonlinear systems to initial conditions, ushering in a deeper understanding of chaotic behaviors [88]. As computational prowess grew, so did the ambition and scope of multi-scale models, with

researchers attempting to bridge quantum mechanics with classical physics, or intracellular processes with tissue-level phenomena [89, 90].

Nonlinear and multi-scale systems stand out due to their distinct and multifaceted properties that set them apart from simpler linear systems. One of the most defining attributes of nonlinear systems is their sensitivity to initial conditions. This phenomenon, often referred to as the “butterfly effect”, suggests that minor variations at the system's onset can lead to vastly divergent outcomes, making long-term prediction extremely challenging [88]. The ramifications of this effect have been deeply studied, revealing that it isn't mere unpredictability, but a structured form of unpredictability, termed chaos [88]. Moreover, multi-scale systems inherently exhibit behaviors across different scales, both temporally and spatially. This necessitates a comprehensive modeling approach that considers the cross-interactions between various scales. For instance, in material science, the properties observed at the macro scale are often deeply influenced by interactions at the atomic or even quantum scale [88]. Similarly, in ecological systems, interactions at the level of individual organisms can influence population dynamics and even shape entire ecosystems [90]. Another hallmark characteristic is the emergence, a phenomenon where the collective behavior of a system arises from the interactions of its individual parts, often producing outcomes that are not intuitively predictable from the sum of its components [47]. This is widely observed in biological systems where, for example, collective cell behavior forms patterns or structures that individual cells might not exhibit on their own [91]. Feedback loops, both positive and negative, are ubiquitous in nonlinear systems. These loops can amplify or stabilize system responses, respectively. In the context of physiological systems, feedback loops play pivotal roles in maintaining homeostasis [92]. Lastly, the presence of bifurcations, points where a slight change

in a system parameter can lead to a qualitative change in its long-term behavior, further emphasizes the intricate landscape of nonlinear dynamics [93].

Over the decades, a diverse array of methodologies has been developed to understand and represent nonlinear and multi-scale systems. One foundational approach in the context of nonlinear systems is bifurcation analysis. This involves a detailed exploration of how slight parameter changes influence system behavior, leading to phenomena like limit cycles, chaos, or even system collapse [94, 95]. Phase plane analysis provides another geometric viewpoint, allowing researchers to visualize system trajectories and identify stable and unstable equilibria in two-dimensional systems [96]. In the realm of multi-scale modeling, the methodologies often depend on the specific domain and the scales of interest. The bridging of scales can be tackled using a range of techniques. In materials science, for example, quantum mechanics can be used to derive properties at the atomic scale, which can then be linked to continuum mechanics at macroscopic scales via molecular dynamics and statistical mechanics [97]. This hierarchical approach ensures that properties and behaviors are consistently represented across different scales. Furthermore, the wavelet transform has emerged as a potent tool, especially when dealing with systems exhibiting behaviors at multiple temporal scales. By decomposing signals into components associated with different frequencies, it offers a resolution in both the time and frequency domains, proving invaluable in areas like signal processing and image compression [98]. Despite the rich toolkit available, no single method universally applies across all nonlinear or multi-scale systems. The choice often hinges on the specific characteristics of the system in question, the scales of interest, and the goals of the analysis. However, the collective advancements in these modeling techniques have undeniably enriched our understanding and predictive capabilities across a swath of complex systems domains [99, 100].

Modeling complex systems, particularly those that are both nonlinear and span multiple scales, presents many challenges. One fundamental issue is the vast computational effort required. As models seek to represent dynamics across different scales, computational demands often grow exponentially, posing scalability issues [101]. Even with advances in computational power, many multi-scale models remain computationally intensive, especially when simulating over extended periods or for large systems. Inter-scale interactions further complicate modeling endeavors. It's often insufficient to model each scale independently and then link them, as emergent behaviors may arise from their interactions [102]. Capturing these emergent phenomena, which might be counter-intuitive or not evident when scales are considered in isolation, remains a significant challenge [38]. Additionally, nonlinearities introduce challenges like sensitivity to initial conditions, often termed “chaos” [88]. This sensitivity makes long-term predictions challenging, as tiny perturbations can lead to vastly different outcomes. Model validation is another critical concern. Given the high degrees of freedom and potential overfitting in nonlinear models, ensuring that they are both accurate and generalizable to new scenarios is nontrivial [103].

Despite these challenges, there are optimistic prospects on the horizon. Techniques from machine learning and data science are increasingly being integrated with traditional modeling approaches, providing innovative ways to handle nonlinearity and multi-scale dynamics. Deep learning, for instance, has shown promise in capturing intricate patterns and behaviors without requiring explicit formulations of all underlying processes [104]. Furthermore, advances in cloud computing and parallel processing offer avenues to manage the computational demands of these models [105]. In terms of methodologies, hybrid models, which blend agent-based, continuum, and other modeling paradigms, are emerging as powerful tools to capture the full spectrum of behaviors in complex systems [106]. Techniques like Proper Orthogonal Decomposition (POD)

[107] and the Mori-Zwanzig formalism [108] are also being explored to reduce system dimensions while retaining essential dynamics, providing a balance between model detail and computational feasibility.

2.3 Control Strategies in Complex Systems

In the study of complex systems, control strategies stand as a pivotal component, orchestrating harmony in a web of intricate interdependencies and multifaceted behaviors. From the early days of engineering and mathematics, the desire to predictably influence the dynamics of systems has driven remarkable innovations. Classical linear control theories [109], which dominated the mid-20th century, provided foundational methods to stabilize and manage simple systems. Yet, the innate intricacy of real-world systems, coupled with their non-linearities and unpredictable behaviors, compelled researchers to seek advanced and adaptive control techniques. Recognizing this, the advent of cybernetics in the 1940s [110], showcased the potential of integrating interdisciplinary knowledge, especially from biology and engineering, into developing comprehensive control mechanisms. Later, the groundbreaking works of Kalman in the 1960s elucidated the principles of optimal control, introducing a new paradigm in which control strategies could be theoretically optimal and practically effective even in the face of system uncertainties [111]. This rich tapestry of advancements underscores the profound significance and growing complexity of control strategies tailored for the sophisticated elements within complex systems.

The journey of control strategies in complex systems has been a testament to the evolving nature of our understanding and technological advancements. As we moved past the seminal works in linear controls of the early 20th century, the latter half of the century brought forth a paradigm shift. The 1970s and 1980s marked the rise of non-linear and adaptive control theories [112]. These

theories, while groundbreaking, addressed the glaring limitations of their linear counterparts, especially when applied to systems exhibiting chaotic or unpredictable behaviors. Around the same period, the development of the H-infinity method provided a robust framework, capable of handling uncertainties and disturbances inherent in real-world systems [113]. The turn of the century witnessed the confluence of these methodologies with computational tools and algorithms, paving the way for hybrid control strategies that effectively leverage both analytical models and data-driven insights [114]. This evolutionary path, with its myriad innovations, attests to the relentless pursuit of precision and adaptability in controlling the multifaceted dynamics of complex systems.

In recent years, the landscape of control strategies for complex systems has been markedly shaped by the fusion of traditional methodologies with emerging technologies. Model Predictive Control (MPC) [115], which leverages a model of the system to predict future outcomes and adjust control inputs accordingly, has seen widespread adoption across various sectors, from energy optimization in smart grids to autonomous vehicle navigation [116, 117]. Simultaneously, there's been a surge in the application of reinforcement learning (RL) in control systems, where agents learn optimal control policies by interacting with their environment, demonstrated prominently in applications like robotics and game playing [118, 119]. Furthermore, the advent of networked control systems, which use networks for control loop feedback, is reshaping decentralized control, especially pertinent in distributed systems like sensor networks or multi-agent systems [120]. Deep learning, too, is making inroads into this arena, facilitating the modeling and control of systems with high-dimensional inputs and intricate interdependencies, showcased in its application to tasks like speech recognition or image processing [6]. In essence, the current epoch of control strategies is characterized by a harmonious blend of time-tested methodologies and avant-garde algorithms,

driving unparalleled precision and adaptability in managing today's sophisticated complex systems.

Despite the notable advancements in control strategies for complex systems, several persistent challenges continue to shape the trajectory of future research in this arena. One of the predominant challenges is the trade-off between control precision and computational overhead, especially in real-time systems where delay or computational constraints might impede optimal control [121]. Additionally, in many systems, especially in sectors like healthcare, the nonlinearity and multi-scale nature of the processes can confound conventional control strategies. In healthcare contexts, designing control strategies becomes even more intricate. Treatment regimens and therapeutic interventions must be tailored not just based on the immediate symptoms, but also considering long-term implications, patient-specific variabilities, and potential side effects, posing significant hurdles to the formulation of universally effective control policies [122]. Moreover, the inherent variability in human responses demands adaptive strategies that can learn and evolve in real-time. Ethical considerations, especially in areas like healthcare or autonomous systems, further complicate the design space, as decisions made by control systems can have profound societal implications [123]. As we peer into the future, a concerted focus on interdisciplinary collaboration, leveraging domain knowledge, and embracing the potential of emerging technologies will be paramount to surmount these challenges, heralding a new era of robust and ethical control strategies for an increasingly complex world.

2.4 Summary of Research Gaps

2.4.1 Domain Knowledge Integration in Machine Learning

- The first gap is *black-box dilemma*. Many state-of-the-art ML models, particularly deep learning architectures, operate as "black boxes". Their internal workings are often

obscured, making it challenging to interpret and understand the decisions they make. In many scientific and medical applications, interpretability is not just a luxury but a necessity.

- The second gap is *harmonizing granularity*. Finding the right balance between the specificity of domain knowledge and the generalizability of ML models is a persistent challenge. Integrating overly specific domain insights can result in overfitting, where models perform well on training data but fail to generalize. Conversely, overly broad integration might miss essential domain-specific subtleties.
- The third gap is *effective embedding of domain knowledge*. Current techniques to incorporate domain knowledge into ML architectures vary, from modifying neural network architectures to informed feature engineering. Identifying the most effective methods for different applications remains an open question.

2.4.2 Multi-Scale and Nonlinear Dynamics Modeling

- The first gap is *scale bridging*: Efficiently bridging between various scales, both temporal and spatial, remains a significant challenge. Coherent integration between microscopic interactions and macroscopic behaviors is yet to be achieved seamlessly.
- The second gap is *inherent complexity*: Nonlinear systems display behaviors like chaos and bifurcations, while multi-physics systems often exhibit complex interactions between different physical phenomena. Capturing these intertwined behaviors is a persistent challenge.
- The third gap is *validation and verification*. Validating multi-scale, multi-physics models against experimental data is notoriously challenging due to the breadth of dynamics they capture. Robust methodologies for model validation are essential.

- The last gap is *physical process interactions*. Multi-physics models need to consider how different physical phenomena interact, influence, and possibly counteract each other. Current models might capture individual processes well but falter when integrating multiple processes together.

2.4.3 Control Strategies for Complex Systems

- The first gap is *adaptability and flexibility*. Control strategies often struggle to adapt to rapidly changing dynamics or unforeseen disturbances within complex systems. Developing adaptive controls that can adjust in real-time to changing system states is crucial.
- The second gap is *multi-objective optimization*. Complex systems often have multiple conflicting objectives. Designing control strategies that can optimize multiple objectives simultaneously, without compromising system stability, is a challenging frontier.
- The third gap is *uncertainties and noise*. Complex systems are inherently subjected to uncertainties and external noise. Control strategies that are robust to these uncertainties, ensuring stability and performance even under adverse conditions, are essential.
- The last gap is *integration in healthcare*. In healthcare, the challenge amplifies where treatment regimens and therapeutic interventions serve as control mechanisms. There's a need to ensure that these interventions are optimally timed and dosed to achieve the desired therapeutic outcomes while minimizing side effects.

Chapter 3: Research Methodologies

In contemporary research landscapes, the study of complex systems necessitates a delicate fusion of domain knowledge, sophisticated algorithms, and precise modeling. As our understanding of such systems advances, the associated intricacies magnify, revealing research gaps that persist despite rapid technological evolution. Addressing these gaps requires a meticulously crafted methodology—a roadmap for discovery—that not only targets these deficiencies but also weaves the solutions into a cohesive tapestry of understanding. This chapter introduces and elaborates on the proposed research methodology for this dissertation, centralizing around the theme of "domain-informed sensor-based data-driven modeling for complex systems". The structure of the methodology is embodied in a comprehensive overview Figure 3-1, this visual representation the convergence of the three primary research directions:

- The first direction is *integration of machine learning with domain knowledge*, emphasizing the synergy between domain-specific insights and advanced algorithms to strengthen predictive power.
- The second direction is *multi-physics and multi-scale dynamics modeling*, probing the intricate scales and physical processes in complex systems to derive robust models.
- The third direction is *advanced control strategies for system robustness and optimization*, forming methods to ensure systems retain efficiency in dynamic environments.

The methodology is enriched by two translational research projects: (1) Real-Time Monitoring and Diagnosis Of COVID-19 Using Magnetic Respiratory Sensing Technology and Machine Learning, and (2) Multifractality in Surface Potential for Cancer Diagnosis.

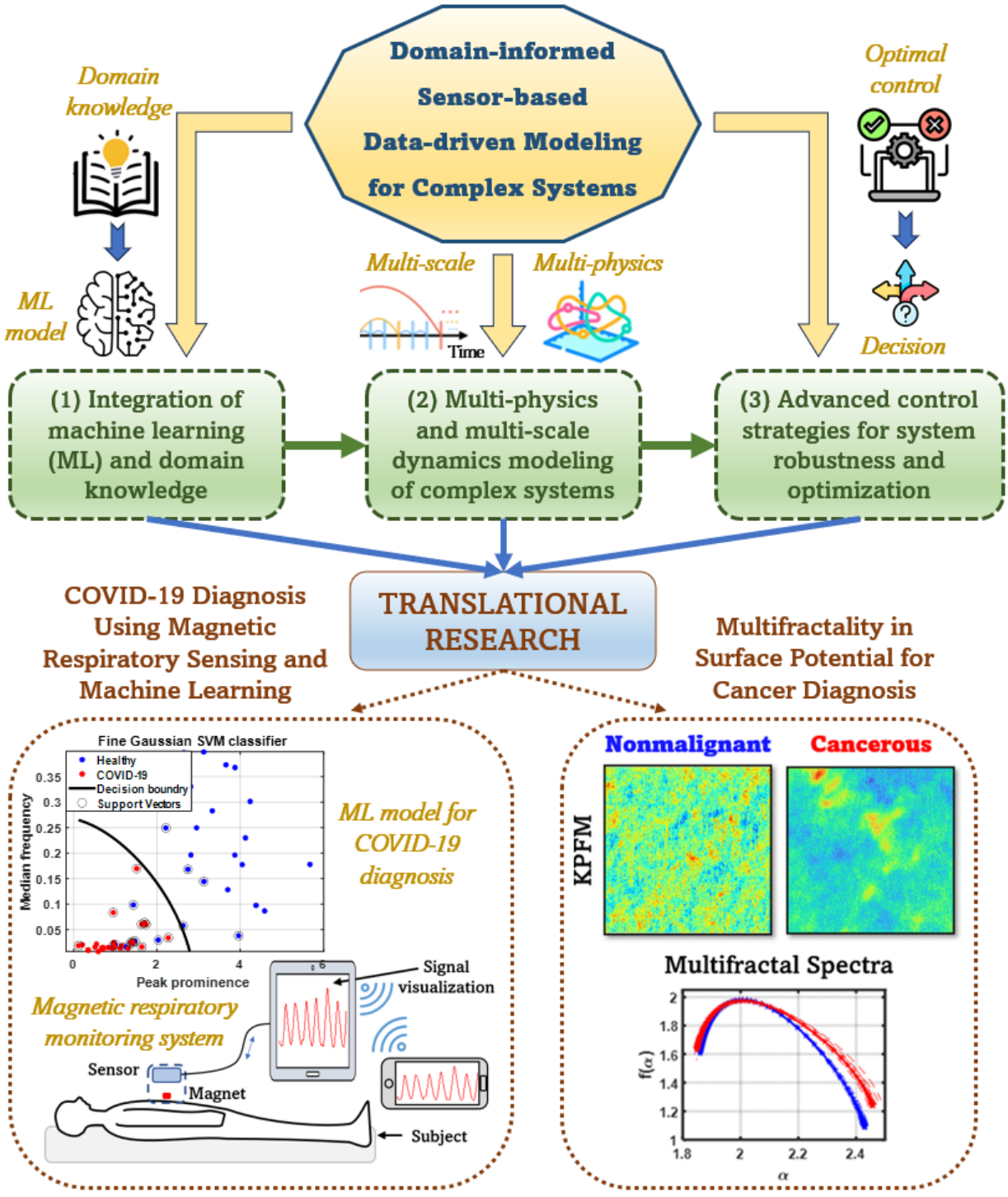

Figure 3-1 Overview of the research methodologies. The central theme of this dissertation is "domain-informed sensor-based data-driven modeling for complex systems". The methodology is divided into three primary research directions: (1) integration of machine learning with domain knowledge to enhance predictive accuracy and generalizability, (2) delving deep into multi-physics and multi-scale dynamics for a comprehensive modeling of complex systems; and (3) development and application of advanced control strategies

3.1 Integration of Machine Learning with Domain Knowledge

The domain of complex systems research underscores the pressing need to combine ML with domain knowledge. While ML excels in processing vast datasets, it often falls short in interpretability without domain insights. On the flip side, domain-centric models, isolated from ML's flexibility, may struggle with evolving data. Addressing this, our research seeks a cohesive approach, integrating these two paradigms essential for untangling complex systems. To overcome the identified research gaps, we have proposed 3 pivotal works:

- The first work is *Probabilistic Domain-Knowledge Modeling of Disorder Pathogenesis for Dynamics Forecasting of Acute Onset* [124]. Traditional ML models in medical diagnostics have inadequately harnessed the depth of domain knowledge on disease pathogenesis, primarily due to the complexity and variability inherent to individual patients. Our innovative Pathogenesis Probabilistic Graphical Model (PPGM) bridges this divide. It integrates patient-specific data with domain-centric pathogenetic knowledge, enhancing both interpretability and prediction accuracy. Such a synthesis ensures models not only capture intricate patterns but are also rooted in tangible medical contexts, a step forward in enhancing forecasting capabilities for disorders like OSA and PAF. This work will be explored in Chapter 4.
- The second work is *A Physics-informed Latent Variable Model of Corrosion Growth in Oil and Gas Pipelines* [125]. Corrosion modeling in pipelines has long grappled with inherent stochasticity and the challenge of aligning observational data with hidden physics-based variables. Conventional models often resort to assumptions that may not truly represent the corrosion processes. Our approach, combining physics-informed insights with data-driven methodologies, offers a holistic perspective on corrosion dynamics. It ensures that

predictions about corrosion growth are not merely data-driven but also anchored in authentic physical principles, ensuring a more comprehensive and reliable model for corrosion management. This work will be elaborated in Chapter 5.

- The third work is *A Domain-Knowledge Modeling of Hospital-Acquired Infection Risk in Healthcare Personnel from Retrospective Observational Data: a Case Study for COVID-19* [126]. Hospital-acquired infections present a significant risk to healthcare professionals worldwide. Traditional risk models, while informative, may not holistically incorporate domain-specific intricacies tied to real-world healthcare scenarios. By incorporating domain knowledge with empirical data-driven paradigms, our model presents a more nuanced understanding of infection risks. By quantifying individual and population-level risks grounded in domain insights, this work aids in optimizing strategies for PPE allocation, healthcare worker safety, and staffing. This work has been fully reported in my master's thesis in Industrial Engineering and Management at North Dakota State University.

3.2 Multi-Physics and Multi-Scale Dynamics Modeling

The realm of complex systems is replete with phenomena that span multiple scales and physical principles. To unravel these intricacies, innovative modeling techniques are paramount. Below are our three groundbreaking works that address these challenges:

- The first work is *A Noise-Robust Koopman Spectral Analysis of an Intermittent Dynamics Method for Complex Systems: A Case Study in Pathophysiological Processes of Obstructive Sleep Apnea* [127]. This work leverages the Koopman operator theory and the HAVOK model [128] to investigate chaotic dynamics, specifically in the context of intermittent forcing. The novel methodology proposed stands out for its ability to

characterize varying intermittent dynamics modes via spectral decomposition and wavelet analysis. We apply our method to the study of obstructive sleep apnea (OSA), unveiling a strong correlation between active forcing and the occurrence of hypopnea-apnea events. With its noise-robustness and aptitude to uncover intricate dynamics, this method provides a refined lens to peer into the complexities of systems like OSA, allowing for a deeper understanding and enhanced predictability of the pathophysiological nonlinear dynamics. This work will be explored in Chapter 6.

- The second work is *Detecting Transition to Turbulence in Intracranial Aneurysms by Optimized Dynamic Mode Decomposition*. This research employs the Optimized Dynamic Mode Decomposition (OptDMD) [129] to study the inflow jet dynamics within brain aneurysms. By harnessing high-resolution Computational Fluid Dynamics (CFD) data, the dynamic modes of the inflow jet are analyzed. The emphasis is on proving that these dynamic modes are shaped not just by the parent artery's hemodynamics but also by interactions with the distal wall. By implementing the OptDMD, a clearer understanding of blood flow patterns in brain aneurysms is attained. The insights have the potential to revolutionize clinical practices and diagnostic methodologies concerning intracranial aneurysms. This work will be elaborated in Chapter 7.
- The third work is *Noise-Robust Optimal Sampling Strategy for Multi-scale Complex Systems Using Deep Reinforcement Learning*. The study introduces a deep Q-learning based reinforcement learning framework crafted for multi-scale complex systems. This novel strategy dynamically adapts to multi-scale intricacies and excels in noisy, high-dimensional scenarios. The utility and potency of this approach are illustrated through numerical studies on coupled oscillator systems. With its capability to delineate complex

dynamics and sample efficiently, this method offers a significant advancement in modeling and controlling multi-scale systems. Traditional sampling methods often fall short in capturing the essence of multi-scale systems, particularly in noise-prone scenarios. Our reinforcement learning model fills this gap by autonomously determining optimal sampling strategies, proving pivotal in understanding and controlling intricate dynamics. This work will be explored in Chapter 8.

3.3 Advanced Control Strategies for System Robustness and Optimization

The quest for achieving robustness and optimization in complex systems mandates innovative control strategies. Herein, we present our contributions that leverage advanced methodologies to reinforce system robustness and enhance optimization:

- The first work is *Noise-Robust Optimal Sampling Strategy for Multi-scale Complex Systems Using Deep Reinforcement Learning*. As mentioned in Section 3.2, the challenges inherent in modeling multi-scale systems traditionally involve the struggles with dynamic adaptability, noise tolerance, and computational efficiency. Addressing these challenges, our deep Q-learning based reinforcement learning framework emerges as an innovative control strategy. By dynamically adapting its sampling techniques, our framework tailors data acquisition to the intricate demands of system dynamics, thus offering enhanced control optimization. Its adaptability ensures comprehensive system feedback, enabling more precise and timely control adjustments, especially in high-dimensional systems where noise can greatly compromise control fidelity. Through its autonomic determination of the best data sampling strategy, the method not only elevates control precision but also optimizes computational resources, pushing the boundaries of current control strategies and paving the way for greater system robustness and optimization.

- The second work is *Adaptive Control Strategies in Therapeutic Intervention: A Multicentric Randomized Controlled Trial on Obstructive Sleep Apnea Management*. Leveraging data from the BestAIR study from *sleepdata.org*, our research investigates the therapeutic implications of apnea interventions on cardiovascular outcomes and unraveling the wider cardiovascular repercussions of sleep-disordered breathing. The BestAIR dataset allows for a multi-faceted analysis: comparing intervention effects, discerning variations in response based on pre-existing cardiovascular conditions, correlating adherence levels, and longitudinally assessing blood pressure trends. This perspective refines our understanding of the cardiovascular consequences of sleep disorders and the therapeutic efficacy of apnea interventions. This work will be explored in Chapter 9.

3.4 Translational Research

This section focuses on two prominent studies that highlight the potential of leveraging cutting-edge technology and advanced methods in domain-informed sensor-based data-driven modeling for complex systems for pressing real-world challenges in the realm of disease diagnosis.

- The first study is *Real-Time Monitoring and Diagnosis Of COVID-19 Using Magnetic Respiratory Sensing Technology and Machine Learning*. In the period of the COVID-19 pandemic, the urgent requirement for accurate, affordable, and non-invasive diagnostic tools became apparent. Addressing this, we combined the strengths of advanced magnetic respiratory sensing technology (MRST) with machine learning. MRST's precision in measuring breathing patterns and rates provides valuable data, serving as a foundation for our model training. We explored various machine learning models, including support vector machines, random forest, and deep learning, to create a versatile diagnostic system that ensures adaptability to diverse healthcare contexts. The resulting system demonstrated

remarkable diagnostic prowess, identifying COVID-19 respiratory abnormalities with over 90% accuracy. Such innovative sensor technology, ready for deployment in various healthcare settings, promises real-time patient monitoring, significantly augmenting healthcare responses during pandemics.

- The second study is *Multifractality in Surface Potential for Cancer Diagnosis* [130]. Cancer diagnosis, while traditionally reliant on morphological indicators, is witnessing a revolution with the incorporation of electrical and biochemical cell/tissue properties via high-resolution biomedical imaging. In our study, we examined human ovarian cancer cells through Kelvin probe force microscopy (KPFM), capturing detailed surface potential variations. But the true breakthrough was our use of multifractal analysis. By adopting an adaptive versus median threshold for image binarization, we refined our ability to differentiate malignant from non-malignant cells. The discovery of multifractality in cancer cells not only opens a new frontier in cancer diagnosis but also heralds the promise of a novel biomarker, potentially transforming how we approach cancer diagnostics. Both works are elaborated upon in Chapter 10 of this dissertation.

3.5 Summary of Novel Contributions

3.5.1 Integration of Machine Learning with Domain Knowledge

- The first is *synergy between domain insights and algorithms*. A hallmark of this research direction is the amalgamation of domain-specific knowledge with the power of machine learning algorithms. This convergence has led to models that not only predict but also interpret complex phenomena with enhanced accuracy.

- The second is *redefining predictive power*. By infusing domain insights into machine learning frameworks, a notable advancement in predictive capability was achieved. This represents a paradigm shift in how machine learning models are designed and validated.
- The third is *bridging the gap between theory and data*. This research has emphasized the importance of not solely relying on data-driven approaches but also enriching them with domain expertise, resulting in holistic models with greater real-world relevance.

3.5.2 Multi-Physics and Multi-Scale Dynamics Modeling

- The first is *decoding complex systems*. This direction undertook the daunting task of understanding complex systems that operate across multiple scales and are governed by various physical processes. The models developed provide a nuanced view of these systems, capturing their intricate behaviors.
- The second is *holistic representation of systems*. By considering both multi-physics and multi-scale dynamics, the research offers a comprehensive modeling approach. This stands in contrast to conventional models that might overlook critical interactions and scales.
- The third is *towards robust models*. The deep dive into the physical processes inherent in complex systems has paved the way for models that are both resilient and reflective of real-world systems.

3.5.3 Advanced Control Strategies for System Robustness and Optimization

- The first is *innovative control mechanisms*. The research introduced groundbreaking control strategies designed to ensure systems maintain stability even under unpredictable and dynamic environments.

- The second is *optimization in dynamic contexts*. Beyond just stability, the focus has been on ensuring systems operate optimally, adjusting and adapting to changing conditions. This dynamic optimization is a testament to the adaptability of the devised strategies.
- The third is *ensuring real-world robustness*. The emphasis has always been on real-world application. The developed control strategies are not just theoretical constructs but have tangible implications for diverse domains, from engineering systems to healthcare processes.

Lastly, the translational research includes two studies:

- The first is *real-time COVID-19 monitoring and diagnosis*. A standout contribution that marries magnetic respiratory sensing technology with machine learning. In the face of the COVID-19 pandemic, this work showcased how timely and innovative research can make a significant difference, offering over 90% diagnostic accuracy for detecting respiratory abnormalities linked to COVID-19.
- The second is *advances in cancer diagnosis*. By delving into the multifractality of surface potentials, a novel avenue for cancer diagnosis was introduced. Using high-resolution imaging techniques and innovative data processing, this work highlights the potential of recognizing new biomarkers for cancer, paving the way for transformative changes in oncological diagnostics.

Chapter 4: Probabilistic Domain-Knowledge Modeling of Disorder Pathogenesis for Dynamics Forecasting of Acute Onset [1]

Disease pathogenesis, a type of domain knowledge about biological mechanisms leading to diseases, has not been adequately encoded in machine-learning-based medical diagnostic models because of the inter-patient variabilities and complex dependencies of the underlying pathogenetic mechanisms. We propose 1) a novel pathogenesis probabilistic graphical model (PPGM) to quantify the dynamics underpinning patient-specific data and pathogenetic domain knowledge, 2) a Bayesian-based inference paradigm to answer the medical queries and forecast acute onsets. The PPGM model consists of two components: a Bayesian network of patient attributes and a temporal model of pathogenetic mechanisms. The model structure was reconstructed from expert knowledge elicitation, and its parameters were estimated using Variational Expectation-Maximization algorithms. We benchmarked our model with two well-established hidden Markov models (HMMs) – Input-output HMM (IO-HMM) and Switching Auto-Regressive HMM (SAR-HMM) – to evaluate the computational costs, forecasting performance, and execution time. Two case studies on Obstructive Sleep Apnea (OSA) and Paroxysmal Atrial Fibrillation (PAF) were used to validate the model. While the performance of the parameter learning step was equivalent to those of IO-HMM and SAR-HMM models, our model forecasting ability was outperforming those two models. The merits of the PPGM model are its representation capability to capture the dynamics of pathogenesis and perform medical inferences and its interpretability for physicians. The model has been used to perform medical

[1] This chapter was published in Artificial intelligence in medicine, 2021, Vol. 115, p.102056. Permission is included in Appendix C.

queries and forecast the acute onset of OSA and PAF. Additional applications of the model include prognostic healthcare and preventive personalized treatments [124].

4.1 Introduction

Pathogenesis-based machine learning (ML) models have been established to incorporate pathogenesis domain knowledge into the ML pipeline and enable novel knowledge discovery and feature engineering [131]. Many pathogenesis insights have been gained by using various ML techniques, *e.g.*, applying the weighted gene co-expression network analysis to analyze the gene expression associated with asthma pathogenesis [132], achieving novel insights regarding neurodegeneration pathogenesis by deploying random forest classification models [133], and using different exploratory and predictive models to draw novel insights about the SARS-COV-2 pathogenesis [134]. For feature engineering, domain knowledge of pathogenesis has been utilized to extract features from raw data. For example, useful pathogenesis-based features were extracted for automated diagnosis of lumbar neural foraminal stenosis [135] and cardiovascular diseases [136]. Furthermore, recent advances in omics and the data science field have facilitate the understanding of disease mechanisms, using methods such as ingenuity pathway analysis (IPA) and deep learning to identify molecular and disease pathways of pathogenesis [137]. However, very few methods are concerned with pathogenesis domain knowledge representation and the interpretability of pathogenesis-based ML models.

Encoding disease pathogenesis knowledge into interpretable machine learning (ML) models is a challenging task due to the inherent issues of multifactorial predictors and stochastic temporal dependencies of the underlying pathogenic mechanisms. To encode the domain knowledge in healthcare, traditional ML representations, such as ontologies [138], first-order logic rules [139], temporal tree for similarity calculation between patients [140], or probabilistic

reasoning systems [141-143], have been utilized to achieve plausible interpretation (*e.g.*, causal reasoning for a disease). Today, clinical knowledge-based computer-assisted systems, including MYCIN [144], CADUCEUS [145], and Internist-I [146], are established as reasoning systems for medical consultations. However, these representations are not able to handle discrete multi-variate inputs and outputs to capture the interference of patient-specific characteristics, which directly govern the behaviors of pathogenesis. The optimization of these representations for task specifications, such as answering medical queries and forecasting the disease onset, is still a challenging issue. Modeling efforts to capture the stochastic dynamics underlying pathogenetic mechanisms have been made. However, linear models, such as ARIMA, ARMAX [147], m-gram models [148], or variable-length Markov models [149, 150], show limitations in capturing nonstationary and stochastic features. Black-box models, such as deep learning models [151, 152], parametric maps, or manifold learnings, are notoriously difficult to interpret [153]. Compared to classical models, state-space models are superior in many aspects [154-157]. They can capture patient-specific, multifactorial predictors and stochastic dynamics of the disease pathogenesis while maintaining model interpretability for medical queries and prognosis.

We propose a probabilistic graphical model [158] that is based on integrating a state-space modeling approach and domain knowledge of individualized disease pathogenesis into a probabilistic framework to address the aforementioned challenges. The model exhibits a hierarchical structure with two layers: a static Bayesian network to model the distribution of patient attributes at the population level and a temporal model using a dynamic Bayesian network (DBN) to track the pathogenetic dynamics at the individual level of the underlying pathophysiological mechanism. This representation enables the characterization of the impact of patients' attributes on pathogenetic state variables, which varies dynamically over time, and the development of an

individualized model to better capture pathogenesis dynamics. Moreover, the model predictions are generated through prior assumptions about stochastic variable dependencies and the use of Bayes rule to update their beliefs about data. This property is essential in a high-risk environment such as healthcare, where physicians can evaluate the reliability of the predictions. Bayesian networks have been extensively applied in various areas such as genomics [159, 160], diagnosis, prognosis, disease outcome prediction [161], and treatment optimization [162, 163]. One superior characteristic of Bayesian networks over traditional ML methods is their ability to incorporate domain knowledge from experts to construct interpretable model structure even in cases where data is limited. The hierarchical structure of this framework is transparent in describing complex relationships between stochastic variables, in which human experts, such as doctors, are capable of understanding and assessing the structure semantics and properties. Our major contributions of the proposed method are: (1) a probabilistic graphical domain-knowledge representation of multivariate predisposing factors of the pathogenetic mechanisms, (2) a pathogenesis-knowledge-integrated inference paradigm to perform medical inference and k-step-ahead forecast of acute onset.

4.2 Methodologies

4.2.1 Study Overview

Figure 4-1 illustrates the proposed methods. This block diagram has been designed to convey the detailed steps taken to implement the proposed model. It describes the general representation of a 2-layer pathogenesis representation, model learning step, and model evaluation step. Accordingly, the pathogenesis representation has two layers: (1) a Bayesian network of patient attributes layer that models the inter-relations of predisposing factors and pathogenetic attributes, and (2) a temporal model of pathogenetic mechanism layer that captures the

pathogenetic dynamics of acute disorders. We will take four main steps: (1) reconstruct PPGM 2-layer representations; (2) formulate their inference paradigms to answer conditional medical queries and to forecast disease onsets; (3) accomplish both model structure learning and parameter learning, which are shared by both layers; and lastly (4) perform model validations by examining two case studies: obstructive sleep apnea (OSA) and paroxysmal atrial fibrillation (PAF).

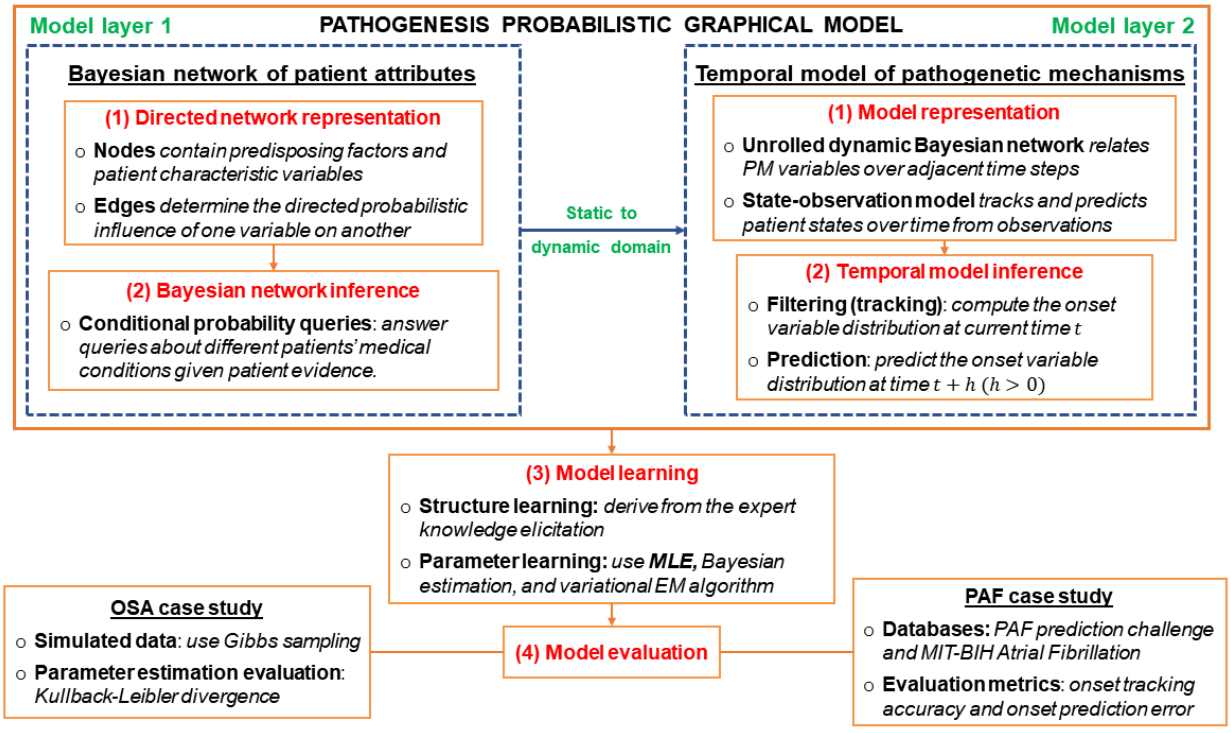

Figure 4-1 Block diagram of the PPGM model composed of two sub-models with 4 main steps

4.2.2 PPGM Model

The Bayesian network of patient attributes is modeled from two pathogenesis properties. First, using predisposing factors characterizing a patient's vulnerabilities to a certain disease which include risk factors (***RF***), structural abnormalities (***SA***), and functional abnormalities (***FA***). Structural abnormalities characterize the structural or anatomical changes of the body (*e.g.*,

fibrosis, atrial dilatation), while functional abnormalities are the biological dysfunction of a system at the organ, tissue, or molecular level (*e.g.*, atrial remodeling). These factors directly influence the disease progress and exacerbation [164, 165], specifically the disease pathogenetic mechanisms. Next, epidemiological observations ***(EO)*** are the variable realizations obtained from clinical tests or cohort studies that are utilized to analyze and determine the distribution of disease conditions [166]. These observations help to infer the distribution of relevant variables in ***RF, SA,*** and ***FA*** subsets. The ***RF, SA, FA*** and ***EO*** variables were represented as four subsets of random variables (illustrated in Figure 4-2).

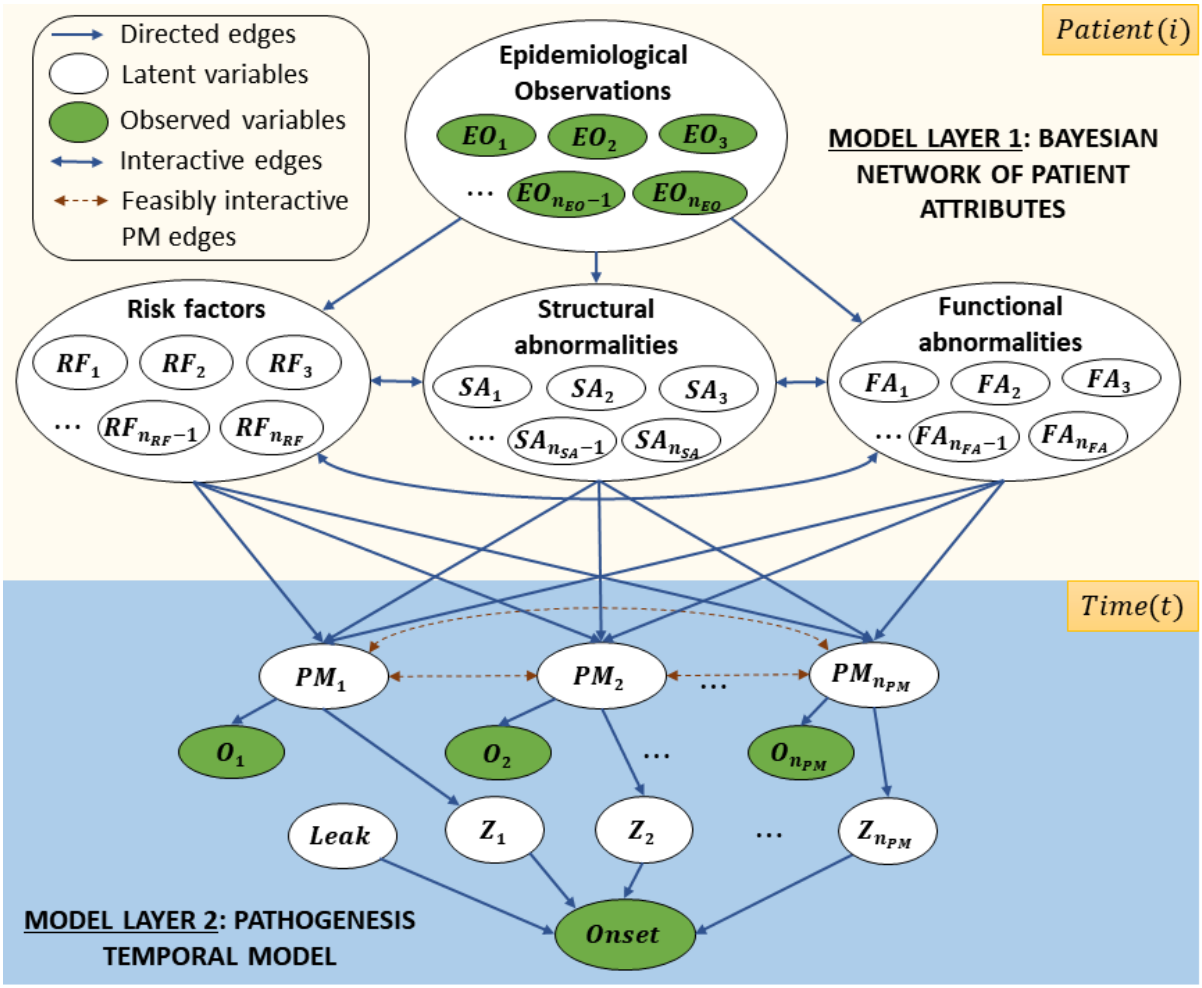

Figure 4-2 The PPGM model is comprised of two layers: static layer (top) and dynamic layer (bottom) with two corresponding models.

We defined the static variable set as $\boldsymbol{\mathcal{X}}_{static} = \{\{RF_i\}, \{SA_i\}, \{FA_i\}, \{EO_i\}\} = \{X_1, X_2, \dots, X_{n_{static}}\}$. Here, a Bayesian network $\boldsymbol{\mathcal{G}}$ [16] was selected for the representation of patient attributes. The variables in $\boldsymbol{\mathcal{X}}_{static}$ were denoted as the nodes and possible directed probabilistic influences $X_i \rightarrow X_j$ were represented as edges in the network. The value set of a random variable X_i is denoted as $Val(X_i)$. The influence of variable X_i (parent node) on another variable X_j (child node) can be cast as a conditional probability distribution (CPD) $P(X_j|X_i)$. The concept of CPD yields finer-grained independencies, where the joint distribution over $\boldsymbol{\mathcal{X}}_{\boldsymbol{static}}$ variables that factorizes over the graph $\boldsymbol{\mathcal{G}}$ can be derived using the Bayesian network chain rule as:

$$P(X_1, X_2, \dots, X_{n_{static}}) = \prod_i^{n_{RF}} P(RF_i|Pa_{RF_i}) \prod_i^{n_{SA}} P(SA_i|Pa_{SA_i}) \prod_i^{n_{FA}} P(FA_i|Pa_{FA_i}) \quad (4.1)$$

where Pa_{X_i} is the set of X_i's parent nodes. In Equation 4.1, the component $\prod_i^{n_{FA}} P(EO_i|Pa_{EO_i}) = 1$ because the subset $\boldsymbol{EO}$ includes observable variables. Next, the conditional probability query of patient attributes, $P(\boldsymbol{PA}|\boldsymbol{EO} = \boldsymbol{\zeta})$, is defined by the Bayes rule as:

$$P(\boldsymbol{PA}|\boldsymbol{EO} = \boldsymbol{\zeta}) = P(\boldsymbol{PA}, \boldsymbol{\zeta})/P(\boldsymbol{\zeta}) \quad (4.2)$$

where $\boldsymbol{PA} \subset \{\boldsymbol{RF}, \boldsymbol{SA}, \boldsymbol{FA}\}$ is a subset of patient attributes and $\boldsymbol{\zeta}$ is the realization vector of $\boldsymbol{EO}$. Let $\boldsymbol{W} = \boldsymbol{\mathcal{X}}_{\boldsymbol{static}} \backslash (\boldsymbol{PA} \cup \boldsymbol{EO})$, then $P(\boldsymbol{PA}, \boldsymbol{\zeta})$ was computed by marginalizing out $\boldsymbol{W}$ from the joint distribution $P(\boldsymbol{PA}, \boldsymbol{\zeta}, \boldsymbol{W})$. The conditional probability query $P(\boldsymbol{PA}|\boldsymbol{EO} = \boldsymbol{\zeta})$ was estimated using the exact junction-tree inference algorithm [158] that employed the Clique Trees structure to manipulate CPDs over the variables in $\boldsymbol{\mathcal{X}}_{static}$. Next, the pathogenesis dynamics were modeled as the system dynamic states using a temporal set $\boldsymbol{\mathcal{T}} = \{T_i | 1 \leq i \leq n_{temp}\}$. The notation $\boldsymbol{\mathcal{T}}^{(t)}$ is the instantiation of $\boldsymbol{\mathcal{T}}$ at time t, where $\boldsymbol{\mathcal{T}}$ has 3 subsets and 2 variables. The three subsets are: 1) pathogenetic mechanism states $\boldsymbol{PM}^{(t)} = \{PM_i^{(t)} | 1 \leq i \leq n_{PM}\}$ where n_{PM} is the number of

pathogenetic mechanisms, 2) dynamic observations $\boldsymbol{O}^{(t)} = \left\{O_i^{(t)} | 1 \leq i \leq n_{PM}\right\}$, and 3) filters $\boldsymbol{Z}^{(t)} = \left\{Z_i^{(t)} | 1 \leq i \leq n_{PM}\right\}$. The two variables are the $Onset^{(t)}$ and $Leak^{(t)}$ which characterize the probability of onset at time t and the un-modelled causes. This establishment, based on the Noisy-OR graphical model [167], was used to capture the non-deterministic disjunctive interactions between the causes of mechanisms leading to onset as shown in Figure 4-3.

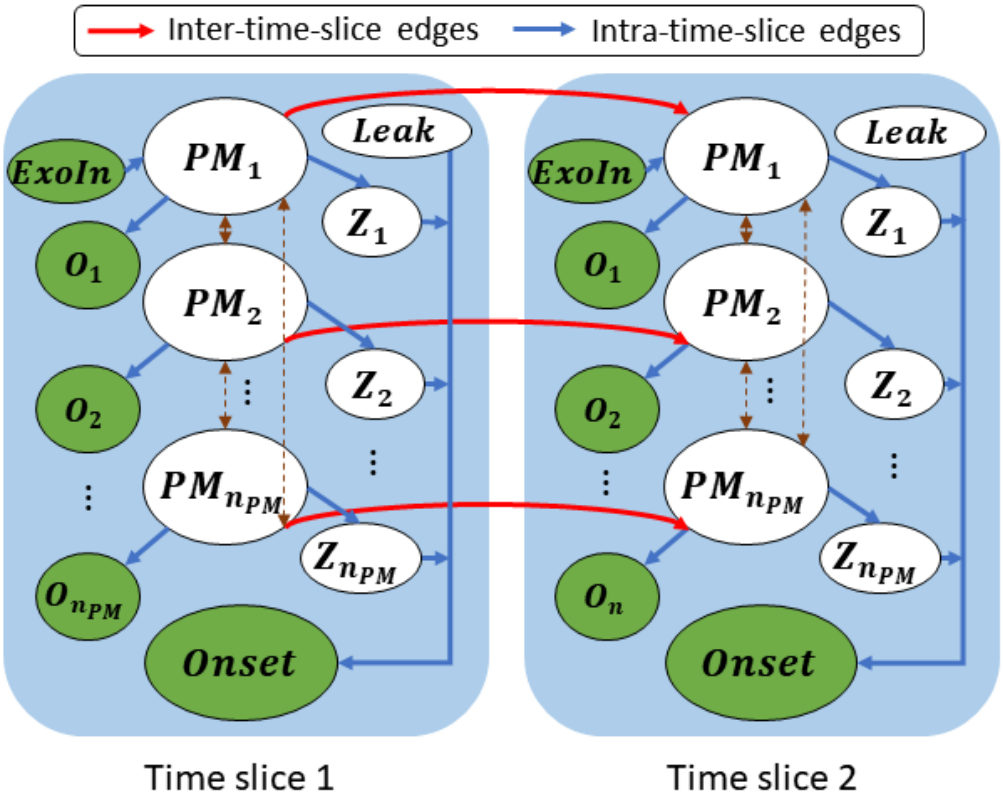

Figure 4-3 Two-time-slice Bayesian network (2TBN) model. The model consists of 3 main components: the transition model $P(\boldsymbol{PM}_i'|\boldsymbol{PM}_i)$ characterized by inter-time-slice edges $\boldsymbol{PM}_i \rightarrow \boldsymbol{PM}_i'$, the observation model $P(\boldsymbol{O}_i|\boldsymbol{PM}_i)$ depicted by intra-time-slice edges $\boldsymbol{PM}_i \rightarrow \boldsymbol{O}_i$, and the Noisy-OR model including filter nodes $\boldsymbol{Z}$, $\boldsymbol{Leak}$ node, and $\boldsymbol{Onset}$ node, which represents the independent pathogenetic pathways to onset

The states $\boldsymbol{PM}^{(t)}$ were deduced from the dynamic observations $\boldsymbol{O}^{(t)}$ (*e.g.*, bio-signals, airflow pressure, etc.). The onset presence probability was computed from the activation of

pathogenetic mechanisms, which were filtered by $\boldsymbol{Z}^{(t)}$ before reaching the $\boldsymbol{Onset}^{(t)}$ node by using the concept of inhibition probability – the probability that a pathogenetic mechanism cannot turn the onset on by itself. The interactions between the mechanisms denoted by dashed brown edges in Figure 4-3 were negligible for the PAF case because of the independence of the PAF mechanisms [168]. To model pathogenetic progression over time, we defined $\boldsymbol{\mathcal{T}}^{(t_1:t_2)} = \left\{\mathcal{T}^{(t_1)}, \mathcal{T}^{(t_1+1)}, \ldots, \mathcal{T}^{(t_2)}\right\}, (t_1 < t_2)$ as a set of variables $\left\{\boldsymbol{\mathcal{T}}^{(t)}: t \in [t_1, t_2]\right\}$, which model the pathogenetic trajectories from t_1 to t_2, *i.e.*, the joint probability distribution of $\boldsymbol{\mathcal{T}}^{(t_1:t_2)}$.

The space of possible trajectories can be complex and infinitely large; thus, three assumptions were established. First, time was discretized into time slices with time granularity Δ. The second was the assumption of a Markovian system [158], which states that PM_i satisfies the condition $PM_i^{(t+1)} \perp PM_i^{(0:t-1)} | PM_i^{(t)}$ ($\perp$ symbolizes the independence) for all $t \geq 0$ over trajectory distributions $P\left(PM_i^{(0)}, \ldots, PM_i^{(TS)}\right)$, abbreviated as $P\left(PM_i^{(0:TS)}\right)$. The third assumption was stationarity [158] of the system, *i.e.*, the transition probability $P(PM_i^{(t+1)} | PM_i^{(t)})$ is equal for all $t \in [0, TS]$, where TS is the number of total time slices. Piecewise-stationary methods can be used to solve the problem of nonstationary long sequential data. A 2-time-slice Bayesian network (2TBN) [158] was employed to model the pathogenetic state transitions and expanded to an unrolled dynamic Bayesian network (DBN). The $PM_i^{(t)}$ and $O_i^{(t)}$ variables were modeled by a state-observation model consisting of a transition model $P\left(PM_i^{(t+1)} \middle| PM_i^{(t)}\right)$ and an observation model $P\left(O_i^{(t)} | PM_i^{(t)}\right)$ (see Figure 4-3), in which the variables $O_i^{(t)}$ were conditionally independent of the past states $PM_i^{(0:t-1)}$ given the current states $PM_i^{(t)}$. This model has two well-established architectures: hidden Markov models (HMMs) [169] to represent transitions between hidden states and linear dynamical systems [158] to temporally update and predict continuous variables. We

modeled the personalized variables $\boldsymbol{RF}, \boldsymbol{SA}, \boldsymbol{FA}$ in the static domain as exogenous inputs (root CPD) to the temporal model in the time domain. These inputs were assumed to be observed either from the measured data or from the most probable values in their distributions. We denoted those exogenous inputs by $\boldsymbol{ExoIn}$, and they are the parents of the $\boldsymbol{PM}^{(t)}$ nodes.

Temporal inference including filtering and forecasting was performed for $\boldsymbol{PM}^{(t+h)}$, where $h > 0$ was the short-term forecasting step. The filtering goal was to iteratively update $P\left(PM_i^{(t+1)} \middle| o_i^{(1:t+1)}\right)$ and then forecast the future hidden state probability $P\left(PM_i^{(t+1)} \middle| o_i^{(1:t)}\right)$, where o_i is the realization of O_i. The variables $\boldsymbol{ExoIn}$ are not shown in the equations for notation simplicity. A forward propagation technique [158] was applied to compute $P\left(PM_i^{(t+1)} \middle| o_i^{(1:t+1)}\right)$:

$$\begin{aligned} P\left(PM_i^{(t+1)} \middle| o_i^{(1:t+1)}\right) &\propto P\left(o_i^{(t+1)} | PM_i^{(t+1)}\right) P\left(PM_i^{(t+1)} \middle| o_i^{(1:t)}\right) \\ &= P\left(o_i^{(t+1)} | PM_i^{(t+1)}\right) \sum_{PM_i^{(t)}} P\left(PM_i^{(t+1)} \middle| PM_i^{(t)}\right) P\left(PM_i^{(t)} \middle| o_i^{(t)}\right) \end{aligned} \tag{4.3}$$

Here, the 1-step prediction, $PM_i^{(t+1)} | \boldsymbol{o}_i^{(1:t)}$, was estimated from the prior belief state of $P\left(PM_i^{(t)} \middle| o_i^{(t)}\right)$ and transition probability $P\left(PM_i^{(t+1)} \middle| PM_i^{(t)}\right)$ using the marginalization technique. Next, the h-step ahead prediction $P\left(PM_i^{(t+h)} \middle| \boldsymbol{o_i}^{(1:t)}\right)$ was obtained by summing out $PM_i^{(t:t+h-1)}$ from the joint distribution $P\left(PM_i^{(t:t+h)} | o_i^{(1:t)}\right)$:

$$P\left(PM_i^{(t+h)} \middle| o_i^{(1:t)}\right) = \sum_{PM_i^{(t:t+h-1)}} P\left(PM_i^{(t:t+h)} | o_i^{(1:t)}\right) \tag{4.4}$$

Equation 4.4 involves the computation $P\left(PM_i^{(t+\delta)} | \boldsymbol{o}^{(1:t)}\right)$, where δ is the intermediate forecasting steps ($1 \leq \delta < h$), hence $P\left(PM_i^{(t+\delta)} | \boldsymbol{o}^{(1:t)}\right)$ was estimated as:

$$P\left(PM_i^{(t+\delta)}|o_i^{(1:t)}\right) = \sum_{PM_i^{(t+\Delta-1)}} P\left(PM_i^{(t+\delta)}|PM_i^{(t+\delta-1)}, o_i^{(1:t)}\right)P\left(PM_i^{(t+\delta-1)}|o_i^{(1:t)}\right) \quad (4.5)$$

The derivation of $P\left(PM_i^{(t+\delta)}|o_i^{(1:t)}\right)$ for Equation 4.5 is relatively similar to that of $P\left(PM_i^{(t+1)}\middle|o_i^{(1:t)}\right)$ in Equation 3. From Equation 4.4 and Equation 4.5, we yielded h-step ahead prediction of $PM_i^{(t)}$ as:

$$P\left(PM_i^{(t+h)}|o_i^{(1:t)}\right) = \sum_{PM_i^{(t:t+h-1)}} \prod_{\delta=1}^{h} \sum_{PM_i^{(t+\delta-1)}} \frac{P\left(PM_i^{(t+\delta)}|PM_i^{(t+\delta-1)}, o_i^{(1:t)}\right)}{P\left(PM_i^{(t+\delta-1)}|o_i^{(1:t)}\right)^{-1}} \quad (4.6)$$

The derivation of Equation 4.6 is elaborated in Appendix A. Next, the predictive CPD of the variable $Onset^{(t+h)}$ was modeled using the Noisy-OR model, and $P\left(Z_i^{(t+h)}\middle|PM_i^{(t+h)}\right)$ was computed for $1 \le i \le n_{PM}$ as:

$$P\left(Z_i^{(t+h)}\middle|PM_i^{(t+h)}\right) = \begin{cases} 0 \; if \; PM_i^{(t+h)} = 0 \\ 1 - \rho_i \; if \; PM_i^{(t+h)} = 1 \end{cases} \quad (4.7)$$

where ρ_i is the inhibition probability that the i^{th} pathogenetic mechanism itself cannot cause the onset. The other unmodeled cause that can trigger onset was denoted by the variable $Leak$ with $Leak^{(t)} = 1 - \rho_0 \; \forall t \in [0, TS]$. The probability that $Onset^{(t+h)} = 1$ is estimated as:

$$P\left(Onset^{(t+h)} = 1\middle|Z_1^{(t+h)}, Z_2^{(t+h)}, \dots, Z_{n_{PM}}^{(t+h)}\right) = 1 - \rho_0 \prod_{i=1:PM_i^{(t+h)}=1}^{n_{PM}} \rho_i \quad (4.8)$$

where $\rho_0 \prod_{i=1:PM_i^{(t+h)}=1}^{n_{PM}} \rho_i$ is the probability that no pathogenetic mechanism becomes activated and causes the onset with the assumption of independency between pathogenetic pathways. The forwards-backwards algorithm [170] was employed for unrolled DBN to compute the inference for all CPDs of interest. The model learning is illustrated in Appendix A.

4.2.3 Case Study Data Description

In the OSA case study, a simulated sample was generated from prespecified distributions with known parameters using Gibbs' sampling method [171] for evaluating the parameter learning process. For PAF, we selected the PAF Prediction Challenge Database [172] and the MIT-BIH Atrial Fibrillation Database [173] to validate and benchmark the performance of our proposed model with those from previous methods.

4.3 Results

4.3.1 OSA Case Study

We validated the proposed PPGM model using the OSA case study. The PPGM model was implemented using MATLAB software with the Bayesian network implementation from the Bayes Net Toolbox [174]. The structure of the model $\mathbb{M}^*$ and parameters were learned using the OSA pathophysiology proposed by previous works [175-177] and illustrated in Figure 4-4.

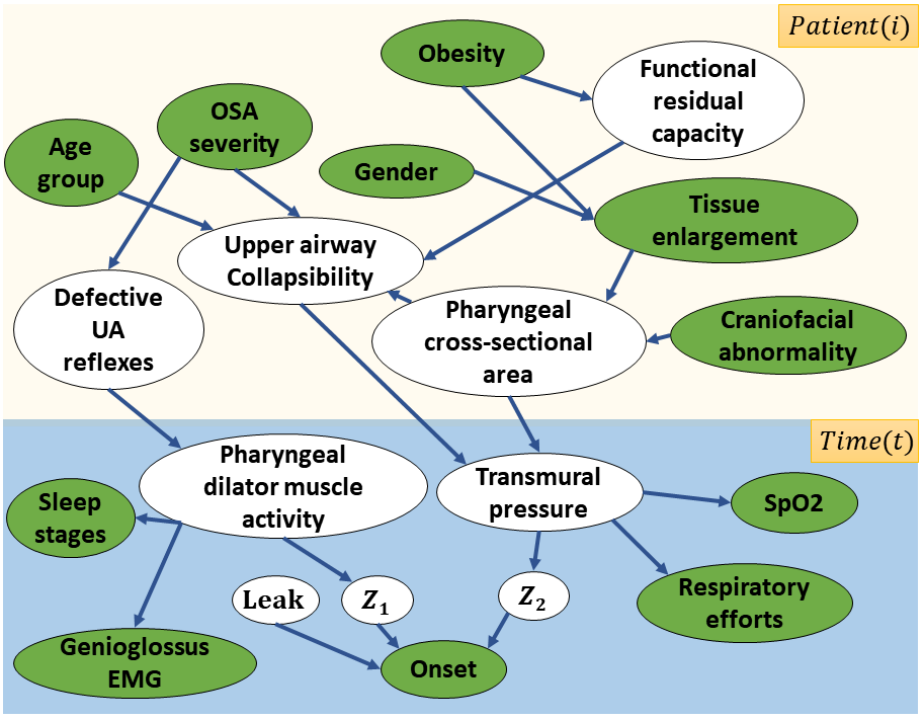

Figure 4-4 Representation of OSA PPGM model. The parameters were derived from the mentioned studies [175-177]

A simulated data set was sampled from the CPDs with known parameters using the Gibbs sampling method [171]. To reconstruct parameters $\boldsymbol{\Theta}^*$ from data, maximum likelihood estimation (MLE) and Bayesian estimation methods were used to estimate the parameters from the simulated instance set. Subsequently, Kullback-Leibler divergence (KLD) was estimated as an average over the parameters in the static network. From the estimated parameters $\widetilde{\Theta}$, the inference algorithms were validated by 4 distinct hypothetical patient groups that mimic real OSA patients [176, 177], namely mild OSA, moderate OSA, young severe OSA without craniofacial abnormality, senior severe OSA with craniofacial abnormality, as shown in Table 4-1. The variable acronyms are described in Appendix A - Table A-1.

Table 4-1 Patient evidence table of six variables in four cases

Cases	$\boldsymbol{CA}$	$\boldsymbol{OB}$	$\boldsymbol{G}$	$\boldsymbol{TE}$	$\boldsymbol{OS}$	$\boldsymbol{AG}$
Mild OSA	1	1	2	2	1	1
Moderate OSA	2	2	1	2	2	2
Young severe OSA without CA	1	3	2	2	3	1
Senior severe OSA with CA	2	3	2	2	3	3

Given the patient evidence, we subsequently computed the posterior probability distribution of 4 patient attributes $\boldsymbol{PA}$: defective reflexes **DUAR**, functional residual capacity $\boldsymbol{FRC}$, pharyngeal cross-sectional area $\boldsymbol{PCSA}$, and upper airway collapsibility $\boldsymbol{UAC}$, as illustrated in Figure 4-5. Overall, the results of four cases revealed significant correlations between OSA severity and the posterior distributions. For $\boldsymbol{DUAR}$, the probability of having defective upper airway reflexes $P(\boldsymbol{DUAR} = 2)$ rose from 0.37 to 0.96 when OSA conditions were exacerbated. Likewise, the chance of abnormal $\boldsymbol{FRC}$ increased with OSA severity, but there was no difference between the two last cases (probability 0.93) because $\boldsymbol{AG}$ and **CA** nodes do not influence $\boldsymbol{FRC}$.

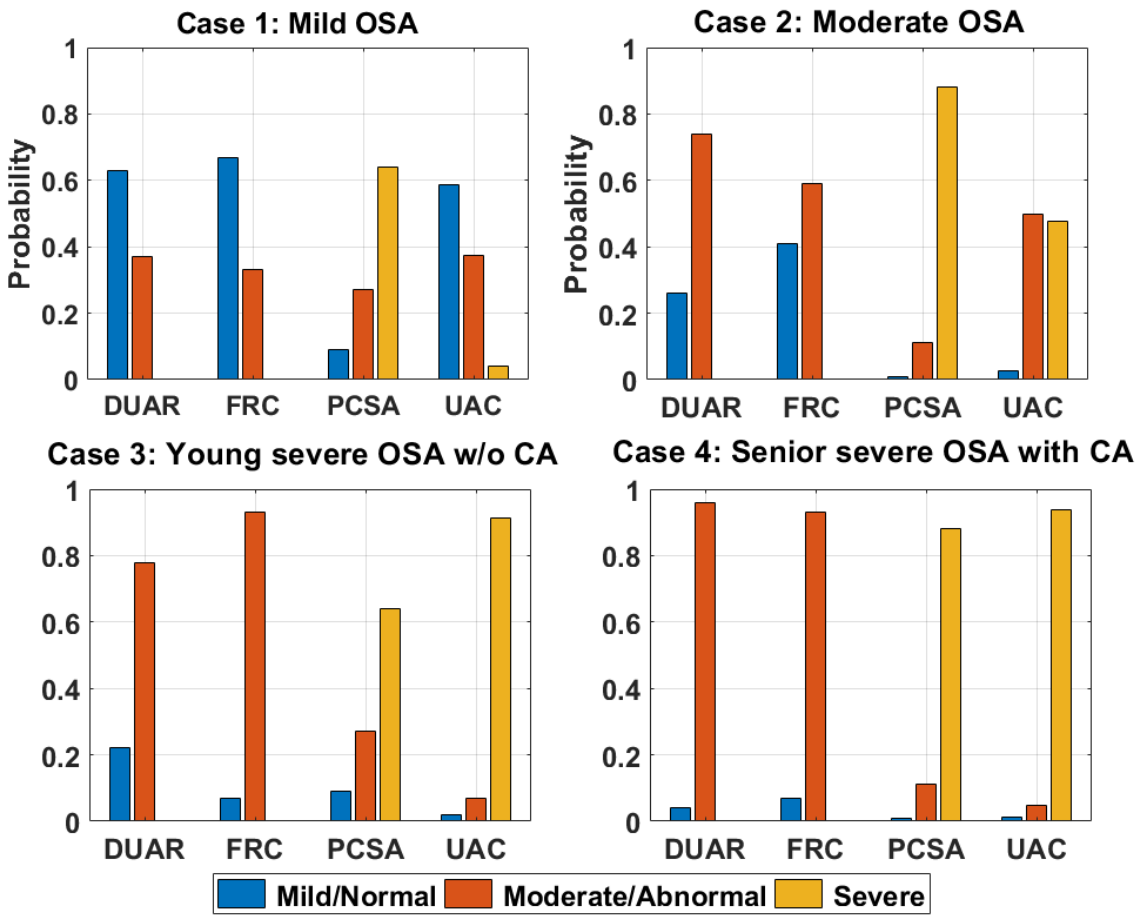

Figure 4-5 Posterior probability distribution of 4 hidden variables: defective reflexes $\boldsymbol{DUAR}$, functional residual capacity $\boldsymbol{FRC}$, pharyngeal cross-sectional area $\boldsymbol{PCSA}$, and upper airway collapsibility $\boldsymbol{UAC}$

4.3.2 PAF Case Study

To process electrocardiogram (ECG) data, we designed a 5th order Butterworth 0.5–30 Hz bandpass filter to eliminate noises and baseline wandering. Subsequently, the Hamilton-Tompkins algorithm [178-180] was employed to detect R peaks. We estimated their widths (duration), amplitudes, and areas to detect premature atrial complexes (PACs) beats, which are the first-order indicator of PAF onset [168]. The detector was used to identify various types of PACs (bigeminy, trigeminy, quadrigeminy, couplet, triplet, and isolated). The detailed classification of those PACs

beats and their significance were presented in the study [181]. To capture the behaviors of PACs, we define a feature called accumulation level $\boldsymbol{AL}^{(t)}$ of PACs as follows:

$$\boldsymbol{AL}^{(t)} = \sum_{i=1}^{n_{PAC}} \beta_j \, exp \, t_{ij} \tag{4.9}$$

where n_{PAC} is the total number of PAC beats occurring within the interval $[t-w, t]$ (w is the sliding window length), $\beta_{j,\boldsymbol{S}}$ is the weight corresponding the PAC type j^{th} ($1 \leq j \leq 6$), and t_{ij} is the relative occurrence time of PAC of the i^{th} beat and type j^{th} within the sliding window. The graphical structure $\mathbb{M}^*$, as shown in Figure 4-6, represents ectopic foci and reentry substrates pathophysiological mechanisms driving PAF onset and maintenance [168].

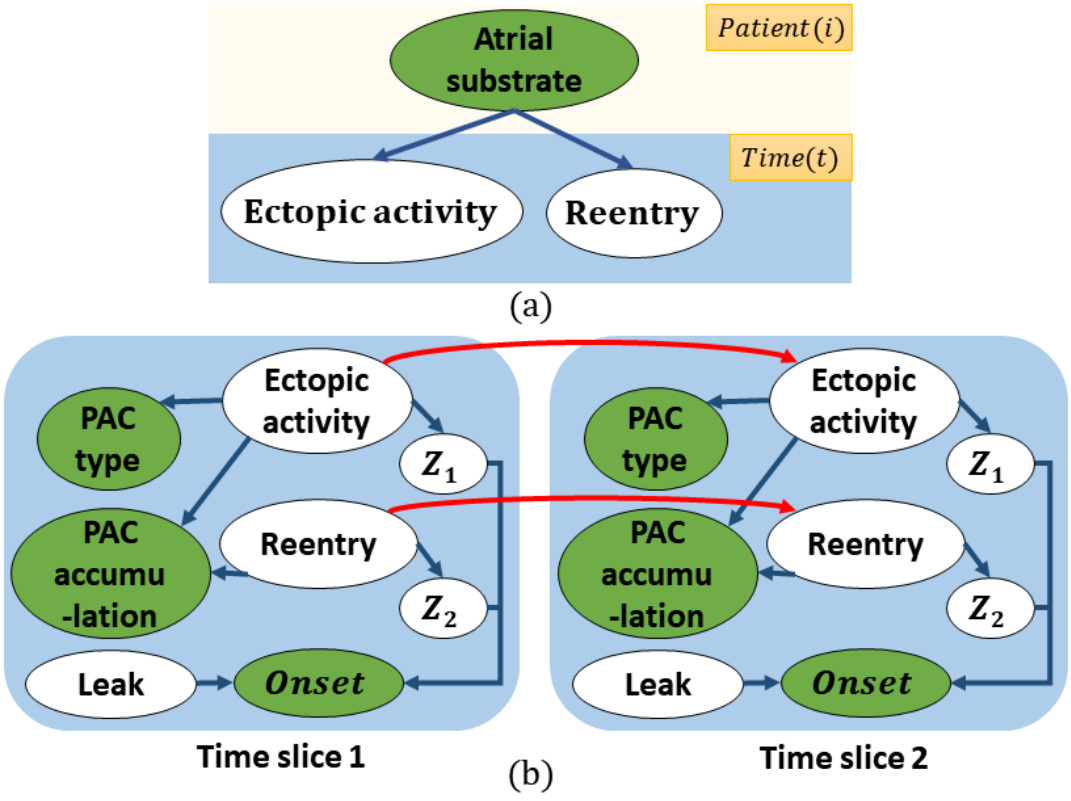

Figure 4-6 Representation of the PAF PPGM model: (a) PAF PPGM structure: atrial substrate is the main driving factor of two pathogenetic mechanisms of PAF ectopic activity and reentry. (b) PAF 2TBN model using the Noisy-OR model: $\boldsymbol{Ectopic\ activity}$ and $\boldsymbol{Reentry}$ variables evolve over time and are subsequently filtered by $\boldsymbol{Z_1}$ and $\boldsymbol{Z_2}$ leading to PAF onset

The detailed descriptions of variables in PAF-PPGM model are presented in Appendix A - Table A-2. Two temporal inferences were implemented, namely filtering (tracking) and prediction for the variable $\boldsymbol{PM}^{(t)}$, and the probability of PAF onset was computed from $\boldsymbol{PM}^{(t)}$. The filtering results and 1-step to 5-step forecasts $P\left(\boldsymbol{Onset}^{(t+h)} = 1 \middle| \text{all } \boldsymbol{Z}_i^{(t+h)}\right)$ were computed as follows: 0.9621 ± 0.0426, 0.9534 ± 0.0387, 0.8946 ± 0.0444, 0.8310 ± 0.0535, 0.8176 ± 0.0687, 0.7856 ± 0.0874, respectively, as illustrated in Figure 4-7.

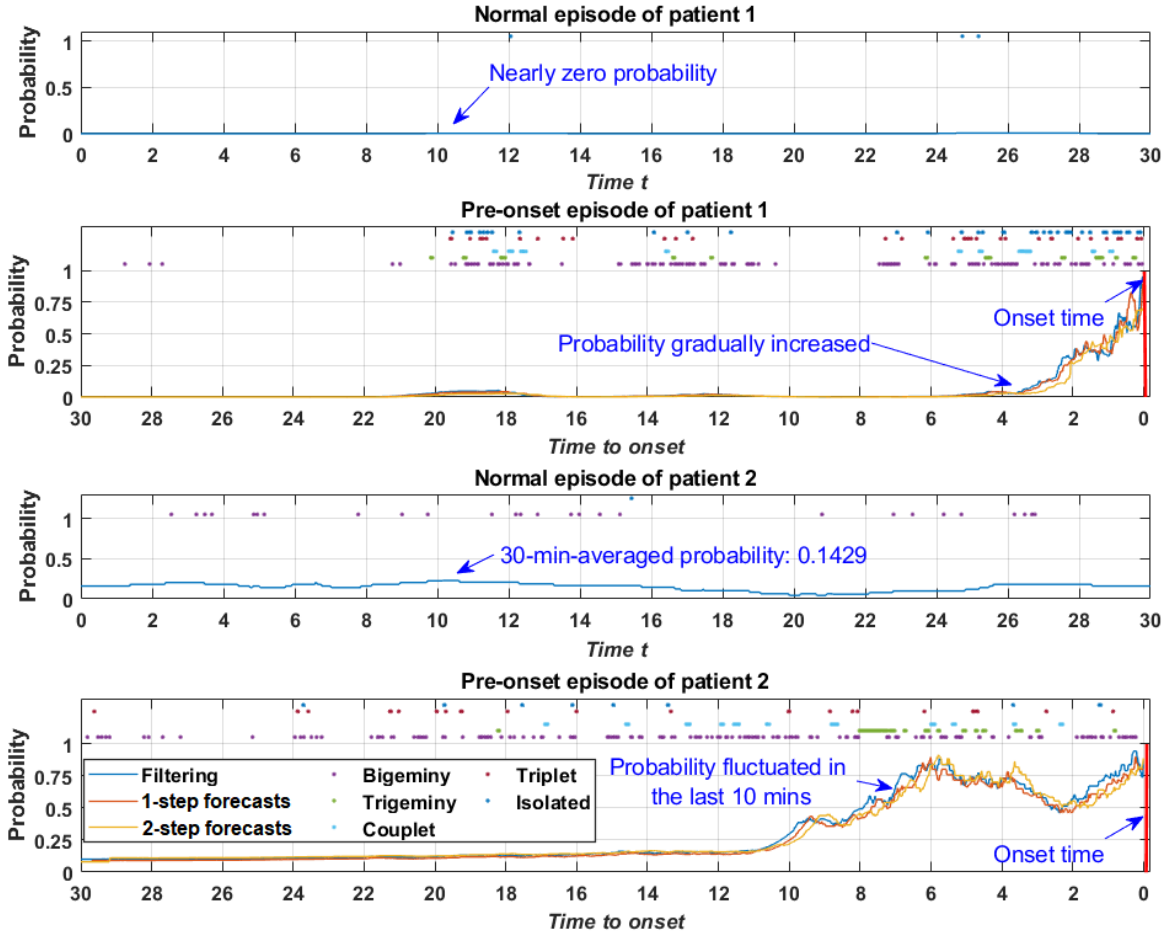

Figure 4-7 Filtering (tracking) and prediction results for the $\boldsymbol{Onset}$ variable of two representative patients

For model comparison, we benchmarked our models with Input-output Hidden Markov Models (HMM) [182] and Switching Auto Regressive HMM [154] models to compare

computational costs, algorithmic complexities, forecasting performance, and elapsed time of model running as shown in Table 4-2.

Table 4-2 Model comparison of algorithmic complexity and elapsed time

Model step	**Algorithm complexity**	**Model**	**Total elapsed time (seconds)**	**Log-likelihood in EM algorithm/ 1-step forecasting onset probability**
Parameter learning using Batch-EM algorithm [183] (run one time)	Approximately $O(mn^3)$, where m is the # of EM iterations, n is the # of parameters.	Input-output HMM ($m = 7, n = 26$)	0.0445	-715.4473
		Switching Auto Regressive HMM ($m = 4, n = 35$)	0.0145	-293.0968
		PPGM model ($m = 3, n = 47$)	0.0114	-147.9359
Temporal inference using forwards-backwards algorithm [174] (run 48 times corresponding to 48 patients)	$O(N^2T)$, where N is the # of hidden states at each time point, T is the # of time slices.	Input-output HMM ($N = 4, T = 89.5 \pm 20.23$)	0.0087	0.8373 ($\pm$ 0.0739)
		Switching Auto Regressive HMM ($N = 4, T = 89.5 \pm 20.23$)	0.0110	0.9102 ($\pm$ 0.0543)
		PPGM model ($N = 6\ , T = 89.5 \pm 20.23$)	0.0147	0.9534 ($\pm$ 0.0387)

4.4 Discussion

Compared to other benchmark models, the performance of the PPGM model was superior in terms of model learning and forecasting accuracy, indicated by log-likelihood of the EM algorithm and 1-step forecasting results, respectively. In addition, the PPMG model exhibited the capability to encode the domain knowledge of disease pathogenesis into an integrated probabilistic framework while maintaining interpretability of the model, which is another outstanding feature.

The OSA case study showed that the Bayesian approaches were superior to the MLE method with a faster convergence rate. This implies that a strong bias with large equivalent size α is still a better compromise than a non-smoothing MLE learning curve. By leveraging the equivalent techniques in the PAF case study, PPGM gained a better result with the ground truths from the clinical diagnosis. In both case studies, domain knowledge of disease pathogenesis played an essential role in establishing the model graphical structure and optimal learned parameters. Sensitivity analysis of the forecasting horizon showed that the uncertainty level of onset forecasting will increase as we forecast further into the future. Furthermore, conditional probabilistic queries of patient characteristics and temporal inference were performed accurately when benchmarked against the ground truth. With the flexibility of latent variable inclusion, the proposed PPGM model can be combined with various data-driven approaches to form robust state-observation models to accurately capture the true parameters of the CPDs. It is possible to update the encoded knowledge because PPGM is an interpretable and flexible model, and the parameters and structure of PPGM can be subsequently fine-tuned to fit the new data or knowledge using Bayesian schemes, *e.g.*, Bayesian parameter estimation and score function for structure learning.

There are several limitations of the proposed PPGM model. First, the performance of the PPGM model cannot be completely validated through the OSA and PAF case studies because we used simulated OSA data and had only a limited sample size of 48 patients from the PAF dataset. Second, the small-time granularity Δ to perform a fine-grained time frame of the pathogenesis dynamics adversely affects prediction tasks with long forecast horizons (*e.g.*, 1 hour). Further analysis of the convergence of the prediction performance and Δ will be performed in future work. In addition, some assumptions about the distribution of variables, possible directed edges, and model selection need to be justified, especially the assignment of the parameters' values, which

also necessitates the provision of a larger amount of data. Moreover, Graphical neural networks [184], have been established to model dynamic graphs in which the graphical structure is dynamic and evolve over time.

4.5 Conclusion

In this study, the PPGM model was introduced to address the problem of incorporating pathogenesis domain knowledge into ML pipeline for novel knowledge discovery and feature engineering. In particular, the proposed model characterizes the influence of static patient characteristics on the dynamic pathogenetic mechanisms by assimilating the patient data and expert knowledge into a parameterized and structured dynamical Bayesian network. We performed the inference of interest in both static and temporal models for medical queries and acute onset forecasting. The interpretable structure of the PPGM model allowed experts to understand and investigate the disease pathogenesis using tractable, data-driven methods of inference and learning. The model was validated using two case studies, which presented favorable results regarding parameter learning and inference. The model can be exploited effectively to address a broader range of research problems for acute disorders, which greatly benefits the development of prognostic models and systems, reduces physicians' workload, and enhances preventive treatments.

Chapter 5: A Physics-Informed Latent Variable Model of Corrosion Growth in Oil and Gas Pipelines [2]

Corrosion defects in oil and gas pipelines are the major risk factor that threatens the structural integrity of buried pipelines. Pipeline corrosion management, which typically requires high-resolution inline inspections (ILI) to characterize the corrosion growth process, is an important task to assess the corrosion defects. However, the corrosion process is inherently stochastic, temporal-spatial dependent, and driven by various hidden physics-related variables. In this study, we proposed a physics-informed latent variable corrosion growth model that integrates the known physics from complex processes into modeling the relations between observable and latent variables and the actual stochastic process that generate the corrosion time series data. We validated the model by a case study on a simulated corrosion process in oil and gas pipelines, in which both latent variables and ILI data were sampled from pre-defined distributions. The results indicated that the model could predict the growth of corrosion defects and capture the variance of the stochastic processes demonstrated by the low mean absolute percentage errors (MAPE) of 3.0082%, 3.9532%, and 3.6831%, which corresponds to the three corrosion growth processes causes by three types of soil. The proposed model can be used to facilitate the development of reliability models and corrosion management [125].

5.1 Introduction

Corrosion defect in pipeline systems is one of the significant threats to the structural integrity of buried pipelines worldwide [185]. Therefore, the pipeline corrosion management is a

[2] This chapter was published in Annual Reliability and Maintainability Symposium, pp. 1-7., 2023. Permission is included in Appendix C.

crucial task, which includes an engineering assessment of corrosion defects called high-resolution inline inspections (ILI) to inspect the pipeline conditions and mitigate the effect of defects. To determine a re-inspection plan and a sound defect mitigation strategy, modeling the corrosion growth is substantially important. In the literature, methods to model corrosion growth in oil and gas pipelines can be categorized into three groups: deterministic, stochastic and machine-learning-based models. Power law model [186] – one of the widely accepted deterministic models – has been used to estimate the time-dependent atmospheric corrosion. For predicting internal corrosion rate, the de Waard-Milliams model was proposed, which relates the corrosion rate with the CO_2 partial pressure and the temperature [187]. However, those deterministic models cannot capture the stochastic nature of the corrosion process. To overcome it, various stochastic-process-based models have also been developed to capture the growth of corrosion defects on pipelines, such as inverse Gaussian processes [188], gamma processes [189], Markov chain models [190], and hierarchical Bayesian models [191]. These models impose many unjustified assumptions regarding the mean growth path (e.g., a linear or power law function) and the probability distributions. In recent years, there has been considerable interest in employing machine learning models to predict the corrosion growth of pipelines. For example, Ossai et al. [192] predicted the time-dependent corrosion depth using Particle Swarm Optimization & Feed-Forward Artificial Neural Network (PSO-FFANN), Gradient Boosting Machine (GBM), and Deep Neural Network (DNN). Support Vector Machine (SVM) models [193-195] were used to capture the growth of the corrosion process, which capitalizes on the integration of SVM with the meta-heuristic optimization techniques. Despite the remarkable capabilities of predicting the corrosion growth behavior, the inherently stochastic and hidden-physics-driven nature of the corrosion growth process were not fully addressed by the previously developed models.

Latent variable models [196, 197] assume there exist latent (hidden) variables that induce the observed variables–have become a practical statistical method to address the problem of modeling complex stochastic dependencies of observed variables. Latent variable models for time series are a special class of models that consider the input as a sequence of observations. The first group of modeling approach is the latent chain model [198]. Two commonly used models in this group are: linear Gaussian state space models (SSMs) [199] and hidden Markov models (HMMs) [200]. Different extensions of linear Gaussian SSMs and HMMs to handle more complex time series data are input-output HMMs [201], constrained HMMs [202], hierarchical models HMMs [200], switching SSMs [203], factorial HMMs [204], and dynamic Bayesian network [205]. Those models are considered directed probabilistic graphical models. The second modeling approach is graph-based models. Conditional random fields (CRFs) [206] models are the most commonly used models in which the dependencies between the variables and the observations are modeled by considering the "neighboring samples" without any causal assumptions.

In engineering fields, the tremendous amount of multi-sensory time series data obtained from complex systems [207] (e.g., metabolic pathways, ecosystems, power grids, or oil and gas pipelines) has posed not only the challenge for time series latent variable modeling [18] but also the system dynamics modeling [208]. Physics-informed machine learning has been investigated [209] to integrate high-dimensional time series data models and mathematical physics models, even though partially understood physics and dynamics are given. This approach is believed to complement the latent variable models in terms of system physics and dynamics modeling and discovery. The known physics of complex systems can guide to select the accurate parsimonious candidate model structure [124] and avoid statistical model misspecification [210].

This study proposes a physics-informed latent variable model for nonstationary time series data. The model integrates the known physics and system dynamics from complex processes to characterize the relations of observed and latent variables and the actual stochastic process generating the time series. Those relations were modeled using physics-informed parametric regression models. The latent groupings that give rise to the time series were identified by using agglomerative hierarchical clustering [211]. We validated the model by a simulated case study on corrosion in oil and gas pipelines, in which both latent variable realizations and inline inspection (ILI) data were sampled from pre-defined distributions [212].

5.2 Methodologies

In this section, we will elaborate on: (1) the structure of the multivariate nonstationary time series model with latent physics-related variables, (2) the physics-informed regression models of the deterministic and stochastic components, and (3) the long-term time series forecasting algorithm.

5.2.1 Multivariate Nonstationary Time Series Model with Latent Variables

Consider a multivariate time-series data matrix $\boldsymbol{X}_{n\times T}$ that consists of n time series obtained from the sensors and uniformly sampled from time $t = 1$ to $t = T$ as follows:

$$\boldsymbol{X}_{n\times T} = \begin{bmatrix} X_{1,1} & X_{1,2} & \cdots & X_{1,T} \\ X_{2,1} & X_{2,2} & \cdots & X_{2,T} \\ \vdots & \vdots & \ddots & \vdots \\ X_{n,1} & X_{n,2} & \cdots & X_{n,T} \end{bmatrix} \tag{5.1}$$

where X_{it} is the value of the i^{th} time series at time t, each time series $\{X_{i,t}\}_{t=1}^{T}$ represents the measurement of the same variable at n locations. A discrete-time multivariate nonstationary time series model was assumed to have the following form:

$$X_{i,t} = \underbrace{f(\boldsymbol{\xi}_i, t; \boldsymbol{\theta}_f)}_{deterministic} + \underbrace{g(\boldsymbol{\xi}_i, t; \boldsymbol{\theta}_g)}_{stochastic} + \underbrace{\varepsilon_{i,t}}_{\substack{measurement \\ error}} \tag{5.2}$$

where $f(\cdot)$ and $g(\cdot)$ are the deterministic and the stochastic components of $X_{i,t}$ parametrized by $\boldsymbol{\theta}_f$ and $\boldsymbol{\theta}_g$ respectively $\boldsymbol{\xi}_i = [\xi_{i,1}, \xi_{i,2}, \dots \xi_{i,L}]$ represents the vector of latent variables for the i^{th} time series and $\varepsilon_{i,t} \overset{iid}{\sim} \mathcal{N}(0, \sigma_\varepsilon^2)$, where $\mathcal{N}(\mu, \sigma^2)$ denotes the normal distribution with mean μ and variance σ^2, is the measurement error. For simplicity of the modeling process, we assumed $g(\cdot) \equiv \mathcal{N}\left(\mu_{i,t}(\boldsymbol{\xi}_i, , t; \boldsymbol{\nu}), \sigma_{i,t}^2(\boldsymbol{\xi}_i, , t; \boldsymbol{\varphi})\right)$, which models the non-stationarity of the time series $X_{i,t}$ (i.e., the change of stochastic process parameters over time). The true underlying model structure was depicted as in Figure 5-1.

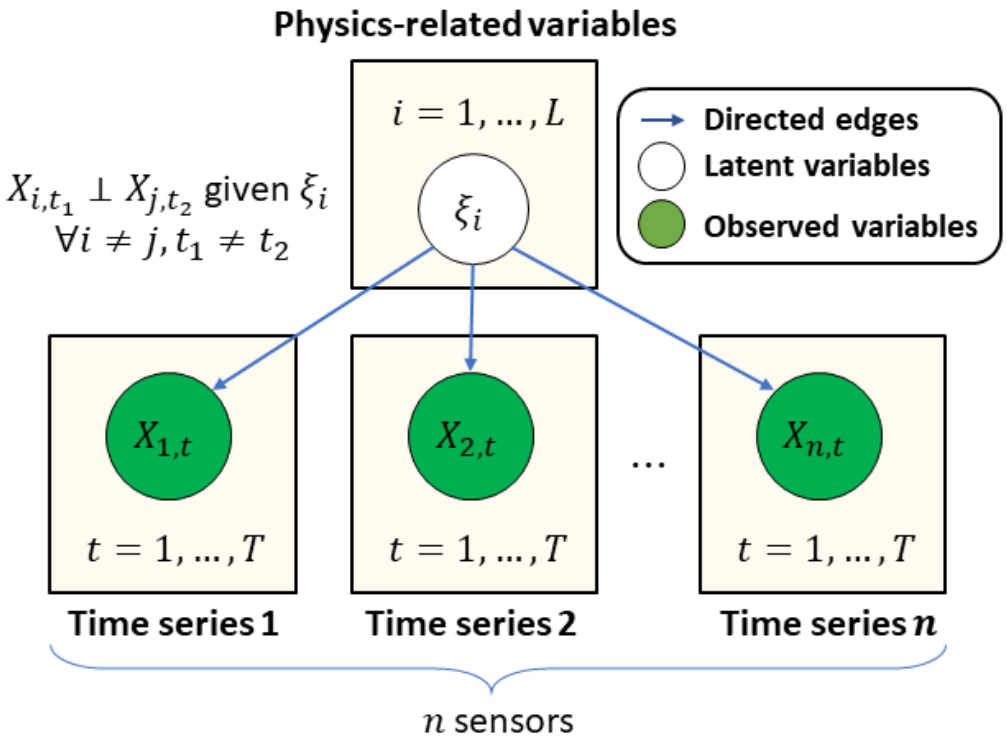

Figure 5-1 True underlying model structure with latent variables

Given the normality assumption of the true distribution of the stochastic process $\mathcal{N}\left(\mu_{i,t}(\cdot), \sigma_{i,t}^2(\cdot)\right)$, the component $f(\cdot)$ was separated from the stochastic component and noise by using simple moving average data-driven method [213] with the window length k:

$$\hat{f}_{i,t} = \begin{cases} X_{j,t} & if\ t < k \\ \frac{1}{k} \sum_{j=t-k+1}^{t} X_{j,t}\ \forall t \geq k\ if\ t \geq k \end{cases} \tag{5.3}$$

where $\{\hat{f}_{i,t}\}_{t=1}^{T}$ denotes the moving average estimates computed by taking the mean of the last k data points. This is a typical time series smoothing techniques used in time series analysis to capture the dominant time series trend, which approximates the deterministic component $f(\cdot)$. Next, the stochastic component was computed as:

$$\hat{g}_{i,t} = X_{i,t} - \hat{f}_{i,t} \tag{5.4}$$

The estimated deterministic and stochastic components $\{\hat{f}_{i,t}\}_{t=1}^{T}$ and $\{\hat{g}_{i,t}\}_{t=1}^{T}$ and were used to build the physics-informed regression models.

5.2.2 Physics-Informed Regression Models with Latent Variables for Deterministic and Stochastic Components

To identify the latent variables of $\boldsymbol{\xi}_i$'s and discover the underling relationships between the time series and the latent variables, the agglomerative hierarchical clustering [211] and physics-informed regression models were used. To determine which clusters are combined, a distance metric is required to measure the dissimilarity between two time series denoted by $\mathcal{D}\left(\{X_{i,t}\}_{t=1}^{T}, \{X_{j,t}\}_{t=1}^{T}\right)$. A linkage method is defined to specify the method to measure the dissimilarity between sets as a function of the pairwise distances of time series in the sets. A cut-off value for the distance needs to be chosen to obtain the number of clusters and the cluster indices

for each time series. The agglomerative hierarchical clustering was performed on the time series $\{\hat{f}_{i,t}\}_{t=1}^{T}$ and $\{\hat{g}_{i,t}\}_{t=1}^{T}$ for $i = 1, \dots, n$ separately. After selecting the distance threshold, the estimated latent cluster of the deterministic and the stochastic components can be obtained, which are denoted by $cd_i \in \{1,2, \dots, K_d\}$ and $cs_i \in \{1,2, \dots, K_s\}$, respectively. The time series model built on the estimated latent groupings cd_i and cs_i was described as:

$$X_{i,t} = \tilde{f}\left(cd_i, t; \boldsymbol{\theta}_{\tilde{f}}\right) + \tilde{g}\left(cs_i, t; \boldsymbol{\theta}_{\tilde{g}}\right) + r_{i,t} \tag{5.5}$$

where $\tilde{g} \equiv \mathcal{N}\left(0, \sigma_{\tilde{g}}^2\left(cs_i, t; \boldsymbol{\theta}_{\tilde{g}}\right)\right)$, $r_{i,t}$ is the residual of the model that represents the unexplained component of $X_{i,t}$ by the latent cd_i and cs_i. The hyperparameters of the hierarchical clustering algorithm including the linkage method, the distance metric, and the number of clusters K_d and K_s can be selected to minimize the sum of squared residuals $r_{i,t}$'s of the above model. The structure of the model was demonstrated in Figure 5-2.

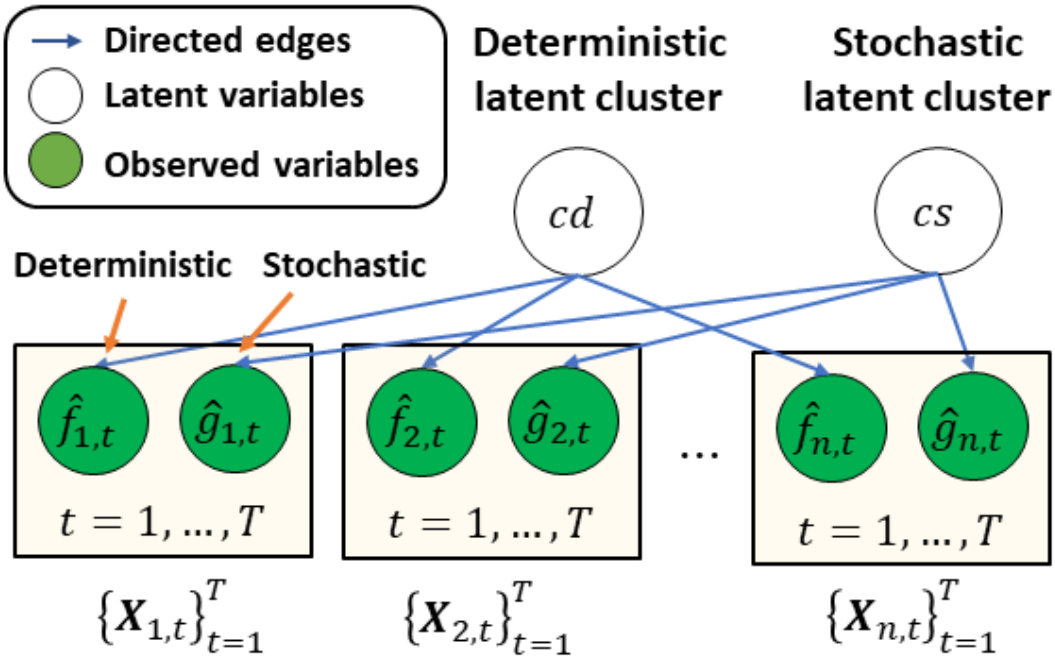

Figure 5-2 Model structure associated with the physics-informed regression model built on latent groupings obtained from the hierarchical clustering algorithm.

The function $\tilde{f}(\cdot)$ was derived from the process physics and dynamics. The estimated parameters $\widehat{\boldsymbol{\theta}}_{\tilde{f}}$ and can be learned using the given objective function:

$$\widehat{\boldsymbol{\theta}}_{\tilde{f}} = \underset{\boldsymbol{\theta}_{\tilde{f}} \in \Theta_{\tilde{f}}}{\operatorname{argmin}} \frac{1}{nT} \sum_{i=1}^{n} \sum_{t=1}^{T} \left[\tilde{f}\left(cd_i, t; \boldsymbol{\theta}_{\tilde{f}}\right) - \hat{f}_{i,t}\right]^2 \tag{5.6}$$

To estimate the parameters of the model of $\sigma_{\tilde{g}}^2\left(cs_i, t; \boldsymbol{\theta}_{\tilde{g}}\right)$, we obtained the upper and lower root-mean-square envelopes [214] of $\hat{g}(\cdot)$ with a sliding window length wl, which are denoted by $\{\boldsymbol{U}_{i,t}\}_{t=1}^{T}$ and $\{\boldsymbol{L}_{i,t}\}_{t=1}^{T}$. The upper and lower envelopes are approximately equal given $\tilde{g}$ is normal, and they are the non-parametric approximation of $\hat{\sigma}_g\left(cs_i, t; \boldsymbol{\theta}_{\tilde{g}}\right)$. The form of the physics-informed regression model $\hat{\sigma}_g\left(cs_i, t; \boldsymbol{\theta}_{\tilde{g}}\right)$ was assumed to be known. The objective function for learning $\widehat{\boldsymbol{\theta}}_{\tilde{g}}$:

$$\widehat{\boldsymbol{\theta}}_{\tilde{g}} = \underset{\boldsymbol{\theta}_{\tilde{g}} \in \Theta_{\tilde{g}}}{\operatorname{argmin}} \frac{1}{nT} \sum_{i=1}^{n} \sum_{t=1}^{T} \left[\hat{\sigma}_g\left(cs_i, t; \boldsymbol{\theta}_{\tilde{g}}\right) - U_{i,t}\right]^2 \tag{5.7}$$

If the equations $\tilde{f}(\cdot)$ and $\hat{\sigma}_g(\cdot)$ were unknown, universal function approximators, such as machine learning and deep learning models [215], could be used.

5.2.3 Long-Term Forecasting of Time Series Using the Physics-Informed Latent Variable Model

The time series forecasting algorithm using the latent variable model was elaborated in Algorithm 5-1.

Algorithm 5-1: Time series forecasting using the regression model with latent variables

1 Input: a new time series $\{\boldsymbol{X}_t^*\}_{t=1}^{T_{train}}$
2 Output: $\mathbb{E}[cd^*], \mathbb{E}[cs^*]$ of $\boldsymbol{X}_t^*$, and $\{\widehat{\boldsymbol{X}}_t^*\}_{t=T_{train}+1}^{T}$
3 Estimate $\mathcal{D}\left(\{\boldsymbol{X}_t^*\}_{t=1}^{T_{train}}, \{\boldsymbol{X}_{i,t}\}_{t=1}^{T_{train}}\right)\ \forall i = 1, \dots, n$
4 Choose K "nearest neighbors" of $\boldsymbol{X}_t^*$
5 Estimate the probability distribution of cd^* and cs^* from the K "nearest neighbors":
6 $P(cd^* = c) \leftarrow \frac{\sum_{k=1}^{K} I(cd_k = c)}{K}\ \forall c = 1, \dots K_d,$
7 $P(cs^* = c) \leftarrow \frac{\sum_{k=1}^{K} I(cs_k = c)}{K}\ \forall c = 1, \dots K_s$

8 Return: $\mathbb{E}[cd^*] \longleftarrow \sum_{c=1}^{K_d} P(cd^* = i)c$

9 Return: $\mathbb{E}[cs^*] \longleftarrow \frac{1}{K}\sum_{c=1}^{K_s} P(cs^* = c)c$

10 Compute the estimated parameters $\widehat{\boldsymbol{\theta}}_{\tilde{f}}$ and $\widehat{\boldsymbol{\theta}}_{g}$ using the iterative least squares method [216]

11 Obtain the predicted the time series $\left\{\widehat{\boldsymbol{X}}_t^*\right\}_{t=T_{train+1}}^{T}$:

12 Return: $\hat{X}_t^* \longleftarrow \tilde{f}\left(\mathbb{E}[cd^*], t; \widehat{\boldsymbol{\theta}}_{\tilde{f}}\right) + \tilde{g}\left(\mathbb{E}[cs^*], t; \widehat{\boldsymbol{\theta}}_{\tilde{g}}\right)$

5.3 Results

5.3.1 Case Study Description

In this case study, we simulated noisy high-resolution ILI data using a well-known corrosion growth model [217] coupled with a nonstationary Gaussian stochastic process [218]. To simulate the time series data $\left\{\boldsymbol{CD}_{i,t}\right\}_{t=0}^{T}$ $(i = 1, \dots, n)$ the maximum corrosion depth model was:

$$CD_{i,t} = \underbrace{k(t - t_0)^{\alpha}}_{deterministic} + \underbrace{\mathcal{N}(\mu, \sigma^2) + \varepsilon}_{stochastic} \tag{5.8}$$

where t_0 is the corrosion starting time, k and α are the pitting corrosion proportionality and exponent factor, and $\varepsilon \sim N(0, \eta^2)$ is the measurement error. We assumed that k, t_0 and α are the functions of the latent variable ξ_i that represents the soil characteristics at the i^{th} sensor's location:

$$k(\xi_i) = \theta_0 + \theta_1 \xi_i \tag{5.9}$$

$$\mu(\xi_i, t) = \nu_0 + \nu_1 \xi_i + \nu_2 t + \nu_3 \xi_i t \tag{5.10}$$

$$\sigma^2(\xi_i, t) = \varphi_0 + \varphi_1 \xi_i + \varphi_2 t + \varphi_3 \xi_i t \tag{5.11}$$

The parameter vectors $\boldsymbol{\theta}_f, \boldsymbol{\nu}$, and $\boldsymbol{\varphi}$ presented in sub-section 2.1. are defined as $\boldsymbol{\theta}_f \overset{\text{def}}{=} [\theta_0\ \theta_1]$, $\boldsymbol{\nu} \overset{\text{def}}{=} [\nu_0\ \nu_1\ \nu_2\ \nu_3]$, and $\boldsymbol{\varphi} = [\varphi_0\ \varphi_1\ \varphi_2\ \varphi_3]$

5.3.2 Case Study Implementation

First, the corrosion pit depth time series $\left\{\boldsymbol{CD}_{i,t}\right\}_{t=q\Delta t}^{400\Delta t}$ and ξ_i's were simulated for $i = 1, \dots n, q = 0, \dots, 400$ with $\Delta t = 0.01$ using Equation (8) and Equation (10). All required parameters were specified as follows:

- $\boldsymbol{\theta}_f = [1, 0.2], \boldsymbol{\nu} = [0.05, 0.05, 0.05, 0.05],\ \boldsymbol{\varphi} = [0.05\ 0.05\ 0.05\ 0.01], \eta = 0.1$
- $\mu_1 = 2, \mu_2 = 5, \mu_3 = 8, \sigma_\xi = 0.7,\ t_0 = 8, \alpha = 0.6, n = 150, K_d = K_c = 3$

Here, we had a total of 150 time series for training the latent variable model, in which each soil type had 50 time series. The simulated data of corrosion depth and moving average time series were represented in Figure 5-3. The simulated "soil" values presented in Figure 5-4 formed three Gaussian distributions with small overlapping regions to cause troubles for clustering method. The implementation of physics-informed regression models with latent variables and long-term forecasting of time series using the latent variable model was demonstrated in Figure 5-5 and Figure 5-6. For each time series in the training set, we performed moving average method to extract the deterministic component and computed the root-mean-square envelope of the stochastic component, which was shown in Figure 5-5.

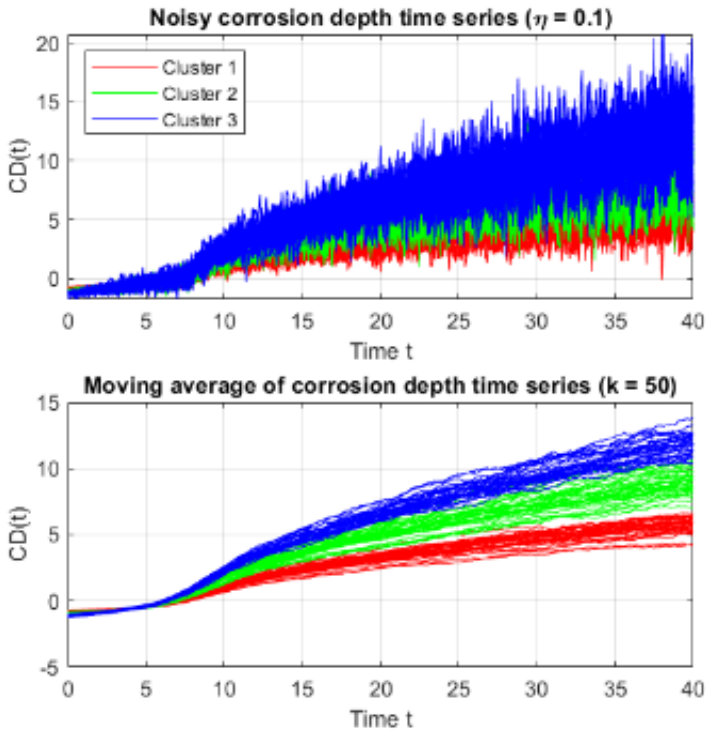

Figure 5-3 Noisy simulated corrosion depth time series ($\eta = 0.1$) and their moving average with $k = 50$

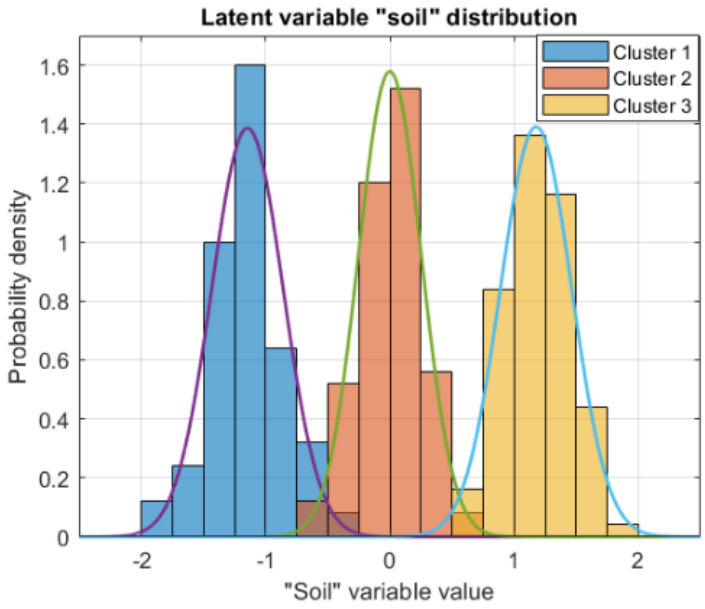

Figure 5-4 Histogram of the simulated latent variable ξ_i values with the probability distribution functions of three clusters

For simplicity, we assumed the latent groupings of the deterministic and stochastic component were the same (i.e., $cd_i \equiv cs_i$), which can be generalized later in a real case study. Therefore, we performed the clustering on only deterministic time series $\{\hat{\boldsymbol{f}}_{i,t}\}_{t=1}^{T}$ and obtained the cluster indices for all the training time series $(cd_i, i = 1, \ldots 150)$. Subsequently, we built the time series model on the estimated latent groupings cd_i's given the form of the physics-informed regression models:

$$k(\xi_i) = \theta_0 + \theta_1 \xi_i \tag{5.13}$$

$$\mu(\xi_i, t) = \breve{\nu}_0 + \breve{\nu}_1 cd_i + \breve{\nu}_2 t + \breve{\nu}_3 cd_i t \tag{5.14}$$

$$\sigma^2(\xi_i, t) = \breve{\varphi}_0 + \breve{\varphi}_1 cd_i + \breve{\varphi}_2 t + \breve{\varphi}_3 cd_i t \tag{5.15}$$

We validated the above model by simulating additional 50 time series for testing. For each time series, we held 50% of the time series as the input of Algorithm 5-1 for training and used the remaining data for testing. Long-term time series forecasts of 3 representative corrosion depth time

series from 3 different clusters were reported in Figure 5-6. We used mean absolute percentage error (MAPE) to evaluate the performance of the model, the formula of MAPE for the i^{th} time series is given as:

$$MAPE_i = 100 \sum_{t=1}^{T_{test}} \frac{\left| CD_{i,t}^{(true)} - \widehat{CD}_{i,t} \right|}{\left| CD_{i,t}^{(true)} \right|} \ (\%) \tag{5.16}$$

where T_{test} is the length of the testing data, $CD_{i,t}^{(true)}$ is the true deterministic values, and $\widehat{CD}_{i,t}$ is the forecasted values.

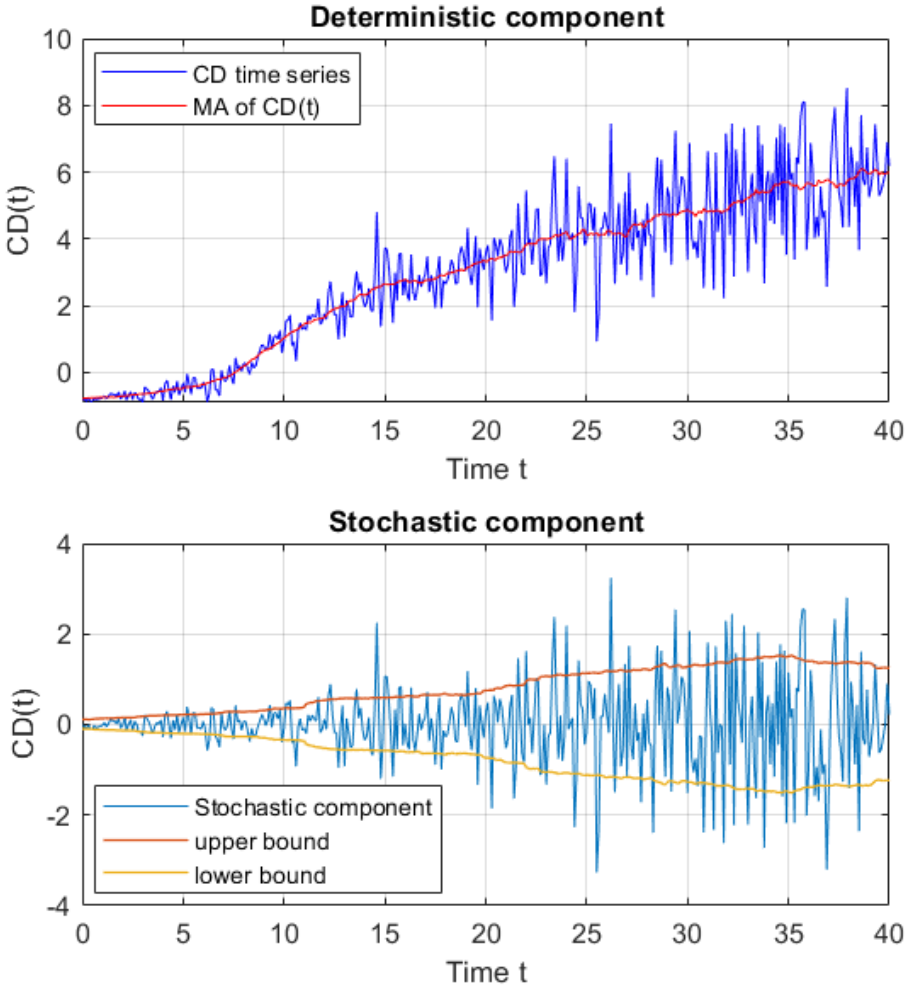

Figure 5-5 Decomposition of time series data into the deterministic component and stochastic component. The deterministic component was illustrated by red line in the first subplot. In the second plot, the root-mean-square envelope of the stochastic component was obtained

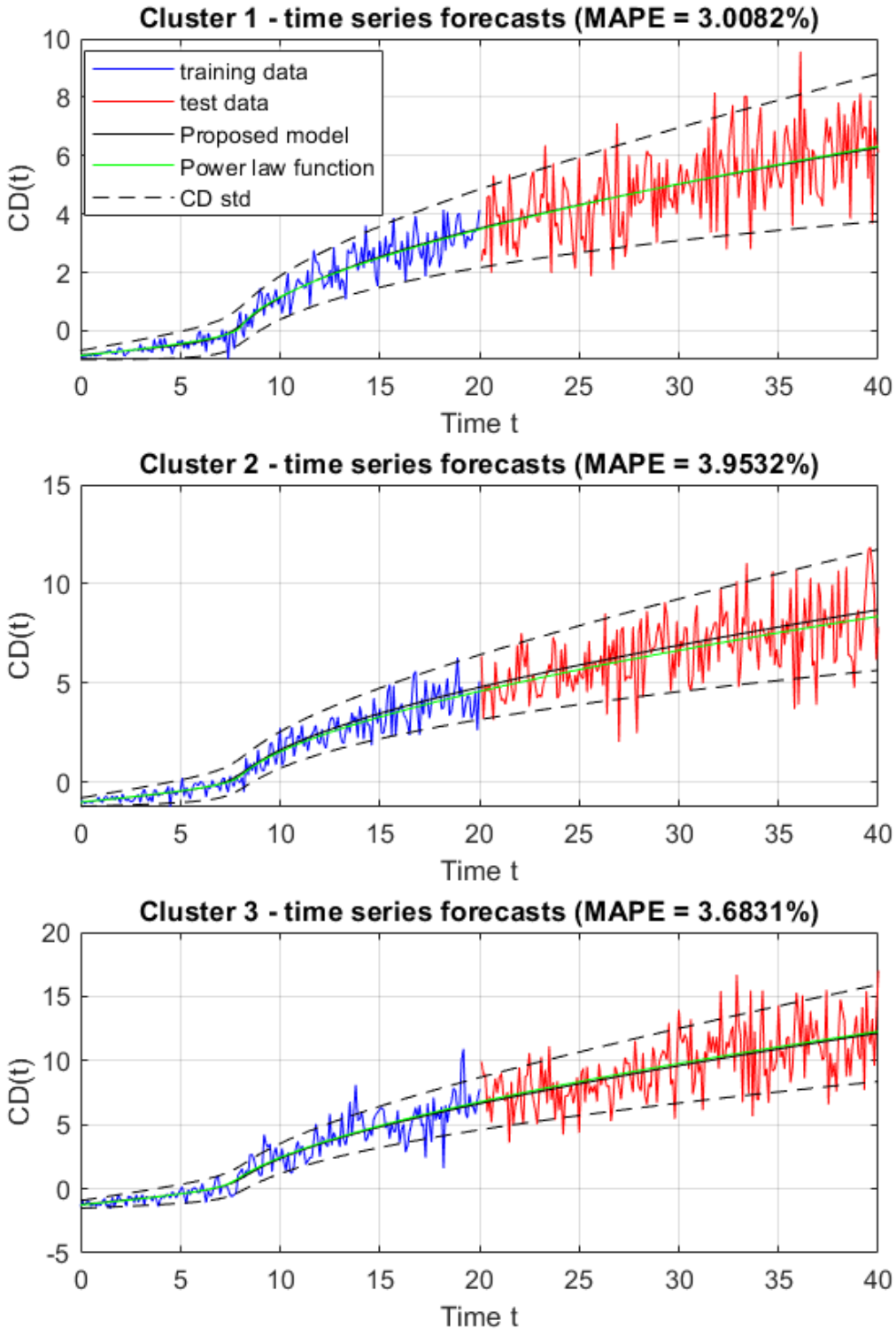

Figure 5-6 Long-term time series forecasts of 3 representative corrosion depth time series from three different clusters. The forecasted time series was plotted by solid black line with the 95% forecast interval plotted by the dashed black line. The green line represents the true value of the deterministic component for measuring the forecast error MAPE

5.4 Conclusion

We have proposed a physics-informed latent variables model that integrates the known physics and system dynamics into modeling the stochastic and hidden physics-driven nature of the corrosion growth processes. The model can characterize the complex relationships between observed and latent variables and the underlying stochastic process generated from the nonstationary time series. We validated the model by a simulated case study on corrosion in oil and gas pipelines, in which both latent variable realizations and inline inspection (ILI) data were sampled from pre-defined distributions. The proposed model can capture the time-heterogeneous variance of the underlying stochastic process. The results indicated that the model could predict the growth of corrosion defects demonstrated by the low mean absolute percentage errors (MAPE) of 3.0082%, 3.9532%, and 3.6831%, which corresponds to the three corrosion growth processes caused by three different types of soil. The proposed model can be used to facilitate the development of corrosion process modeling and establish a well-informed re-inspection plan and mitigation strategy for maintenance of oil and gas pipelines and corrosion management.

Chapter 6: A Noise-Robust Koopman Spectral Analysis of an Intermittent Dynamics Method for Complex Systems: a Case Study in Pathophysiological Processes of Obstructive Sleep Apnea [3]

Koopman operator theory and the Hankel alternative view of the Koopman (HAVOK) model have been widely used to investigate the chaotic dynamics in complex systems. Although the statistics of intermittent dynamics have been evaluated in the HAVOK model, they are not adequate to characterize intermittent forcing. In this paper, we propose a novel method to characterize the intermittent phases, chaotic bursts, and local spectral-temporal properties of various intermittent dynamics modes using spectral decomposition and wavelet analysis. We compared the sensitivity to noise level and sampling period of the HAVOK and our proposed method in the Lorenz system. Our results show that the prediction accuracy of lobe switching and the intermittent forcing identifiability were highly sensitive to the sampling rate. While it is possible to maintain the desired accuracy in high noise-level cases with an appropriately selected rank in the HAVOK model, our proposed method is demonstrated to be more robust. To show the applicability of our proposed method, obstructive sleep apnea—a complex pathological disorder—was selected as a case study. Our proposed method has been demonstrated to be a promising data-driven method to provide key insights into the dynamics of complex systems [127].

6.1 Introduction

Intermittency is defined as the erratic alternations between periodic (i.e., regular and laminar) dynamics and chaotic (i.e., irregular and turbulent), commonly characterized by short

[3] This chapter was published IISE Transactions on Healthcare Systems Engineering, 13(2), pp.101-116. Permission is included in Appendix C.

bursts in the signal [219]. Intermittency also exists in the other form of chaotic dynamics called crisis-induced intermittency [220]. Two groups of explanations have been proposed to clarify the origins of the intermittency phenomena. First, intermittency may originate from Hamiltonian chaos [221] and hydrodynamical systems [222]. Second, intermittent behaviors can also arise from small control parameter fluctuations around critical values [223, 224]. To avoid confusion between the non-intermittent dynamics mode of non-stationarity and the dynamical intermittency for fixed parameters of dynamical systems, the statistics of intermittent phases and chaotic bursts need to be studied [219]. The study of intermittent dynamics is considerably challenging. Bifurcation analysis from the governing equations is the classical approach to studying the system behaviors as the parameters are perturbed. However, there are increasing numbers of complex systems for which we have abundant measurement data from sensors but do not have access to the underlying parameterized governing equations. Hence, an interpretable data-driven method that accurately models the intermittent dynamics of high-dimensional complex systems with unknown governing equations is needed.

A pioneering work that has contributed to the intermittent nonlinear dynamics analysis is Takens' delay embedding theorem [225]. In this method, the delay embeddings were used to reconstruct the state space and characterize intermittent nonlinear chaotic systems [226-228]. The Takens' embedding theorem has also been applied in system decomposition and identification analysis such as the eigensystem realization algorithm (ERA) [229], singular spectrum analysis (SSA) [230], and nonlinear Laplacian spectrum analysis [231]. However, these methods were limited in modeling and interpreting the intermittent and nonlinear behaviors in complex systems. To address the limitations, Brunton et al. have developed a data-driven Hankel alternative view of Koopman (HAVOK) model [232] and the modern Koopman operator theory [233] [234] to

decompose a chaotic system into a forced linear system and identify invariant subspaces for nonlinear systems with multiple attractors and periodic orbits. This method is well-suited to modeling nonlinear dynamics that are chaotic and intermittent, in which the trajectories of the system dynamics evolve to a densely filled attractor. Although different statistics of the intermittent forcing have been proposed to characterize intermittencies in the HAVOK model, they have not been adequate to characterize the mode switching of nonlinear dynamics and the fat-tailed non-Gaussian distribution originating from high-frequency bursts and rarely-observed intermittent switching events [219, 235, 236]. Therefore, the intermittent forcing interpretation in the HAVOK model has not been fully elucidated, and the connection between the complex nonlinear dynamics and the intermittent forcing modeled by the model has not been thoroughly studied.

This study proposes an intermittency analysis method that systematically decomposes and analyzes the intermittent forcing. We propose additional statistics, including burst starting-ending time, burst duration, and inter-burst duration quantifiers, to better characterize the intermittent phases and chaotic bursts in addition to the distribution of the intermittent forcing. The temporal spectra of the intermittent forcing signal estimated from the Fourier transform (DFFT) [237] was used to characterize the changes in the spectral properties of the intermittent forcing (e.g., predominant frequency bands or power spectral density) and potentially explain the switching between linear dynamics and nonlinear dynamics. Moreover, adaptive continuous-time wavelet (CWT) analysis [238] with different types of mother wavelets chosen to match the morphological features of the bursts was performed to extract local spectral and temporal information. To quantify the sensitivity of the HAVOK model and our intermittency analysis methods to noise and sampling rate, we carried out the validation on the Lorenz system, which is a well-controlled numerical

simulation study. Afterward, obstructive sleep apnea (OSA) was selected as a case study to verify the applicability of the methods for real-life systems. The main contributions of our study are the following: (1) numerical analysis of the HAVOK model robustness with respect to the noise level and sampling rate in the chaotic Lorentz system, (2) a noise-robust intermittency analysis framework to characterize the intermittent phases, the chaotic bursts, and the spectral-temporal properties of different intermittent dynamics modes, and (3) an attempt to characterize chaos in pathophysiological processes as an intermittently forced linear system and thoroughly analyze the intermittency forcing.

6.2 Background

Throughout this study, we will consider continuous-time dynamical systems with state vector $\boldsymbol{x}(t) \in \mathbb{R}^n$ in the form of:

$$\frac{d}{dt}\boldsymbol{x}(t) = \boldsymbol{f}\big(\boldsymbol{x}(t)\big) \tag{6.1}$$

where $\boldsymbol{f}(\cdot)$ denotes the flow map operator. Correspondingly, the discrete-time dynamical system is defined as:

$$\boldsymbol{x}_{k+1} = \boldsymbol{F}(\boldsymbol{x}_k) \tag{6.2}$$

where $\boldsymbol{x}_k = \boldsymbol{x}(k\Delta t)$ is the sample of the system trajectory from Equation (6.1). The discrete-time propagator $\boldsymbol{F}$ is given by:

$$\boldsymbol{F}(\boldsymbol{x}_k) = \boldsymbol{x}_k + \int_{k\Delta t}^{(k+1)\Delta t} \boldsymbol{f}\big(\boldsymbol{x}(s)\big)ds \tag{6.3}$$

6.2.1 Koopman Operator Theory

The Koopman operator theory [239] constructs a linear representation of strongly nonlinear systems by augmenting the n-dimensional state vector to an infinite-dimensional state vector. The Koopman operator $\boldsymbol{\mathcal{K}}$ is defined as an infinite-dimensional linear operator that acts on

measurement functions (i.e., Koopman observables) $g: M \mapsto \mathbb{R}$ of the state $\boldsymbol{x}$ where M is the manifold. The Koopman operator is defined as:

$$\boldsymbol{\mathcal{K}} g \triangleq g \circ \boldsymbol{F} \Longrightarrow \boldsymbol{\mathcal{K}} g(\boldsymbol{x}_k) = g(\boldsymbol{x}_{k+1}) \tag{6.4}$$

Usually, $\boldsymbol{\mathcal{K}}$ is restricted to a p-dimensional measurement subspace $\mathbb{R}^p$ and represented by a $p \times p$ matrix $\boldsymbol{K}$. If $\boldsymbol{K}$ exists, we can obtain an exact linear system that advances the Koopman observables restricted to the subspace as follows:

$$\boldsymbol{y}_{k+1} = \boldsymbol{K}\boldsymbol{y}_k, \boldsymbol{y}_k = \left[g_1(\boldsymbol{x}_k), g_2(\boldsymbol{x}_k), \dots, g_p(\boldsymbol{x}_k)\right]^T \tag{6.5}$$

where $\boldsymbol{y}_k$ is a vector of measurements in the Koopman invariant subspace [232]. In practical applications, there have been many attempts to obtain a finite-dimensional approximation of the Koopman operator $\boldsymbol{\mathcal{K}}$, but they have had limited success. Dynamic mode decomposition (DMD) [240] was applied to obtain a best-fit linear matrix that advances spatial measurements from one time slice to the next; however, this best-fit linear matrix appears not to be a good approximation for the Koopman operator and yields a large error in many nonlinear systems. To overcome that limitation, the DMD method was extended to include nonlinear measurements [241], but no existing theory guarantees that the extended model is closed under the Koopman operator (i.e., the observables advanced by $\boldsymbol{\mathcal{K}}$ are restricted to the measurement subspace). Therefore, a better finite-dimensional approximation of $\boldsymbol{\mathcal{K}}$, which relies on a Koopman invariant subspace, was introduced [242]. This model adopted the intrinsic data-driven measurement coordinates derived from the time-history of measurements, namely eigen time-delay coordinates. This coordinates system selection was based on the Takens' embedding theorem [225], which states that the measurements of a time series $z(t)$ can be enriched by its time-shifted copies $z(t-\tau)$ causing the derived embedded attractor is diffeomorphic to the original attractor under certain conditions.

6.2.2 Modeling Chaos as an Intermittently Forced Linear System: Hankel Alternative View of Koopman (HAVOK)

The first step in the HAVOK analysis is to obtain the measurement time-series $\boldsymbol{z}(t)$ and then reconstruct the Hankel matrix $\boldsymbol{\mathcal{H}}$ under the assumption that the conditions of Takens' embedding theorem are satisfied. In a discrete case, the measurement time-series can be denoted as $\{z(t_i)\}_{i=1}^{T}$, where t_i's are the sampling time points. Next, we compute the eigen-time-delay coordinates from $\{z(t_i)\}_{i=1}^{T}$ by taking the SVD of the Hankel matrix $\boldsymbol{\mathcal{H}}$ or the trajectory matrix $\boldsymbol{\mathcal{D}}$ in singular spectrum analysis (SSA) [230] as:

$$\boldsymbol{\mathcal{H}} = \begin{bmatrix} z(t_1) & z(t_2) & \cdots & z(t_p) \\ z(t_2) & z(t_3) & \cdots & z(t_{p+1}) \\ \vdots & \vdots & \ddots & \vdots \\ z(t_q) & z(t_{q+1}) & \cdots & z(t_T) \end{bmatrix} = \boldsymbol{U\Sigma V}^{*} \tag{6.6}$$

Here, q is the number of points in the trajectory and p is the window length. The window length, p, determines the extent to which we obtain a refined decomposition into basic components and therefore improve the separability of the dynamics. In other words, the window length p defines the longest dynamics periodicity captured by the Hankel matrix in the HAVOK model. The columns $\boldsymbol{U}$ and $\boldsymbol{V}$ are arranged hierarchically corresponding to the descending order of singular values in $\boldsymbol{\Sigma}$. In addition, $\boldsymbol{\mathcal{H}}$ often admits a low-rank approximation by the truncation of the first r columns of $\boldsymbol{U}$ and $\boldsymbol{V}$. The low-rank approximation to $\boldsymbol{\mathcal{H}}$ in Equation 6.6 gives rise to a measurement subspace that is approximately invariant to $\boldsymbol{\mathcal{K}}$ for the states. Consequently, we can rewrite Equation 6.6 with the Koopman operator $\boldsymbol{\mathcal{K}}$:

$$\boldsymbol{\mathcal{H}} = \begin{bmatrix} z(t_1) & \boldsymbol{\mathcal{K}}z(t_1) & \cdots & \boldsymbol{\mathcal{K}}^{p-1}z(t_1) \\ \boldsymbol{\mathcal{K}}z(t_1) & \boldsymbol{\mathcal{K}}^{2}z(t_1) & \cdots & \boldsymbol{\mathcal{K}}^{p}z(t_1) \\ \vdots & \vdots & \ddots & \vdots \\ \boldsymbol{\mathcal{K}}^{q-1}z(t_1) & \boldsymbol{\mathcal{K}}^{q}z(t_1) & \cdots & \boldsymbol{\mathcal{K}}^{T-1}z(t_1) \end{bmatrix} \tag{6.7}$$

The columns and rows of $\boldsymbol{\mathcal{H}}$ in both Equation 6.6 and Equation 6.7 are well-approximated by the first r truncated columns and rows of $\boldsymbol{U}$ and $\boldsymbol{V}$ respectively, which are called an eigen time series, providing a Koopman-invariant measurement system. We can consider the rows of $\boldsymbol{V}$ as a set of coordinates to construct a linear dynamical system. However, a linear model cannot fully capture multiple fixed points, periodic orbits, and the unpredictable chaos with a positive Lyapunov exponent [243]. To overcome , a forced linear system has been proposed after applying the dynamic mode decomposition (DMD) [234] algorithm to the delay coordinates and obtaining an excellent linear fit for the first $r-1$ variables but a bad fit for v_r. Particularly, the connection between the eigentime-delay coordinates and the Koopman operator, $\boldsymbol{\mathcal{K}}$, as shown in Equation 6.7 induce a linear regression model, in which we build a linear model on the first $r-1$ variables in $\boldsymbol{V}$ and consider v_r as an intermittent forcing term as follows:

$$\frac{d}{dt}\boldsymbol{v}(t) = \boldsymbol{A}\boldsymbol{v}(t) + \boldsymbol{B}v_r(t) = \frac{d}{dt}\begin{bmatrix} v_1(t) \\ v_2(t) \\ \vdots \\ v_{r-1}(t) \\ v_r(t) \end{bmatrix} = \begin{bmatrix} \boldsymbol{A} & \boldsymbol{B} \\ \boldsymbol{0} & 0 \end{bmatrix}\begin{bmatrix} v_1(t) \\ v_2(t) \\ \vdots \\ v_{r-1}(t) \\ v_r(t) \end{bmatrix} \tag{6.8}$$

where $\boldsymbol{v} = [v_1\ v_2\ \cdots v_{r-1}]^{\boldsymbol{T}}$ is a vector of the first $r-1$ eigen time-delay coordinates. In principle, we can separate the eigen time-delay variables into $r-s$ high-energy modes for the linear model and s low-energy intermittent forcing modes if $v_r(t)$ is not sufficient to model the intermittent forcing. The partition of nonlinear dynamics into deterministic linear dynamics and chaotic dynamics was proposed in Mezić's [244] study. The truncated rank, r, can be estimated by the optimal hard threshold for singular values [245]. The HAVOK model extends the dynamics splitting concept to fully chaotic systems, in which the Koopman operators have continuous spectra. We can estimate the matrices $\boldsymbol{A}$ and $\boldsymbol{B}$ in Equation 6.8 as follows:

$$\boldsymbol{V}_r = \begin{bmatrix} \boldsymbol{v}^{(1)} & \boldsymbol{v}^{(2)} & \cdots & \boldsymbol{v}^{(q-1)} \\ v_r^{(1)} & v_r^{(2)} & \cdots & v_r^{(q-1)} \end{bmatrix}, \quad \boldsymbol{V}'_r = \begin{bmatrix} \boldsymbol{v}^{(2)} & \boldsymbol{v}^{(3)} & \cdots & \boldsymbol{v}^{(q)} \\ v_r^{(2)} & v_r^{(3)} & \cdots & v_r^{(q)} \end{bmatrix},$$
$$\boldsymbol{\mathcal{A}} \approx \boldsymbol{V}'^{T}_r \boldsymbol{V}_r{}^{\dagger} = \begin{bmatrix} \boldsymbol{A} & \boldsymbol{B} \\ \boldsymbol{a} & b \end{bmatrix} \cong \begin{bmatrix} \boldsymbol{A} & \boldsymbol{B} \\ \boldsymbol{0} & 0 \end{bmatrix} \tag{6.9}$$

In Equation 6.9, $\boldsymbol{V}'_r$ is the 1-step time advanced eigen time-delay coordinates of $\boldsymbol{V}_r$, in which $\boldsymbol{v}^{(k)} = \left[v_1^{(k)}\ v_2^{(k)}\ \ldots\ v_{r-1}^{(k)}\right]^T$ and $v_j^{(k)}$ represents the j^{th} eigen time-delay coordinate at the discrete time step k from discrete-time dynamical system. These matrices, $\boldsymbol{V}_r$ and $\boldsymbol{V}'_r$, are related by a best-fit linear operator, $\boldsymbol{\mathcal{A}}$, that minimizes the Frobenius norm error $\|\boldsymbol{V}'_r - \boldsymbol{\mathcal{A}}\boldsymbol{V}_r\|_F$, and $\boldsymbol{V}_r{}^{\dagger}$ is the pseudo-inverse computed via the SVD of $\boldsymbol{V}_r$. The estimates $\boldsymbol{a}$ and b are considered a bad fit for v_r and approximate to zero. For complex systems of relatively large dimension, operator $\boldsymbol{\mathcal{A}}$ is also large; therefore, the DMD method or more advanced methods (e.g., the sparse identification of nonlinear dynamical systems (SINDy) method [234]) can be applied to consider only the leading eigen-decomposition of $\boldsymbol{\mathcal{A}}$.

6.3 Methodologies

6.3.1 Overview of the Methods

A block diagram of the proposed methods is illustrated in Figure 6-1. The first step is to perform the HAVOK analysis consisting of two sub-steps: (1) state space reconstruction and (2) forced linear dynamical system representation. A state space is reconstructed from the Hankel matrix to obtain eigen time-delay coordinates using the physiological measurement time series $z(t)$. Consequently, a forced linear system using the eigen coordinates was built to model the linear and chaotic intermittent dynamics. The second step is to perform the intermittency analysis proposed by our study, which comprises two steps: (1) intermittent phases and chaotic bursts analysis and (2) spectral analysis and wavelet analysis of the intermittent forcing component.

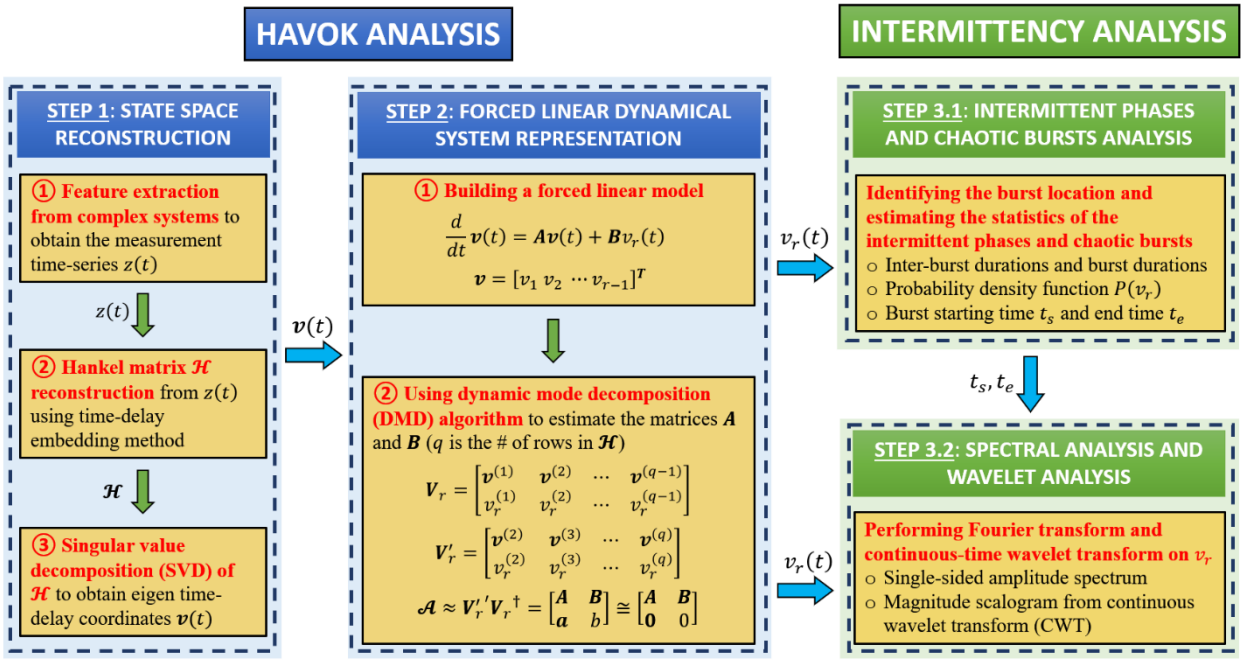

Figure 6-1 Block diagram of the proposed methods, which include the performance of the HAVOK analysis and intermittency analysis

6.3.2 Estimating the Statistics of Intermittent Phases and Chaotic Bursts

HAVOK analysis has been applied to many nonlinear dynamical systems including analytical systems, stochastic magnetic field reversal, and real-world systems. The distribution of the intermittent forcing $v_r(t)$ in those examples was shown to be nearly symmetric with fat tails, i.e., the distributions are non-Gaussian. We considered the distribution of the burst durations denoted as $T_b(k) \in (0, \infty)$, with $k = 1, \ldots, N_b$ as the burst index. First, a hard threshold for detecting the active forcing (i.e., intermittent bursts) is selected such that if $v_r^2(t) \geq \psi \max\{v_r^2(t) | t \geq 0\}$ then the forcing is active, where ψ is a tuning parameter. The ψ parameter can be adjusted to achieve the best alignment with the intermittent behaviors of the system, e.g., lobe switching in the chaotic Lorenz system or disease onsets in pathophysiological processes. However, the statistics of the intermittent forcing are not adequate to characterize the mode

switching of nonlinear dynamics and the fat-tailed non-Gaussian distribution originated from high-frequency bursts and rarely observed intermittent switching events. Therefore, we define additional statistics to better characterize the intermittent phases and chaotic bursts: the starting and ending time of the bursts as $t_s(k)$ and $t_e(k)$ and the burst duration as $T_b(k) := t_e(k) - t_s(k)$. Next, we can also define the inter-burst duration as $T_{ib} = t_s(k) - t_e(k-1)$ for $k = 2, \dots N_b$. These statistics of intermittent phases and chaotic bursts are illustrated in Figure 6-2.

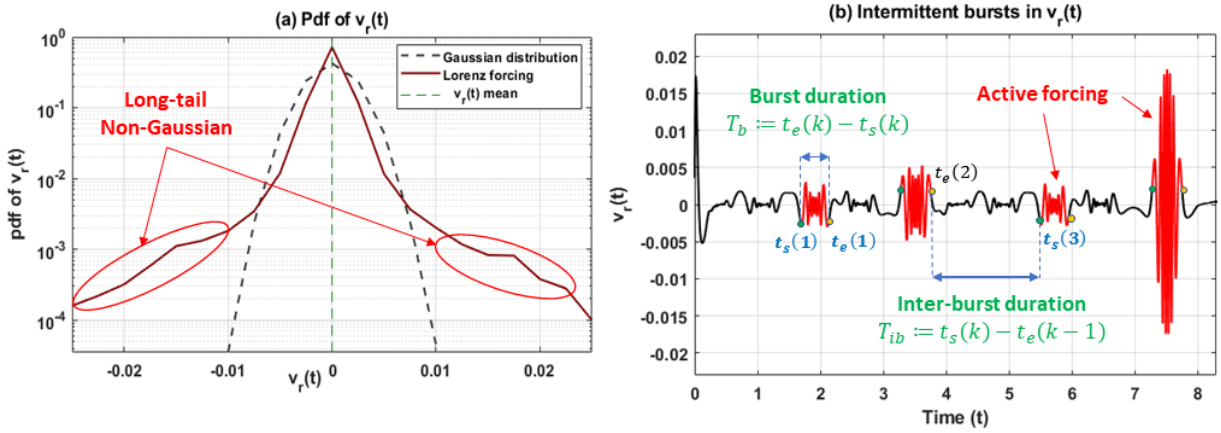

Figure 6-2 Illustration of the statistics of intermittent phases and chaotic bursts. Panel (a) shows the long-tail non-Gaussian distribution of the forcing term $v_r(t)$ for the Lorenz system. Panel (b) illustrates the estimation of burst duration, T_b, and inter-burst duration, T_{ib}, in $v_r(t)$, where $t_s(k)$ and $t_e(k)$ are the starting time and ending time of the bursts

6.3.3 Spectral Analysis and Wavelet Analysis of Intermittent Forcing

To better understand and characterize the changes in the temporal-spectral properties of the intermittency and the switching between linear dynamics and nonlinear dynamics, we propose an intermittency method that capitalizes on the discrete-time fast Fourier transform (FFT) [237] and continuous wavelet transform (CWT) analysis. Specifically, the FFT method can be applied to v_r to convert the forcing signal from the time domain to a representation in the frequency domain by decomposing v_r into components of different frequencies:

$$\boldsymbol{V} = \mathcal{F}(v_r), V_k = \sum_{n=0}^{q-1} v_r^{(n)} \cdot e^{-\frac{i2\pi}{q}kn} \tag{6.10}$$

where the Fourier transform operator is denoted by $\mathcal{F}(\cdot)$, q is the number of rows in the Hankel matrix $\boldsymbol{\mathcal{H}}$, and k is the frequency. In our spectral analysis on v_r, we utilize a plot tool called a single-sided (positive frequencies) amplitude spectrum that computes the amplitude at each positive frequency, i.e., the amplitude of each sinusoidal component in the FFT analysis, and the maximum frequency is equal to half of the sampling frequency, f_s. A continuous wavelet transform (CWT) [238] is applied on v_r to obtain an overcomplete representation of v_r in a time-frequency domain. The CWT of the forcing signal $v_r(t)$ at a scale ($a > 0$) and translational value $b \in \mathbb{R}$:

$$X_w(a,b) = \frac{1}{|a|^{1/2}} \int_{-\infty}^{\infty} v_r(t) \bar{\psi}\left(\frac{t-b}{a}\right) dt \tag{6.11}$$

where $\psi(t)$ is the continuous mother wavelet function (e.g., Morse wavelet) and $\bar{\psi}$ is its complex conjugate. The main objective of the mother wavelet is to provide a function to generate the translated and scaled versions (called "daughter" wavelets) of the mother wavelet. For displaying the results of the CWT, the scalogram is a useful tool to represent the absolute value of the CWT of a signal, which is plotted as a function of frequency and time. For the intermittency analysis, the scalogram representation is well suited to analyze the intermittent forcing $v_r(t)$ that occurs at different frequency scales. The scalogram computes the modulus of CWT coefficients (i.e., $|X_w|$), and we can obtain time-localization for short-duration, high-frequency burst events, and better separate them from low-frequency components and longer-duration events. To determine the active forcing, a hard threshold is defined such that if $|X_w(a^*, b)| \geq \psi_{CWT} \max|X_w(a^*, b)|$ then the forcing is active, where ψ_{CWT} and a^* are the tuning parameter and the optimal scale to achieve the highest forcing prediction accuracy.

6.4 Results

6.4.1 Numerical Validation on a Noise-Induced Chaotic Lorenz System

The Lorenz system was considered as a canonical example of an analytical chaotic dynamical system with intermittency dynamics, with the addition of Gaussian white noise to perform the sensitivity analysis for the HAVOK model and our intermittency analysis methods. The governing equations for the noisy Lorenz system are given as follows:

$$\dot{x}_{noisy} = \sigma(y - x) + w_x \tag{6.12}$$

$$\dot{y}_{noisy} = x(\rho - z) - y + w_y \tag{6.13}$$

$$\dot{z}_{noisy} = xy - \beta z + w_z \tag{6.14}$$

where $\boldsymbol{w} = \begin{bmatrix} w_x & w_y & w_z \end{bmatrix}^T \in \mathbb{R}^3, \boldsymbol{w} \sim \mathcal{N}_3(\boldsymbol{0}, \boldsymbol{Q})$. $\boldsymbol{Q}$ is the process noise covariance matrix:

$$\boldsymbol{Q} = \eta \begin{bmatrix} \sigma_x^2 & \sigma_x\sigma_y & \sigma_x\sigma_z \\ \sigma_x\sigma_y & \sigma_y^2 & \sigma_y\sigma_z \\ \sigma_x\sigma_z & \sigma_y\sigma_z & \sigma_z^2 \end{bmatrix} \tag{6.15}$$

For simplicity of the sensitivity analysis, we assumed that $\boldsymbol{Q} = \eta I_3$ (i.e., $\sigma_x^2 = \sigma_y^2 = \sigma_z^2 = 1$), in which I_3 is a 3×3 identity matrix and η denotes the noise level. We also define the notion of noise to signal ratio (NSR) as $NSR = \sigma^2/\mu^2$. However, we adopted a more robust estimate of NSR, which is:

$$\widehat{NSR} = Med\left[\frac{\eta}{\{\dot{x}_k\}_{k=1}^{n_{samples}}}\right] \tag{6.16}$$

where $Med[\cdot]$ is the median operator that estimates the median of a time series.

6.4.1.1 Measure of Sensitivity of Lorenz Lobe Switching Prediction Accuracy to NSR

The dependence of the Lorenz lobe switching prediction performance on NSR was analyzed by setting the NSR at different levels (0%, 0.1%, 1%, 10%, 50%). The sensitivity analysis results are demonstrated in Figure 6-3.

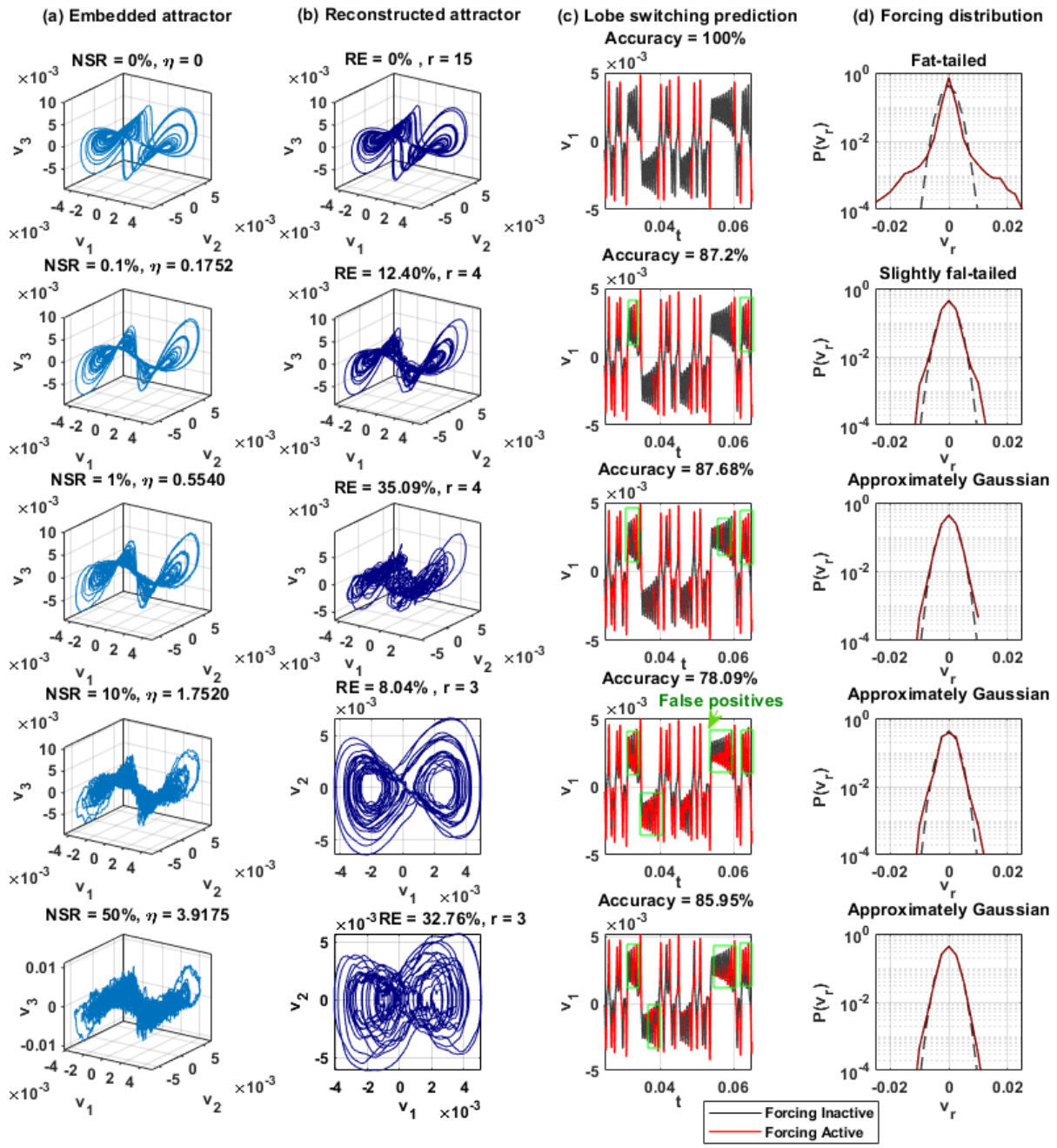

Figure 6-3 Embedded attractor, reconstructed attractor, lobe switching prediction, and forcing distribution of the noise-induced Lorenz system with different noise levels (0%, 0.1%, 1%, 10%, 50%)

6.4.1.2 Measure of Sensitivity of Lorenz Lobe Switching Prediction Accuracy to Sampling Rate

Similarly, the sensitivity analysis results are presented in Figure 6-4.

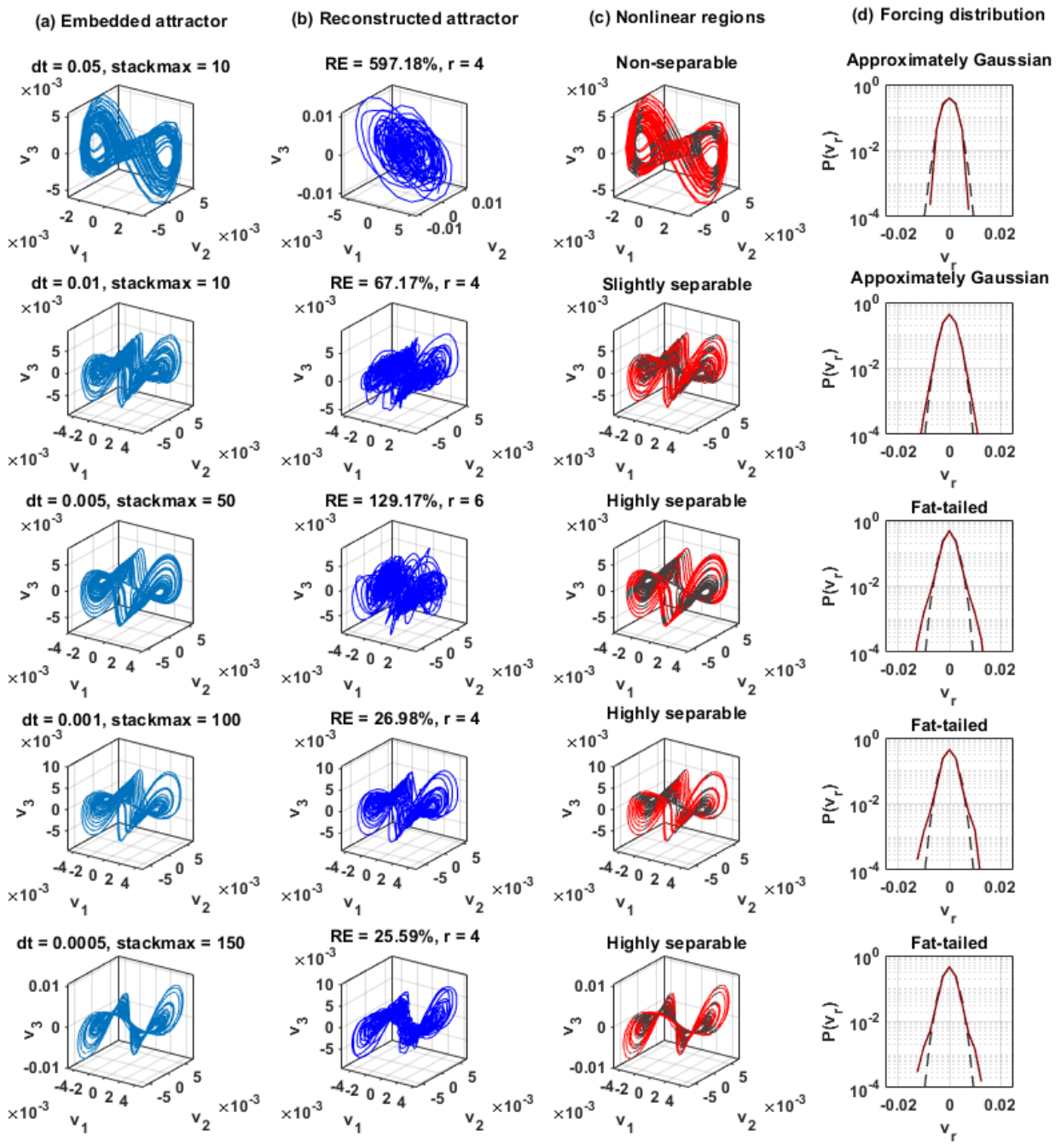

Figure 6-4 Embedded attractor, reconstructed attractor, nonlinear regions, and forcing distribution of the Lorenz system at different sampling periods (0.05, 0.01, 0.005, 0.001, 0.0005) with $NSR = 0.1\%$

6.4.1.3 Intermittency Analysis for Noisy Chaotic Lorenz System

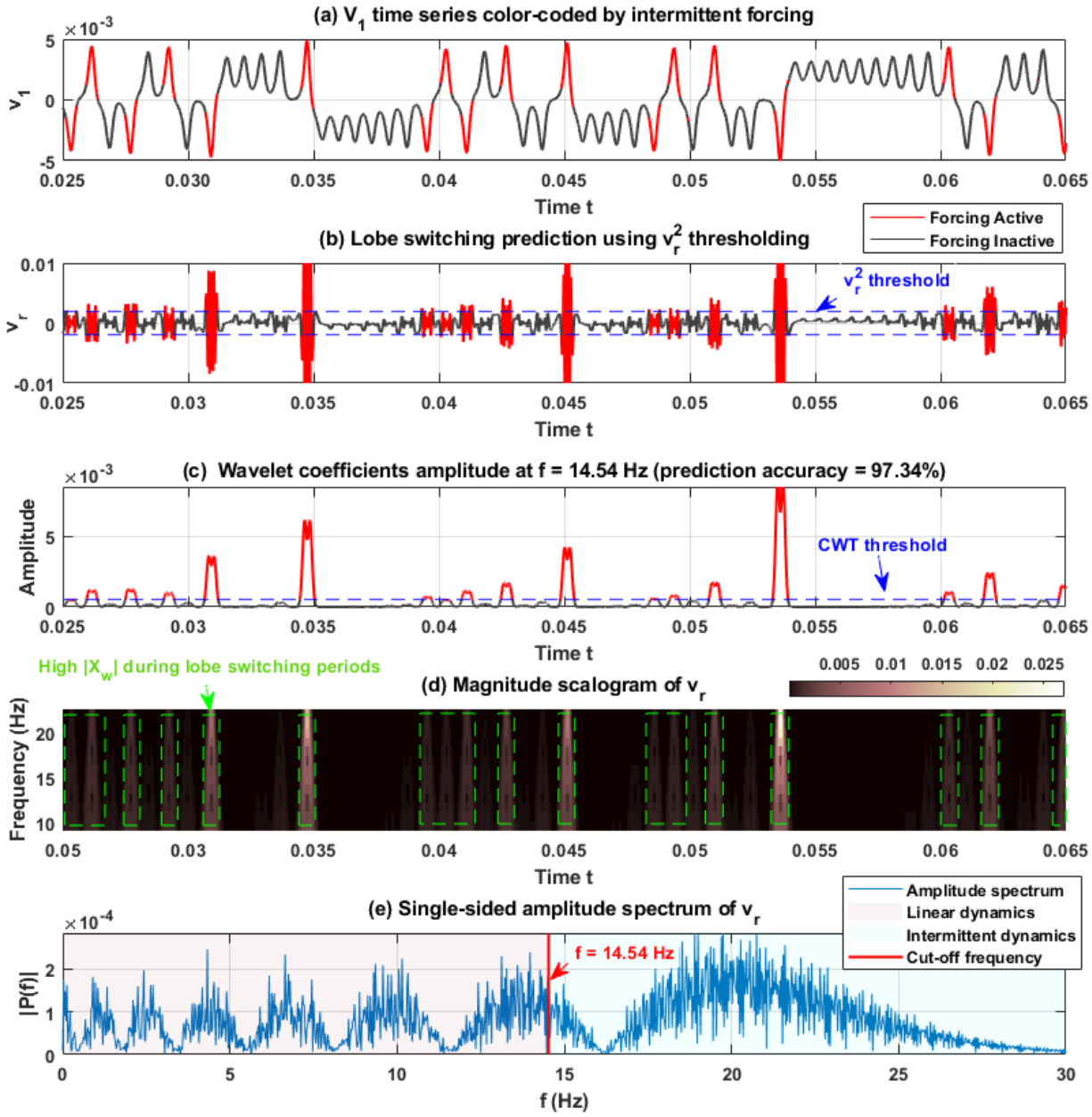

Figure 6-5 HAVOK analysis and intermittency analysis for noise-free chaotic Lorenz system

To decompose chaos and represent chaos as an intermittently forced linear system, the HAVOK analysis was performed. The results for these steps are summarized in Figure 6-5.

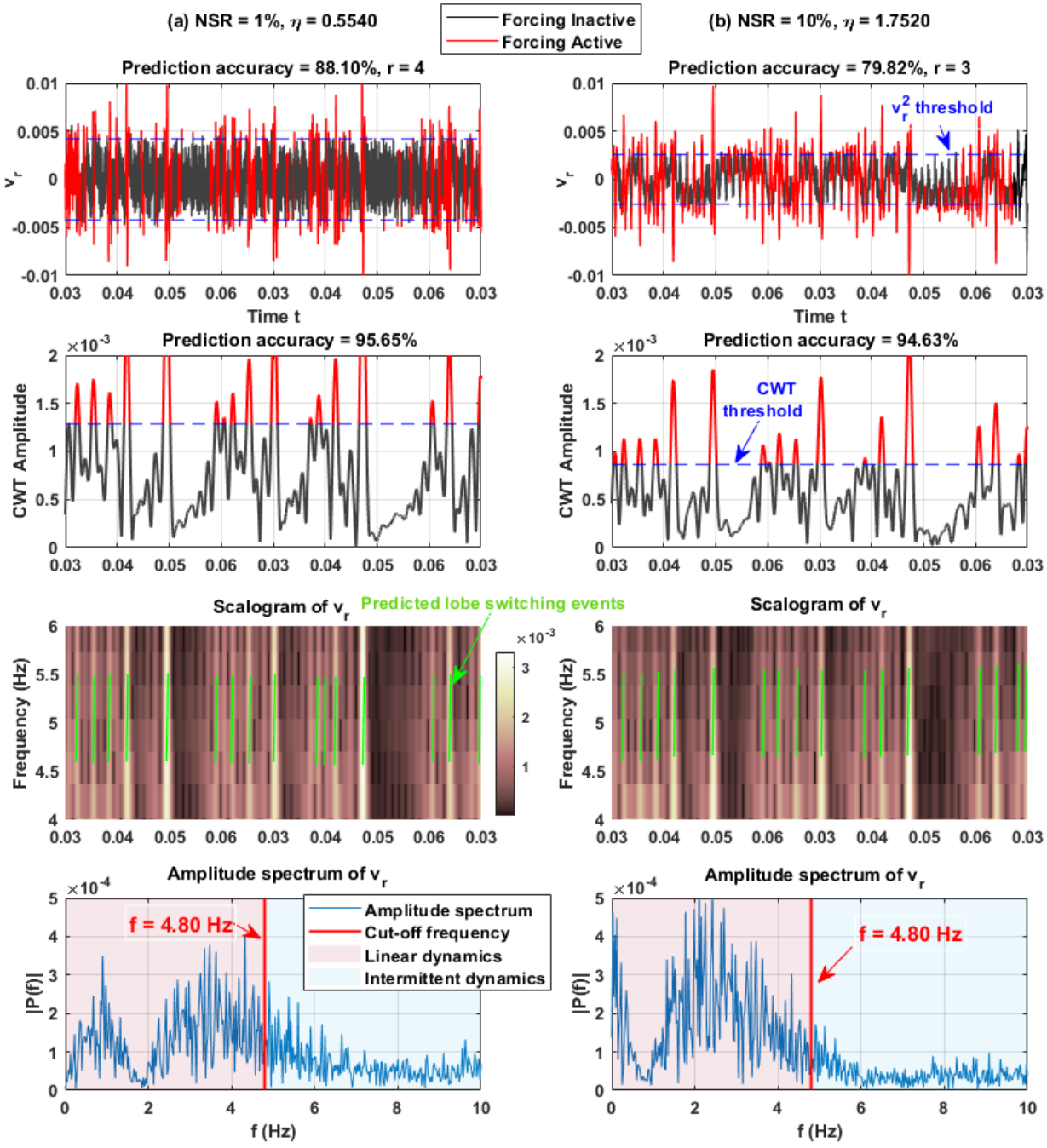

Figure 6-6 HAVOK analysis and intermittency analysis for the noisy Lorenz system at 2 different NSR values, 1% and 10%

6.4.2 OSA Case Study

In the case study of the pathophysiological processes in obstructive sleep apnea (OSA), we performed three main steps: (1) signal processing and feature extraction, (2) HAVOK analysis using HRV features, and (3) intermittent forcing analysis using v_r^2 thresholding and CWT thresholding.

6.4.2.1 Apnea-ECG Database for OSA

We performed the intermittent forcing analysis on the pathophysiological processes of obstructive sleep apnea (OSA)—a common sleep breathing disorder with long-term consequences on the cardiorespiratory system. We selected the Apnea-ECG Database [246] from Physionet.org to investigate the nonlinear intermittent behaviors. The data set has recordings of 70 OSA patients, and the recordings vary from 7 hours to nearly 10 hours each. Each recording comprises a continuous digitized ECG signal and apnea-hypopnea event expert-labeled annotations. The annotations consist of binary-coded events for each minute of the recording: "Normal breathing" (N) or "Disordered breathing" (A). The disordered breathing event may correspond to a single apnea episode, a hypopnea episode or a longer sequence of apneas and hypopneas. The severity of OSA is measured by an apnea-hypopnea index (AHI) that indicates the number of apneas or hypopneas per hour over the sleep study. Records of 22 OSA patients were shortlisted to be included in our HAVOK and intermittency analysis; we do not consider healthy (normal) subjects and patients with very mild OSA (AHI < 5) because healthy and very mild apnea cases do not exhibit significant intermittent switching between apnea-hypopnea events and normal episodes.

6.4.2.2 Signal Processing and Feature Extraction

Signal preprocessing and feature extraction were performed on the electrocardiogram (ECG) signals. First, a 5^{th} order Butterworth 0.5–30 Hz bandpass filter was applied to the signal

to eliminate noise and baseline wandering. Subsequently, the Hamilton-Tompkins algorithm [247] was employed to detect R peaks and compute RR intervals. A set of 18 features was extracted from Heart Rate Variability (HRV) Tool [248], an open-source MATLAB Toolbox that quantifies the spectral energy and nonlinear patterns of the HRV signals. Heart rate variability (HRV) features [249] quantify the fluctuation in the time intervals between adjacent heartbeats, which arise from the neurocardiac functions, the heart-brain interactions, and dynamic non-linear autonomic nervous system (ANS) processes. Next, the sliding window length was selected to be one minute, corresponding to the 1-minute OSA annotations.

6.4.2.3 HAVOK Analysis for OSA Case Study

First, we constructed the Hankel matrix, $\boldsymbol{\mathcal{H}}$, of the size $q \times p$ from a measurement (i.e., extracted HRV feature) time series, where $q = N - p + 1$, N is the length of the feature time series, and p is the window length. The q value (i.e., "stackmax" parameter) was chosen based on the findings of our previous study [250] such that the maximum periodicity of the underlying dynamics can be captured. We selected the most appropriate HRV feature to construct the Hankel matrix and obtain eigen-time-delay coordinates $\boldsymbol{v}(t)$. The HAVOK analysis results for 4 representative patients are illustrated in Figure 6-7.

6.4.2.4 Intermittency Analysis for OSA Case Study

Next, we performed spectral and wavelet analysis on v_r. The results for two representative patients, a03 and a05 are shown in Figure 6-8. To better compare the performance of v_r^2 and CWT thresholding approaches, the correlation between the OSA annotations and the intermittent forcing was estimated for 22 OSA patients as shown in Figure 6-9.

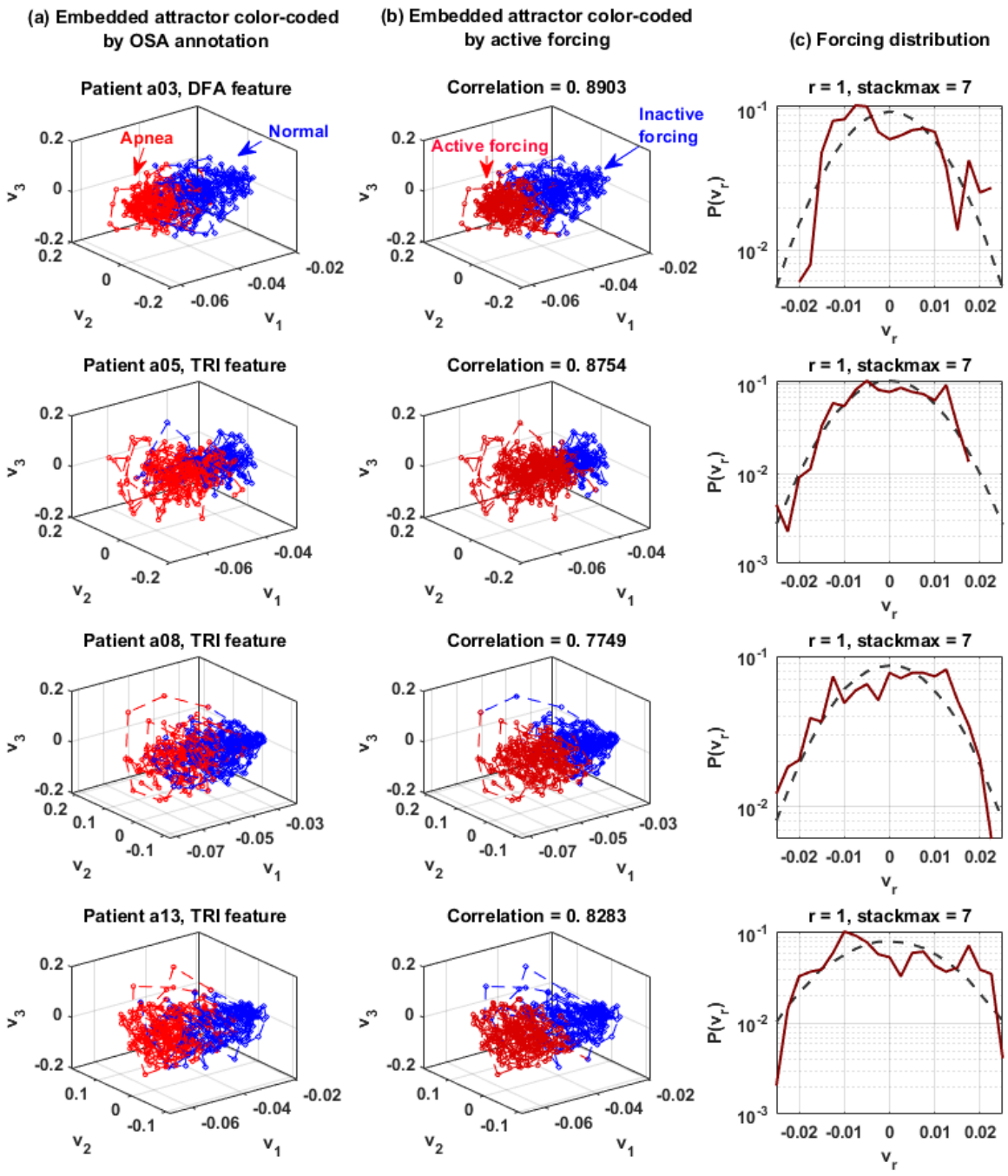

Figure 6-7 Embedded attractor color-coded by OSA annotated by the experts and by predicted active forcing, and the forcing distribution of representative patients a03, a05, a08, and a13

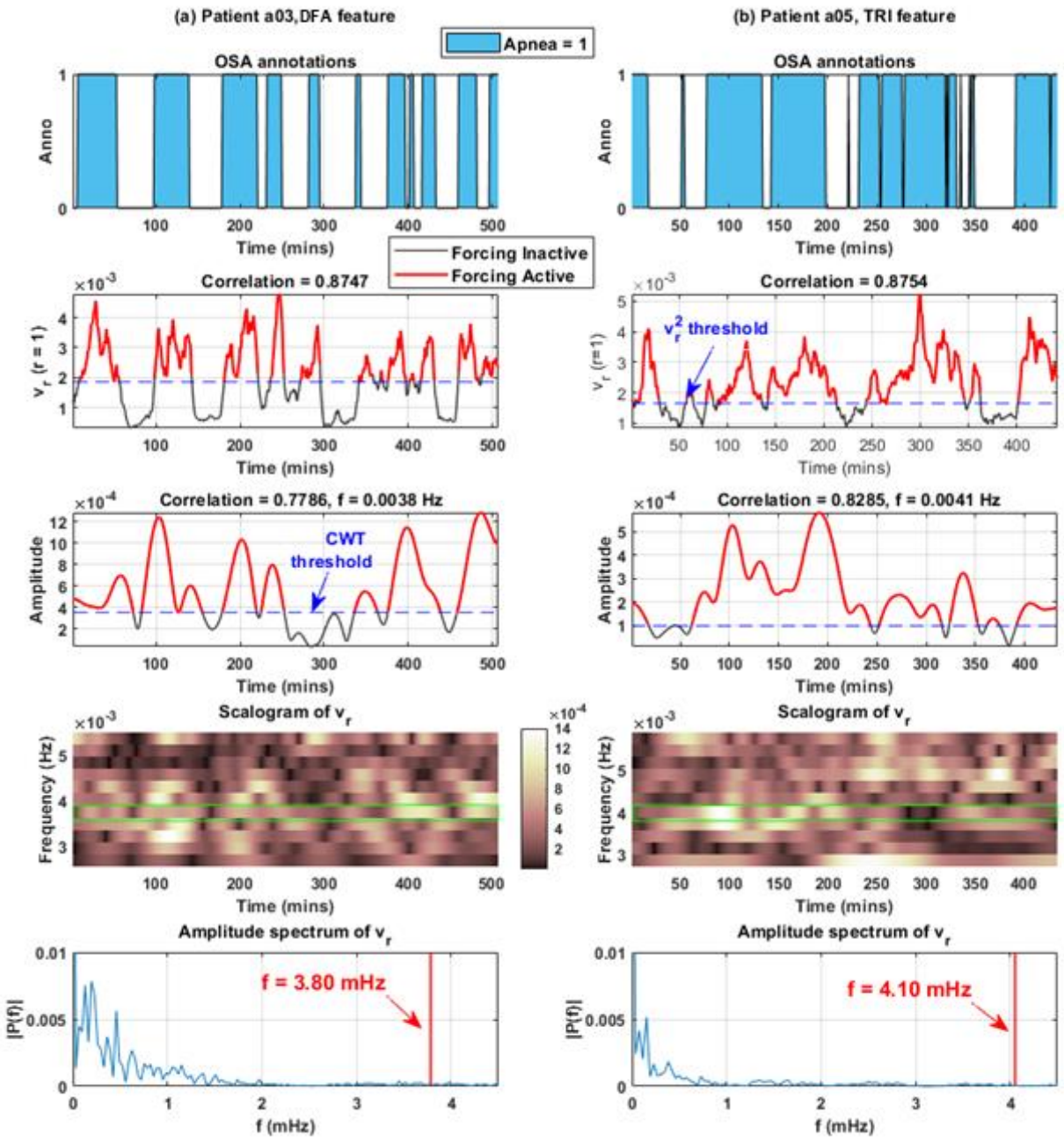

Figure 6-8 HAVOK analysis and intermittency analysis for representative patients a03 and a05. For each patient, the 1-minute OSA annotations were plotted corresponding to each 1-minute window of the ECG record. Next, the hypopnea-apnea event prediction results using v_r^2 and CWT thresholding are presented, followed by the Pearson correlation between the active forcing and the 1-minute OSA annotations. The hard thresholds (indicated by the red lines) applied in both methods were determined to maximize the correlation coefficient

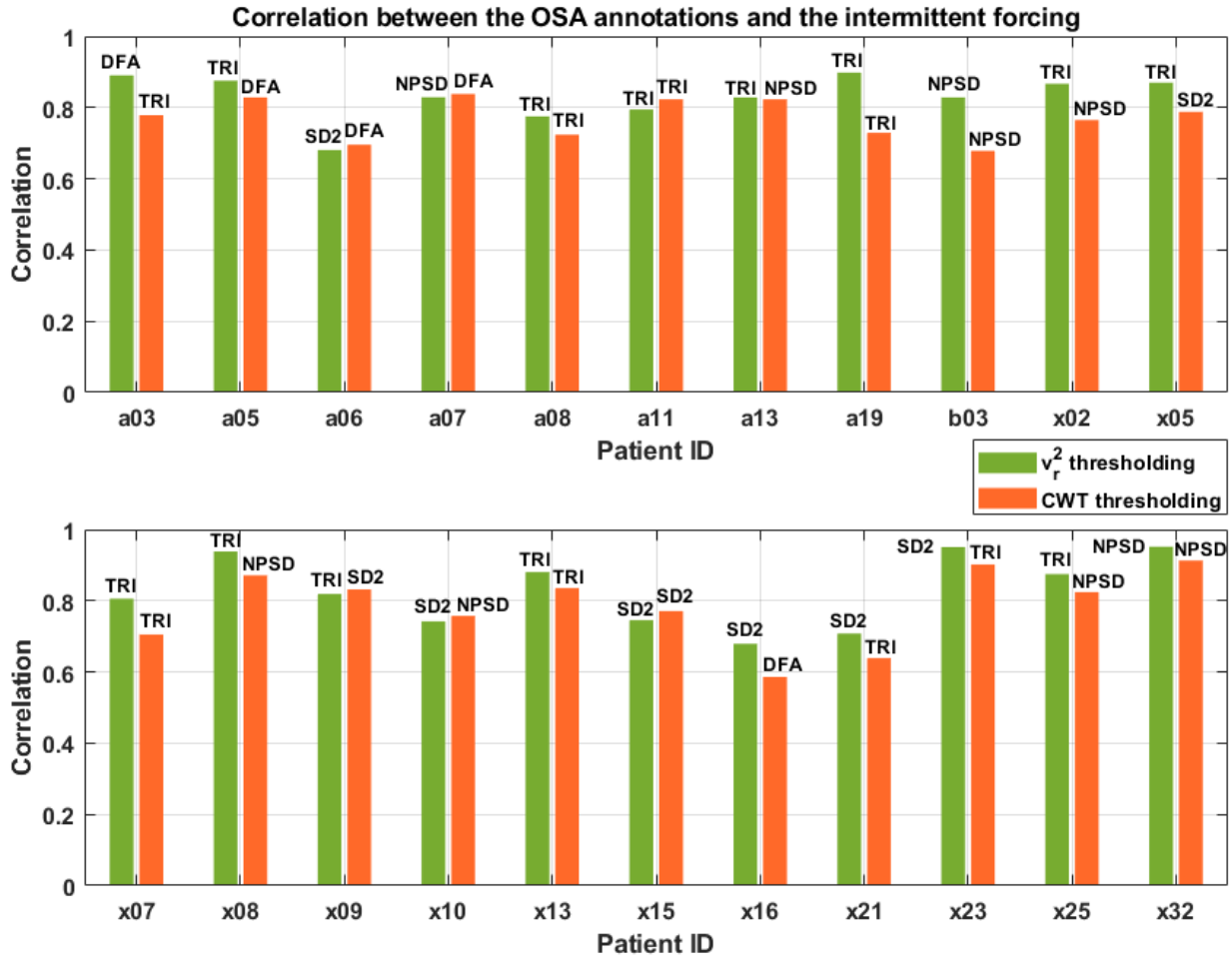

Figure 6-9 Correlation between the OSA annotations scored by an expert and by the intermittent forcing in 22 OSA patients. Here, we obtained the hard threshold for predicting the intermittent forcing using two methods, namely v_r^2 thresholding and CWT thresholding; the HRV features used for each approach are also given. The correlation coefficients estimated from the first method are represented by the green bars, and those estimated from the latter are represented by the orange bars. Overall, the v_r^2 thresholding approach mostly outperforms the CWT thresholding method

6.5 Discussion

Sensor-based and data-driven modeling of the intermittency dynamics in real-life complex systems is challenging because the governing equations are usually unknown. The HAVOK model was proposed to model a chaotic system as an intermittently forced linear system, a method that has been successfully applied to many nonlinear dynamical systems including analytical systems,

stochastic magnetic field reversal, and real-world systems. In this study, we have validated the noise-robustness of the HAVOK model and developed a noise-robust intermittency analysis method based on the HAVOK analysis. Therefrom we characterized the intermittent phases, the chaotic bursts, and the spectral-temporal properties of different intermittent dynamics modes. We investigated the intermittent nonlinear dynamics of obstructive sleep apnea (OSA) as a case study to demonstrate the novelty of our proposed method.

Regarding the numerical simulation validation results, we analyzed the sensitivity of the Lorenz lobe switching prediction accuracy to the noise level and the sampling rate. As seen in Figure 6-2, the lobe switching prediction accuracies were 87.20%, 87.68%, 78.09%, and 85.95%, which respectively correspond to the NSR values of 0.1%, 1%, 10%, and 50%. This result is a little counterintuitive because the prediction accuracy did not monotonically decrease as the Gaussian white noise level increased. Interestingly, this result can be explained by the variation in the optimal truncated rank, r, estimated by the optimal rank selection methods [245]. The truncated rank, r, values corresponding to 4 different mentioned NSR values were $r = 4$, $r = 4$, $r = 3$, and $r = 3$; hence, the energy captured by the v_r component was different in each scenario. Moreover, the distribution of the energy for the v_k modes ($k = 1, \dots q$) depends significantly on the Gaussian white noise contamination and the resulting matrix, $\boldsymbol{V}$, from the Hankel matrix decomposition, which caused the prediction accuracy to fluctuate in response to the amount of energy that v_r captured. The sensitivity of the accuracy may also be partially reflected in the variations in the reconstruction errors that quantify the mean absolute percentage error (MAPE) between the first eigen time-delay trajectory, $v_{1,}$ and the reconstructed trajectory, $\hat{v}_1$, which show that the higher the energy accounted for by v_1, the lower the reconstruction error. The contamination by white noise also affected the probability distribution of v_r, which caused it to be approximately Gaussian

since the high-frequency high-amplitude intermittent bursts were gradually mixed with and then dominated by the broad-frequency-band noise as we increased the NSR.

After performing the sensitivity analysis, the intermittency analysis methods using v_r^2 thresholding and CWT thresholding approaches were performed in the noise-free and noise-induced chaotic Lorenz system. The results from Figure 6-5 and Figure 6-6 demonstrate that our proposed CWT thresholding method is a more reliable, noise-robust, alternative method to predicting lobe switching events that correspond to the nonlinear dynamics. This result can be confirmed by the low-variance prediction accuracy using the CWT thresholding method (97.34% for the noise-free case, 95.65% when $NSR = 1\%$, and 94.63% when $NSR = 10\%$). These values for the noisy cases are higher than the values reported when applying the v_r^2 thresholding method (88.10% when $NSR = 1\%$ and 79.82% when $NSR = 10\%$). The high values of $|X_w|$ showed in the v_r scalogram over the lobe-switching periods demonstrate the active forcing prediction capability of the CWT thresholding. In addition, the v_r frequency spectrum shows the frequency bands associated with the linear dynamics and nonlinear dynamics, in which the linear and nonlinear dynamics regions are separated by a cut-off frequency. This cut-off frequency was chosen to achieve the optimal lobe switching prediction accuracy. We validated the cut-off frequency by applying a bandpass filter on v_r to filter out the low-frequency components corresponding to the linear dynamics; as a result, only the high-frequency high-amplitude bursts remained in the signal.

The HAVOK analysis using HRV features and the intermittent forcing analysis results for the OSA case study are presented. The embedded attractors shown in Figure 6-7 were color-coded by both the OSA annotations and the predicted active forcing; and the correlation coefficients between the active forcing and the hypopnea-apnea events of four representative patients were

significantly high. This result validates the intermittent forcing identifiability using our proposed methods and shows a strong association between the active forcing and hypopnea-apnea events. The forcing distributions are approximately Gaussian in all four representative cases, which potentially results from the low sampling period since we extracted the HRV features for each 1-minute time window. Therefore, the HAVOK analysis captures only the slow-time-scale dynamics and not the fast-time-scale dynamics in the Lorenz system, and the forcing distribution is not necessarily fat-tailed. Moreover, the AHI values of all four patients are substantially high (AHI = 39.1, 41, 42, and 42), so the hypopnea-apnea events are no longer rare events that contribute to the fat tails of the distribution. The comparison of the v_r^2 thresholding and CWT thresholding methods is illustrated in Figure 6-8 and Figure 6-9, which show that the v_r^2 thresholding approach outperformed the alternative method for most of the patients. However, the CWT thresholding method can still be improved by using an adaptive threshold, selecting a more appropriate "mother wavelet," and combining the prediction results at multiple frequencies if the forcing has a broad frequency band and one frequency cannot completely characterize the intermittent dynamics.

The HAVOK analysis and our proposed intermittency analysis methods have several limitations. Based on the concepts of chaos from nonlinear dynamics theory, the chaotic bursts are considered to belong to an invariant subspace; however, we have only limited information about the characteristics of this invariant subspace because of the rare occurrence of those chaotic bursts. Moreover, during "bursting" events, the dynamics time scale appears to be much faster, and the uniform sampling rate of the measurement might not be sufficient to resolve these events for a successful analysis of the intermittent chaotic bursts. Champion et. al. has proposed different sampling strategies that efficiently handle multi-scale systems [251], in which the dynamics can be separated into fast and slow dynamics. Furthermore, additional difficulties arise from the

inhomogeneity of the time series for the intermittent forcing analysis, e.g., the non-stationary data with intermittent behaviors.

6.6 Conclusion

In summary, our study proposes an intermittency analysis method that systematically decomposes and analyzes the intermittent forcing obtained from the HAVOK model. The main contributions of our study are the following: (1) numerical validation of the HAVOK model's robustness with respect to the noise level and sampling rate, (2) a noise-robust intermittency analysis framework to characterize the intermittent phases, the chaotic bursts, and the spectral-temporal properties of different intermittent dynamics modes, and (3) an attempt to characterize chaos in pathophysiological processes as an intermittently forced linear system and thoroughly analyze the intermittent forcing. In particular, in addition to the distribution of the intermittent forcing, we proposed additional statistics such as burst starting-ending time and burst and inter-burst duration quantifiers to better characterize the intermittent phases and chaotic bursts. Moreover, the frequency spectrum of the intermittent forcing signal estimated from the Discrete Fourier transform were used to characterize the spectral properties of the intermittent forcing. The adaptive continuous-time wavelet analysis with different types of mother wavelets chosen to match the morphological features of the bursts was performed to extract local spectral and temporal information simultaneously. To validate our proposed methods, we performed our intermittency analysis methods on both the Lorenz system and an OSA case study. This is the first attempt in the literature to characterize chaos in pathophysiological processes in a sleep disorder like OSA.

Chapter 7: Detecting Transition to Turbulence in Intracranial Aneurysms by Optimized Dynamic Mode Decomposition

Intracranial aneurysms present a significant risk, with the transition to turbulence within the blood flow acting as a crucial predecessor to potential rupture. To better understand these dynamics, patient-specific computational fluid dynamics (CFD) simulations were executed. These simulations, based on real-world patient morphology and blood flow parameters, created a comprehensive and realistic representation of the aneurysmal flow dynamics, laying a solid foundation for subsequent decomposition analyses. Despite the insights provided by traditional Dynamic Mode Decomposition (DMD) [240], its susceptibility to capture "false" modes occasionally compromised its accuracy in deciphering aneurysm dynamics. Addressing this limitation, this study introduces the Optimized Dynamic Mode Decomposition (OptDMD) [129]. This refined algorithm seamlessly incorporates optimization into the DMD process, ensuring a more genuine alignment of computed modes with the intrinsic data dynamics derived from the CFD simulations. Utilizing patient-specific simulated data, hierarchical clustering of aneurysms based on morphological parameters revealed three size-based categories: small, medium, and large. A noticeable reduction in the Frobenius norm error in the OptDMD predictions was observed, emphasizing the method's enhanced data representation capacity. Additionally, the cumulative distribution of mode energy displayed distinct patterns between DMD and OptDMD, offering deeper insights into the blood flow characteristics. Most critically, both methodologies reproduced the first two Fourier modes of inflow; however, OptDMD presented a clearer representation of a high-frequency damped mode associated with turbulence. This mode,

indicative of intermittency within the aneurysm, provides essential insights into potential transition phases to turbulence.

7.1 Introduction

Intracranial aneurysms, spherical dilations of deteriorated blood vessel walls within the brain, pose a dire health risk due to their potential to rupture, leading to catastrophic hemorrhagic strokes [252]. Often referred to as “silent killers”, these aneurysms frequently go undetected because many remain asymptomatic until rupture [253]. A comprehensive meta-analysis by Vlak et al. discovered that intracranial aneurysms are prevalent in nearly 3% of the global population, with variances in prevalence attributable to factors like age, gender, and genetic predisposition [254]. However, the true danger of these aneurysms lies in their rupture. The aftermath of an aneurysmal rupture is grim; mortality rates can soar up to 40%, and nearly half of the survivors experience permanent neurological deficits, further underscoring the severity of this neurovascular condition [255, 256]. Compounding the problem, survivors often grapple with psychological distress and diminished quality of life due to concerns about rebleeds or the presence of other undetected aneurysms [257]. Given the hidden nature of intracranial aneurysms and the devastating consequences following rupture, there is an imperative need for pioneering diagnostic tools, rigorous research, and innovative therapeutic interventions aimed at early detection and effective management [258].

Intracranial aneurysm diagnosis and management have traditionally hinged on a series of different imaging modalities. Computed tomography angiography (CTA) [259] and magnetic resonance angiography (MRA) [260] are the linchpins for non-invasive diagnostic evaluations, providing detailed anatomical information on aneurysm size, shape, and location. These modalities, while instrumental in visualizing aneurysms, can sometimes fall short in risk

assessment for rupture, necessitating more intricate imaging like digital subtraction angiography (DSA) [261] — regarded as the “gold standard”. DSA not only furnishes high-resolution images but also delivers insights into hemodynamic parameters, a critical facet in understanding aneurysm behavior. Furthermore, the burgeoning field of computational fluid dynamics (CFD) provides a groundbreaking approach to mimic the complex flow patterns within aneurysms, thereby shedding light on possible triggers for rupture [262]. A multitude of studies underscore the value of wall shear stress (WSS) and flow impingement, derived from CFD, as potential harbingers of rupture risk [263, 264]. Yet, while the progress in imaging and simulation methods has been commendable, inherent challenges persist. Issues range from the invasive nature of some procedures like DSA to the time-intensiveness of CFD computations. Additionally, with the advent of high-frequency flow data, there's a pressing need for analytical tools capable of dissecting this data to discern nuances that traditional diagnostic methods might overlook [265].

Traditional Dynamic Mode Decomposition (DMD) has emerged as a potent tool for analyzing spatial-temporal patterns in fluid flows, offering insights into the intricate dynamics inherent in intracranial aneurysms [266, 267]. While DMD can parse high-dimensional data into coherent modes, it is not without pitfalls. Inherent noise in data acquisition, sensitivity to perturbations, and the generation of “false” modes have, at times, raised questions about the fidelity and robustness of the DMD-derived features [268, 269]. Addressing these concerns, the Optimized Dynamic Mode Decomposition (OptDMD) technique was introduced. OptDMD refines the mode identification process, enabling an efficient and accurate delineation of dynamic modes by directly integrating the optimization problem into mode computation, thereby eliminating the discrepancies often associated with the traditional DMD [270]. Within this analytical landscape, patient-specific CFD simulations play a pivotal role. By generating high-

fidelity datasets that closely mimic the patient's unique aneurysm flow dynamics, CFD acts as the foundation on which DMD and OptDMD build, translating intricate simulations into actionable insights [271]. Together, these advancements seek to revolutionize our understanding of aneurysm behavior, potentially reshaping diagnostic and treatment paradigms.

This study endeavors to delve deeper into the challenges and opportunities presented by the traditional Dynamic Mode Decomposition in the context of intracranial aneurysms and to validate the efficacy of the OptDMD technique. Central to our objective is the utilization of patient-specific CFD simulations to obtain a granular understanding of the aneurysm flow dynamics. The principal aim is to ascertain whether OptDMD, in conjunction with high-fidelity CFD datasets, can offer a more accurate and robust representation of aneurysm dynamics compared to the conventional DMD. Specifically, we seek to investigate the transition to turbulence within aneurysms, understanding its implications for early detection and intervention. The scope of our study spans the collection and analysis of patient data, the intricate nuances of DMD and OptDMD methodologies, and the potential clinical implications of our findings. Through rigorous analytical and experimental processes, our mission is to bridge the gap between computational innovation and clinical applicability, paving the way for groundbreaking advancements in the diagnosis and treatment of intracranial aneurysms.

7.2 Methodologies

This study integrates patient-specific data collection, advanced CFD simulations, and the analytical prowess of both traditional DMD and its refined variant, OptDMD. Our approach begins with rigorous data acquisition and preprocessing, ensuring robustness and reliability. We then employ CFD simulations to model intricate intracranial aneurysm flow dynamics. Using this simulation data, we apply DMD and OptDMD to extract and analyze dominant dynamic modes,

particularly those indicating turbulent transitions. By combining these methods, we aim to provide a comprehensive and nuanced understanding of the transitions within intracranial aneurysms, setting the groundwork for the detailed methodologies that follow.

7.2.1 Patient-specific Data and Preprocessing

For this study, aneurysm models were sourced from the Aneurisk project, available at https://github.com/permfl/AneuriskData [266]. These models, derived from the segmentation of blood vessels from MRI scans, are pivotal to our analysis. The MRI scans, stored as TIFF files, which are inherently three-dimensional, were processed using the 3D Slicer software — a community-driven platform esteemed for its proficiency in medical image visualization and analysis. In the 3D Slicer, precise thresholds were set to distinguish between the arterial system and surrounding brain tissue, leading to the extraction of the complete cerebral artery network. Once acquired, these segmented models required extensive refinement. By using Meshmixer [272], a tool specialized in mesh manipulation, artifacts were removed, and the aneurysm was centered within a rectangular framework. The major artery connected to the aneurysm was trimmed, ensuring a consistent length from the aneurysm neck, approximately five times the artery's diameter. After this, a remeshing operation was executed, culminating in a mesh with approximately 10,000 vertices. The processed models then underwent measurements in Paraview [273] to gauge critical parameters like aneurysm and artery diameters, as well as aneurysm height, all of which were meticulously documented for further computational analysis. Table 7-1 describes the computed average diameters of the arteries and their aneurysms, as well as the average heights of the aneurysms. With these dimensions at hand, we can proceed with the blood flow modeling.

Table 7-1 Calculated average diameter of each artery and associated aneurysm, and the average height of each aneurysm

Patient ID	Artery Diameter (mm)	Aneurysm Width (mm)	Aneurysm Height (mm)
C0002	3.6275	4.3725	7.7625
C0006	3.2625	7.9025	4.8431
C0014	4.5875	6.9175	5.2375
C0016	3.0825	7.7675	7.4925
C0034	3.0766	8.5366	7.6166
C0036	3.9625	10.7725	14.2625
C0042	3.9425	8.4375	7.7575
C0067	3.5375	4.1125	3.0875
C0075	3.5725	12.0225	11.8025
C0085	3.3275	9.6025	7.1475
C0088b	3.4625	7.3125	7.2875

As illustrated in Figure 7-1, the distinct geometries of aneurysms can be observed for three representative patients.

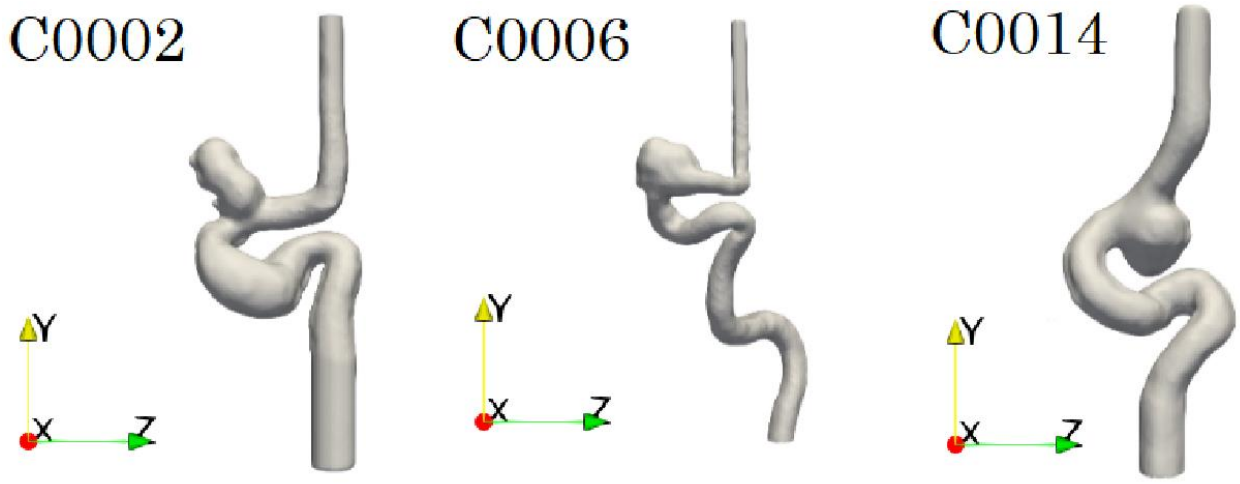

Figure 7-1 Geometries of aneurysms from 3 representative patients: C0002, C0006, and C0014

7.2.2 Aneurysm CFD Simulations

The CFD simulation work conducted in this study built upon the foundational research presented in the papers [266, 274, 275]. The CFD simulations undertaken in this study aimed to capture the intricate blood flow dynamics within patient-specific brain aneurysms. We employed a three-dimensional, unsteady, incompressible Navier-Stokes equations to simulate the blood flow:

- The *continuity equation* is:

$$\nabla \cdot \boldsymbol{u} = 0 \tag{7.1}$$

where $\boldsymbol{u}$ is the velocity vector.

- The *momentum equation* is:

$$\rho\left(\frac{\partial \boldsymbol{u}}{\partial t} + \boldsymbol{u} \cdot \nabla \boldsymbol{u}\right) = -\nabla p + \mu \nabla^2 \boldsymbol{u} \tag{7.2}$$

Here, ρ denotes the fluid density and is set to 1000 kg/m^3 for blood, t represents time, p is the fluid pressure, and μ signifies the dynamic viscosity of the fluid, which is specified as 1.2 mPa s for blood. By employing these equations with the mentioned parameters, we aimed to accurately represent the flow dynamics of blood within the aneurysms. These governing equations were discretized and solved using the CURVIB method [276], with a fractional step method facilitating temporal integration. Our computational setup involved a rectangular domain, generated in Pointwise, in which each patient-specific aneurysm was encapsulated. For consistency across simulations, a fixed resolution of 201x201x321 was adopted for the x, y, and z axes, respectively. However, to achieve finer granularity at critical regions, a denser unstructured grid was employed within the aneurysm, ensuring a resolution ranging from 0.05 to 0.1 mm.

The geometry and mesh were then processed using the Reversed CURVIB method, which is particularly efficient for complex geometries like the arterial endothelial wall. This method reversed the conventional CURVIB approach, remeshing the solid domain into a fluid domain

post-detection, without considering endothelial wall deformations. For boundary conditions, we applied Neumann-type conditions at both the inlet and outlet. The inflow utilized a pulsatile waveform that mirrored measurements from the internal carotid artery of a human subject, with peak velocities reaching 0.5 m/s. The no-slip and no-flux conditions were imposed on the rigid arterial walls. Our numerical scheme was based on established methods which have been validated against both in vitro and in vivo datasets, with further details available in referenced papers. The non-dimensional parameters derived from the simulations, including Reynolds number and non-dimensional timescale, helped guide our understanding of the flow dynamics. We conducted the simulations over four cardiac cycles, with the fourth cycle's solutions being analyzed further through DMD and OptDMD.

7.2.3 Dynamic Mode Decomposition (DMD)

The DMD algorithm is a robust mathematical procedure primarily used for investigating the inherent dynamics of high-dimensional, non-linear systems. In the context of our study, it is utilized to understand the intricate fluid dynamics associated with intracranial aneurysms and their progression into turbulence. Let's break down the DMD algorithm into a step-wise process:

- *Step 1 is data matrix construction*. Start by gathering sequential data snapshots over time. These are then arranged into two matrices, $\boldsymbol{X}$ and $\boldsymbol{X}'$, with $\boldsymbol{X}$ containing the snapshots from time 1 to time t and $\boldsymbol{X}'$ containing the snapshots from time 2 to time $t+1$. Here, each column of $\boldsymbol{X}$ and $\boldsymbol{X}'$ is a snapshot of the vector field reshaped into a column vector.

$$\boldsymbol{X} = [\boldsymbol{x}(1), \boldsymbol{x}(2), \dots, \boldsymbol{x}(m-1)], \qquad \boldsymbol{X}' = [\boldsymbol{x}(2), \boldsymbol{x}(3), \dots, \boldsymbol{x}(m)] \tag{7.3}$$

- *Step 2 is singular value decomposition (SVD)*. The data matrix $\boldsymbol{X}$ is decomposed using SVD. This yields three matrices $\boldsymbol{U}$, $\boldsymbol{\Sigma}$, and $\boldsymbol{V}^*$. Here, $\boldsymbol{U}$ and $\boldsymbol{V}$ are orthogonal matrices, and Σ is a diagonal matrix containing the singular values of $\boldsymbol{X}$. This decomposition is expressed:

$$\boldsymbol{X} = \boldsymbol{U}\boldsymbol{\Sigma}\boldsymbol{V}^{*} \tag{7.4}$$

- *Step 3 is reduction to a low-dimensional subspace*. The full set of data may be of very high dimensionality. To reduce the computational cost, the full matrices $\boldsymbol{U}$, $\boldsymbol{\Sigma}$, and $\boldsymbol{V}^{*}$ are truncated to a lower rank r:

$$\boldsymbol{X} \approx \boldsymbol{U}_r\boldsymbol{\Sigma}_r\boldsymbol{V}_r^{*} \tag{7.5}$$

  Here, $\boldsymbol{U}_r$, $\boldsymbol{\Sigma}_r$, and $\boldsymbol{V}_r^{*}$ represent the first r columns of $\boldsymbol{U}$, the first r singular values in $\boldsymbol{\Sigma}$, and the first r columns of $\boldsymbol{V}_r^{*}$ respectively.

- *Step 4 is computation of the reduced A matrix*. In the lower dimensional subspace, the best-fit linear operator $\boldsymbol{A}$ is approximated by the matrix $\widetilde{\boldsymbol{A}}$, defined as:

$$\widetilde{\boldsymbol{A}} = \boldsymbol{U}_r\boldsymbol{X}'\boldsymbol{V}_r\boldsymbol{\Sigma}_r^{-1} \tag{7.6}$$

- *Step 5 is eigenvalue and eigenvector calculation*. An eigen-decomposition of the $\tilde{A}$ matrix is performed, yielding the matrices W and Λ. The eigenvalues of $\tilde{A}$ correspond to the eigenvalues of the full A matrix, which represent the temporal dynamics of the system.

$$\widetilde{\boldsymbol{A}}\boldsymbol{W} = \boldsymbol{W}\boldsymbol{\Lambda} \tag{7.7}$$

  where W is the matrix of eigenvectors of $\tilde{A}$, and Λ contains the eigenvalues of Λ.

- *Step 6 is DMD modes calculation*. Lastly, the DMD modes, denoted by Φ_{DMD}, are obtained by projecting the eigenvectors of $\tilde{A}$ back into the original high-dimensional space:

$$\boldsymbol{\Phi}_{DMD} = \boldsymbol{X}'\boldsymbol{V}_r\boldsymbol{\Sigma}_r^{-1}\boldsymbol{W} \tag{7.8}$$

These steps of the DMD algorithm serve to distill high-dimensional datasets into a manageable number of modes, which encapsulate the dominant spatio-temporal features of the system's dynamics. In the context of intracranial aneurysms, DMD provides us with the ability to identify and track the evolution of distinct patterns in blood flow, thereby offering insights into the onset of turbulence within aneurysms. The DMD modes, $\boldsymbol{\Phi}_{DMD}$, capture the spatial information

about the dynamic features in the vector field. The eigenvalues in $\boldsymbol{\Lambda}$ capture the temporal information, such as the growth or decay rate and oscillation frequency.

7.2.4 Optimized Dynamic Mode Decomposition (OptDMD)

Building on the concept of DMD, we continue to introduce OptDMD, a significant enhancement of the original DMD method. OptDMD refines the mode identification process, allowing for a more efficient and accurate delineation of dynamic modes. OptDMD employs an optimization process that avoids the "false" modes that might be generated from the original DMD process. This refined algorithm integrates the optimization problem directly into the computation of the DMD modes, ensuring the modes computed align well with the actual data dynamics. Here is a step-wise outline of the OptDMD algorithm:

- *Step 1 is data matrix construction and SVD*. As with DMD, data snapshots are collected over time and arranged into $\boldsymbol{X}$ and $\boldsymbol{X'}$. $\boldsymbol{X}$ is decomposed using SVD to obtain $\boldsymbol{U}$, $\boldsymbol{\Sigma}$, and $\boldsymbol{V}^*$.
- *Step 2 is low-dimensional subspace projection*. The SVD matrices are truncated to a reduced order r to derive $\boldsymbol{U}_r$, a lower-dimensional representation of the data that retains the most significant components.
- *Step 3 is solving optimization problem*. Unlike traditional DMD, OptDMD solves an optimization problem to find the optimal dynamic modes $\boldsymbol{\Phi}_{Opt}$ and their corresponding eigenvalues $\boldsymbol{\alpha}$. The objective of the optimization problem is to minimize the difference between the projected data and a linear combination of modes. The objective function for this problem is given by:

$$\min_{\boldsymbol{\alpha},\boldsymbol{\Phi}_{Opt}} \left\| \boldsymbol{X'} - \boldsymbol{\phi} diag(\exp(\boldsymbol{\alpha})) {\boldsymbol{\Phi}_{Opt}}^* \boldsymbol{X} \right\|_F^2 \tag{7.9}$$

Here, $\boldsymbol{\Phi}_{Opt}$ is the matrix of the dynamic modes, $\boldsymbol{\alpha}$ are the corresponding eigenvalues, and the diag(exp($\boldsymbol{\alpha}$)) represents the diagonal matrix of the exponentiated eigenvalues. $\|\cdot\|_F$

denotes the Frobenius norm, representing the Euclidean distance in matrix space. Solving this optimization problem involves finding the best values for $\boldsymbol{\alpha}$ and $\boldsymbol{\Phi}_{Opt}$ that minimize the objective function. This is achieved through an iterative variable projection method [270]. In the first stage, we keep $\boldsymbol{\Phi}_{Opt}$ fixed and solve for $\boldsymbol{\alpha}$. Then in the next stage, we keep $\boldsymbol{\alpha}$ fixed and solve for Φ_{Opt}. These stages are alternated repeatedly until convergence, leading to optimized $\boldsymbol{\alpha}$ and $\boldsymbol{\phi}$ that best represent the data dynamics. Note that the variable projection method is a nonlinear optimization approach, which is a powerful method for solving least squares problems.

- *Step 4 is calculation of OptDMD modes and eigenvalues*. Upon convergence of the optimization, the resulting optimized modes $\boldsymbol{\Phi}_{Opt}$ and their corresponding eigenvalues $\boldsymbol{\alpha}$ are the dynamic modes and eigenvalues of the OptDMD. The modes $\boldsymbol{\Phi}_{Opt}$ carry spatial information about the dynamic features of the blood flow within the aneurysm, while the eigenvalues $\boldsymbol{\alpha}$ provide information about the corresponding temporal behavior, such as growth, decay, and oscillation frequencies. Through these steps, OptDMD manages to provide a more accurate and robust representation of the original data dynamics compared to traditional DMD. Specifically for intracranial aneurysms, OptDMD provides an effective tool to accurately capture and track the evolution of blood flow patterns.

7.3 Results

Setting our study apart is the innovative approach of patient-specific clustering based on aneurysm morphological characteristics. This individualized analysis underscores the realization that generic methods often fall short in capturing the nuances of varied aneurysm types. Through our results, we will gain critical insights into variations in blood flow parameters across different aneurysm sizes. The comparative analysis between DMD and OptDMD further deepens this

understanding, offering clarity on the advantages and intricacies of each technique. As we delve deeper, the aim is to furnish a thorough grasp of intracranial aneurysm dynamics rooted in computational rigor. Intracranial aneurysms are varied and complex structures. Figure 7-2 serves as a visual representation of our clustering approach.

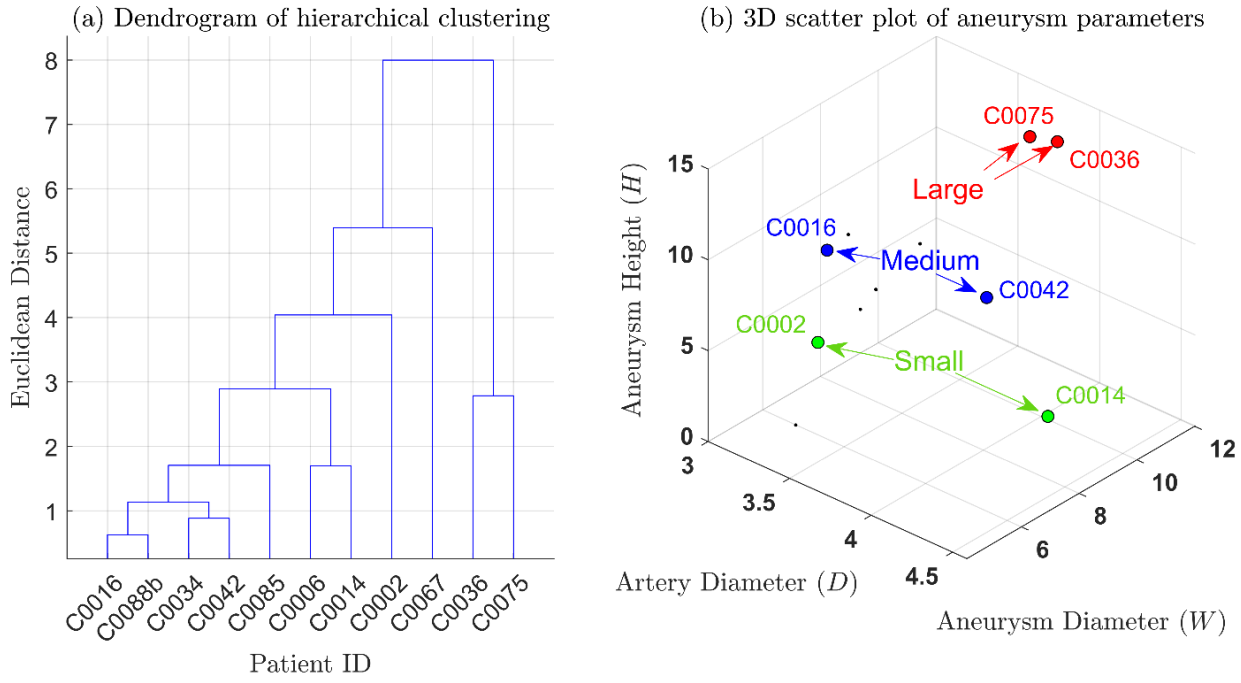

Figure 7-2 Patient-specific intracranial aneurysm clustering and morphological characteristics. Panel (a) depicts a dendrogram generated from hierarchical clustering of patient data based on three aneurysm parameters (artery diameter, aneurysm diameter, and aneurysm height). The color-coded labels represent six representative patients identified through clustering, belonging to three different groups: small (red), medium (green), and large (blue) size aneurysms. Panel (b) showcases a 3D scatter plot of the aneurysm parameters for all patients by group

Dendrograms are tree-like diagrams that display the arrangement of clusters created by hierarchical clustering. In Panel (a) of Figure 7-2, each leaf of the tree represents an individual patient's data. As one moves up the tree, leaves merge into branches, representing the formation of clusters. The depth at which two leaves merge showcases the similarity between them: the

deeper the merge, the more similar the data points. We categorized these merges into three distinct groups, thereby categorizing aneurysms into small (red), medium (green), and large (blue) sizes.

Panel (b) introduces a 3D scatter plot, which projects the three aneurysm parameters onto a three-dimensional space. Each point in this plot signifies a patient, with its position determined by the respective artery diameter, aneurysm diameter, and aneurysm height. The color-coding remains consistent with Panel (a), differentiating the patients into the three size categories. This visualization offers a bird's-eye view of our data, emphasizing the distribution and inter-relations of aneurysm morphologies across our patient cohort. The scatter plot not only affirms the cluster groupings from the dendrogram but also enriches our understanding by highlighting the spatial relationships and concentrations of these aneurysms in a dimensional context. Through this patient-specific approach, our study fosters a more refined understanding of intracranial aneurysms, accounting for their intrinsic variabilities and unique morphological footprints.

Within the context of analyzing blood flow dynamics in intracranial aneurysms, Figure 7-3 artfully captures the results derived using both DMD and OptDMD methods, plotting the eigenvalues for our set of patients, segmented by aneurysm sizes: small, medium, and large. These eigenvalues serve as signposts, indicating the dominant dynamics present in the blood flow of each patient. At the heart of our analysis lies Figure 7.3, which presents the eigenvalues derived from both the DMD and OptDMD methods for patients categorized by aneurysm sizes.

A primary observation from Figure 7-3 is the clustering of eigenvalues. These clusters hint at specific dynamical behaviors in the blood flow patterns that correlate with the size of the aneurysms. In particular, eigenvalues for smaller aneurysms may reside closer to one another, indicating more consistent flow patterns, whereas larger aneurysms might display a wider spread of eigenvalues, alluding to a greater diversity in flow behaviors.

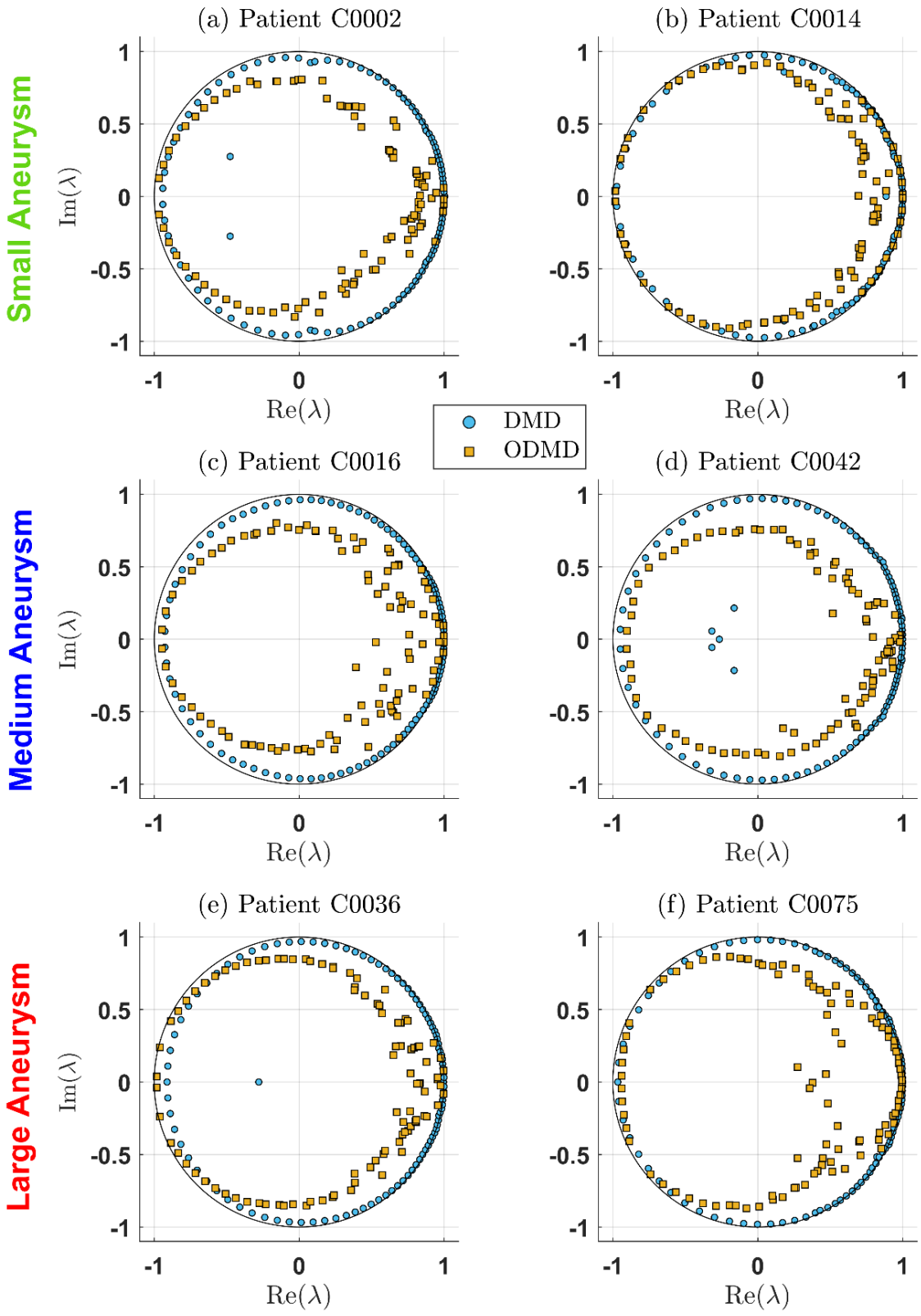

Figure 7-3 Eigenvalues of the DMD and OptDMD algorithms for six representative patients, categorized by their aneurysm sizes into small (blue), medium (green), and large (red) groups

Central to our exploration of prediction accuracy is Figure 7-4, which delves into the Frobenius norm error, denoted as $\|\boldsymbol{X} - \widehat{\boldsymbol{X}}\|_F$. This specific metric quantifies the difference between the actual and the predicted datasets, providing a tangible measure of how close our simulations are to the observed data. The lesser the Frobenius norm error, the closer our model predictions align with the real-world data, thus instilling confidence in the derived insights and subsequent clinical or research applications. The Frobenius norm error exhibits variability across the spectrum of aneurysm sizes. This suggests that certain sizes, be it small, medium, or large, might inherently pose more challenges in achieving accurate predictions than others. Such variations could arise due to complexities in the flow patterns, geometric intricacies, or even the boundary conditions associated with the respective sizes.

While both Dynamic Mode Decomposition (DMD) and its optimized counterpart (OptDMD) strive to predict the blood flow dynamics, their efficacy, as evidenced by Figure 7-5, is distinct. Certain aneurysm sizes might see a closer convergence between the two methods, while others might display a wider gap in prediction accuracies. This divergence emphasizes the value of the optimization procedures in OptDMD, potentially highlighting scenarios where OptDMD can outshine the traditional DMD in capturing the nuanced dynamics of blood flow. In conclusion, the pursuit of achieving impeccable prediction accuracy in CFD simulations for intracranial aneurysms remains an ongoing challenge. Yet, through tools like DMD and OptDMD, and metrics such as the Frobenius norm error, we edge closer to bridging the gap between theoretical models and their clinical representations.

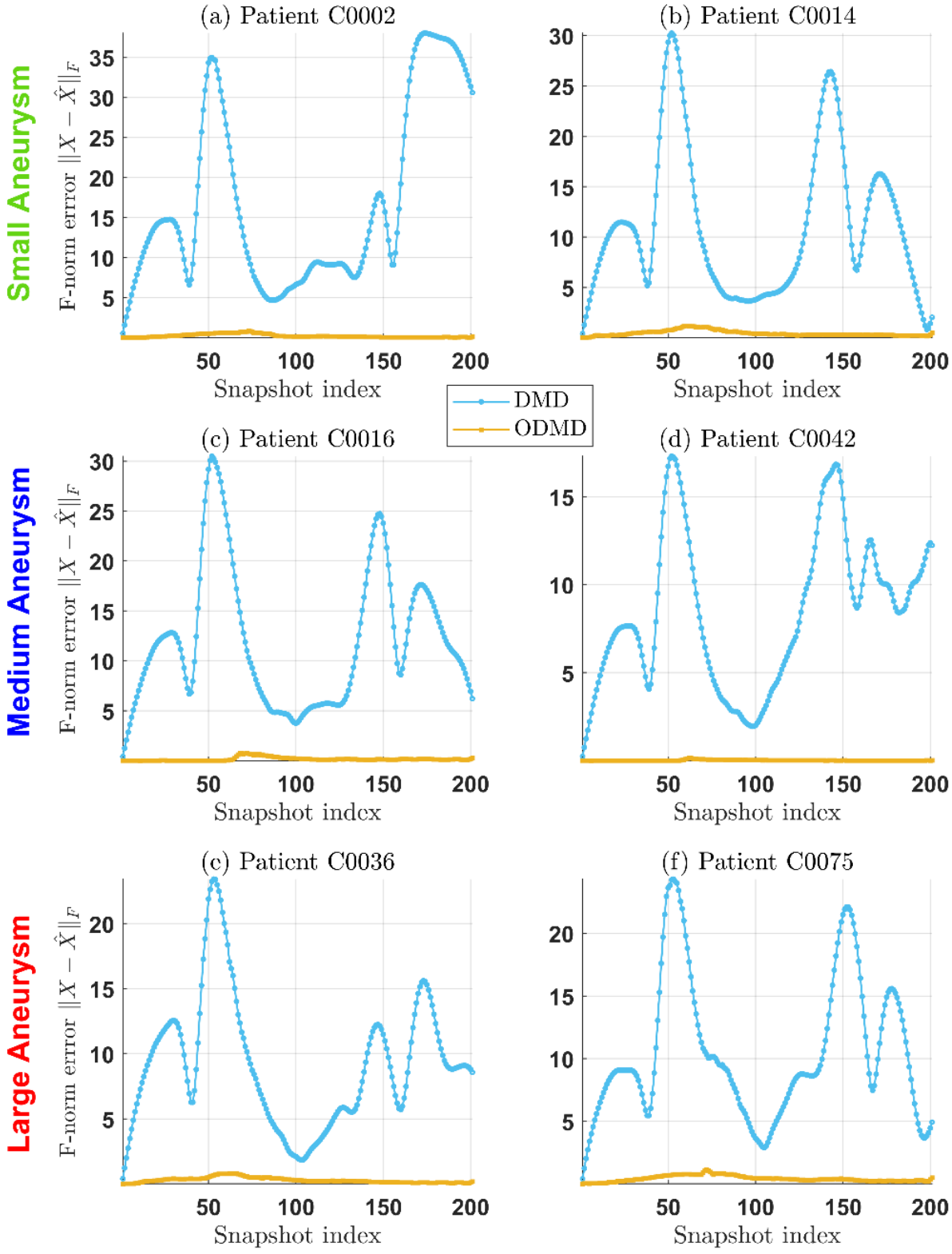

Figure 7-4 Comparison of Frobenius norm error $\|X - \hat{X}\|_F$ for DMD and optimized DMD prediction in patients with varying aneurysm sizes: small, medium, and large

In Figure 7-5, we find a comprehensive visualization of this mode energy distribution for both the DMD and its optimized counterpart, the OptDMD. The first observation drawn from the subplots is the differential energy distributions between DMD and OptDMD. While certain modes might show parallel energy levels in both methods, others exhibit stark contrasts. Such disparities highlight the optimization procedures inherent to OptDMD, which can occasionally lead to a reshuffling of energy across modes, potentially offering a more accurate representation of the aneurysm dynamics. The color-coded markers in Figure 7-5 further accentuate the distinctions in energy distributions across the small, medium, and large aneurysm groups. These variations are not mere coincidences; they are emblematic of the unique flow dynamics associated with each size category. Larger aneurysms, for instance, might house more complex flow structures, thereby resulting in a different mode energy landscape compared to their smaller counterparts.

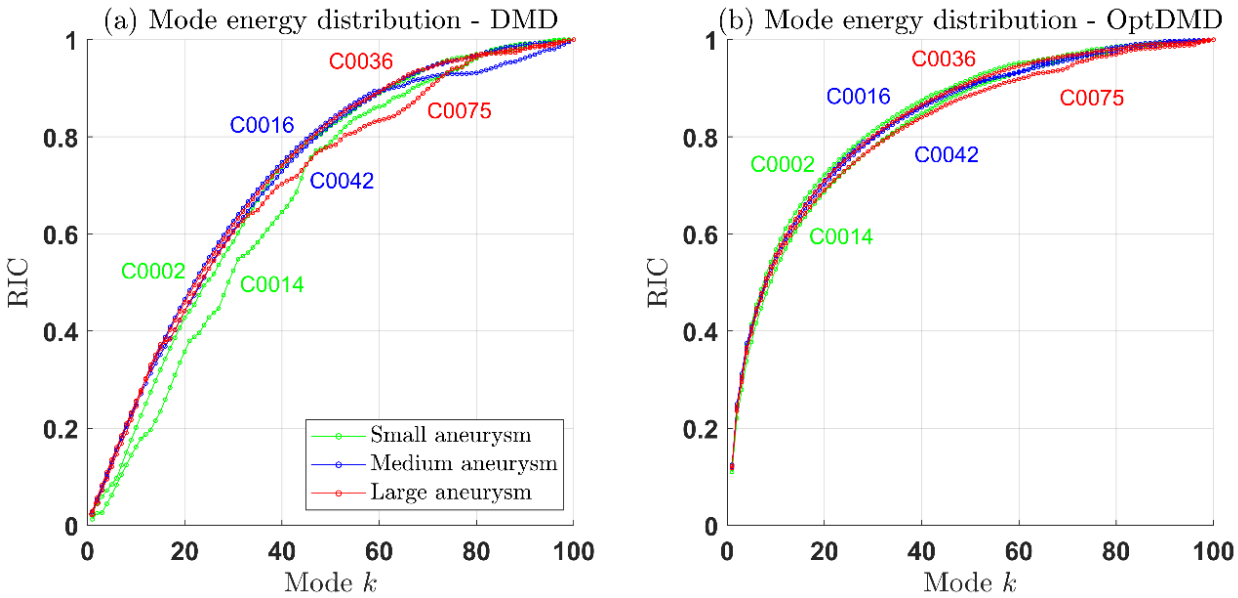

Figure 7-5 Cumulative distribution of mode energy calculated using DMD and OptDMD for different patients with aneurysm. Each patient is represented by a colored marker, corresponding to the patient's group (small, medium, or large aneurysm). In each subplot, the y-axis shows the relative importance contribution (RIC) of each mode, while the x-axis represents the mode number. Subplot (a) displays the distribution for DMD, while subplot (b) shows the distribution for OptDMD

Table 7-2 serves as the primary instrument for this comparative endeavor. A meticulous analysis of this table uncovers the similarities and contrasts between the modes obtained from DMD and OptDMD across varied aneurysm sizes.

Table 7-2 Comparison of the three dynamic modes with the corresponding frequencies f_1, f_2, and f_3 obtained from DMD and OptDMD for 3 different aneurysm sizes

Aneurysm group	**Patient ID**	**DMD**			**OptDMD**		
		f_1	f_2	f_3	f_1	f_2	f_3
Small	C0002	2.3568	3.5245	11.7080	2.2602	3.8813	37.7710
	C0014	2.4322	3.5730	24.1298	1.4753	3.5781	13.2871
Medium	C0016	2.3410	3.5248	7.0239	1.3949	3.5330	26.1135
	C0042	2.3520	3.5269	16.5195	0.7560	3.3461	25.4833
Large	C0036	2.3417	3.5172	13.3535	2.8584	3.0436	19.7064
	C0075	2.2584	3.4592	14.5911	1.8175	3.3756	32.2388

At the heart of Table 7-2 lie the three dynamic modes characterized by their respective frequencies f_1, f_2, and f_3. These frequencies capture the oscillatory nature of the flow within the aneurysm, with each frequency corresponding to a distinct flow pattern. The first two frequencies, f_1 and f_2, are of particular note, as they correspond to the primary Fourier modes of the inflow at 2.33 Hz and 3.5 Hz respectively. Interestingly, both DMD and OptDMD successfully reproduce these foundational modes, underlining their robustness and the universality of these modes across different decomposition techniques. The third mode f_3 encapsulates a more elusive, high-frequency damped pattern. This mode, as its description suggests, is synonymous with the intermittency or turbulence occurring within the aneurysm. Turbulent flows, with their erratic and

chaotic behavior, can significantly influence the stress exerted on the aneurysm walls, hence understanding this mode is paramount for gauging potential rupture risks.

7.4 Discussion

The results obtained from our study underscore the dynamic intricacies of intracranial aneurysm hemodynamics. Our use of DMD, both the standard and optimized algorithms, enabled a detailed characterization of the flow patterns within aneurysms of varying sizes. Specifically, the hierarchical clustering of patient-specific aneurysms revealed clear categorizations into small, medium, and large groups based on morphological characteristics, as delineated in Figure 7-2. This demarcation was further validated by the eigenvalues derived from the DMD and OptDMD algorithms, with Figure 7-3 revealing distinct patterns for each size group. Furthermore, our focus on prediction accuracy, highlighted by the Frobenius norm errors (Figure 7-4), demonstrates the robustness and potential applicability of the OptDMD technique over the conventional DMD, especially in the context of larger aneurysms. Lastly, the mode energy distributions and dynamic modes comparison between the two decomposition techniques (as seen in Figure 7-5 and Table 7-2, respectively) offer new insights into the turbulence and flow dynamics within the aneurysm.

The discoveries in our study not only expand the academic understanding of intracranial aneurysm dynamics but also carry considerable clinical and technical implications. Clinically, discerning the precise hemodynamic behavior of aneurysms—across sizes—offers neurologists and neurosurgeons a more granular insight into potential rupture risks. For instance, the high-frequency damped mode associated with turbulence within the aneurysm, as demonstrated in Table 7-2, can serve as an indicator for monitoring or intervention, especially in larger aneurysms where the implications of rupture are more severe. From a technical standpoint, the superiority of the OptDMD technique over traditional DMD in terms of prediction accuracy paves the way for its

broader application in computational fluid dynamics (CFD) simulations. Enhancing modeling accuracy can be invaluable in patient-specific treatment planning, optimizing interventional strategies, and even in the development of medical devices tailored to aneurysm management. Moreover, the ability to accurately capture and represent the mode energy distributions (as seen in Figure 7-5) provides bioengineers with a refined toolset for simulating and studying vascular flow dynamics.

The trajectory of our findings aligns with some past research while shedding new light on certain aspects of aneurysm dynamics. For example, the relevance of the high-frequency damped mode in indicating turbulence within the aneurysm, as observed in our analysis, echoes the results found by Le et al. (2021) [266]. They identified these turbulent markers too, emphasizing their potential in prognostic assessments. However, where our research stands out is in the application of the OptDMD algorithm. Previous studies, such as the one conducted by Yu et al. (2022) [277], have predominantly relied on traditional DMD for decomposition, potentially missing out on the heightened accuracy offered by optimized techniques. Our observation on the differentiation in mode energy distributions across aneurysm sizes further consolidates the work of Le et al. (2021) [266]. They had intimated at these variations but lacked the advanced computational tools we employed. It is noteworthy, however, that while many foundational aspects of our study find resonance in the existing literature, the comprehensive nature of our approach, combined with the utilization of contemporary algorithms, ensures a more nuanced and precise understanding of intracranial aneurysm dynamics.

7.5 Conclusion

In conclusion, our study provides a comprehensive examination of intracranial aneurysm dynamics using both traditional DMD and the more contemporary OptDMD algorithms. The

results offer nuanced insights, particularly with respect to the high-frequency damped mode's role in detecting turbulence and the differentiation in mode energy distributions across aneurysm sizes. By juxtaposing these findings with existing research, we have fortified the understanding of this complex neurovascular ailment and opened avenues for more precise prognostic evaluations. Looking ahead, it's clear that the evolving landscape of computational fluid dynamics holds significant promise for neurovascular research. While our study has unveiled several key points, there remains an expanse of uncharted territory. Future endeavors might consider harnessing the potential of emerging machine learning algorithms in tandem with DMD-based techniques, aiming for even greater accuracy in prediction and understanding. Furthermore, multi-center trials involving larger and more diverse datasets can help validate and refine our observations, fostering a global collaborative approach to mitigate the challenges posed by intracranial aneurysms.

Chapter 8: A Noise-Robust Optimal Sampling Strategy for Multi-Scale Complex Systems Using Deep Reinforcement Learning

Modeling multi-scale complex systems is challenging due to the coupled dynamics across various scales of the systems. For these systems, the critical problem lies in devising optimal sampling strategies that effectively capture these dynamics without incurring unnecessary computational costs or missing crucial details. Contemporary state-of-the-art methods often fail to adapt dynamically to multi-scale complexities leading to inefficiencies and inaccuracies. Furthermore, these existing strategies lack robustness in noisy real-life systems and have limitations in scalability when confronting high-dimensional systems. Recognizing this, we proposed a reinforcement learning framework based on deep Q-learning to adaptively capture this multi-scale complexity. By constructing the agent's reward signals to reflect the system's complex dynamics, the agent is capable of optimally sampling data to reveal the complex multi-scale behaviors. Furthermore, to discover and predict the system dynamics, we employ the Sparse Identification of Nonlinear Dynamical Systems (SINDy) approach. The performance and effectiveness of our method were assessed through two rigorous numerical studies: (1) a coupled fast and slow Van der Pol oscillator, and (2) a noisy fast Van der Pol oscillator coupled with a noisy slow Lorenz system. In each case, the reinforcement learning model demonstrated its robustness and efficiency by autonomously determining the optimal data sampling strategy to accurately capture the multi-scale dynamics. Importantly, we observed that the reinforcement learning model could develop intricate policies which significantly mitigated the issues related to non-convergence, reduced the sample size, and enhanced the robustness of SINDy in the presence

of noise. Our work contributes significantly to developing data-efficient reinforcement learning methodologies for modeling and controlling multi-scale complex systems. This advancement has the potential to improve our understanding, prediction, and control of such systems, opening new avenues for optimizing sampling strategies and fostering more accurate discovery of complex systems.

8.1 Introduction

Multi-scale complex systems refer to complex systems that exhibit significant interactions and phenomena across multiple temporal or spatial scales, each with its unique dynamics and intricacies. These systems pervade numerous domains, from sophisticated biological processes [278, 279] to advanced engineered networks [280, 281]. The inherent complexity of these systems arises not just from the individual dynamics at each scale, but critically from the interactions between these scales. Capturing the entirety of such systems demands comprehensive models that respect the details of each scale while faithfully representing the cross-scale interactions. The burgeoning availability of data from multi-scale complex systems has propelled advancements in data-driven methods for modeling and predicting these intricate systems, which aim to capture system behaviors, predict future dynamics, facilitate control, and elucidate underlying governing equations. A significant body of research has focused on multi-scale dynamics modeling, such as the heterogeneous multi-scale modeling approach [282, 283] and equation-free methods for bridging across scales [284, 285]. Other works have concentrated on cost-efficient computational methods that capture the multi-scale dynamics and analyze multi-scale systems [286, 287]. Additionally, various multi-scale dynamics models have been proposed to robustly decompose dynamics into a hierarchy of time-scale components, such as multi-resolution dynamic mode decomposition [288] and hierarchical multi-scale differential equation time steppers using deep

learning [289]. In 2019, Champion et al. [251] proposed an extended version of sparse identification of nonlinear dynamics (SINDy) model for the discovery of nonlinear multi-scale dynamical systems.

Having recognized the intricate nature of multi-scale systems and the advancements in modeling them, a major challenge in multi-scale systems modeling is the requirement to simultaneously sample data from multi-scale dynamics, given their interactions and couplings across varying scales [251]. We require not only the substantial volume of data but also the granularity, quality, and temporal-spatial distribution of data, governed by a sampling strategy, which plays a decisive role in the faithfulness of the resulting models [290, 291]. Studies have shown that oversampling of fast dynamics can inadvertently overshadow crucial slower dynamical processes, whereas under-sampling fast dynamics can lead to missing transient but essential behaviors [251, 286, 287]. This imbalance, which arises from the sampling biases, can hinder accurate modeling, potentially resulting in misguided insights and predictions of systems' behavior. Poorly chosen sampling rates might misrepresent slower dynamics as static backgrounds or, conversely, could consider rapid events as statistical noise. Hence, addressing the challenges of model discovery for nonlinear multi-scale dynamics calls for not only advanced modeling approaches but also the application of optimal sampling strategies that tailors to the unique characteristics of multi-scale systems. While the significance of incorporating an effective sampling strategy is evident in maintaining the robustness of multi-scale systems modeling, it's imperative to explore the methodologies that address this, ranging from model-based to machine learning techniques.

Optimal sampling strategy for multi-scale complex systems modeling [292] typically addresses the challenge of selecting a subset of variables or observations from a large sensor

dataset that can accurately represent the underlying nonlinear multi-scale dynamics. The first group of optimal sampling strategies for sensing data is model-based methods [293, 294], which are grounded in the principles of system modeling and estimation. These methods seek to design an optimal sampling strategy that maximizes the information gain [295] in the estimation process given a model of the system dynamics. Examples of model-based methods include input design [296], observer design [297], and maximum likelihood estimation [298]. However, these methods are computationally intensive for high-dimensional complex systems, and the resulting sampling strategy can be suboptimal if the model is incomplete or incorrect. Another group of optimal sampling methods is based on machine learning techniques, such as active learning [299] (i.e., optimal experimental design (OED) [300]) and Bayesian optimization [301]. Active learning involves iteratively selecting the most informative samples with respect to some statistical criterion that allows parameters to be estimated without bias and with minimum variance. Balancing exploration and exploitation (e.g., seeking to understand the unknown regions of the data vs. focusing on refining the model's knowledge in the familiar regions) with active learning can be challenging. Furthermore, noise or missing data can adversely impact the selection of informative samples. Bayesian optimization method has been used to optimize a function by sequentially selecting the most promising points for evaluation. However, this method relies on assumptions about the function such as smoothness or continuity, and it can be computationally intensive, especially for high-dimensional problems.

Although recent advances in sensing data sampling strategies and dynamical system identification methods have been proposed to model multi-scale complex systems yet the challenges remain. One key development is the use of sparse sensing techniques (*e.g.*, compressed sensing [302, 303], L1-minimization sparsity promotion [304], Orthogonal Matching Pursuit

[305], and sparse Bayesian learning [306]) to exploit the sparsity of signals or underlying structures in the data to efficiently acquire and reconstruct them using a limited number of measurements or samples while maintaining model accuracy. However, these approaches assume that the data is noise-free or has low noise levels leading to an inaccurate model identification or reconstruction [307]. Additionally, many sparse sensing techniques require cautious parameter tuning to achieve optimal performance, such as regularization parameters in the L1-minimization method or hyperparameters in sparse Bayesian learning, which can be relatively challenging when limited information is available about the system dynamics or the noise characteristics [308]. In the context of multi-scale complex systems, Champion et al. (2019) [251] proposed data-driven methods for the discovery of nonlinear multi-scale dynamical systems and their embeddings, and they have introduced several sampling strategies, including burst sampling, delay spacing, and iterative modeling, which were designed to optimally collect data for SINDy [234] and HAVOK models [232] in various noise-free multi-scale systems. The main limitations of their work are: (1) the data-sampling strategies lack the robustness, which were designed and evaluated for noise-free scenarios, (2) the specification of parameters, such as sampling period, burst size, and burst locations for burst sampling strategy, is challenging when system dynamics are not well understood and poses the problem of adaptability, (3) the proposed sampling strategies are heuristic sampling methods, which are not supported a formalized underlying theory, and (4) it is difficult to scale up to high-dimensional systems, where the complexity and computational demands increase significantly. Hence, it motivates the development of efficient, noise-robust, scalable algorithms for optimal sampling strategies that can solve the problems of the previously proposed methods.

In addressing the identified limitations in existing data sampling methods, this paper introduces an innovative approach that incorporates the SINDY algorithm with a deep Q-learning agent within a reinforcement learning framework to design a noise-robust optimal data sampling strategy for multi-scale complex systems discovery. Our method is designed to overcome the limitations through three key innovative elements: adaptability, robustness, and scalability. Firstly, it employs an adaptive sampling strategy that leverages reinforcement learning. Unlike traditional uniform-sampling strategies, our approach can dynamically modify the sampling policy based on the evolving multi-scale dynamics of the system. This innovation ensures greater accuracy and efficiency in data acquisition by catering to the specific demands of the system at any given point in time. Secondly, our approach incorporates a novel design for the state space, observation space, and reward signals, which is grounded on active learning principles and information theory. The design aims to minimize the impact of noise, model output variance, generalization error, and solution instability on model identification and reconstruction. This element enhances the robustness of our method, ensuring that our methodology can withstand and adapt to different types and levels of uncertainties and instabilities. Lastly, we leverage a deep Q-learning algorithm that is capable of scaling to high-dimensional systems. This feature significantly broadens the applicability of our methodology, making it a suitable tool for a wide variety of complex system types, irrespective of their dimensionality. This innovation, therefore, addresses a major limitation of previous methods and establishes our methodology as a novel solution in the field. We have chosen two analytical systems as numerical studies to validate our proposed methods: (1) Two coupled fast and slow Vander Pol oscillators, and (2) a noisy fast Van der Pol oscillator coupled with a noisy slow Lorenz system. These cases were selected as they collectively represent a range

of complexities and challenges in multi-scale dynamics and provide a comprehensive assessment of our method's effectiveness.

8.2 Background

In this section, we provide the background of two-time-scale deterministic coupled systems and reinforcement learning, which will be used to develop the methodologies.

8.2.1 Two-time-scale Deterministic Coupled Systems

Our study focuses on the complex systems that exhibit dynamics on multiple time scales. As a first step in our research, we consider a simplified version of such multi-scale systems that features linear coupling and two distinct time scales:

$$\begin{aligned} \tau_{fast}\dot{\boldsymbol{u}} &= \boldsymbol{f}(\boldsymbol{u}) + \boldsymbol{C}\boldsymbol{v} \\ \tau_{slow}\dot{\boldsymbol{v}} &= \boldsymbol{g}(\boldsymbol{v}) + \boldsymbol{D}\boldsymbol{u} \end{aligned} \tag{8.1}$$

where τ_{fast} and τ_{slow} are two parameters that controls the time resolution of the fast and slow dynamics, $\boldsymbol{u}(t) \in \mathcal{M}_{\boldsymbol{u}} \equiv \mathbb{R}^n$ and $\boldsymbol{v}(t) \in \mathcal{M}_{\boldsymbol{v}} \equiv \mathbb{R}^l$ are the set of "fast" and "slow" variables on two manifolds $\mathcal{M}_{\boldsymbol{u}}$ and $\mathcal{M}_{\boldsymbol{v}}$ respectively, $\boldsymbol{f}(\cdot)$ and $\boldsymbol{g}(\cdot)$ are the "fast" and "slow" flow map operators [295]. The linear coupling effects between $\boldsymbol{u}$ and $\boldsymbol{v}$ are represented by the matrices $\boldsymbol{C} \in \mathbb{R}^{n\times l}$ and $\boldsymbol{D} \in \mathbb{R}^{l\times n}$, which captures the coupling between the fast and slow dynamics of the complex system. The time scale separation can be quantified by the ratio $\phi_\tau = \tau_{slow}/\tau_{fast}$, between the "fast" and "slow" scales of $\boldsymbol{u}$ and $\boldsymbol{v}$. This simplified system serves as a starting point for the development of our proposed reinforcement learning-based data sampling strategy aiming to capture the multi-scale dynamics in a more general context.

8.2.2 Reinforcement Learning Framework

In order to capture the multi-scale dynamics of the complex systems and design the optimal sampling strategy, we leverage the Reinforcement Learning (RL) [309]. In this machine learning

paradigm, an artificial RL agent learns to make decisions by interacting with its environment, typically modeled through a Markov Decision Process (MDP) [310]. The agent's goal is to maximize its long-term performance quantified as the sum of discounted rewards over time.

8.2.2.1 Controlled Markov Process

A controlled Markov process (CMP) is defined as a tuple $(S, \mathcal{A}, P, \mu, \gamma)$, in which $\mathcal{S}$ is the state space, $\mathcal{A}$ is the action space, $P: S \times \mathcal{A} \mapsto \Delta(S)$ is the transition model such that the next state is drawn as $\boldsymbol{s}' \sim P(\cdot\,|\boldsymbol{s}, a)$ given the current state $\boldsymbol{s} \in S$ and action $a \in \mathcal{A}$, $\mu: \Delta(S)$ is the initial state distribution such that the initial state is drawn as $\boldsymbol{s} \sim \mu(\cdot)$, and $\gamma \in [0,1]$ is the discount factor. The behavior of an agent interacting with a CMP can be modeled through a Markovian parametrized policy $\pi_{\boldsymbol{\phi}}: S \mapsto \Delta(\mathcal{A})$ such that an action is drawn as $a \sim \pi_{\boldsymbol{\phi}}(\cdot\,|\boldsymbol{s})$, where $\boldsymbol{\phi} \in \Phi \subseteq \mathbb{R}^m$ are the policy parameters, and the set Π_Φ is called the policy space.

8.2.2.2 Policy Optimization

To achieve optimal decision-making in RL tasks, we employ the concept of Policy Optimization (PO). PO is a set of methods to find the best policy — a mapping from states to actions — that an agent can follow to maximize its performance on an RL task. The task is generally modeled through a Markov Decision Process (MDP) $\mathcal{M}^{\mathcal{R}} \coloneqq \mathcal{M} \cup \mathcal{R}$, i.e., the combination of a CMP $\mathcal{M}$ and a reward function $\mathcal{R}: \mathcal{S} \times \mathcal{A} \mapsto [-R_{max}, R_{max}]$ that the agent collects by selecting an action a in a state $\boldsymbol{s}$. The agent's performance is defined by the expected sum of discounted rewards (i.e., accumulated reward or gain) collected by its policy as:

$$G_t(\boldsymbol{\theta}) \coloneqq \mathop{\mathbb{E}}_{\substack{s_0 \sim \mu(\cdot), a_t \sim \pi_{\boldsymbol{\theta}}(\cdot|\boldsymbol{s}_t) \\ \boldsymbol{s}_{t+1} \sim P(\cdot|\boldsymbol{s}_t, a_t)}} \left[\sum_{t=1}^{\infty} \gamma^t \mathcal{R}(\boldsymbol{s}_t, a_t) \right] \tag{8.2}$$

8.2.2.3 Deep Q-network (DQN)

In situations where the state space is high-dimensional in complex systems, traditional RL methods may be inadequate. To overcome these challenges, we propose a Deep Q-Networks (DQN), which combines the strengths of deep learning and Q-learning. By approximating the optimal action-value function, known as the Q-function with a neural network, we can effectively handle environments with high-dimensional state space. Q-learning is a model-free reinforcement learning algorithm since it does not require a model of the environment. This algorithm aims to learn the mapping from a state-action pair to its value (i.e., state-action-value function) which is suitable for the environment with discrete action and continuous observation space. The state-action-value function $Q(\boldsymbol{s}, a): S \times \mathcal{A} \longmapsto \mathbb{R}$ is defined as the expected total reward for agent performing the action a at the current state $\boldsymbol{s}$. The output of this function is called Q-value. For any finite MDP, the main goal of Q-learning is to find an optimal policy that maximizes the expected total reward, or equivalently Q-value. Before the algorithm starts, $Q(\boldsymbol{s}, a)\ \forall \boldsymbol{s} \in \boldsymbol{S}, a \in \boldsymbol{\mathcal{A}}$ is initialized to an arbitrary fixed value (i.e., $Q_0(\boldsymbol{s}, a)$). To update the Q-values, the Bellman equation [309] acts as a foundational principle behind the Q-value update process. Specifically, it allows Q-values to be updated based on the difference between the estimated future reward of the best subsequent action and the current Q-value, often referred to as the "temporal difference" or TD error. The Q-value for a state-action pair is iteratively updated as a weighted average of the old Q-value and this estimated reward difference, ensuring convergence towards the optimal Q-value. The Q-value estimate from final update is denoted by $\hat{Q}(\boldsymbol{s}, a)$, which is the approximation of the true Q-value $Q^*(\boldsymbol{s}, a)$ and can help to formulate a deterministic policy π as:

$$\pi(\boldsymbol{s}) = \underset{a \in \mathcal{A}}{\operatorname{argmax}}\, \hat{Q}(\boldsymbol{s}, a)\ \ \forall \boldsymbol{s} \in \boldsymbol{S} \tag{8.3}$$

Deep Q-network (DQN) is a combination of deep learning and reinforcement learning to handle more complex finite MDPs, in which the model target is to approximate $Q^*(\boldsymbol{s}, a)$, and the Q-value is updated through back propagation. In the DQN framework, two primary neural networks are crucial: the critic and the target critic [311]. The critic, represented as $Q(\boldsymbol{s}, a; \boldsymbol{\phi})$, employs parameters $\boldsymbol{\phi}$ to estimate the Q-value of an action given the current state. This neural network estimates the expected reward for a chosen action based on its current knowledge of the environment. In parallel, the target critic, denoted as $Q_t(\boldsymbol{s}_t, a_t; \boldsymbol{\phi}_t)$, utilizes its own set of parameters, $\boldsymbol{\phi}_t$ to provide a stable estimate of the anticipated Q-value for the next state. Both these networks are constructed as deep neural architectures, processing environmental states and associated actions to predict expected cumulative rewards. Here, the deep neural network serves as a function approximator of $Q^*(\boldsymbol{s}, a)$, in which the state $\boldsymbol{s}$ is the input and the Q-value of all possible actions is the output, which is denoted as $\hat{Q}_{\boldsymbol{\psi}}(\boldsymbol{s}, a)$. Similarly, the policy is formulated as:

$$\pi(\boldsymbol{s}) = \underset{a \in \mathcal{A}}{\operatorname{argmax}}\, \hat{Q}(\boldsymbol{s}, a) \;\; \forall \boldsymbol{s} \in \boldsymbol{S} \tag{8.4}$$

8.3 Methodologies

The proposed method consists of two key computational components: the SINDy algorithm for multi-scale model discovery and the reinforcement learning framework for the optimal sampling strategy. The SINDy algorithm to discover the multi-scale models will be introduced. This algorithm allows us to understand and predict the behavior of complex systems across multiple scales. We will detail how to formulate the problem, develop the sparse regression, and discover the governing equations. The reinforcement learning framework focuses on the design and optimization of sampling strategy. The process of data sampling is crucial for the success of any data-driven model, and our use of reinforcement learning techniques enables us to effectively sample high-dimensional complex spaces. The reinforcement learning framework

section is divided into several subsections: we will provide an overview of our framework, define the environment, action, and state spaces, outline the reward signal and terminal conditions, and detail the reinforcement learning algorithm employed.

8.3.1 SINDy Algorithm for Multi-Scale Discovery

Based on the extant SINDy algorithm [234], we extend this algorithm to search for a parsimonious model that approximates the multi-scale dynamics $\boldsymbol{f}(\cdot)$ and $\boldsymbol{g}(\cdot)$, which can be represented by the functions $\widehat{\boldsymbol{f}}(\cdot)$ and $\widehat{\boldsymbol{g}}(\cdot)$ that contain only a few active terms (*i.e.*, they are sparse in the a basis of possible candidate functions) corresponding to predominant dynamics. In this framework, the model discovery problem is cast as a sparse regression problem, in which the snapshots of system states $(\boldsymbol{u}, \boldsymbol{v})$ and their derivatives $(\dot{\boldsymbol{u}}, \dot{\boldsymbol{v}})$ are available or can be computed from data. The snapshots are usually stacked to form two data matrices sampled at different time points $t_1, t_2, \dots, t_m$ as follows:

$$\boldsymbol{X} = \begin{bmatrix} \boldsymbol{u}(t_1) & \cdots & \boldsymbol{u}(t_m) \\ \boldsymbol{v}(t_1) & \cdots & \boldsymbol{v}(t_m) \end{bmatrix}^T = \begin{bmatrix} u_1(t_1) & \cdots & u_n(t_1) & v_1(t_1) & \cdots & v_l(t_1) \\ u_1(t_2) & \cdots & u_n(t_2) & v_1(t_2) & \cdots & v_l(t_2) \\ \vdots & \ddots & \vdots & \vdots & \ddots & \vdots \\ u_1(t_m) & \cdots & u_n(t_m) & v_1(t_m) & \cdots & v_l(t_m) \end{bmatrix} \tag{8.5}$$

$$\dot{\boldsymbol{X}} = \begin{bmatrix} \dot{\boldsymbol{u}}(t_1) & \cdots & \dot{\boldsymbol{u}}(t_m) \\ \dot{\boldsymbol{v}}(t_1) & \cdots & \dot{\boldsymbol{v}}(t_m) \end{bmatrix}^T = \begin{bmatrix} \dot{u}_1(t_1) & \cdots & \dot{u}_n(t_1) & \dot{v}_1(t_1) & \cdots & \dot{v}_l(t_1) \\ \dot{u}_1(t_2) & \cdots & \dot{u}_n(t_2) & \dot{v}_1(t_2) & \cdots & \dot{v}_l(t_2) \\ \vdots & \ddots & \vdots & \vdots & \ddots & \vdots \\ \dot{u}_1(t_m) & \cdots & \dot{u}_n(t_m) & \dot{v}_1(t_m) & \cdots & \dot{v}_l(t_m) \end{bmatrix} \tag{8.6}$$

where $\boldsymbol{X}, \dot{\boldsymbol{X}} \in \mathbb{R}^{m \times (n+l)}$. Next, a library $\boldsymbol{\Theta}(\boldsymbol{X})$ of K possible candidate functions (e.g., constant, polynomial, and trigonometric functions) is constructed, in which each column corresponds to one function:

$$\boldsymbol{\Theta}(\boldsymbol{X}) = \begin{bmatrix} | & | & | & | & | & | & | & | \\ \boldsymbol{1} & \boldsymbol{X} & \boldsymbol{X^2} & \boldsymbol{X^3} & \cdots & \sin(\boldsymbol{X}) & \cos(\boldsymbol{X}) & \cdots \\ | & | & | & | & | & | & | & | \end{bmatrix} \tag{8.7}$$

Based on our "sparsity" assumption for $\boldsymbol{f}$ and $\boldsymbol{g}$, the SINDy algorithm applies the thresholded least squares method to learn a sparse coefficient vector $\boldsymbol{\Xi} := [\boldsymbol{\xi}_1\ \boldsymbol{\xi}_2 \dots \boldsymbol{\xi}_{n+l}] \in \mathbb{R}^{K\times(n+l)}$ which indicates which nonlinear terms are active. The sparse regression problem is given as

$$\dot{\boldsymbol{X}} = \boldsymbol{\Theta}(\boldsymbol{X})\boldsymbol{\Xi} \tag{8.8}$$

Once $\boldsymbol{\Xi}$ has been learned, the governing equations can be discovered as follows:

$$\begin{gathered} \dot{u}_1 = \boldsymbol{\Theta}(\boldsymbol{x})\boldsymbol{\xi}_1, \dot{u}_2 = \boldsymbol{\Theta}(\boldsymbol{x})\boldsymbol{\xi}_2, \cdots, \dot{u}_n = \boldsymbol{\Theta}(\boldsymbol{x})\boldsymbol{\xi}_n \\ \dot{v}_1 = \boldsymbol{\Theta}(\boldsymbol{x})\boldsymbol{\xi}_{n+1}, \dot{v}_2 = \boldsymbol{\Theta}(\boldsymbol{x})\boldsymbol{\xi}_{n+2}, \cdots, \dot{v}_l = \boldsymbol{\Theta}(\boldsymbol{x}^{\boldsymbol{T}})\boldsymbol{\xi}_{n+l} \end{gathered} \tag{8.9}$$

where $\boldsymbol{\Theta}(\boldsymbol{x})$ is a vector of symbolic functions of elements of $\boldsymbol{x} = [\boldsymbol{u}^T \quad \boldsymbol{v}^T]$.

8.3.2 Reinforcement Learning for Optimal Sampling Strategy

The block diagram of the proposed methods consisting of 5 main steps is illustrated in Figure 8-1. The first step focuses on data simulation from multi-scale complex systems. An adaptive Runge-Kutta method [312] is employed to solve the system's ordinary differential equations and subsequently introduce Gaussian noise. For real-life systems, we either directly use complete datasets or employ state estimation techniques, such as Kalman filter [312] or particle filter [313], for incomplete data. Additionally, based on observed real-life data, we might create a "digital twin" environment simulator. This simulator serves as a controlled training ground for the DRL agent, ensuring the strategies developed are adaptable and robust for both simulated and real-world scenarios [314]. Next, we use a low-pass filter [315] to reduce the noise with high frequencies and estimate the state derivatives $d\boldsymbol{x}/dt$, where $\boldsymbol{x} = [\boldsymbol{u}^T \quad \boldsymbol{v}^T]$, via the explicit fourth-order central finite difference scheme [316]. For the highly noise-distorted state measurements, the total variation regularized derivative estimation methods [317] can provide more accurate derivative estimates. The third and fourth steps aim to develop training experiences for the RL

agent to learn the sampling policy, which is essential for generating the SINDy algorithm's training data. The last step is to benchmark the policy $\pi_\psi(\boldsymbol{s})$ obtained from DRL framework.

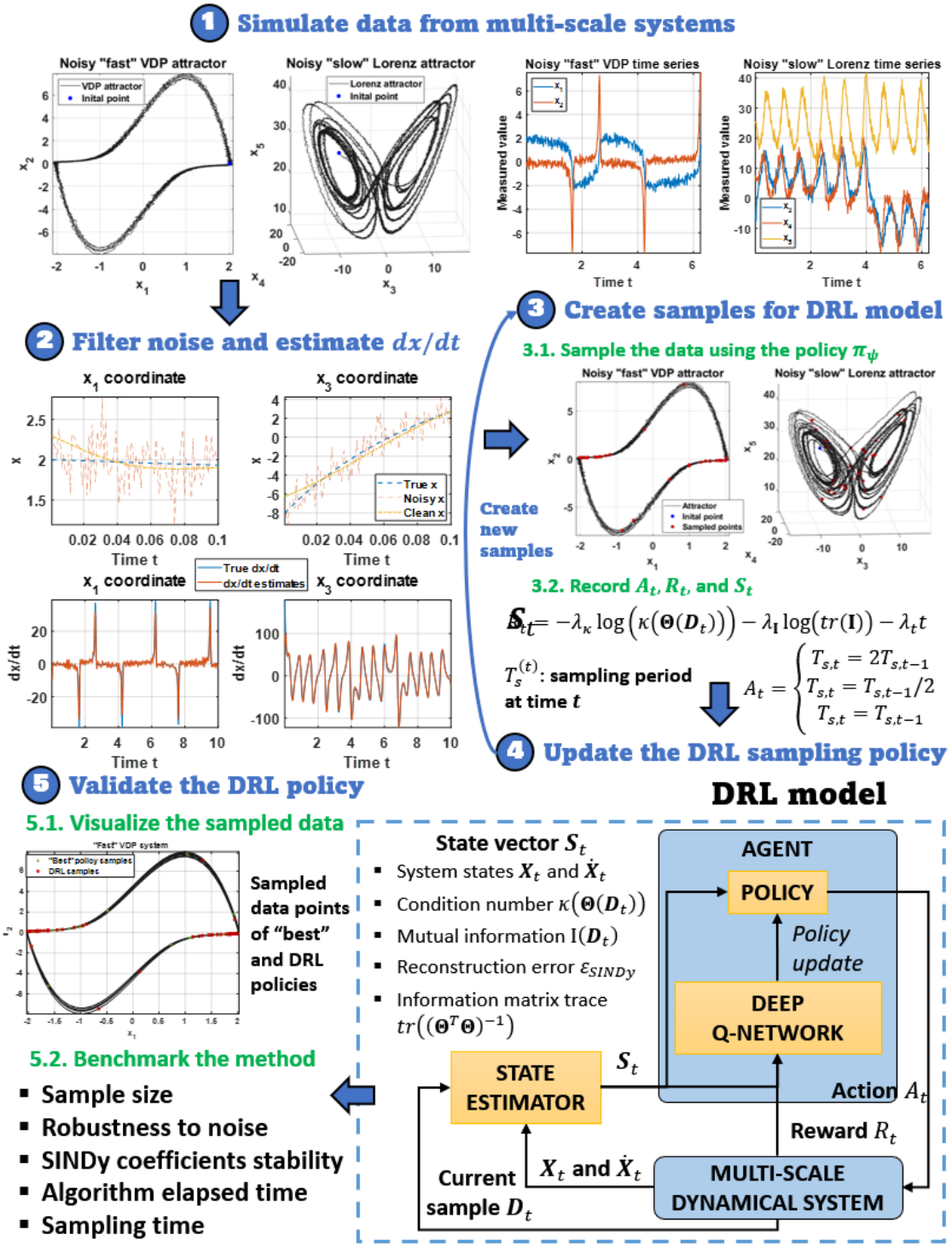

Figure 8-1 Schematic illustration of the proposed deep reinforcement learning (DRL) framework for optimal sampling strategy

8.3.2.1 RL Environment

Following the overall framework, we now delve deeper into the environment component, which governs the optimal sampling policy learning process. In our study, the environment is defined as a two-time-scale deterministic coupled system corrupted by Gaussian noise to represent real-world uncertainties and random fluctuations. The system dynamics are characterized by two different temporal scales - fast and slow - representing the behavior of two sets of variables, respectively denoted as $\boldsymbol{u}(t)$ and $\boldsymbol{v}(t)$. The mathematical form of the deterministic coupled system with two distinct timescales, corrupted by the Gaussian noise, is expressed as follows:

$$\begin{aligned} \tau_{fast}\dot{\boldsymbol{u}} &= \boldsymbol{f}(\boldsymbol{u}) + \boldsymbol{C}\boldsymbol{v} + \boldsymbol{\varepsilon_u} \\ \tau_{slow}\dot{\boldsymbol{v}} &= \boldsymbol{g}(\boldsymbol{v}) + \boldsymbol{D}\boldsymbol{u} + \boldsymbol{\varepsilon_v} \end{aligned} \tag{8.10}$$

where $\boldsymbol{\varepsilon_u} \in \mathbb{R}^n$ and $\boldsymbol{\varepsilon_v} \in \mathbb{R}^l$ represent the Gaussian noise affecting each of the states in $\boldsymbol{u}(t)$ and $\boldsymbol{v}(t)$ respectively. Each of these noise terms is modeled as a multivariate Gaussian distribution with zero mean and a covariance matrix, which means $\boldsymbol{\varepsilon_u} \sim \mathcal{N}(\boldsymbol{0}, \boldsymbol{\eta_u^T I}_n)$ and $\boldsymbol{\varepsilon_v} \sim \mathcal{N}(\boldsymbol{0}, \boldsymbol{\eta_v^T I}_l)$, where $\boldsymbol{I}_k$ denotes the identity matrix of size k, and $\boldsymbol{\eta_u} \in \mathbb{R}^n$ and $\boldsymbol{\eta_v} \in \mathbb{R}^l$ represent the variances of the noise associated with the "fast" and "slow" variables, respectively. To quantify the impact of this noise on the dynamics of the system, we also introduce the concept of the noise-to-signal ratio (NSR) for each state variable. The NSR is calculated as the ratio of the variance of the noise (noise power) to the expected power of the signal, which provides a measure of the relative strength of the noise in comparison to the signal, serving as an important factor in the design and evaluation of the sampling policy. Thus, the NSR for the state variable $x \in \boldsymbol{u} \vee \boldsymbol{v}$ is defined as $NSR \coloneqq \eta_x / \mathbb{E}[x^2]$, where $\mathbb{E}[x_i^2]$ and η_x are the expected value of x and the variance of the state x. A higher NSR indicates that the noise power is high compared to the signal power, which can make it more challenging for the RL agent to learn an optimal sampling policy. In contrast, a lower NSR suggests

that the signal power dominates over the noise power, making it potentially easier for the RL agent to learn from the system's dynamics.

8.3.2.2 Action Space $\boldsymbol{\mathcal{A}}$

For our deep RL framework, we define a discrete action space $\boldsymbol{\mathcal{A}}$ that comprises three possible actions. The choice to employ a discrete action space instead of a continuous one originates from the practical nature of the optimal sampling strategy task for the multi-scale dynamics discovery, in which the sampling periods typically require adjustments by integer multiples to capture the dynamics across various scales. Such changes are well-represented through a discrete action space, which consists of simple and definite actions such as doubling, halving, remaining the current sampling period. These discrete actions are computationally efficient and easy to implement, making the task of managing and discovering multi-scale dynamics more streamlined and manageable. Each action alters the sampling period, T_s, thereby influencing the multi-scale dynamics of the system. At each transition, the three possible sampling actions $A_t \in \boldsymbol{\mathcal{A}}$ are: (1) $A_t = 1$ (double T_s for down-sampling), (2) $A_t = 0$ (remain the same T_s), and (3) $A_t = -1$ (halve T_s for up-sampling). At each transition, the sampling action A_t decides the location of the next sampled point of $\boldsymbol{X}$. The initial sample in $\boldsymbol{X}$ is $\boldsymbol{x}_0$, and the initial sampling period T_0 is pre-specified. These actions are mathematically represented as:

$$A_t = \begin{cases} T_{s,t+1} = 2T_{s,t} \; if \; A_t = 1 \wedge 2T_{s,t} \geq T_{high} \\ T_{s,t+1} = T_{s,t} \; if \; A_t = 0 \\ T_{s,t+1} = \dfrac{T_{s,t}}{2} \; if \; A_t = -1 \wedge \dfrac{T_{s,t}}{2} \leq T_{low} \end{cases} \tag{8.11}$$

In Equation (8.11), the effects of each action are conditioned by the current sampling period and the thresholds T_{low} and T_{high}, which are the lower and upper limits of T_s, respectively. The action space $\boldsymbol{\mathcal{A}}$ is a critical component as it directly drives the evolution of the system dynamics through the sampling strategy, affecting the learning process of the agent. In the subsequent

sections, we will focus on other significant components of the reinforcement learning framework, namely the state space, the reward function, the terminal conditions, and the RL algorithm for updating the optimal sampling policy. The primary interactive component of the environment, the "sampling action" A_t, carries out three potential tasks. Each action directly influences the sampling period T_s, subsequently modifying the multi-scale dynamics that the system experiences. These actions are not arbitrary; instead, they are driven by the current sample characteristics and the system states. As a response to these actions, an intermediate reward R_t gets generated, which guides the learning process of the agent. This generated reward gives feedback on the efficiency of the sampling strategy, thus informing the learning agent on how to refine its future decisions. In the next sections, we will proceed to explain the characteristics of the state space, and reward signal in detail.

8.3.2.3 State Space $\boldsymbol{S}$

Next, the state space defines the input variables for the Deep Q-network that approximate the state-action-value function $Q(\boldsymbol{s}, a)$. The space $\boldsymbol{S}$ comprises of the SINDy reconstruction error ε_{SINDy}, the condition number [318], $\kappa\big(\boldsymbol{\Theta}(\boldsymbol{D}_t)\big)$, of the matrix $\boldsymbol{\Theta}(\boldsymbol{D}_t)$, where $\boldsymbol{D}_t$ is the current sample of $\boldsymbol{X}$ after the transition t, the multivariate mutual information [319] I$(\boldsymbol{D}_t)$, and the trace of the information matrix (*i.e.,* inverse of the variance matrix) $tr\left(\left(\boldsymbol{\Theta}(\boldsymbol{D}_t)^T\boldsymbol{\Theta}(\boldsymbol{D}_t)\right)^{-1}\right)$. The state space has been defined to include the important input variables that can approximate well the state-action-value function $Q(\boldsymbol{s}, a)$. Table 8-1 presents a description of each of these variables, which illustrates their notations, mathematical formulations, and the functions within our state space. These variables collectively facilitate effective approximation of the state-action-value function $Q(\boldsymbol{s}, a)$. The state space variables are carefully selected based on their relevance to the optimal sampling task. System states and derivatives ($\boldsymbol{X}_t$ and $\dot{\boldsymbol{X}}_t$) provide real-time understanding of the

system dynamics, helping predict future evolution and guide optimal sampling decisions. SINDy error $\varepsilon_{SINDy}(\boldsymbol{D}_t)$ quantifies the algorithm's performance. Condition number $\kappa\big(\boldsymbol{\Theta}(\boldsymbol{D}_t)\big)$ serves as an indicator of the stability of the solution. Multivariate mutual information $\mathrm{I}(\boldsymbol{D}_t)$ measures the mutual dependence among the samples. Lastly, the trace of the information matrix $tr(\mathbf{I})$ offers an estimate of the uncertainty inherent in the sparse coefficient vector estimation.

Table 8-1 Description of the variables in the RL state space for multi-scale dynamics discovery

State variables	**Notation**	**Mathematical formulation**	**Description**
System states and derivatives	$\boldsymbol{X}_t$ and $\dot{\boldsymbol{X}}_t$	$\boldsymbol{X}_t = [\boldsymbol{u}^{\boldsymbol{T}}(t) \quad \boldsymbol{v}^{\boldsymbol{T}}(t)]$ $\dot{\boldsymbol{X}}_t = [\dot{\boldsymbol{u}}^{\boldsymbol{T}}(t) \quad \dot{\boldsymbol{v}}^{\boldsymbol{T}}(t)]$ where $\boldsymbol{u}(t)$ and $\boldsymbol{v}(t)$ "fast" and "slow" variables at time t	These variables serve as the main elements of the system's dynamics.
SINDy reconstruction error	$\varepsilon_{SINDy}(\boldsymbol{D}_t)$	$\varepsilon_{SINDy} \coloneqq \left\|\widehat{\boldsymbol{\Xi}}_{\boldsymbol{D}_t} - \boldsymbol{\Xi}^*\right\|_F^2$ where $\widehat{\boldsymbol{\Xi}}_t$ and $\boldsymbol{\Xi}^*$ are the estimated and true sparse coefficient vectors, and $\|\cdot\|_F$ is the Frobenius norm operator.	The SINDy algorithm uses a thresholded least squares method [234] to find sparse coefficient vectors $\boldsymbol{\Xi} \coloneqq [\boldsymbol{\xi}_1\ \boldsymbol{\xi}_2 \dots \boldsymbol{\xi}_K]$ that solves the sparse regression problem $\dot{\boldsymbol{X}} = \boldsymbol{\Theta}(\boldsymbol{X})\boldsymbol{\Xi}$,
Condition number	$\kappa\big(\boldsymbol{\Theta}(\boldsymbol{D}_t)\big)$	$\kappa\big(\boldsymbol{\Theta}(\boldsymbol{D}_t)\big) \coloneqq \sigma_{\boldsymbol{max}}(\boldsymbol{\Theta}) / \sigma_{\boldsymbol{min}}(\boldsymbol{\Theta})$ where $\sigma_{\boldsymbol{max}}(\boldsymbol{\Theta})$ and $\sigma_{\boldsymbol{min}}(\boldsymbol{\Theta})$ are the maximum and minimum singular values of the matrix $\boldsymbol{\Theta}$	The condition number of $\boldsymbol{\Theta}$ can quantify the stability of the estimated $\widehat{\boldsymbol{\Xi}}_t$ after solving $\dot{\boldsymbol{X}} = \boldsymbol{\Theta}(\boldsymbol{X})\boldsymbol{\Xi}$
Information matrix trace	$tr((\boldsymbol{\Theta}^T\boldsymbol{\Theta})^{-1}) \equiv tr(\mathbf{I})$	$tr((\boldsymbol{\Theta}^T\boldsymbol{\Theta})^{-1}) = tr(\mathbf{I}) = \sum_{i=1}^{n} \mathbf{I}_{ii}$ where $\mathbf{I}$ is the information matrix and $\mathbf{I}_{ii}$ denotes the main diagonal elements of $\mathbf{I}$.	The trace of the inverse of the information matrix $\mathbf{I}$ computes the average variance of $\widehat{\boldsymbol{\Xi}}_t$

8.3.2.4 Reward Signal and Terminal Conditions

The primary purpose of reinforcement learning is to maximize a cumulative reward, which serves as a measure of the agent's success in achieving its goal. In our proposed framework, the reward signal is designed to encourage the efficient discovery of multi-scale dynamics while maintaining stability and precision in the sparse coefficient estimation. The reward function is formulated as:

$$R_t = -\lambda_\kappa \log\left(\kappa\left(\boldsymbol{\Theta}(\boldsymbol{D}_t)\right)\right) - \lambda_{\mathbf{I}} \log\left(tr(\mathbf{I})\right) - \lambda_t t \tag{8.12}$$

where $\lambda_\kappa, \lambda_{\mathbf{I}}$, and λ_t are the non-negative weights that balance the importance of the three terms: $\log\left(\kappa\left(\boldsymbol{\Theta}(\boldsymbol{D}_t)\right)\right)$, $\log\left(tr(\mathbf{I})\right)$, where $\mathbf{I} = (\boldsymbol{\Theta}(\boldsymbol{D}_t)^T \boldsymbol{\Theta}(\boldsymbol{D}_t))^{-1}$, and the current system time t. Our framework's reward signal formulation is specifically designed for addressing the challenges of multi-scale dynamics discovery, with each component representing a distinct objective. The logarithm of the condition number $\log\left(\kappa\left(\boldsymbol{\Theta}(\boldsymbol{D}_t)\right)\right)$, a measure of a matrix's sensitivity to errors, is included in the reward to encourage stability of the SINDy algorithm, as lower condition numbers lead to more stable coefficient estimations. The logarithm transforms the multiplicative condition number into an additive factor, compatible with the additive nature of Q-values in RL, while inversely associating high condition numbers with lower rewards. For the $\log\left(tr(\mathbf{I})\right)$ term, we penalize the high trace of the information matrix $tr(\mathbf{I})$, indicating the inverse of the average variance of the sparse coefficient estimates $\widehat{\boldsymbol{\Xi}}_t$ at the time t. By inversely associating high trace with lower rewards, the RL agent is motivated to explore dynamic and diverse samples, leading to greater variability in the multi-scale system dynamics. The direct inclusion of the current system time t promotes the efficiency with actions facilitating faster discovery of multi-scale dynamics leading to shorter time periods and higher rewards. Together, these components target the stability,

the dynamical variability, and the efficiency with weighting factors $\lambda_\kappa, \lambda_{\mathbf{I}}$, and λ_t providing a mechanism to fine-tune the reward function based on specific problem requirements, which adds an extra layer of versatility to the RL framework.

In terms of terminal conditions, an episode terminates when the number of training episodes exceeds the predefined limit E_{max} or when the reconstruction error of the SINDy model ε_{SINDy} falls below a certain threshold ε_{tol}. First, the incorporation of E_{max} guarantees computational feasibility and reflects the real-world constraints, which compels the agent to find an optimal strategy within a finite timeframe. Second, the terminal condition based on ε_{SINDy} aligns with our main objective to achieve a precise sparse dynamical model. This error measures the discrepancy between the sparse dynamical system derived from the data sampled by the agent and the true underlying dynamical system. When this error falls below the threshold ε_{tol}, it signifies that the agent has collected enough useful data samples that yield an accurate model of the system's dynamics. Thus, we can confidently terminate the episode knowing that the agent has accomplished its objective. However, in real-world scenarios, we rarely have access to the true sparse coefficient vectors $\boldsymbol{\Xi}^*$ of complex systems, making it impossible to evaluate ε_{SINDy} directly. In such cases, the convergence of the condition number $\kappa\big(\boldsymbol{\Theta}(\boldsymbol{D}_t)\big)$ can be an alternative criterion. The condition number measures the stability of the estimated sparse coefficient vectors after solving the sparse regression problem. A converging condition number suggests that the regression solution has stabilized, which implies the agent's data sampling has become effective enough to capture the underlying dynamics. Thus, it is a practical and viable indicator of when the agent should terminate the episode. In summary, these terminal conditions are designed to guide the agent towards a robust and efficient learning process, even when dealing with complex real-world systems.

8.3.2.5 Deep Q-Network Agent Training

In our methodology, the next crucial stage is the creation and training of the DQN agent. We rely on a deep Q-network algorithm to design an optimal sampling policy. The creation of our DQN agent involves initializing the critic and target critic that will approximate the value function. Here, we denote the critic as $Q(\boldsymbol{s}, a; \boldsymbol{\phi})$ and the target critic as $Q_t(\boldsymbol{s}_t, a_t; \boldsymbol{\phi}_t)$, where $\boldsymbol{\phi}$ and $\boldsymbol{\phi}_t$ are the critic parameters. Our critic and target critic are created as deep neural networks that map the environment states and selected sampling action to the expected cumulative reward. The schematic architecture of the deep Q-network is illustrated in Figure 8-2 below.

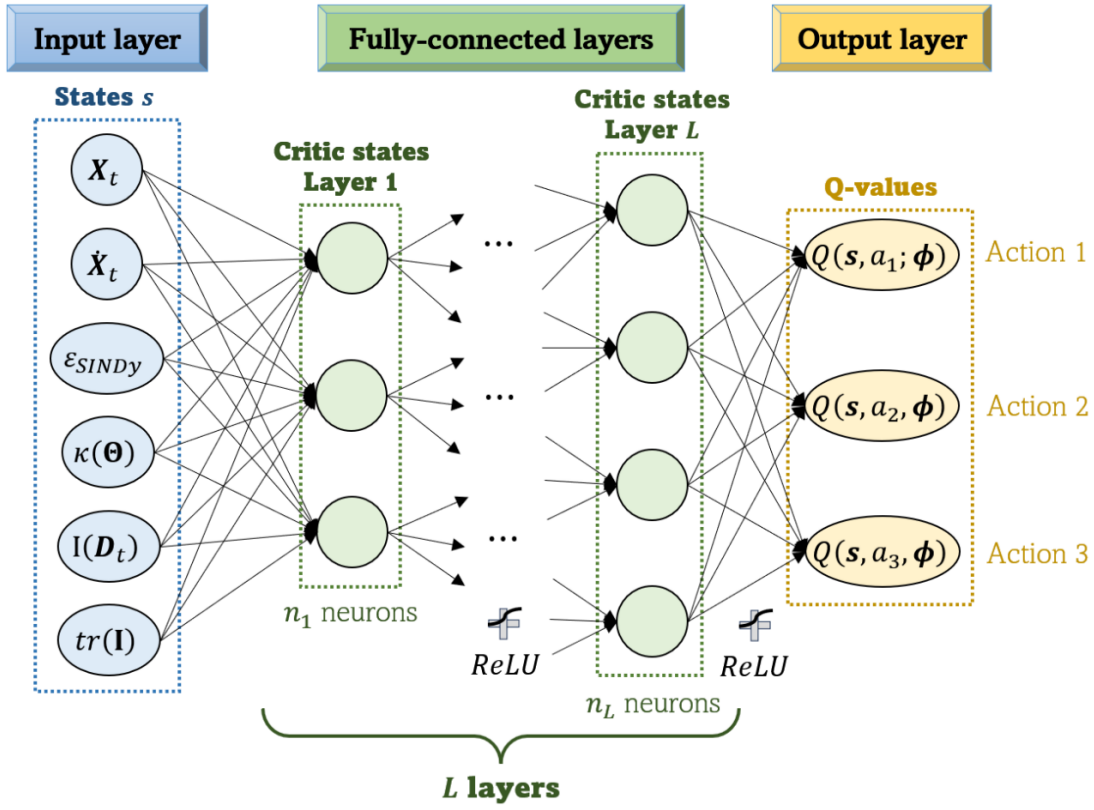

Figure 8-2 Schematic neural network architecture for the DQN agent. The architecture starts with an input layer that involves the states of the environment, followed by L fully connected layers that represent critic states with n_k $(k = 1, \dots, L)$ nodes each. Both fully connected layers utilize ReLU activation functions. The network's output layer corresponds to the Q-values for each action in the action space

Following the initialization of these critic function approximators, the configuration of the DQN agent is performed. The DQN agent is designed to adopt an epsilon-greedy exploration strategy during its training phase. Here, at each decision point, the agent either randomly explores a new action with a probability ε, or exploits the action that maximizes the current value function with a probability of $1-\varepsilon$. This strategic balance of exploration and exploitation aids in the robust and comprehensive learning of the optimal sampling policy within our noise-infused environment. In the training phase of our DQN agent, we implement the Q-Learning algorithm that is tailored to our environment with its specific multi-scale deterministic coupled system and noise characteristics. At each training time step, the agent selects an action a according to its current state $\boldsymbol{s}$, and the action a is subsequently executed resulting in an immediate reward r and a new state observation $\boldsymbol{s}'$. This sequence creates totally n_t experience tuples $\{(\boldsymbol{s}_i, a_i, r_i, \boldsymbol{s}_i')\}_{i=1}^{n_t}$, where $(\boldsymbol{s}_i, a_i, r_i, \boldsymbol{s}_i')$ represents the i^{th} sampled experience tuple, which will be stored in a circular buffer known as the experience replay buffer [320]. A mini-batch of experiences is then sampled randomly from this buffer to provide the data for updating our value function targets y_i. If the sampled next state $\boldsymbol{s}_i'$ is a terminal state, y_i is set to the immediate reward r_i. Otherwise, derived from the Bellman equation, we compute y_i as:

$$y_i = R_i + \gamma Q_t\left(\boldsymbol{s}_i', \underset{a}{\operatorname{argmax}}\, Q(\boldsymbol{s}_i', a; \boldsymbol{\phi})\,; \boldsymbol{\phi}_t\right) \tag{8.13}$$

Here, γ is the discount factor and $\underset{a}{\operatorname{argmax}}\, Q(\boldsymbol{s}_i', a; \boldsymbol{\phi})$ represents the best action at $\boldsymbol{s}_i'$ according to the critic's current parameters $\boldsymbol{\phi}$. In the training phase, by comparing this y_i with the Q-value approximated by the neural network $Q(\boldsymbol{s}_i, a_i; \boldsymbol{\phi})$, we can iteratively refine our critic's approximations to the optimal Q-values that represent the true expected returns. The critic's

parameters $\boldsymbol{\phi}$ are then updated by minimizing the mean squared loss between y_i and $Q(\boldsymbol{s}_i, a_i; \boldsymbol{\phi})$ over all experiences in the sampled mini-batch as follows:

$$\mathcal{L}(\boldsymbol{\phi}) = \frac{1}{2M}\sum_{i=1}^{M}\left(y_i - Q(\boldsymbol{s}_i, a_i; \boldsymbol{\phi})\right)^2 \tag{8.14}$$

where M is the size of the mini-batch. After we update $\boldsymbol{\phi}$, the target critic parameters $\boldsymbol{\phi}_t$ are estimated based on the selected target update method [321], which may comprise smoothing, periodic, or periodic smoothing techniques. As training progresses, we gradually reduce the probability threshold ε for choosing a random action. This is adjusted according to a pre-defined decay rate, balancing the exploration and exploitation dynamics during the learning process. Hence, our DQN agent is trained to learn the optimal sampling policy by considering the intricate dynamics of our multi-scale deterministic coupled system and its inherent noise properties.

8.3.2.6 RL-Based and Heuristic Approaches for Finding Optimal Sampling Policy

After the establishment and training of the DQN agent, we proceed with the implementation of the RL algorithm for seeking the optimal sampling policy. This algorithm is specifically formulated to work in conjunction with our trained DQN agent and leverages the knowledge acquired during the training phase. The purpose of this RL algorithm is to navigate the unique complexities of our multi-scale deterministic coupled system and utilize this understanding to produce a parametrized sampling policy that optimizes the chosen reward function, even in the presence of inherent noise. The reinforcement learning algorithm for finding the optimal sampling policy is outlined as Algorithm 8-1. In our study, apart from the RL-based approach (Algorithm 8-1), we also developed 2 other algorithms for finding the optimal sampling policy **(**Algorithms S1 and S2 in Appendix B), which are provided in the supplementary file. These methods are the benchmarks to evaluate the performance of our primary RL-based strategy. Algorithm B-1

employs a randomized brute-force search to determine the optimal sampling policy. The central premise of this method is the execution of M simulations, each implementing a different random sampling strategy π_i, where the action for the current state is selected randomly.

Algorithm 8-1: Reinforcement learning for SINDy optimal sampling policy in noisy multi-scale complex systems

Input: $\boldsymbol{\mathcal{A}}$, $\boldsymbol{S}$, E_{max}, $\boldsymbol{\eta_u}$, $\boldsymbol{\eta_v}$, T_s^{init}, ε_{tol}, $\boldsymbol{x}_0$, $\boldsymbol{\Xi}^*$, $\boldsymbol{\Theta}$, $\max_{iter}$, N, λ_κ, $\lambda_{\mathbf{I}}$, and λ_t
Output: optimized RL-based parametrized sampling policy $\hat{\pi}_{\boldsymbol{\psi}}^*(\boldsymbol{s})$
Initialize environment:
for $i \in \{1, \dots, E_{max}\}$ **do**
    Reset the environment:
    Introduce Gaussian noise to $\boldsymbol{x}(t)$ and $\dot{\boldsymbol{x}}(t)$ with noise levels $\boldsymbol{\eta_u}$, $\boldsymbol{\eta_v}$:
    $\widetilde{\boldsymbol{x}}(t) \longleftarrow \boldsymbol{x}(t) + \boldsymbol{\varepsilon_u}, \qquad \widetilde{\dot{\boldsymbol{x}}}(t) \longleftarrow \boldsymbol{f}\big(\boldsymbol{x}(t)\big) + \boldsymbol{\varepsilon_v}$
    Estimate $\widehat{\boldsymbol{\Xi}}_t$ and $\varepsilon_{SINDy,t}$ from $\widetilde{\boldsymbol{x}}(t), \widetilde{\dot{\boldsymbol{x}}}(t)$: $\varepsilon_{SINDy,t} \longleftarrow \left\|\widehat{\boldsymbol{\Xi}}_t - \boldsymbol{\Xi}^*\right\|_F^2$
    while $(\varepsilon_{SINDy,t} < \varepsilon_{tol})$ and $(n_{iter} < \max_{iter})$ **do**
        $n_{iter} \longleftarrow n_{iter} + 1$
        Select action $a_t \in \boldsymbol{\mathcal{A}}$ at state $\boldsymbol{s}$ using ε-greedy policy derived from critic $Q(\cdot)$
        Update sampling period T_s according to action a_t using Equation (3.6)
        Update t according to action a_t, $t \longleftarrow t + T_s$
        Sample new $\widetilde{\boldsymbol{x}}(t)$ and $\widetilde{\dot{\boldsymbol{x}}}(t)$ from noisy system and append them to $\boldsymbol{D}_t$
        Estimate new $\widehat{\boldsymbol{\Xi}}_t$ and $\varepsilon_{SINDy,t}$ using SINDy algorithm
        Calculate states $\kappa\big(\boldsymbol{\Theta}(\boldsymbol{D}_t)\big)$, $tr(\mathbf{I})$, and $\mathrm{I}(\boldsymbol{D}_t)$
        Calculate intermediate reward r_t using Equation (3.7)
        Store experience $(\boldsymbol{s}, a_t, r_t, \boldsymbol{s}')$ in buffer B
        Update critic parameters $\boldsymbol{\phi}$ by minimizing loss function in Equation (3.9)
        Every N steps, update target critic parameters $\boldsymbol{\phi}_t = \boldsymbol{\phi}$
        Update current state: $\boldsymbol{s}' \longleftarrow \boldsymbol{s}$
    end
end
Return optimized sampling policy $\hat{\pi}_{\boldsymbol{\psi}}^*(\boldsymbol{s})$, where $\boldsymbol{\psi}$ is parameters of DQN network

After the terminal conditions are satisfied, the algorithm evaluates the performance of each policy π_i by calculating the loss function $\mathcal{L}(\pi_i)$, and the optimal sampling policy is obtained by selecting the best π_i that minimizes $\mathcal{L}(\pi_i)$. In Algorithm B-2, we resort to a greedy sampling

method for finding the optimal sampling policy. This method differs from the first two by continuously choosing the best available action, driven by a defined optimality-criteria function $\Phi(\boldsymbol{D}_t)$ based on optimal design theory [300]. Unlike Algorithm B-1, which randomly selects an action, this method samples the best new data within the search range Δ_s according to the optimality-criteria $\Phi(\boldsymbol{D}_t)$. After the terminal conditions are met, the optimal sampling policy can be acquired. In addition to those 3 algorithms, we also employed the traditional uniform sampling strategy for comparison. The uniform sampling strategy operates under a fixed sampling rate, disregarding the state of the system. Therefore, its limitation lies in its inability to adapt to the state dynamics, making it potentially sub-optimal when dealing with systems that exhibit complex, multi-scale behaviors. By contrasting this method with the RL-based and heuristic sampling strategies, we aim to highlight the benefits of adaptive, state-aware sampling in dealing with the challenges posed by the multi-scale deterministic coupled system.

8.4 Results

To demonstrate the efficacy and versatility of our reinforcement learning-based approach for optimal sampling policy in complex systems, we conducted a series of experiments across two numerical studies. Our aim is to perform a rigorous evaluation of the performance of our approach and contrast it against the other proposed sampling strategies: randomized brute-force search, greedy sampling, and the traditional uniform sampling method. The chosen numerical studies represent multi-scale complex systems, specifically, the coupled fast and slow Van der Pol oscillator and a noisy fast Van der Pol oscillator coupled with a noisy slow Lorenz system. Both these systems present distinct complexities and challenges that make them ideal for a thorough assessment of the various sampling strategies.

We started by setting up each experiment and determining the appropriate parameters for the system under examination. Next, we applied the four different sampling strategies to the system. We ensured to maintain consistency in our approach, keeping other factors constant to allow for a fair comparison. The application of each strategy was methodically carried out, and the results were documented. Subsequently, we synthesized the results to evaluate the performance of each strategy on each system. This was done by assessing 6 evaluation metrics: sample size n, ε_{SINDy}, $\log\left(\kappa\left(\boldsymbol{\Theta}\left(D_{T_{train}}\right)\right)\right)$, $\log\left(tr\left(\boldsymbol{I}\left(D_{T_{train}}\right)\right)\right)$, total training time T_{train}, and total elapsed time of the sampling algorithm $T_{elapsed}$, where $D_{T_{train}}$ is the final sample obtained when the SINDy sampling process converges. Firstly, the sample size n provides an insight into the quantity of data points required by the algorithm to accurately identify the system's dynamics. A smaller sample size generally indicates greater data efficiency of the sampling process. ε_{SINDy} represents the error associated with the SINDy model, reflecting the accuracy of the identified models. The evaluaton metric $\log\left(\kappa\left(\boldsymbol{\Theta}\left(D_{T_{train}}\right)\right)\right)$ measures the condition number of the matrix associated with the sampled data, which plays a critical role in determining the stability and reliability of the system identification process. $\log\left(tr\left(\boldsymbol{I}\left(D_{T_{train}}\right)\right)\right)$ quantifies the trace of the information matrix for the sampled data, serving as an indicator of the data's informative content. Total training timeT_{train} is a direct measure of the computational cost associated with the training process using the sampled data. Lastly, total elapsed time of the sampling algorithm $T_{elapsed}$ offers an overview of the efficiency and speed of the sampling algorithm itself. In the following sections, we will delve into the specifics of our numerical studies, detailing the process and results of our comparative analysis for each system. We begin with the evaluation of the coupled fast and slow Van der Pol oscillator.

8.4.1 Numerical Study 1: Two Noisy Coupled Vander Pol Oscillators

8.4.1.1 Experiment Setup and Parameters

In this study, we consider the case of 2 coupled fast and slow Van der Pol oscillators described by the following system of ordinary differential equations (ODEs):

$$\begin{aligned} \tau_{\text{fast}}\dot{x_1} &= x_2 + c_1 x_3 + \varepsilon_{u_1} \\ \tau_{\text{fast}}\dot{x_2} &= \mu_1(1 - x_1^2)x_2 - x_1 + \varepsilon_{u_2} \\ \tau_{\text{slow}}\dot{x_3} &= x_4 + c_2 x_1 + \varepsilon_{v_1} \\ \tau_{\text{slow}}\dot{x_4} &= \mu_2(1 - x_3^2)x_4 - x_3 + \varepsilon_{v_2} \end{aligned} \tag{8.15}$$

The variables x_1 and x_2 represent the fast dynamics, while x_3 and x_4 represent the slow dynamics of the system. The parameters c_1 and c_2 serve to couple the two dynamical systems, the time constants τ_{fast} and τ_{slow} differentiate the fast and slow dynamics, respectively. Here, $\varepsilon_{u_1} \sim \mathcal{N}(0, \eta_u)$, $\varepsilon_{u_2} \sim \mathcal{N}(0, \eta_u)$, $\varepsilon_{v_1} \sim \mathcal{N}(0, \eta_v)$, and $\varepsilon_{v_2} \sim \mathcal{N}(0, \eta_v)$ are Gaussian noise terms with zero mean added to each of the state variables to reflect the presence of noise and uncertainty. The noise levels η_u and η_v are set in accordance with the chosen noise-to-signal ratio (NSR) for each experiment. We set the initial condition $\boldsymbol{x}_0 = (2,0,0,2)$, the coupling constants $c_1 = 0.005$, $c_2 = 1$, the coefficients $\mu_1 = \mu_2 = 5$, and the time constants $\tau_{fast} = 0.2$, $\tau_{slow} = 1$. In subsequent sections, we provide an analysis of the performance of different sampling policies on this system under varying conditions.

8.4.1.2 Implementing and Evaluating Sampling Policies

Given the system dynamics and initial settings outlined in section 4.1.1, we implemented and compared 4 distinct sampling strategies for the two coupled Van der Pol oscillator systems, namely: (1) uniform Sampling, (2) greedy sampling, (3) randomized brute-force search, and (4) Reinforcement Learning (RL), under three levels of Noise-to-Signal

Ratios (NSR) - 0%, 0.1%, and 1%. The results of these comparisons are presented in Figure 8-3 below. In the noise-free environment ($NSR = 0\%$, panel (a)), the sample size varied significantly across the four methods. The brute-force search resulted in the smallest sample size of 22, showcasing its efficiency in sample minimization, despite its extensive computational demand. The uniform and RL-based strategies produced a slightly larger sample size (30 and 34, respectively), while the greedy sampling strategy achieved an even smaller sample size of 24. Regarding the accuracy of learned dynamics measured by ε_{SINDy}, all strategies demonstrated comparably low values, suggesting that they could accurately capture the system dynamics. Remarkably, the RL-based strategy achieved the lowest ε_{SINDy} value, signifying superior learning accuracy despite its moderately larger sample size.

In panel (b), when $NSR = 0.1\%$, the uniform and RL-based strategies maintained high convergence rates of 95% and 61%, respectively. Despite the increased noise level, both methods effectively learned the system dynamics as reflected in the relatively low ε_{SINDy} values. However, the sample sizes required by these methods increased markedly compared to the noise-free scenario. On the other hand, the greedy sampling method, which performed well under noise-free conditions, could not be evaluated due to the inability to ensure convergence in the presence of noise. This result underscores the sensitivity of the greedy method to noise disturbances. Upon further increase of the noise level to $NSR = 1\%$, the convergence rates for the uniform and RL-based strategies dropped to 79% and 31%, respectively. The RL-based method exhibited a larger ε_{SINDy} value and required an increased sample size, indicating that learning the system dynamics became more challenging in the presence of higher noise. Yet, it maintained a reasonably low $\log(\kappa(\boldsymbol{\Theta}))$ and $\log(\mathrm{tr}(\mathbf{I}))$, highlighting the diversity of the samples collected. On the other hand, the uniform sampling method required a larger sample size but displayed a considerably larger

ε_{SINDy}, which signifies compromised learning accuracy under high noise conditions. Figure 8-4 provides a comprehensive view of the sampling patterns of both strategies under three noise scenarios ($NSR = 0\%$, 0.1%, and 1%), revealing their robustness and adaptability.

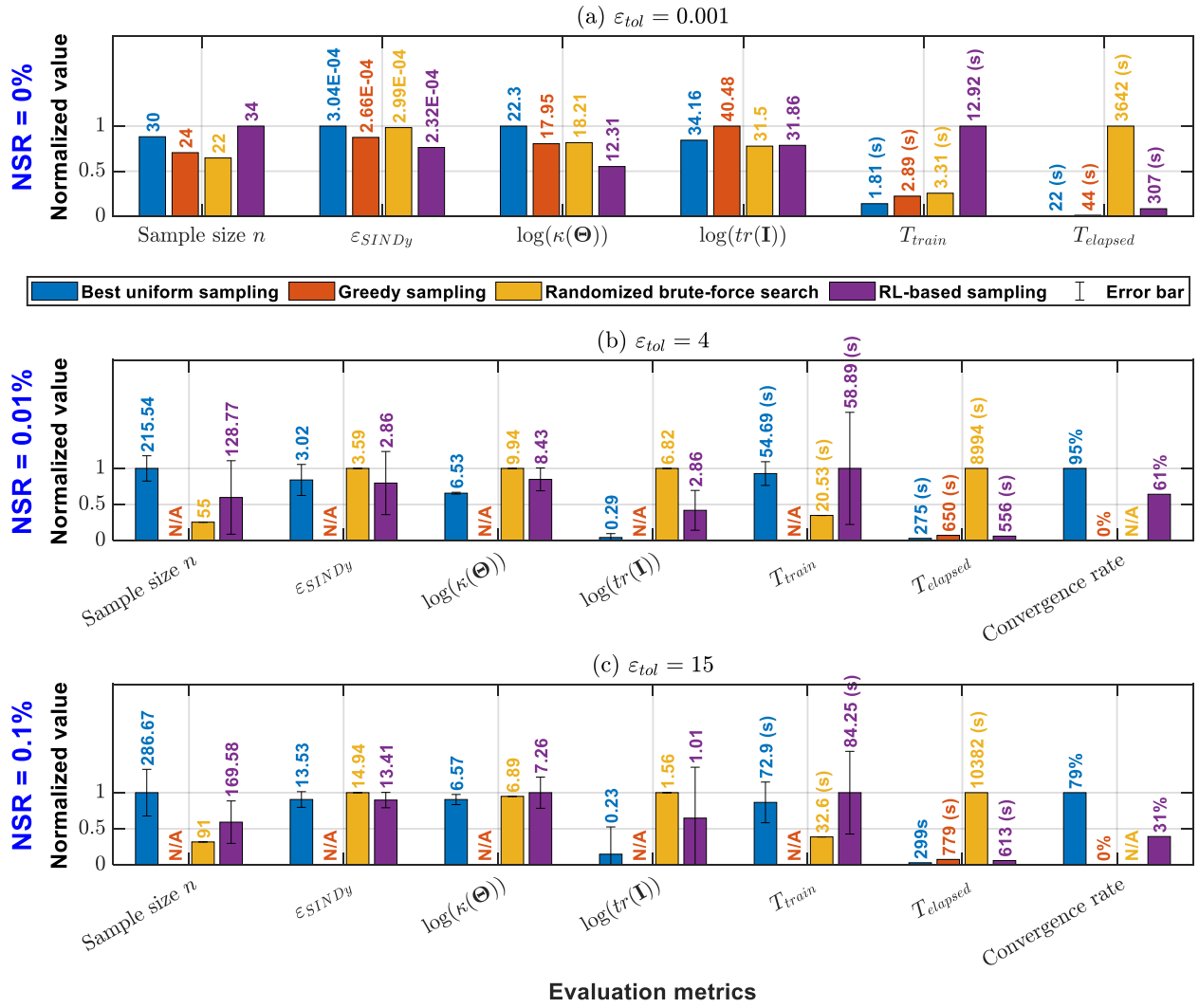

Figure 8-3 Comparative analysis of 4 different sampling strategies under 3 noise-to-signal ratio settings. The figure consists of three panels: (a) noise-free scenario ($NSR = 0\%$), (b) low noise conditions ($NSR = 0.1\%$), and (c) moderate noise conditions ($NSR = 1\%$). In panel (a), we considered 6 sampling policy evaluation metrics. For the noisy systems represented in panels (b) and (c), an additional metric was introduced called convergence rate, defined as the percentage of simulations among 100 simulations where the SINDy sampling process converges under noise conditions. The error bars represent the standard deviations of the metric values across 100 simulation runs

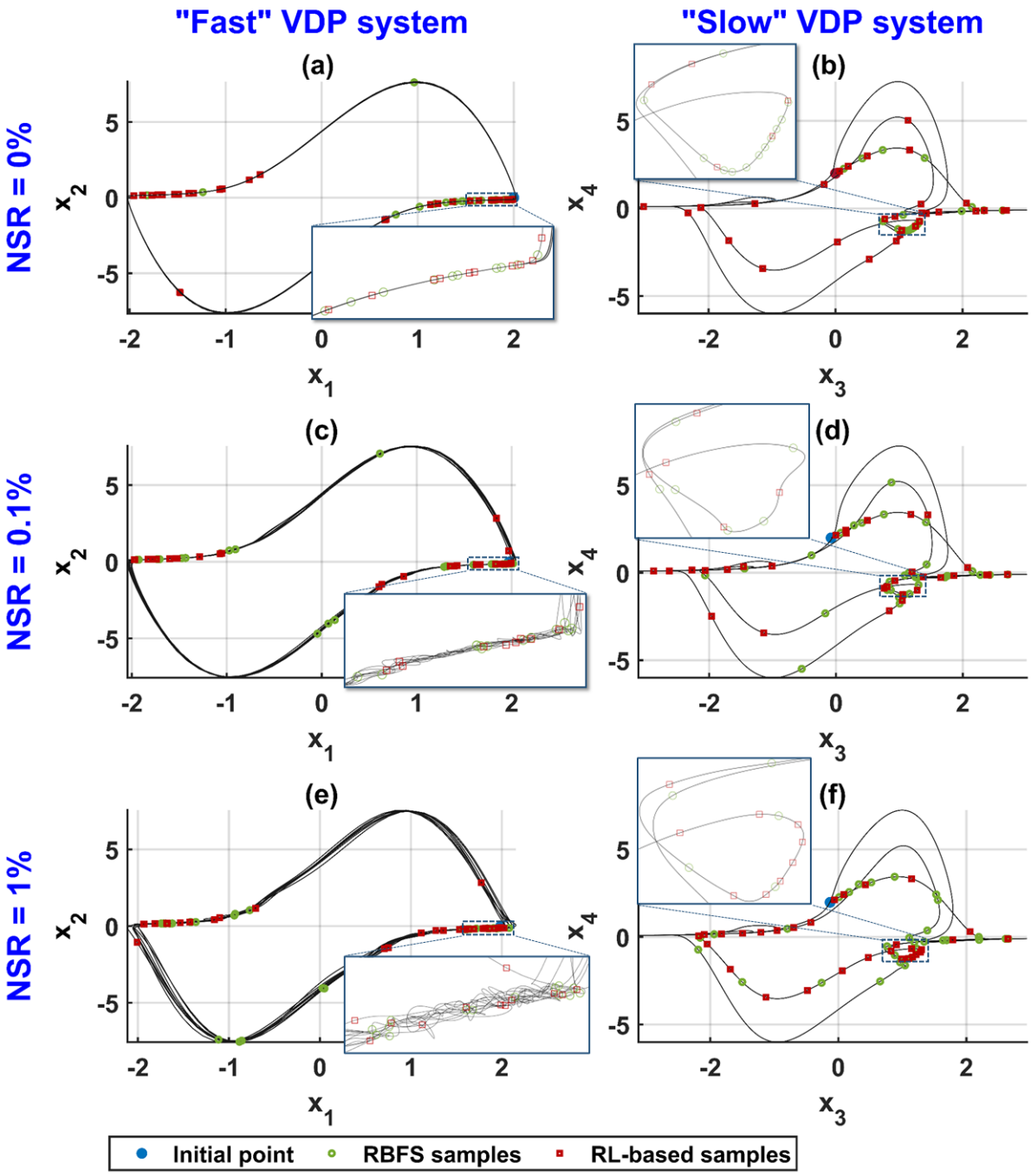

Figure 8-4 Visualization of samples obtained from the best sampling strategy — randomized brute-force search (RBFS) and the RL-based sampling policy under varying noise conditions for the coupled "fast" and "slow" Van der Pol (VDP) systems. Panels (a), (c), and (e) depict the samples for the fast VDP system under NSR settings of 0%, 0.1%, and 1% respectively. Panels (b), (d), and (f) mirror these NSR settings for the "slow" VDP system. In each scatter plot, the red squares represent samples obtained from the RL-based method, and the green circles represent samples obtained from the RBFS.

Figure 8-4 visualizes the similarities in the sampling strategies of the randomized brute-force search (RBFS), deemed as the optimal approach, and the RL-based sampling policy under varying noise conditions for the coupled fast and slow Van der Pol (VDP) systems. In the noise-free scenario ($NSR = 0\%$), panels (a) and (b), both the RL-based and the randomized brute-force search methods primarily maintained or doubled T_s, reflecting a mutual understanding of the system's dynamics and confirming the RL-based approach's strategy in mimicking the optimal strategy. For the low noise level ($NSR = 0.1\%$), shown in panels (c) and (d), the RL-based policy's adaptability became evident. It mirrored the RBFS strategy of mainly maintaining or doubling the sampling period for the fast and slow dynamics. This indicates the RL-based method's ability to adjust to system complexity changes, matching the sampling actions of the optimal approach. With a further increase in noise level to $NSR = 1\%$, the RL-based sampling policy continued to mirror the optimal approach effectively, as seen in panels (e) and (f). Both strategies primarily maintained or doubled the sampling period, reflecting their adaptability to the increased system complexity introduced by higher noise levels.

In addition, the Van der Pol (VDP) system is a nonlinear oscillator that exhibits a limit cycle behavior, which means that its state variables oscillate around a stable equilibrium. In the VDP system, there is an “excitation” or “bursting” region characterized by rapid changes in the system's state variables. This region typically occurs when the system is initially perturbed or excited and can exhibit chaotic or irregular behavior. On the other hand, the “limit cycle” region is characterized by slower oscillations, where the dynamics are more predictable and less chaotic. In Figure 8-4, both RBFS and RL-based sampling approaches align with the inherent properties of the VDP system. In the limit cycle region, the system exhibits periodic oscillations, thereby necessitating more frequent sampling for an accurate depiction of the system dynamics. On the

contrary, the transient region is characterized by a rapid movement towards the limit cycle, which may not necessitate a dense sampling strategy due to its short duration and quick convergence to the stable state. Therefore, it highlights the method's ability to capture and adapt to the complexities of multi-scale dynamical systems.

8.4.2 Numerical Study 2: a Fast Van Der Pol Oscillator Coupled with a Slow Lorenz System

8.4.2.1 Experiment Setup and Parameters

In this study, we considered a more complex coupled system that involved a fast Van der Pol oscillator and a slow Lorenz system. The Van der Pol oscillator represents a system with nonlinear dynamics and a limit cycle, while the Lorenz system, famous for its butterfly-like chaotic behavior, introduces an additional level of complexity. The coupled system of differential equations was as follows:

$$\begin{aligned}
\tau_{fast}\dot{x_1} &= x_2 + c_1 x_3 + \varepsilon_{u_1} \\
\tau_{fast}\dot{x_2} &= \mu(1 - x_1^2)x_2 - x_1 + \varepsilon_{u_2} \\
\tau_{slow}\dot{x_3} &= \sigma(x_4 - x_3) + c_2 x_1 + \varepsilon_{v_1} \\
\tau_{slow}\dot{x_4} &= x_3(\rho - x_5) - x_4 + \varepsilon_{v_2} \\
\tau_{slow}\dot{x_5} &= x_3 x_4 - \beta x_5 + \varepsilon_{v_3}
\end{aligned} \tag{8.16}$$

The system parameters included the coupling constants $c_1 = 0.01$, $c_2 = 10$, the coefficients $\sigma = 10, \rho = 28, \beta = 8/3$, and $\mu = 5$. The choice of these parameters was made to ensure that the system dynamics remain interesting and non-trivial, while the influence of both the fast and slow variables is significant. Here, $\varepsilon_{u_1} \sim \mathcal{N}(0, \eta_u)$, $\varepsilon_{u_2} \sim \mathcal{N}(0, \eta_u)$, $\varepsilon_{v_1} \sim \mathcal{N}(0, \eta_v)$, $\varepsilon_{v_2} \sim \mathcal{N}(0, \eta_v)$, and $\varepsilon_{v_3} \sim \mathcal{N}(0, \eta_v)$ are Gaussian noise terms with zero mean. The initial condition was set to $\boldsymbol{x}_0 = (2,0,-8,8,27)$, which represents the starting point. In the subsequent section, we implemented and evaluated the sampling strategies on this system with noise levels (NSR) at 0%, 0.1%, and 1%.

8.4.2.2 Implementing and Evaluating Sampling Policies

Figure 8-5 illustrates the performance outcomes across the same set of evaluation metrics.

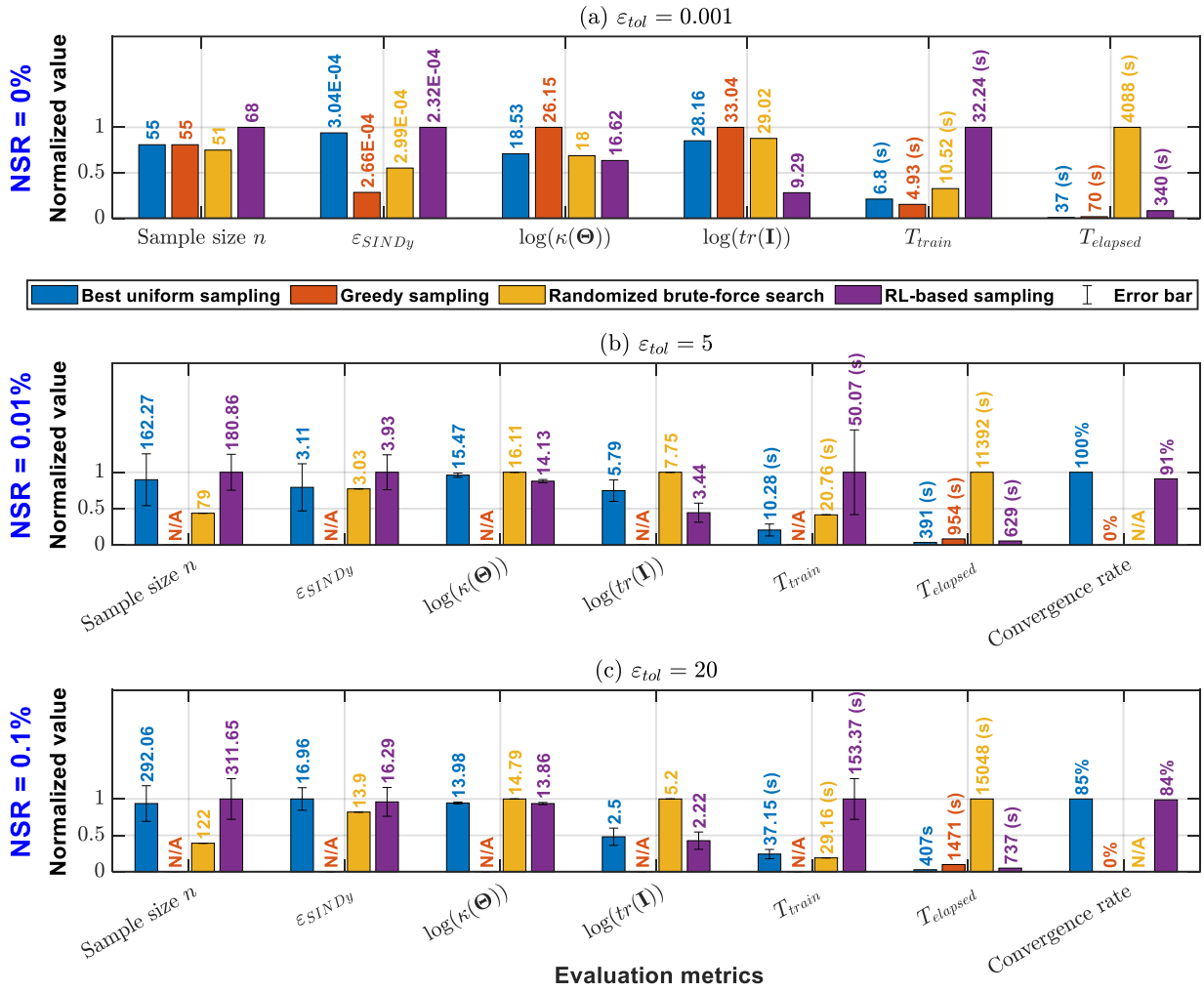

Figure 8-5 Comparative analysis of sampling strategies on the coupled Van der Pol oscillator and Slow Lorenz system. Here, we applied the same evaluation metrics and sampling algorithms as presented in Figure 8-3

Under noise-free conditions ($NSR = 0\%$, panel (a)), while the brute-force search yielded the smallest sample size of 51, it was closely followed by the uniform and greedy sampling strategies which achieved sample sizes of 55. The RL strategy, however, maintained a balance with a slightly larger sample size of 68. The RL strategy and the brute-force search achieved the smallest ε_{SINDy},

indicating the best fit to the true model. Notably, the greedy sampling strategy led in $\log(\kappa(\boldsymbol{\Theta}))$ and $\log(\mathrm{tr}(\mathbf{I}))$ values, indicating the best-conditioned Θ matrix and the most informative sample set. However, the brute-force search demanded a significantly higher elapsed time. In panel (b), upon introducing a low noise level ($NSR = 0.1\%$), all strategies showed an increase in ε_{SINDy} and sample size, and a decrease in $\log(\kappa(\boldsymbol{\Theta}))$ and $\log(\mathrm{tr}(\mathbf{I}))$ values. Among them, the RL approach exhibited the least increase in ε_{SINDy} and sample size and the least decrease in $\log(\kappa(\boldsymbol{\Theta}))$ and $\log(\mathrm{tr}(\mathbf{I}))$, demonstrating its robustness against noise. Despite the noise, the convergence rate for the RL strategy was 91%, significantly higher than the uniform sampling, which fell to 1%.

When the noise level was increased to $NSR = 1\%$ (panel (c)), every method experienced further escalation in ε_{SINDy} and sample size, and a drop in $\log(\kappa(\boldsymbol{\Theta}))$ and $\log(\mathrm{tr}(\mathbf{I}))$. The RL approach, however, retained the lowest rise in ε_{SINDy} and sample size and the smallest reduction in $\log(\kappa(\boldsymbol{\Theta}))$ and $\log(\mathrm{tr}(\mathbf{I}))$. Moreover, it had an 84% convergence rate, the highest among the strategies, while the uniform sampling method could only achieve 85%. Regarding time-related metrics at different noise levels, while the brute-force search yielded the smallest sample sizes and low ε_{SINDy}, it required the longest elapsed times. Conversely, the RL strategy provided a balance of relatively small sample sizes, competitive ε_{SINDy}, $\log(\kappa(\boldsymbol{\Theta}))$, $\log(\mathrm{tr}(\mathbf{I}))$ values, high convergence rates, and significantly shorter elapsed times than the randomized brute-force search. To further illuminate the behavior of the sampling strategies, we present Figure 8-6, which compares the samples obtained from the RL-based policy and the randomized brute-force search—the most efficient strategy—under three noise conditions ($NSR = 0\%$, 0.1%, and 1%).

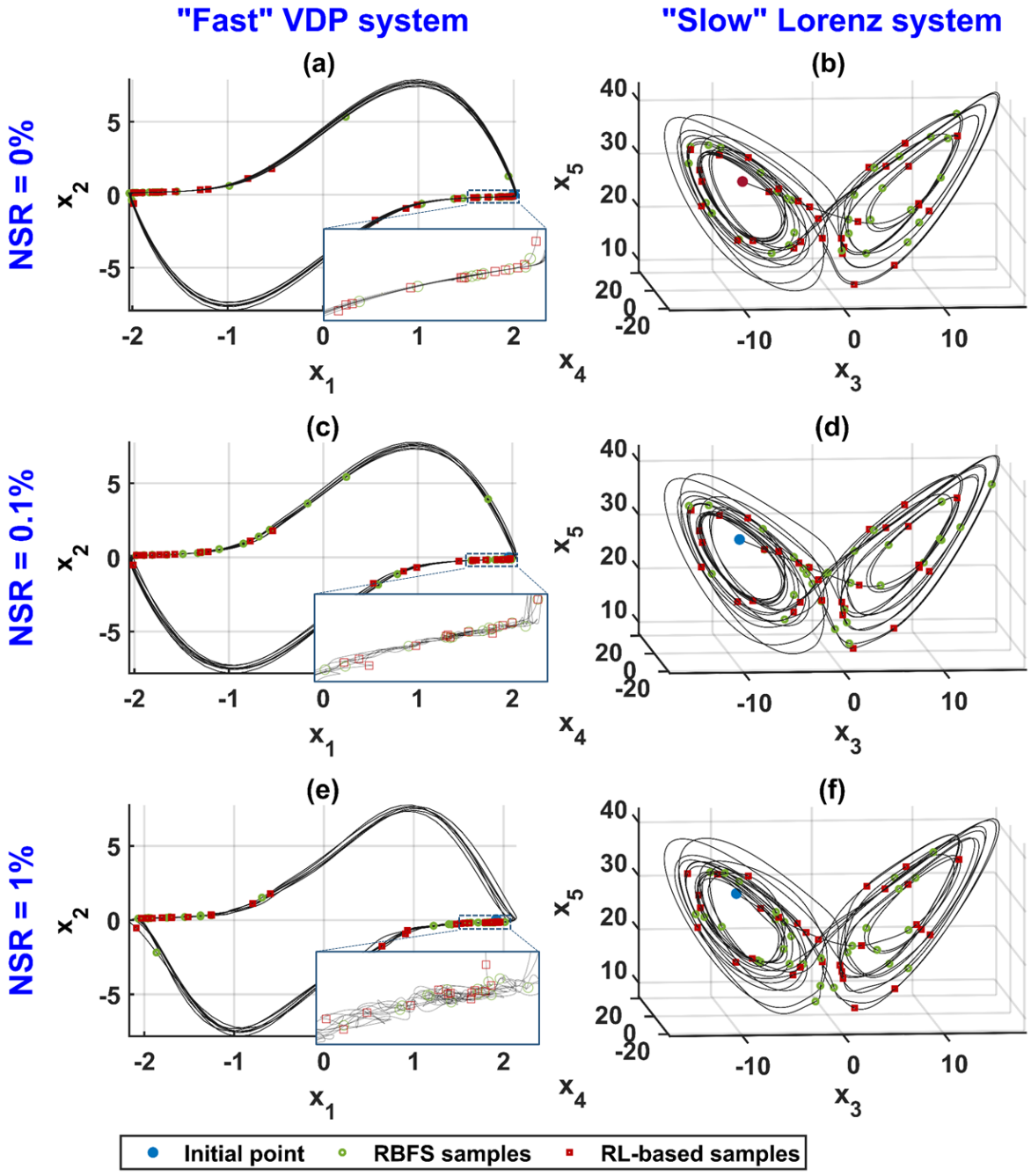

Figure 8-6 Visualization of samples acquired through the RBFS and RL-based techniques for the “fast” Van der Pol oscillator coupled with the “slow” Lorenz system under distinct noise scenarios. Red squares and green circles in panels (a), (c), (e) demonstrate samples from the RL-based method and RBFS respectively, for the "fast" Van der Pol oscillator at NSR levels of 0%, 0.1%, and 1%. Similarly, panels (b), (d), (f) use the same symbols to showcase the "slow" Lorenz system samples under identical NSR conditions

For the noise-free scenario ($NSR = 0\%$, panel (a) and (b)), both RL and RBFS strategies aligned by opting to keep the sampling period consistent. This signified a shared approach in both strategies, indicating the tendency to adapt to slower system dynamics. In panels (c) and (d), with a slight increase in noise level ($NSR = 0.1\%$), both strategies continued to uphold this decision, suggesting a common resilience against minor disturbances. This trend continued even at the higher noise level ($NSR = 1\%$, panel (e) and (f)), revealing the robustness of both methods when faced with increased uncertainty. Intriguingly, there were sampling actions where the RL strategy deviates from the RBFS strategy. Under certain circumstances, the RL strategy chose to decrease the sampling period, an action that the RBFS strategy did not take. This decision underscores an extra layer of flexibility inherent to the RL strategy, highlighting its adaptability to swiftly changing system dynamics.

In this numerical study, the VDP oscillator part of the system maintains its inherent 'limit cycle' and 'excitation' dynamics, while the slower Lorenz system adds another layer of complexity with its chaotic behavior. Notably, both the RL and RBFS strategies cleverly adapted to these dynamics. Similar to the results of the previous numerical study, in the “limit cycle” region of the VDP oscillator, the strategies used a higher sampling frequency to accurately capture the persistent oscillations. Conversely, during the “excitation” phase of the VDP oscillator, characterized by swift progression towards the limit cycle, the strategies opted for less dense sampling. The “slow” Lorenz system added further intricacy with its chaotic dynamics and slower time scale. Despite this, the RL and RBFS strategies adeptly adjusted the sampling methods to capture the complex interactions between the two systems. Both strategies continued to exhibit less intensive sampling in regions where the Lorenz system's dynamics remain relatively unchanged, while intensifying their sampling frequency in regions of chaotic behavior. As the noise scenario increased, both the

RL and RBFS strategies demonstrate impressive adaptability. Despite the increased noise, the strategies maintained their characteristic frequent sampling in the limit cycle region and less dense sampling during the excitation phase of the VDP oscillator. At the same time, they adjusted their sampling methods to capture the intricate dynamics of the slower Lorenz system.

8.5 Discussion

Building upon our previous works [124, 127, 275, 322], our research is situated at the intersection of system identification, sampling strategy optimization, and machine learning. Our study focuses on conducting a comprehensive evaluation of various sampling strategies, specifically uniform sampling, greedy sampling, RBFS, and RL-based sampling, for SINDy algorithm when applied to noisy multi-scale coupled deterministic systems. Prior work by Brunton et al. [234] laid the foundational groundwork for the application of SINDy in system identification. They demonstrated that SINDy could succinctly express the governing equations of a dynamical system from noisy data. Building on Brunton et al.'s work, Champion et al. [251] proposed a burst sampling method for the SINDy algorithm that focused on discovering nonlinear multi-scale dynamical systems from data. Their work introduced a more deliberate, non-uniform sampling strategy that concentrated samples in areas of interest, resulting in a more efficient scaling of the SINDy algorithm. It provided a significant steppingstone towards realizing the potential of smart sampling strategies in system identification. Our study builds upon the work of Champion et al., we diverge from the previous results by investigating the potential of deep reinforcement learning for optimizing the sampling strategy in SINDy algorithm. While Brunton et al. and Champion et al. relied on more traditional mathematical approaches to sample selection, our work leverages the power of reinforcement learning to choose the most informative samples under various noise scenarios adaptively.

The comprehensive results provide us with important implications about the applicability and performance of these methods in different NSR situations. Uniform sampling emerged as an efficient strategy in terms of computational speed across all NSR scenarios. However, the downside of this method is its relative need for accuracy in generating SINDy models, as suggested by higher modeling errors. Therefore, uniform sampling might be beneficial when an approximate understanding of system dynamics is needed, but not necessarily perfect, and some degree of modeling error is tolerable. On the other hand, greedy sampling performed impressively in minimizing sample sizes, especially under noise-free conditions. This attribute can be highly beneficial when data collection is costly, time-consuming, or challenging. Nevertheless, the method's performance markedly deteriorated under noisy conditions, indicating that its applicability might be limited to ideal or controlled environments. The RBFS method employs a random yet comprehensive search across the sample space to identify critical data points at high computational cost, allowing for efficient capture of the crucial dynamics of the system. Our results indicate that the RBFS method retains robust performance even in various noise conditions, making it a versatile choice for dealing with complex, real-world scenarios.

The performance comparison of the four different sampling strategies uncovers some interesting insights regarding their respective capabilities and potential application areas. Uniform sampling exhibited impressive speed in processing time across all NSR scenarios, which underscores its utility in applications where swift computation is a priority. However, it underperformed in terms of generating accurate SINDy models, as indicated by higher errors. This characteristic makes it more suitable for contexts where an immediate, although not perfect, understanding of system dynamics is necessary, and a certain degree of modeling error is tolerable. Contrastingly, greedy sampling excelled in minimizing sample sizes under noise-free conditions,

an attribute that can prove beneficial in cases where data collection is costly or otherwise challenging. Despite this advantage, its efficacy noticeably declined in noisy environments. This suggests that, while the Greedy method can be highly efficient under ideal conditions, its performance might be compromised when dealing with real-world systems that often include some level of noise. Both the RL-based sampling strategy and the RBFS method stood out for their ability to better capture system dynamics, as substantiated by their lower $\log(\kappa(\boldsymbol{\Theta}))$ and $\log(\mathrm{tr}(\mathbf{I}))$ values. These metrics signify the generated samples' diversity and informativeness, and lower values indicate a more comprehensive and accurate representation of the underlying system dynamics. Therefore, these two strategies are more adept at dealing with complex or high-dimensional systems where capturing a wider range of behaviors is crucial. The RL-based sampling strategy, which is the novel contribution of our work, exhibited robust and efficient performance across a range of noise conditions. The RL-based sampling strategy adapts and adjusts to different scenarios, showing a robust performance, whether in the presence or absence of noise. Its key strength lies in its ability to learn and adapt to the system's dynamics, enabling it to efficiently sample crucial points in its trajectory, thus generating accurate SINDy models.

While our study advances the understanding of different sampling strategies for SINDy algorithms in multi-scale systems, several limitations are worth noting. First, the noise scenarios we considered were of a synthetic, idealized nature, which only partially captures the complexity and diversity of real-world noise structures. For instance, real-world noise often includes non-Gaussian, heavy-tailed distributions, or even correlated noise, which still needs to be addressed in our current research. Second, our investigation was primarily confined to single-scale systems. However, many systems, especially in the fields of meteorology, geophysics, and biology, are inherently multi-scale in nature. Our findings, while valuable, may only directly extrapolate to

such complex, multi-scale systems with modification or additional consideration. Third, our study was premised on the availability of full measurements of governing variables, a scenario that might only sometimes be the case in real-world datasets. Incomplete measurements or missing data are common issues that can significantly impact the performance of system identification methods, an aspect not covered in our current research. Lastly, while our reward function in the reinforcement learning context proved effective in the studied systems, its universal applicability across all system types and scales still needs to be proven. The reward function plays a pivotal role in guiding the learning process of the RL agent, and its efficiency can drastically influence the quality of the learned models.

8.6 Conclusion

In conclusion, our research contributes significantly to the field of multi-scale system identification, shedding light on the complexity of modeling such systems and the need for efficient, data-driven algorithms. We successfully implemented a deep Q-learning based reinforcement learning framework to capture this multi-scale complexity. The agent's reward signals were designed to reflect the complex dynamics, enabling the agent to sample data optimally, thereby revealing crucial multi-scale behaviors of the system. In our methodology, Sparse Identification of Nonlinear Dynamics (SINDy) played a key role in discovering and predicting system dynamics. Our framework was assessed in two numerical studies: (1) the coupled fast and slow Van der Pol oscillator, and (2) a noisy fast Van der Pol oscillator coupled with a noisy slow Lorenz system. In each scenario, the reinforcement learning model showcased its ability to autonomously determine the optimal data sampling strategy to capture the multi-scale dynamics effectively. Importantly, we found that the learned policy was intricate, assisting in addressing challenges of non-convergence, reducing the sample size, and improving SINDy's

robustness to noise. These results constitute a significant advancement in the development of data-efficient reinforcement learning methods for multi-scale complex systems. The potential implications of our research extend beyond system identification, with potential applications in diverse fields where understanding and manipulating complex system dynamics are paramount. By facilitating a more accurate understanding and efficient control of these systems, our research paves the way for future advancements in multi-scale modeling. As machine learning continues to evolve, we anticipate our findings will motivate further exploration and research, continually pushing the boundaries of our understanding of complex dynamical systems.

Chapter 9: Adaptive Control Strategies in Therapeutic Intervention: a Multicentric Randomized Controlled Trial on Obstructive Sleep Apnea Management

This multicentric randomized controlled trial aimed to explore the effectiveness and adaptability of various therapeutic interventions in managing Obstructive Sleep Apnea (OSA), and their impact on cardiovascular risk factors over a 6- or 12-month period, employing a system control perspective. A total of 700 patients with moderate to severe OSA were recruited from Brigham and Women's Hospital (BWH), Beth Israel Deaconess Medical Center (BIDMC), and other affiliated clinics. Participants were allocated to one of four treatment arms: Conservative Medical Therapy (CMT), Sham PAP, Active PAP with standard respiratory therapist adherence education (Active-Beh), and Active PAP with enhanced behavioral intervention (Active+Beh). Employing system control theory, the study gauged the dynamic interactions between therapeutic interventions and OSA parameters over time. The primary outcome measure was the Apnea-Hypopnea Index (AHI), while secondary outcomes included sleep efficiency, wake after sleep onset, cardiovascular risk factors, and overall OSA improvement. The Active+Beh group exhibited the most significant improvement in AHI, followed by the Active-Beh group. Conservative Medical Therapy and Sham PAP demonstrated less pronounced benefits. Substantial reductions in cardiovascular risk factors were observed in participants receiving active PAP therapy, aligning with the hypothesis that effective OSA management can mitigate cardiovascular disease risk. Longitudinal analysis revealed dynamic relationships between treatment adherence, OSA parameter improvement, and cardiovascular risk mitigation. The findings advocate for the implementation of adaptive therapeutic interventions in OSA management, emphasizing

personalized treatment regimes to significantly enhance patient outcomes and reduce associated cardiovascular risks. Moreover, the study establishes a precedent for employing system control principles in clinical settings, opening avenues for innovative, adaptive treatment paradigms in managing OSA and potentially other chronic ailments.

9.1 Introduction

Obstructive Sleep Apnea (OSA) is a prevalent sleep disorder characterized by recurrent episodes of airflow cessation during sleep, despite the effort to breathe, due to a temporary obstruction of the upper airway [323]. The chronic intermittent hypoxia and sleep fragmentation associated with OSA have been closely linked to a host of cardiovascular diseases (CVD) including hypertension, atrial fibrillation, stroke, and heart failure [324]. The interaction between OSA and CVD is not merely coincidental but denotes a complex, dynamic interplay of physiological variables. The intermittent hypoxia in OSA, for instance, triggers sympathetic nervous system overactivity and oxidative stress, fostering a pro-inflammatory state and endothelial dysfunction which are critical pathways to cardiovascular morbidity [325]. Furthermore, the adverse cardiovascular repercussions of OSA extend to enhanced atherosclerotic processes and impaired glucose metabolism, each feeding into the vicious cycle of CVD progression [326]. The aforementioned dynamics underscore the need for a robust system control strategy that can effectively modulate the underlying physiological variables, offering a viable route to mitigating the cardiovascular risks inherent in OSA sufferers.

Adaptive control systems are engineered to automatically adjust to variations in the system's environment or in the system's behavior, which is particularly crucial in biomedical fields where patient-specific responses to treatments significantly vary [327]. In the context of OSA and associated cardiovascular complications, the need for adaptive therapeutic interventions is glaring

given the heterogeneous nature of both conditions in terms of severity, symptomatology, and individual response to treatment [328]. Traditional therapeutic approaches, like Continuous Positive Airway Pressure (CPAP) treatment, have shown efficacy in alleviating OSA symptoms and, consequently, its cardiovascular comorbidities [329]. However, the one-size-fits-all approach of such treatments often falls short in optimizing outcomes for every individual, underscoring the need for more personalized, dynamic treatment strategies [330]. Adaptive system control in therapeutic interventions posits a promising solution by continuously monitoring patients' physiological responses and adjusting treatment parameters in real-time to optimize therapeutic outcomes [331]. Moreover, integrating advanced algorithms and machine learning techniques in the control system can further enhance the precision and efficacy of these adaptive treatments, moving towards a more personalized healthcare paradigm [332]. This sophisticated approach not only holds the promise of significantly improving the management of OSA and its associated cardiovascular risks but also contributes to the broader narrative of precision medicine that aims to tailor treatment strategies based on individual patient characteristics and responses.

The employment of system control theories in the domain of healthcare has witnessed significant advancements over the years, transcending from mere theoretical propositions to actionable treatment strategies with promising results. Particularly, the domain of sleep medicine, specifically OSA treatment, has significantly benefited from such interdisciplinary approaches [330]. Contemporary studies have started to delve into the application of control system engineering principles to develop adaptive or dynamic treatment regimens for OSA. This embraces a paradigm where treatment protocols evolve in real-time or near-real-time, responding to the patient's unique physiological conditions and variations [333]. For instance, dynamically adjustable CPAP machines now offer real-time titration of pressure settings in response to detected

respiratory events, a leap from the static pressure settings of traditional CPAP devices [334]. Moreover, the exploration of model-based control systems, incorporating predictive algorithms and feedback loops, has unlocked new avenues for a more precise and personalized management of OSA [335]. Such system control approaches have not only demonstrated superior efficacy in optimizing treatment outcomes but also in ameliorating associated cardiovascular risks, as real-time modulation of treatment parameters can potentially mediate the progression of cardiovascular complications induced by OSA [328]. The promise shown by these emerging methodologies underscores the criticality of further investigation and development in the realm of adaptive and dynamic treatment regimens for OSA.

Despite the significant progress made in applying system control principles in OSA treatment, there remain gaps in understanding and potential areas of further optimization. While adaptive treatment regimens exhibit promise, the comprehensive evaluation of their long-term efficacy, safety, and impact on comorbid conditions is somewhat lacking in the current literature [336]. Moreover, there's a necessity to ascertain how different control strategies compare against one another and against standard care procedures, to determine the most effective and efficient approach [337]. The inherent complexity and variability in human physiological responses to treatment call for a robust analytical framework to adequately capture and analyze the dynamical interactions between therapeutic interventions and patient outcomes over time [333]. Furthermore, real-world data on the feasibility, adherence, and patient satisfaction with adaptive treatment modalities are scant, necessitating empirical studies to fill this knowledge gap [338]. The present study aims to bridge these identified gaps by employing a rigorous statistical analysis framework to investigate the effects of adaptive treatment strategies on OSA outcomes over a longitudinal period. Through comparative analysis of different treatment arms and an in-depth examination of

associated variables, this study endeavors to contribute to the growing body of knowledge aiming to refine system control-based therapeutic approaches for OSA, potentially laying a foundation for enhanced patient-centered care in sleep medicine.

9.2 Methodologies

This study aimed to elucidate the comparative effectiveness of Continuous Positive Airway Pressure (CPAP) therapy and Conservative Medical Therapy (CMT) in treating individuals diagnosed with moderate to severe Obstructive Sleep Apnea (OSA) who also have established cardiovascular disease (CVD) or at least three CVD risk factors. The central hypothesis under investigation was that active treatment for OSA with CPAP reduces CVD morbidity and mortality. The methodologies employed encompassed a well-structured randomized controlled trial across four different treatment arms, with data collection at baseline, 6-months, and 12-months post-intervention initiation. The research questions addressed are:

- How do the different treatment arms (CMT, CMT+ShamCPAP, CMT+ActiveCPAP, and CMT+ActiveCPAP+ME) affect the improvement in OSA?
- What are the estimated coefficients of the representative variables in predicting OSA improvement, and how do these variables influence the effectiveness of the interventions?
- Are there significant differences in OSA improvement distribution between the control group (comprising CMT and CMT+ShamCPAP) and the treatment group (comprising CMT+ActiveCPAP and CMT+ActiveCPAP+ME), and how do these differences translate to clinical relevance in managing OSA and associated cardiovascular risks?

9.2.1 Study Design and Participants

The study utilized data from the Best Apnea Interventions for Research (BestAIR) study, which aimed to investigate the impacts of varying interventions on patients diagnosed with sleep

apnea who either had established cardiovascular diseases (CVD) or at least three risk factors associated with CVD. This pilot randomized controlled trial aimed to evaluate the effectiveness of Continuous Positive Airway Pressure (CPAP) therapy in mitigating the cardiovascular disease (CVD) burden and CVD risk factors among patients with moderate to severe Obstructive Sleep Apnea (OSA). OSA, characterized by a high frequency of breathing pauses during sleep, often accompanies loud snoring and daytime sleepiness, posing an escalated risk for heart disease development or exacerbation in those already diagnosed.

The clinical research was conducted at Brigham and Women's Hospital (BWH) and Beth Israel Deaconess Medical Center (BIDMC), involving a comprehensive comparison of CPAP therapy to Conservative Medical Therapy (CMT). Eligible participants were individuals aged 45-75 with diagnosed heart disease or those aged 55-75 with risk factors for heart disease, as indicated by a sleep doctor or cardiologist. The recruitment aimed at enrolling around 700 patients, newly diagnosed with moderate to severe OSA from affiliated sleep disorder and specialized cardiology clinics, including Massachusetts General Hospital (MGH) and Faulkner Hospital. The intervention span ranged from 6 to 12 months, focusing on exploring alternative OSA treatment modalities to reduce heart disease and prepare for a larger-scale randomized controlled trial in the future. The hypothesis that active OSA treatment with CPAP decreases CVD morbidity and mortality was central to this study. Participants were categorized into four groups post a 2-week run-in period and baseline visit completion:

- The first two groups are *Active-PAP Therapy Groups (Active-Beh or Active+Beh)*. These groups received standard medical treatment for sleep apnea coupled with active-PAP, differentiated by the extent of respiratory and cognitive behavioral therapist involvement.

- The first group is *Active-Pap* with respiratory therapist visits only (*Active-Beh or ActiveCPAP*). The second group is *Active-Pap* with both respiratory therapist and cognitive behavioral therapist visits (*Active+Beh or ActiveCPAP+ME*).
- The third group is *Alternative PAP Group (Sham)*. This group received a lower air delivery level than the *active-PAP* groups, alongside meetings with a respiratory therapist.
- The last group us *Conservative Medical Therapy Group (CMT)*. Participants in this group were provided with a free supply of nasal strips throughout their treatment duration (either 6 or 12 months) and were educated on healthy sleep hygiene practices to minimize apnea occurrences. They received bimonthly follow-ups alternating between phone calls and office visits for safety assessments, adverse events identification, healthcare utilization monitoring, and protocol adherence reinforcement.

For participants randomized before December 31, 2012, a 12-month follow-up assessment was conducted, while those randomized after this date underwent a 6-month follow-up. Throughout the study, key exposure and outcome variables were evaluated at baseline and the 6- and 12-month marks to ascertain the interventions' impacts on OSA and its associated cardiovascular implications.

9.2.2 Data Collection and Outcome Measures

The data collection in this study was meticulously planned and executed to ensure a robust analysis of the interventions' effectiveness. Several measures were employed to comprehensively assess the impacts of the interventions on OSA patients and its cardiovascular comorbidities. The primary physiological outcome was the change in mean 24-hour systolic blood pressure, which is a critical indicator of cardiovascular health.

- *The first procedure is baseline assessment.* Before randomization and post the 2-week run-in period, a baseline assessment was conducted on all participants to establish a starting point for later comparisons. This assessment encompassed a thorough evaluation of participants' sleep apnea severity, cardiovascular risk factors, and existing cardiovascular conditions.
- *The second procedure follow-up assessment.* Follow-up assessments were scheduled at 6- and 12-months post-randomization to evaluate the interventions' impacts over time. For participants randomized after December 31, 2012, the follow-up was only conducted for 6 months. These assessments focused on capturing changes in participants' cardiovascular health and OSA symptoms.
- *The outcome measures consist of 3 types: primary outcome, secondary outcomes, and process measures.* The primary outcome was the change in mean 24-hour systolic blood pressure, a strong predictor of cardiovascular morbidity and mortality. These included changes in other cardiovascular indicators such as diastolic blood pressure, heart rate, and blood lipid levels. Also, the apnea-hypopnea index (AHI), a measure of sleep apnea severity, was evaluated to assess OSA improvement. Process measures such as recruitment yields, retention rates, and CPAP adherence levels were analyzed to evaluate the study's procedural effectiveness and participants' engagement with the interventions.
- Data were collected from multiple sources to ensure a comprehensive analysis. These sources included: (1) *clinical assessments* were conducted at baseline, 6, and 12 months, these assessments included physical examinations, blood pressure measurements, and blood tests to evaluate cardiovascular health and other relevant clinical indicators; (2) *sleep studies* included polysomnography or home sleep apnea tests were utilized to evaluate

participants' sleep apnea severity at different stages of the study; (3) *participant interviews and questionnaires* have participants were periodically interviewed, and questionnaires were administered to collect data on their sleep quality, lifestyle, and adherence to the intervention protocols; and (4) *medical records* were reviewed to obtain historical and ongoing medical information, especially concerning cardiovascular conditions and other comorbidities.

The collected data were securely stored and well-organized for efficient management, abiding by the prevailing data protection and privacy regulations. The entire dataset from this study is publicly available for further analysis and can be accessed at BestAIR dataset on sleepdata.org. A well-structured database was utilized to organize the data efficiently, facilitating accurate and straightforward analyses in the subsequent phases of the study. The structured data collection and outcome measures ensured a thorough evaluation of the interventions, aiding in a comprehensive understanding of the potential benefits of CPAP therapy and conservative medical treatment in managing OSA and reducing cardiovascular risk among the study population.

9.2.3 Statistical Analysis

The statistical analysis undertaken in this study seeks to provide a thorough examination of the effects of various treatment strategies on Obstructive Sleep Apnea (OSA) improvement and associated cardiovascular risk reduction over a 12-month period. Given the dynamic nature of therapeutic interventions akin to system control inputs, the analysis delineates the adaptive capabilities of these interventions in managing OSA and its associated conditions. Initially, descriptive statistics are derived to summarize the demographic and clinical characteristics of subjects across different treatment arms and visits. This provides a foundational understanding of the population under study, essential for contextualizing the subsequent analyses. To evaluate the

degree of OSA improvement across different levels of baseline OSA severity and treatment arms, a multiple linear regression model is constructed. The coefficients estimated provide insight into the quantitative impact of the interventions, and the diagnostic plots assess the model fit and predictive accuracy. The mathematical representation of a multiple linear regression model is generally denoted as follows:

$$Y = \beta_0 + \beta_1 X_1 + \beta_2 X_2 + \cdots + \beta_p X_p + \varepsilon \tag{9.1}$$

where:

- Y is the dependent variable, in this case, the degree of OSA improvement.
- β_0 is the y-intercept or offset.
- $\beta_1, \beta_2, \ldots, \beta_p$ are the coefficients of the explanatory variables.
- $X_1, X_2, \ldots, X_p$ are the explanatory variables.
- ε is the error term capturing the unexplained variation in the model.

In the context of the BestAIR study, we can customize the equation to represent the specific variables in the analysis. Suppose that we consider the treatment arm, age, and BMI as the explanatory variables, the model equation could be represented as:

$$\text{OSA Improvement} = \beta_0 + \beta_1(\text{Treatment Arm}) + \beta_2(\text{Age}) + \beta_3(\text{BMI}) + \varepsilon \tag{9.2}$$

This multiple linear regression model will provide a robust framework to statistically analyze the factors influencing OSA improvement and to draw meaningful conclusions that align with the objectives of the BestAIR study.

Furthermore, a linear mixed-effects model is employed to examine the longitudinal effects of the interventions on the primary outcome measure, Apnea-Hypopnea Index (AHI), across baseline and 12-month visits. In a linear mixed-effects model (LMM) with a random intercept, both fixed and random effects are incorporated to account for correlations in the data, often arising

from repeated measurements on the same individuals over time. The general mathematical representation of a linear mixed-effects model with a random intercept is as follows:

$$Y_{ij} = (\beta_0 + u_i) + \beta_1 X_{1ij} + \beta_2 X_{2ij} + \cdots + \beta_p X_{pij} + \varepsilon_{ij} \quad (9.3)$$

where:

- Y_{ij} is the dependent variable (in this case, AHI) for subject i at time j.
- β_0 is the overall intercept.
- u_i is the random effect for subject i (random intercept).
- $\beta_1, \beta_2, \ldots, \beta_p$ are the coefficients of the fixed effects.
- $X_{1ij}, X_{2ij}, \ldots, X_{pij}$ are the explanatory variables for subject i at time j.
- ε_{ij} is the residual error term for subject i at time j.

In this model, the fixed effects β_k's represent the average effect of the explanatory variables on the dependent variable, AHI. The random intercept u_i allows for individual differences in baseline AHI, accounting for the correlation of repeated measures within subjects. The ε_{ij} term captures the unexplained variation not accounted for by either the fixed or random effects. The random intercept u_i is typically assumed to follow a normal distribution with mean zero and unknown variance σ_u^2, i.e., $u_i \sim \mathcal{N}(0, \sigma_u^2)$, and the residual error ε_{ij} is also typically assumed to follow a normal distribution with mean zero and unknown variance σ^2, i.e., $\varepsilon_{ij} \sim \mathcal{N}(0, \sigma^2)$. This model provides a flexible framework to explore both the average effects of explanatory variables (fixed effects) and the individual variations in the baseline AHI (random intercept) over time, allowing for a comprehensive understanding of the longitudinal effects of the interventions on AHI across the baseline and 12-month visits.

The comparative efficacy of CPAP and control groups over a 12-month period is presented, providing a longitudinal perspective on treatment efficacy. This is further visualized to elucidate

the trends in various sleep-related and cardiovascular parameters across different treatment arms over the study period. A frequency histogram depicting the distribution of OSA improvement across the four treatment arms is presented. This visual representation facilitates a clear comparison of OSA improvement distribution between control and treatment interventions, shedding light on the effectiveness of adaptive control strategies employed. The analysis culminates with an exploration of the system control theory's applicability in dynamically managing complex health conditions like OSA. The adaptive nature of the interventions, akin to dynamic treatment regimes, is discussed in context with the observed outcomes, providing a novel interdisciplinary narrative that bridges system control, therapeutic interventions, and clinical outcomes. All analyses are performed using MATLAB R2023a software, with significant findings being reported at a 5% significance level. The robustness of the findings is further evaluated through sensitivity analyses, ensuring the reliability of the conclusions drawn from the analysis. Through a meticulous statistical examination, this section elucidates the effectiveness of adaptive control strategies in managing OSA and its associated cardiovascular risks, aligning well with the results presented.

9.3 Results

9.3.1 Demographic and Clinical Characteristics

Tables 9-1 and 9-2 encapsulated the demographic and clinical characteristics of subjects, establishing the groundwork for understanding the distribution of participants across different treatment arms and the variety of clinical variables among levels of OSA improvement. Initially, Table 9-1 elucidates the demographic and clinical characteristics of subjects distributed across different treatment arms and visits.

Table 9-1 Demographic and clinical characteristics of subjects across treatment arms and visits

Variables mean (std)	Baseline		6-month visit		12-month visit	
	Control	CPAP	Control	CPAP	Control	CPAP
Subjects, *n*	86	83	69	65	43	34
Age, *years*	64.28 (6.94)	64.41 (7.85)	65.32 (6.35)	65.72 (7.56)	65.67 (6.66)	66.29 (6.82)
Gender						
Male, *n (%)*	55 (63.95)	55 (66.27)	47 (68.12)	45 (69.23)	30 (69.77)	21 (61.76)
Female, *n (%)*	31 (36.05)	28 (33.73)	22 (31.88)	20 (30.77)	13 (30.23)	13 (38.24)
Race						
White, *n (%)*	77 (89.53)	75 (90.36)	63 (91.30)	61 (93.85)	36 (83.72)	34 (100.00)
Other, *n (%)*	9 (11.47)	8 (9.64)	6 (9.70)	4 (6.15)	7 (16.28)	0 (0.00)
BMI, kg/m^2	32.25 (6.47)	31.10 (5.24)	31.62 (5.14)	31.13 (5.55)	31.23 (5.81)	32.12 (5.98)
Agg_ment	0.05 (0.94)	0.05 (1.20)	0.25 (0.94)	0.24 (1.06)	0.41 (1.10)	0.08 (0.98)
Agg_phys	-0.53 (0.96)	-0.43 (0.93)	-0.70 (0.98)	-0.33 (1.38)	-0.51 (1.04)	-0.35 (0.99)
Bl_hemoa1c	6.54 (1.90)	6.20 (1.24)	6.12 (0.85)	6.35 (1.16)	6.22 (0.94)	6.48 (1.24)
Bl_insulfast	15.27 (17.13)	16.15 (17.15)	14.53 (7.90)	15.12 (12.34)	13.42 (19.57)	19.07 (24.17)
Bl_ldlchol	85.62 (25.92)	92.75 (34.66)	89.16 (23.37)	96.69 (39.70)	95.56 (29.00)	92.24 (34.76)
Bl_totalchol	160.45 (31.67)	170.13 (39.52)	164.13 (27.93)	171.98 (45.16)	173.09 (34.51)	171.68 (41.07)
Bl_triglyc	128.10 (74.57)	125.17 (72.53)	123.98 (74.96)	118.23 (50.81)	127.40 (65.44)	133.79 (76.40)
Cal_total	4.78 (0.90)	4.79 (1.04)	4.87 (0.85)	4.70 (0.85)	4.95 (0.83)	4.86 (0.70)
ESS_total	8.38 (4.51)	7.95 (4.45)	7.54 (4.17)	6.23 (3.77)	7.67 (3.96)	5.82 (4.07)
Phq8_total	4.87 (4.32)	5.25 (5.36)	4.25 (4.02)	4.10 (3.89)	4.01 (3.79)	4.18 (4.15)
Prom_sdscal	21.91 (6.41)	21.64 (7.18)	18.57 (6.65)	16.75 (6.86)	17.70 (6.94)	15.68 (6.88)
Bp24dbpweight	71.12 (13.28)	72.49 (8.16)	73.50 (9.53)	71.09 (8.27)	72.55 (8.82)	67.81 (9.00)
Bp24sbpweight	126.44 (14.39)	121.88 (11.47)	128.30 (14.46)	121.94 (10.77)	127.78 (14.31)	121.10 (11.91)

Table 9-1 presents the mean values and standard deviations (mean (std)) or counts and percentages (n (%)) of various demographic and clinical characteristics of subjects within the Control and CPAP treatment arms at baseline, 6-month, and 12-month visits. The total number of subjects in each arm is reported for every visit. Continuous variables are summarized by mean and standard deviation values while categorical variables are summarized by count and percentage values. Characteristics include age, gender, race, Body Mass Index (BMI), aggregate mental and physical scores, baseline hemoglobin A1c, fasting insulin, low-density lipoprotein cholesterol (LDL cholesterol), total cholesterol, triglycerides levels, caloric intake, Epworth Sleepiness Scale

(ESS) total score, Patient Health Questionnaire-8 (PHQ-8) total score, PROMIS Sleep Disturbance (prom_sdscal) scale, and weighted 24-hour diastolic and systolic blood pressure. In Table 9-1, the gender distribution remains relatively consistent across both treatment arms and across all three visit intervals, with a slightly higher proportion of males to females. Interestingly, racial distribution also remained stable, though there's a significant drop in the “Other” racial category in the CPAP arm at the 12-month visit.

On the clinical front, several metrics were observed. Body Mass Index (BMI) is relatively stable across all groups and visits, indicating a consistent body weight among subjects. Blood test results, including hemoglobin A1c, fasting insulin, LDL cholesterol, total cholesterol, and triglycerides, exhibit minor fluctuations but without a discernible pattern across treatment arms or visits. Other clinical variables such as aggregate mental and physical health scores, Epworth Sleepiness Scale (ESS) total, and PHQ-8 total exhibit varied values across the groups and over time, potentially indicating shifts in health conditions and the psychological well-being of the subjects. Blood pressure measurements taken over a 24-hour period also showed some variation across the treatment arms and visit intervals. The summary of clinical questionnaire scores including the PROMIS sleep disturbance scale also provides a lens into the perceived sleep quality and disturbances among subjects. It’s imperative to analyze these trends further to understand the implications of the CPAP treatment, and how these demographic and clinical factors interact with treatment efficacy and the overall health trajectory of the subjects. This table sets a robust foundation for a detailed exploratory and analytical review to ascertain the impact and effectiveness of CPAP treatment in managing or ameliorating the symptoms and conditions of the subjects involved. Following the demographic exposition, Table 9-2 delves into the exploration of clinical variables across distinct levels of OSA improvement. The table aims to associate the

demographic and clinical characteristics with varying degrees of OSA amelioration, thus providing a preliminary glimpse into potential correlations.

Table 9-2 Demographic and clinical variables across different levels of OSA improvement

Variables	**Low OSA improvement**		**Medium OSA improvement**		**High OSA improvement**	
mean (std)	**Control**	**CPAP**	**Control**	**CPAP**	**Control**	**CPAP**
Subjects, *n*	18	8	14	11	11	15
Age, *years*	64.78 (7.31)	68.50 (5.01)	65.07 (6.35)	65.73 (8.00)	67.91 (5.96)	65.53 (6.91)
Gender						
Male, *n (%)*	6 (54.55)	3 (37.50)	11 (78.57)	6 (54.55)	6 (54.55)	12 (80.00)
Female, *n (%)*	5 (45.45)	5 (62.50)	3 (21.43)	5 (45.45)	5 (45.45)	3 (20.00)
Race						
White, *n (%)*	15 (83.33)	8 (100.00)	12 (85.71)	11 (100.00)	9 (81.82)	15 (100.00)
Other, *n (%)*	3 (17.67)	0 (0.00)	2 (14.29)	0 (0.00)	2 (18.18)	0 (0.00)
BMI, kg/m^2	31.11 (5.79)	28.94 (5.85)	31.28 (7.00)	34.29 (7.11)	31.38 (4.58)	32.23 (4.65)
Agg_ment	0.41 (0.86)	-0.59 (1.17)	0.34 (1.39)	0.25 (0.94)	0.49 (1.13)	0.31 (0.78)
Agg_phys	-0.59 (1.18)	-0.33 (0.89)	-0.64 (0.90)	-0.43 (0.74)	-0.19 (1.01)	-0.31 (1.22)
Bl_hemoa1c	6.36 (1.04)	6.30 (1.17)	6.33 (0.96)	6.47 (0.71)	5.85 (0.66)	6.59 (1.59)
Bl_insulfast	11.46 (7.93)	19.40 (27.96)	17.87 (33.10)	10.38 (4.89)	10.98 (6.01)	25.26 (29.46)
Bl_ldlchol	92.00 (25.79)	84.25 (21.67)	87.93 (21.75)	102.27 (43.94)	111.09 (37.63)	89.13 (33.30)
Bl_totalchol	171.28 (32.49)	164.12 (23.19)	158.93 (28.15)	182.09 (50.59)	194.09 (37.50)	168.07 (41.79)
Bl_triglyc	139.44 (69.37)	108.38 (43.41)	118.79 (74.25)	134.27 (36.03)	118.64 (46.79)	147.00 (106.46)
Cal_total	4.95 (0.83)	4.58 (0.89)	4.80 (0.79)	5.12 (0.64)	5.16 (0.92)	4.82 (0.61)
ESS_total	8.44 (3.71)	5.78 (2.75)	7.43 (4.20)	7.00 (5.08)	6.73 (4.17)	4.99 (3.87)
Phq8_total	3.42 (3.18)	5.88 (5.22)	3.86 (3.68)	4.55 (3.33)	5.18 (4.83)	3.00 (3.98)
Prom_sdscal	19.73 (5.73)	19.75 (9.48)	17.43 (8.65)	15.73 (6.18)	14.73 (5.62)	13.47 (4.96)
Bp24dbpweight	70.74 (9.62)	63.27 (15.32)	73.06 (7.02)	68.41 (4.35)	74.86 (9.67)	69.79 (6.61)
Bp24sbpweight	124.81 (17.43)	117.87 (14.14)	129.74 (12.59)	119.66 (11.18)	130.13 (10.49)	123.88 (11.36)

Table 9-2 delineates a detailed breakdown of demographic and clinical attributes among subjects within two distinct treatment arms—Control and CPAP—across three levels of Obstructive Sleep Apnea (OSA) improvement: Low, Medium, and High, based on the percentiles of improvement scores. Low level corresponds to the 0-33 percentile range, Medium to 34-66

percentile range, and High to 67-100 percentile range. This categorization allows for a segmented analysis of how different variables relate to the levels of OSA improvement among Control and CPAP groups across these defined categories. OSA improvement is gauged by the variance in Apnea-Hypopnea Index (AHI) between baseline and 12-month visit. A noteworthy observation is the variation in subject count among the OSA improvement levels, indicating differing responses to the treatment modalities over time.

According to Table 9-2, a subtle age variation is observed across the OSA improvement categories, yet the age distribution remains relatively consistent within each treatment arm. The gender distribution varies markedly across the OSA improvement levels, particularly in the Medium and High improvement categories, suggesting a potential gender-related influence on the treatment outcome. Racial distribution largely leans towards White subjects, with a 100% White representation in several CPAP groups, hinting at a lack of diversity that might impact the generalizability of the findings. Clinically, Body Mass Index (BMI) shows slight variations across groups, yet remains within a comparable range, indicating a uniform body weight distribution among subjects. Other clinical metrics including aggregated mental and physical scores, blood hemoglobin A1c, fasting insulin, cholesterol levels, and blood pressure readings exhibit variances across both treatment arms and OSA improvement levels. The table also underscores the assessment of sleep and psychological well-being through variables such as the Epworth Sleepiness Scale (ESS) total, PHQ-8 total, and PROMIS sleep disturbance scale.

9.3.2 Longitudinal Data Analysis and Visualization

Transitioning from tabular to graphical representation, Figure 9-1 depicts a longitudinal data visualization of key sleep-related parameters across the four different treatment arms over the duration of the study.

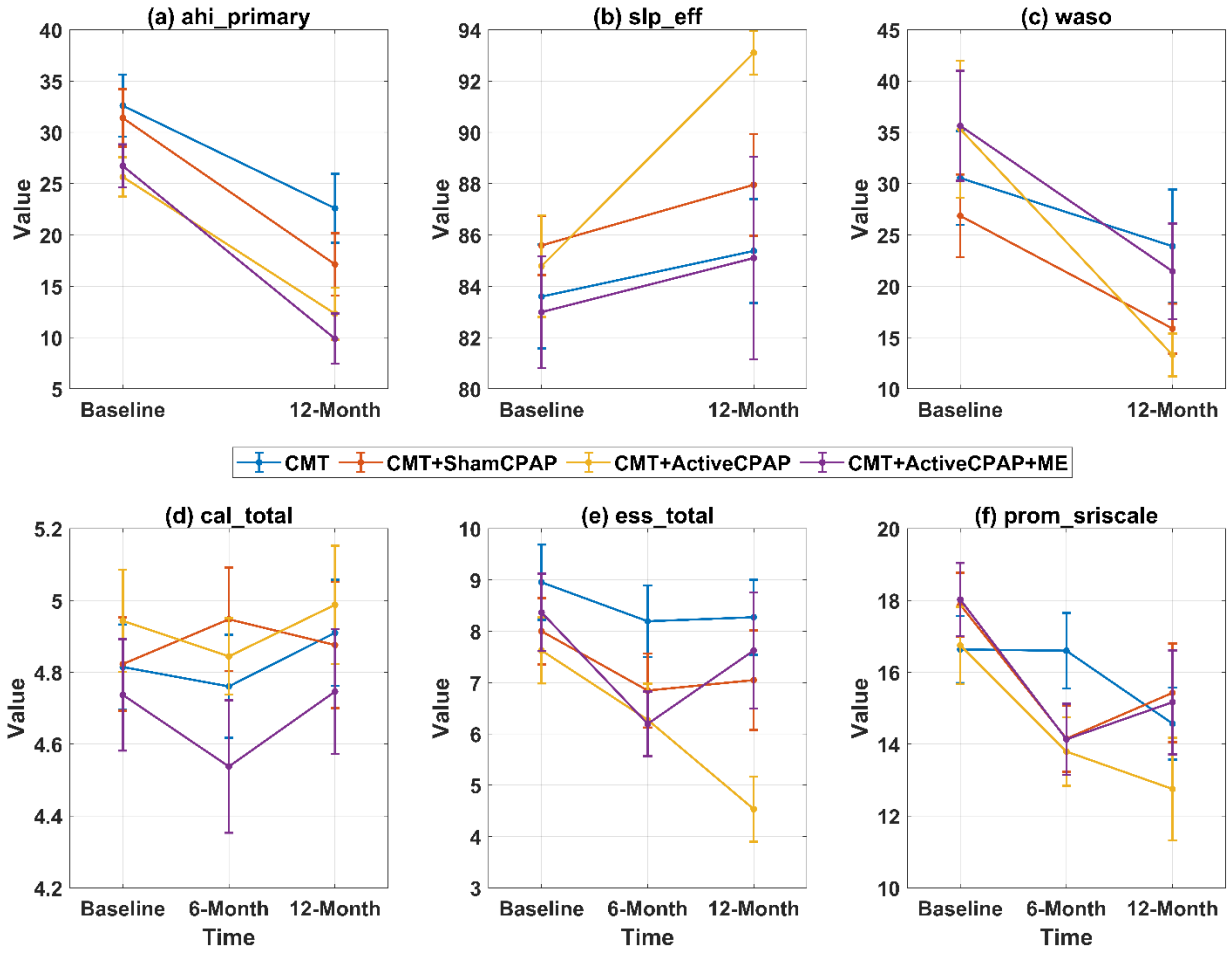

Figure 9-1 Longitudinal data visualization of various sleep-related parameters across 4 different treatment arms over the study period. Panels (a) to (c) depict the trends in Apnea-Hypopnea Index (ahi_primary), sleep efficiency (slp_eff), and wake after sleep onset (waso) at baseline and the 12-month visit, respectively. Panels (d) to (f) elucidate the trends in total caloric intake (cal_total), Epworth Sleepiness Scale total score (ess_total), and self-reported insomnia rating scale (prom_sriscale) across three time points: baseline, 6-month, and 12-month visits. Each panel portrays four line graphs representing different treatment arms: CMT, CMT+ShamCPAP, CMT+ActiveCPAP, and CMT+ActiveCPAP+ME. At each time point, mean values and standard deviations are provided

In Figure 9-1, panels (a) to (c) underscore the temporal evolution of three pivotal parameters at baseline and the 12-month visit. In Panel (a), the Apnea-Hypopnea Index (ahi_primary) is plotted, showcasing its fluctuation across the four treatment arms. A discernible trend is the mitigation of apnea-hypopnea episodes across most treatment arms from baseline to

the 12-month mark, accentuating the longitudinal impact the treatments exert on alleviating sleep apnea. Panel (b) unfurls the trend in sleep efficiency (slp_eff), with the line graphs illustrating a general enhancement in sleep efficiency over time. Conversely, Panel (c) delineates the trend in wake after sleep onset (waso), presenting a visual narrative of how interventions potentially diminish wakefulness after sleep onset, a boon for enhancing sleep quality. Transitioning to Panels (d) to (f), a broader spectrum of parameters is scrutinized across three pivotal time junctures: baseline, 6-month, and 12-month visits. Panel (d) divulges the trends in total caloric intake (cal_total), offering a glimpse into how dietary habits might be intertwined with other sleep parameters. The trajectories in different treatment arms underscore the potential influence of treatments on caloric consumption. Panel (e) elaborates on the trends in the Epworth Sleepiness Scale total score (ess_total), providing a lens through which the alleviation of daytime sleepiness can be gauged over time across the different treatments. Lastly, Panel (f) sheds light on the self-reported insomnia rating scale (prom_sriscale), revealing the longitudinal efficacy of treatments in ameliorating insomnia symptoms. In each panel, four line graphs epitomize the journey of these parameters across the four treatment arms: CMT, CMT+ShamCPAP, CMT+ActiveCPAP, and CMT+ActiveCPAP+ME. The meticulous representation of mean values and standard deviations at each time point enriches the figure with a layer of statistical rigor, allowing for a nuanced understanding of the variability and central tendency of these parameters within the purview of each treatment arm. Extending the longitudinal analysis to cardiovascular and lipid profile parameters, Figure 9-2 illustrates the trends across different treatment arms over the study period. This graphical representation offers a visual summary of how cardiovascular health metrics evolve over time in response to varying treatments.

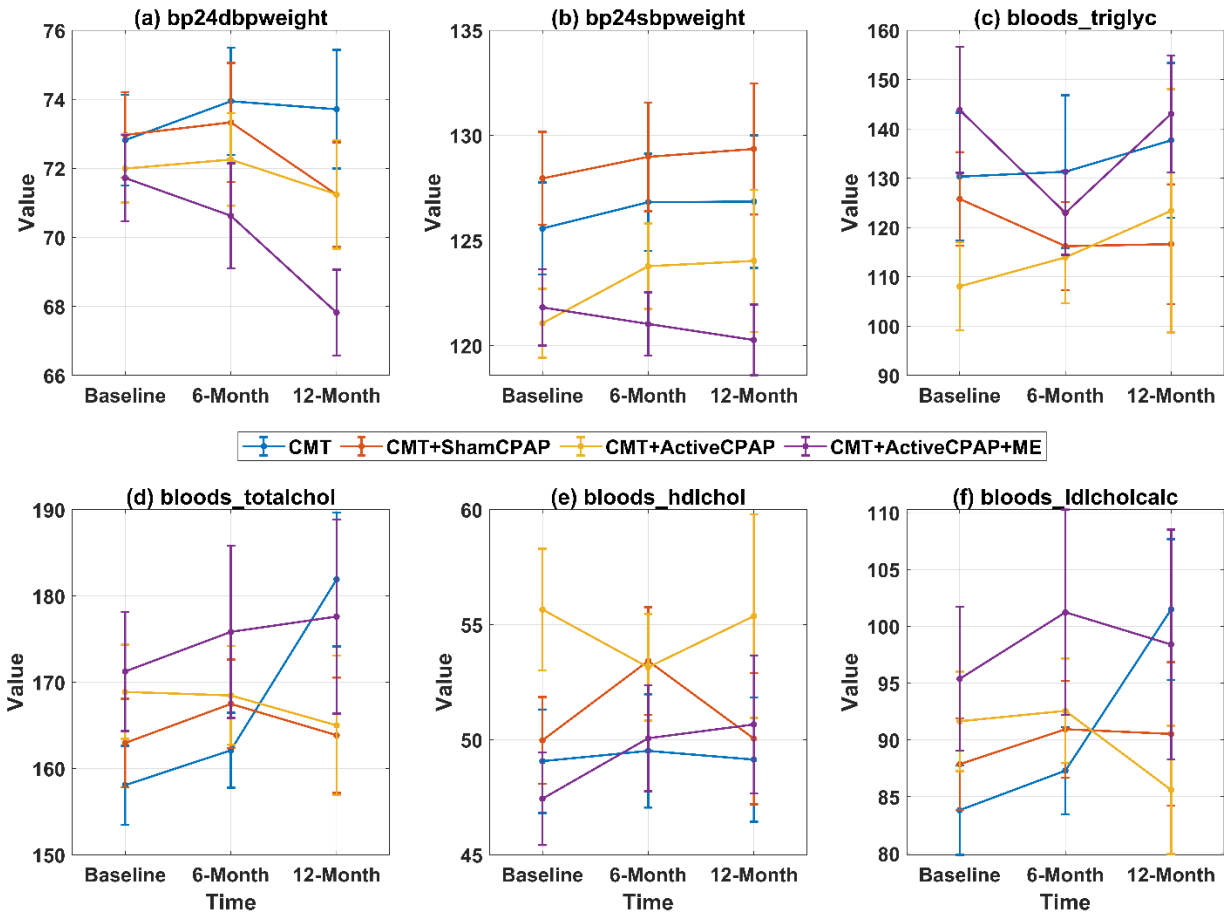

Figure 9-2 Longitudinal data visualization of various cardiovascular and lipid profile parameters across different treatment arms throughout the study duration. Panels (a) to (f) display the trends in weighted 24-hour diastolic blood pressure (bp24dbpweight), weighted 24-hour systolic blood pressure (bp24sbpweight), triglycerides level (bloods_triglyc), total cholesterol level (bloods_totalchol), high-density lipoprotein cholesterol level (bloods_hdlchol), and low-density lipoprotein cholesterol level calculated (bloods_ldlcholcalc) at baseline, 6-month, and 12-month visits, respectively. Each panel includes four line graphs representing different treatment arms: CMT, CMT+ShamCPAP, CMT+ActiveCPAP, and CMT+ActiveCPAP+ME. At each time point, mean values and standard deviations are provided

According to Figure 9-2, Panel (a) and (b) depict the modulation of diastolic and systolic blood pressures respectively across the treatment arms, indicating potential cardiovascular benefits associated with the treatments. Panel (c) to (f) unveil the trends in lipid profile parameters, highlighting the interplay between sleep interventions and lipid metabolism. Triglycerides, total

cholesterol, and low-density lipoprotein cholesterol levels may exhibit modulation with the treatment, potentially hinting at metabolic implications of sleep interventions. Meanwhile, the high-density lipoprotein cholesterol levels suggests a potential positive impact on cardiovascular health.

9.3.3 Treatment Efficacy and Comparative Analysis

Following the trend analysis, Figure 9-3 offers a frequency histogram representation of OSA improvement across the four treatment arms.

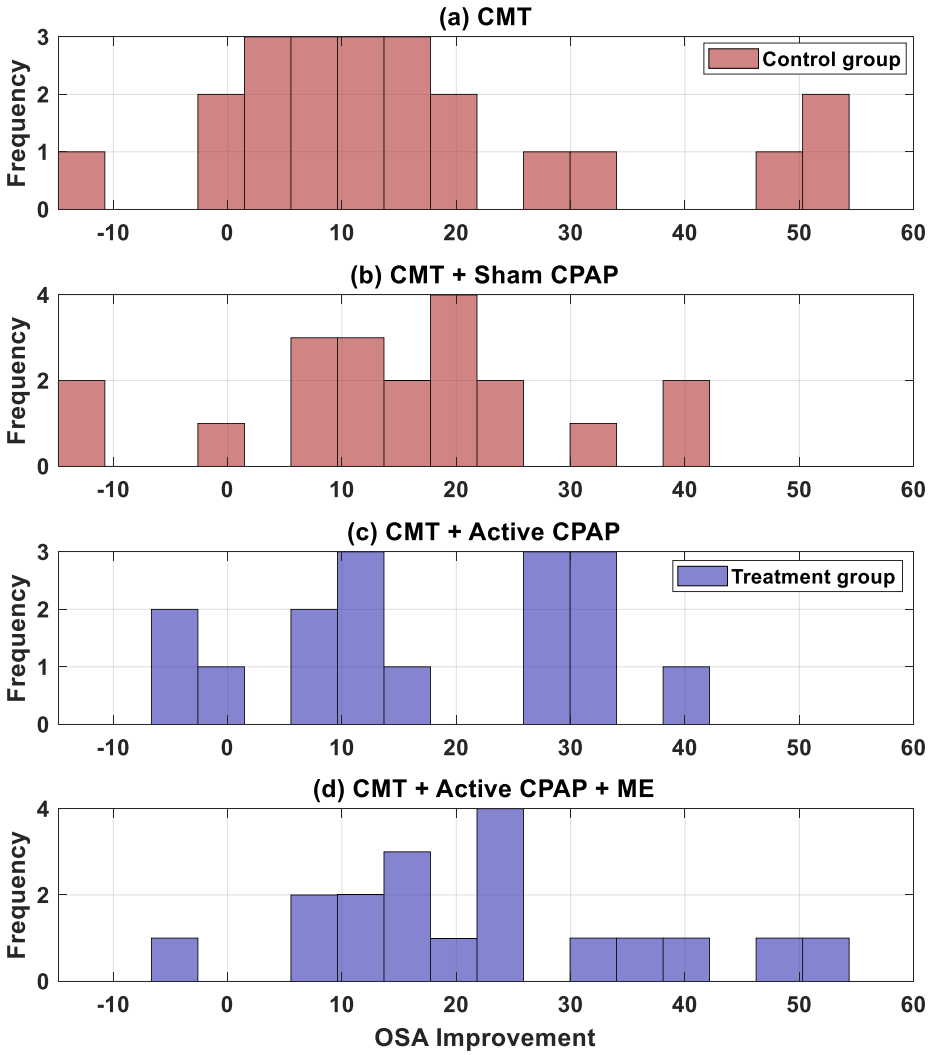

Figure 9-3 Frequency histogram of OSA improvement across four treatment arms, denoted by panels (a) to (d).

In Figure 9-3, it was observable that the distribution of OSA improvement varied across the different treatment arms. For instance, the treatment arms of CMT+ActiveCPAP and CMT+ActiveCPAP+ME (panels (c) and (d)) exhibited a noticeable shift towards higher values of OSA improvement compared to the control arms (panels (a) and (b)). This potentially signified a more substantial amelioration in OSA conditions for subjects under active treatment interventions. Furthermore, the histograms provided insight into the spread and skewness of OSA improvement across different interventions. The data suggested a greater dispersion in OSA improvement in the treatment group, especially the CMT+ActiveCPAP+ME arm. Moreover, the visual depiction facilitated an understanding of the frequency and distribution of OSA improvement, rendering a foundational comprehension of the impact of various treatment interventions on OSA amelioration over the study duration. Next, Table 9-3 proceeds to deliver a comparative analysis of the CPAP and control groups over the 12-month study period.

Table 9-3 Comparative analysis of CPAP and control groups over a 12-month period

Visit time	Variables	CPAP group mean (std)	Control group mean (std)	p-value	Sig code
Baseline	embqs_cannula_flow_qcode	4.37 (1.00)	4.61 (0.87)	0.091488	.
	ahi_primary	26.19 (12.92)	32.01 (19.08)	0.021717	*
	avghipcm	111.65 (11.79)	115.52 (14.93)	0.063839	.
	bp24mapweight	88.96 (8.50)	92.52 (12.30)	0.030313	*
	bp24sbpweight	121.88 (11.47)	126.44 (14.39)	0.024183	*
	semsa_pr	2.36 (0.58)	2.22 (0.53)	0.09037	.
	shq_gerd	0.47 (0.59)	0.31 (0.48)	0.048831	*
	shq_famparapnea	0.99 (0.95)	0.75 (0.90)	0.085317	.
	phq8_down_hopeless	0.57 (0.89)	0.33 (0.60)	0.037502	*
	waso	34.85 (38.52)	28.05 (28.01)	0.189806955	
	slp_eff	83.69 (13.26)	83.06 (14.50)	0.768176077	
	bloods_totalchol	170.13 (39.52)	160.45 (31.67)	0.080291889	.
	bloods_triglyc	125.17 (72.53)	128.10 (74.57)	0.795758603	
	bloods_hdlchol	51.46 (15.55)	49.51 (13.59)	0.38581003	
	bloods_ldlcholcalc	92.75 (34.66)	85.62 (25.92)	0.130837113	
	bloods_hemoa1c	6.20 (1.24)	6.54 (1.90)	0.17763617	
	bloods_totalchol	170.13 (39.52)	160.45 (31.67)	0.080291889	.
	bp24dbpweight	72.49 (8.16)	71.12 (13.28)	0.422277278	
	cal_total	4.79 (1.04)	4.78 (0.90)	0.90650716	
	ess_total	7.95 (4.45)	8.38 (4.51)	0.530895099	
	prom_sdscale	21.64 (7.18)	21.91 (6.41)	0.795969076	

Table 9.3 (Continued)

6-month	bp24sbpweight	121.94 (10.77)	128.30 (14.46)	0.004769	**
	ess_total	6.23 (3.77)	7.54 (4.17)	0.059795	.
	semsa_oe	2.72 (0.82)	2.29 (0.76)	0.00232	**
	semsa_tse	2.92 (0.77)	2.39 (0.83)	0.000187	***
	pf_norm	46.83 (9.57)	43.77 (10.72)	0.083453	.
	agg_phys	-0.33 (1.38)	-0.70 (0.98)	0.077978	.
	prom_satisfied	2.38 (1.32)	1.86 (1.31)	0.023395	*
	prom_refreshing	2.22 (1.23)	1.80 (1.18)	0.046929	*
	prom_quality	3.62 (0.88)	3.35 (0.94)	0.090897	.
	prom_daytime	0.75 (0.79)	1.03 (1.01)	0.083544	.
	ess5	1.47 (0.95)	1.80 (1.07)	0.062932	.
	phq8_movingslowly	0.11 (0.36)	0.25 (0.55)	0.089603	.
	shq_typnightsleep	1.52 (0.87)	1.78 (0.86)	0.083665	.
	bloods_totalchol	171.98 (45.16)	164.13 (27.93)	0.225082697	
	bloods_triglyc	118.23 (50.81)	123.98 (74.96)	0.60617545	
	bloods_hdlchol	51.68 (13.19)	51.28 (14.11)	0.866102095	
	bloods_ldlcholcalc	96.69 (39.70)	89.16 (23.37)	0.18035065	
	bloods_hemoa1c	6.35 (1.16)	6.12 (0.85)	0.189993967	
	bloods_insulinfast	15.12 (13.34)	14.53 (7.90)	0.752854204	
	bmi	31.13 (5.55)	31.62 (5.14)	0.597156519	
	bp24dbpweight	71.09 (8.27)	73.50 (9.53)	0.121852925	
	cal_total	4.70 (0.85)	4.87 (0.85)	0.254900575	
	prom_sdscale	16.75 (6.86)	18.57 (6.65)	0.122959899	
	prom_sdscale	16.75 (6.86)	18.57 (6.65)	0.122959899	
12-month	ahi_primary	7.57 (8.42)	14.90 (13.84)	0.008224	**
	bp24mapweight	85.75 (8.98)	92.28 (14.46)	0.023822	*
	bp24sbpweight	121.10 (11.91)	127.78 (14.31)	0.031831	*
	bp24dbpweight	67.81 (9.00)	72.55 (8.82)	0.023002	*
	lvedd	4.19 (0.48)	4.41 (0.52)	0.065775	.
	ess_total	5.82 (4.07)	7.67 (3.96)	0.047853	*
	semsa_tse	2.85 (0.97)	2.35 (0.89)	0.02119	*
	bp_norm	49.15 (9.64)	44.42 (10.56)	0.046178	*
	prom_refreshing	2.53 (1.11)	1.63 (1.27)	0.001647	**
	prom_quality	3.88 (0.77)	3.53 (1.00)	0.08951	.
	ess1	1.12 (0.91)	1.53 (0.91)	0.049569	*
	ess3	0.57 (0.60)	1.00 (0.98)	0.028427	*
	shq_trbacktosleep	1.07 (1.27)	0.58 (0.96)	0.06015	.
	waso	13.67 (13.60)	15.44 (17.72)	0.6311259	
	slp_eff	85.27 (20.84)	85.15 (18.14)	0.979761964	
	bloods_totalchol	171.68 (41.07)	173.09 (34.51)	0.869833867	
	bloods_triglyc	133.79 (76.40)	127.40 (65.44)	0.693500634	
	bloods_hdlchol	52.88 (15.22)	49.58 (12.69)	0.302782454	
	bloods_ldlcholcalc	92.24 (34.76)	95.56 (29.00)	0.648783726	
	bloods_hemoa1c	6.48 (1.24)	6.22 (0.94)	0.294270708	
	bloods_insulinfast	19.07 (24.17)	13.42 (19.57)	0.260942546	
	bmi	32.12 (5.98)	31.23 (5.81)	0.512646653	
	cal_total	4.86 (0.70)	4.95 (0.83)	0.602123186	
	prom_sdscale	15.68 (6.88)	17.70 (6.94)	0.2059509	

Significance codes: $p < 0.001$ '***', $p < 0.01$ '**', $p < 0.05$ '*', and $p < 0.1$ '.'

Table 9-3 illustrates a comprehensive comparison between two groups—those receiving Continuous Positive Airway Pressure (CPAP) therapy and a Control group—over a span of 12

months. This comparison is delineated across several variables, primarily focusing on sleep metrics, blood parameters, and cardiovascular indicators. At the baseline, the significant difference ($p < 0.05$) is observed in the variables ahi_primary, bp24mapweight, bp24sbpweight, shq_gerd, and phq8_down_hopeless, indicating that before intervention, these parameters differ between the two groups. For instance, the average Apnea-Hypopnea Index (ahi_primary) is higher in the Control group compared to the CPAP group, suggesting a higher frequency of apnea and hypopnea episodes in the control group at baseline. At the 6-month checkpoint, notable improvements ($p < 0.05$) in the variables bp24sbpweight, semsa_oe, semsa_tse, prom_satisfied, and prom_refreshing are visible within the CPAP group. This suggests that half-year CPAP intervention may positively influence blood pressure, sleep experience, and satisfaction levels among patients. The 12-month data further substantiates the potential benefits of CPAP therapy. Significant improvements are seen in ahi_primary, several blood pressure variables (bp24mapweight, bp24sbpweight, bp24dbpweight), ess_total, semsa_tse, bp_norm, prom_refreshing, ess1, and ess3, indicating a sustained positive impact of CPAP on reducing sleep apnea symptoms, controlling blood pressure, and enhancing sleep experience over a longer term. Interestingly, the lvedd (Left Ventricular End-Diastolic Dimension) values, indicative of cardiac function, although not statistically significant, show a trend towards a smaller dimension in the CPAP group at 12 months, hinting at a possible protective cardiac effect of CPAP intervention.

9.3.4 Statistical Model Analyses

A more nuanced statistical analysis was introduced through Table 9-4, which reports the estimated fixed effects from the linear mixed model analysis for the outcome AHI across baseline and 12-month visit. This table aims to quantify the influence of various factors on the primary outcome, AHI, over time.

Table 9-4 Estimated fixed effects from the linear mixed model analysis for the outcome AHI across baseline and 12-month visit

Variables	Estimate	SE	p-value	CI lower	CI upper	Sig code
(Intercept)	16.7996	18.4927	0.3646	-19.6477	53.2469	
avgneckcm	0.4932	0.2481	0.048	0.0043	0.9821	*
avgwaistcm	-0.2748	0.116	0.0187	-0.5034	-0.0463	*
bmi	0.8032	0.275	0.0039	0.2611	1.3452	**
bp24mapweight	0.1079	0.0762	0.1582	-0.0423	0.258	
dianondipping	2.3362	1.8191	0.2004	-1.2491	5.9215	
ess1	3.493	1.4156	0.0144	0.703	6.283	*
ess3	4.385	1.5193	0.0043	1.3906	7.3794	**
ess_total	-0.9111	0.3979	0.023	-1.6954	-0.1268	*
phq8_bad_failure	2.6339	1.3466	0.0517	-0.02	5.2878	.
prom_satisfied	-2.5633	1.3181	0.0531	-5.1612	0.0346	.
prom_sdscale	-1.2756	0.4353	0.0037	-2.1335	-0.4177	**
prom_staying	3.4159	1.3273	0.0107	0.7998	6.0319	*
rand_treatmentarm	-2.5852	0.8315	0.0021	-4.224	-0.9464	**
semsa_oe_nmiss	0.3171	0.8474	0.7086	-1.3529	1.9872	
semsa_pr_nmiss	-1.8575	0.9221	0.0452	-3.6749	-0.0401	*
shq_typnightsleep	3.4431	1.5197	0.0245	0.448	6.4383	*
waso	0.0298	0.0327	0.3617	-0.0345	0.0942	
whiirs_total	-0.103	0.3559	0.7724	-0.8044	0.5983	
Time_12-Month	-16.2009	2.0755	0	-20.2915	-12.11	***

Significance codes: $p < 0.001$ '***', $p < 0.01$ '**', $p < 0.05$ '*', and $p < 0.1$ '.'

Table 9-4 demonstrates the findings derived from a linear mixed model analysis, targeting the primary outcome, which is the Apnea-Hypopnea Index (AHI) at two distinct time points: baseline and the 12-month visit. The table meticulously lays out how various factors have a bearing on the AHI. The estimated coefficients of fixed effects unveils the anticipated shift in AHI accompanying a one-unit augmentation in the respective variables. A salient point to notice is the positive association between avgneckcm (average neck circumference in cm) and AHI, signified by an estimate of 0.4932. Conversely, there's a negative association observed between avgwaistcm (average waist circumference in cm) and AHI, indicated by an estimate of -0.2748. A pronounced dip in AHI from baseline to the 12-month visit is manifested by an estimate of -16.2009 in the Time_12-Month variable. The "Standard Error (SE)" column portrays the precision of these

estimates, where lower SE values suggest more accurate estimates. The subsequent 'p-value' column is instrumental in identifying the statistical significance of these estimates. A p-value below 0.05 is indicative of statistical significance. Key variables such as avgneckcm, avgwaistcm, bmi, and ess1 exhibit p-values under 0.05, accentuating their statistical relevance. The Time_12-Month variable is particularly noteworthy with a p-value of 0, indicating a highly significant alteration in AHI across the span of the study. Furthermore, certain other variables like ess3, ess_total, prom_sdscale, prom_staying, and rand_treatmentarm also showcase statistical significance, as denoted by p-values less than 0.05. This outlines the substantial effects these variables have on the primary outcome, AHI, over the duration scrutinized in the study. To further assess the accuracy and performance of the linear mixed model, Figure 9-4 presents diagnostic plots. This figure aids in verifying the model's assumptions and its predictive performance, which is crucial for ensuring the robustness of the findings.

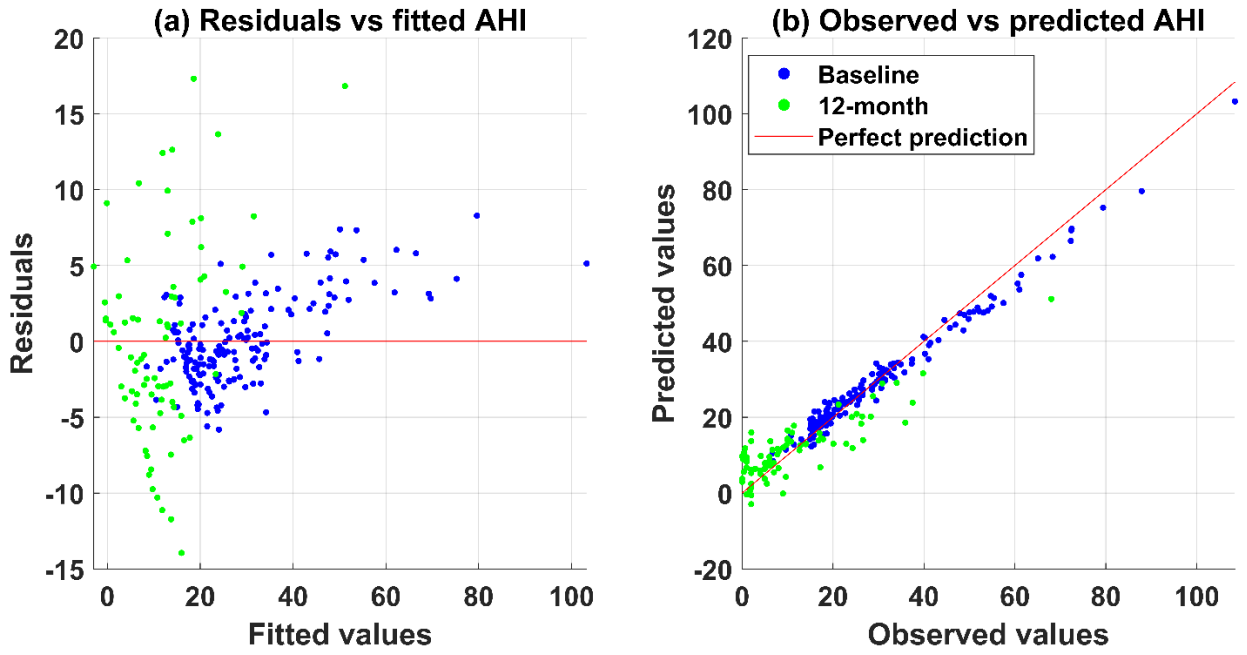

Figure 9-4 Diagnostic plots from the linear mixed effects model for the outcome AHI. Panel (a) displays the residuals versus the fitted values of AHI, aiding in assessing the model's assumptions and potential heteroscedasticity. Panel (b) presents a comparison between observed and predicted AHI values, showcasing the model's predictive performance.

In Figure 9-4, the model demonstrates a good fit, as seen in both panels, which is critical for accurately interpreting the effects of different treatments on AHI. Panel (a) specifically showcases a plot of residuals versus the fitted values of AHI. This plot is crucial for assessing the model's assumptions and investigating the presence of any heteroscedasticity. A clear pattern or trend would indicate a violation of assumptions, while a random scatter would suggest a good model fit. In this case, a generally random scatter is observed, underlining a good fit of the model. However, it's notable that the variance of residuals at the 12-month visit is significantly larger compared to the baseline. This increase in variance could be due to multiple factors such as changes in treatment effects, patient adherence, or other external variables over time. On the other hand, panel (b) illustrates a comparison between the observed and predicted AHI values, rendering a visual evaluation of the model's predictive performance. The closeness of the data points to this red line indicates a commendable predictive capability of the model, reinforcing the notion of a good fit. In conclusion, Figure 9-4 demonstrates a good fit of the linear mixed effects model to the data, aiding in a reliable interpretation of the treatment effects on AHI. However, the enlarged variance in residuals at the 12-month visit compared to the baseline points to potential areas for further investigation to understand the underlying causes of this discrepancy and improve the model's robustness over time.

The evaluation metrics for the model are depicted through various statistical values. The model exhibits an AIC of 2062 and a BIC of 2342.4, which are criteria for comparing model fit with a preference for lower values. The log-likelihood wasrecorded at -950.99, indicating the probability of observing the given set of data under the proposed model. The RMSE, a measure of the average discrepancies between predicted and observed outcomes, was found to be 4.3104. The model demonstrates a strong explanatory power with an $R^2_{marginal}$ of 0.8943, showcasing the

variance elucidated by the fixed effects solely. On the other hand, the $R^2_{conditional}$ is 0.8598, denoting the total variance explained by both fixed and random effects in the model. These R^2 values reveal a substantive understanding of the observed variance within the data, emphasizing the model's robustness in capturing the underlying relationships and trends in the dataset. Following the mixed model analysis, Table 9-5 provides the estimated coefficients of representative variables from the multiple linear regression model predicting OSA improvement. This table extends the predictive analysis, focusing on the OSA improvement outcome.

Table 9-5 Estimated coefficients of the representative variables from the multiple linear regression model predicting OSA improvement

Variables	Estimate	SE	p-value	CI lower	CI upper	Sig code
(Intercept)	382.5285	223.8335	0.1068	-91.9773	857.0343	
waso	-0.3149	0.1676	0.0786	-5.5314	6.28	.
blood_creactivepro	1.6435	0.6099	0.0159	-0.6702	0.0404	*
blood_fibrinactivity	-0.0888	0.0602	0.1593	-0.2152	0.504	
avgwaistcm	0.5406	0.2532	0.0485	-0.2186	0.5352	*
heartnondipping	-31.8574	6.2539	0.0001	0.3506	2.9364	***
ivs	-47.8434	24.4528	0.0681	-0.2163	0.0387	.
a4crveda	2.0634	1.3554	0.1474	0.0039	1.0773	
pvr	-0.2113	0.1233	0.1058	-0.8688	0.8785	
semsa_pr_nmiss	6.1835	3.3976	0.0875	-0.406	0.9602	.
vt_norm	3.7881	1.9312	0.0675	-0.6447	-0.0033	.
agg_phys	-0.7817	0.4832	0.1252	-11.1985	21.0618	
shq_trpills	73.5796	34.3964	0.0482	-45.1151	-18.5998	*
sf36_pcs	-6.6181	3.539	0.0799	-0.2428	0.4792	.
prom_restless	-10.8182	5.8547	0.0832	-99.681	3.9943	.
prom_sleeping	11.3087	6.2563	0.0895	-35.3083	69.579	.
prom_quality	-10.333	7.3288	0.1777	-0.6314	0.1851	
ess1	7.0423	5.0111	0.179	-0.179	0.2133	

Significance codes: $p < 0.001$ '***', $p < 0.01$ '**', $p < 0.05$ '*', and $p < 0.1$ '.'

Table 9-5 illustrates the estimated coefficients obtained from the multiple linear regression model employed to predict the degree of OSA improvement. Several variables emerged as significant predictors within this model. Notably, heart non-dipping showcased a notable negative

association with OSA improvement, as depicted by its coefficient estimate of -31.8574 ($p < 0.001$). This finding suggests that subjects with a lesser degree of nocturnal blood pressure reduction, known as non-dipping, are likely to exhibit lesser OSA improvement. Conversely, variables such as blood C-reactive protein, average waist circumference, and the use of sleep medications demonstrated a positive association with OSA improvement, with coefficient estimates of 1.6435 ($p < 0.05$), 0.5406 ($p < 0.05$), and 73.5796 ($p < 0.05$), respectively. These results hint at the potential influence of inflammatory markers, body adiposity, and the use of sleep medications on the improvement trajectory of OSA among subjects.

Furthermore, certain variables such as blood fibrin activity and pulmonary vascular resistance (PVR) did not exhibit significant associations with OSA improvement (p-values of 0.1593 and 0.1058, respectively). This could imply that these variables may not be pivotal in the prediction of OSA improvement within the context of this model. The model also exhibited a range of confidence intervals across different variables. Some variables, notably the intercept and sleep medications, displayed wide confidence intervals, indicating a higher degree of uncertainty surrounding these estimates. On the other hand, variables like heart non-dipping exhibited narrower confidence intervals, signifying a more precise estimate within this model. These varied confidence intervals highlight the diverse range of certainty associated with the estimated coefficients and underscore the need for cautious interpretation, particularly where wide confidence intervals are observed. Figure 9-5 renders diagnostic plots for the multiple linear regression model with the OSA improvement outcome.

In Panel (a) of Figure 9-5, it appears that the residuals are fairly randomly distributed, indicating the assumptions of homoscedasticity are reasonably met. On the other hand, Panel (b) portrays the relationship between observed and predicted values of OSA improvement. This plot

is quintessential for assessing the model's predictive accuracy. The data points are color-coded based on the four different treatment arms: CMT, CMT+ShamCPAP, CMT+ActiveCPAP, and CMT+ActiveCPAP+ME, which allows for a nuanced examination of how well the model performs within each treatment group. From the plot, it can be inferred that the model exhibits a decent level of accuracy in predicting OSA improvement across the different treatment arms, although there may be some variation in predictive accuracy among the groups. The model exhibited a substantial level of fit and predictability as reflected by the evaluation metrics. The AIC was recorded at 594.98 and the BIC at 737.95. The log-likelihood value obtained was -236.49. RMSE, which quantifies the prediction error, was noted at 11.45. Furthermore, a high R^2 value of 0.9072 was achieved, indicating that approximately 90.72% of the variability in the OSA improvement outcome was explained by the model. This set of evaluation metrics underscored the model's ability to robustly interpret the data and predict OSA improvement outcomes.

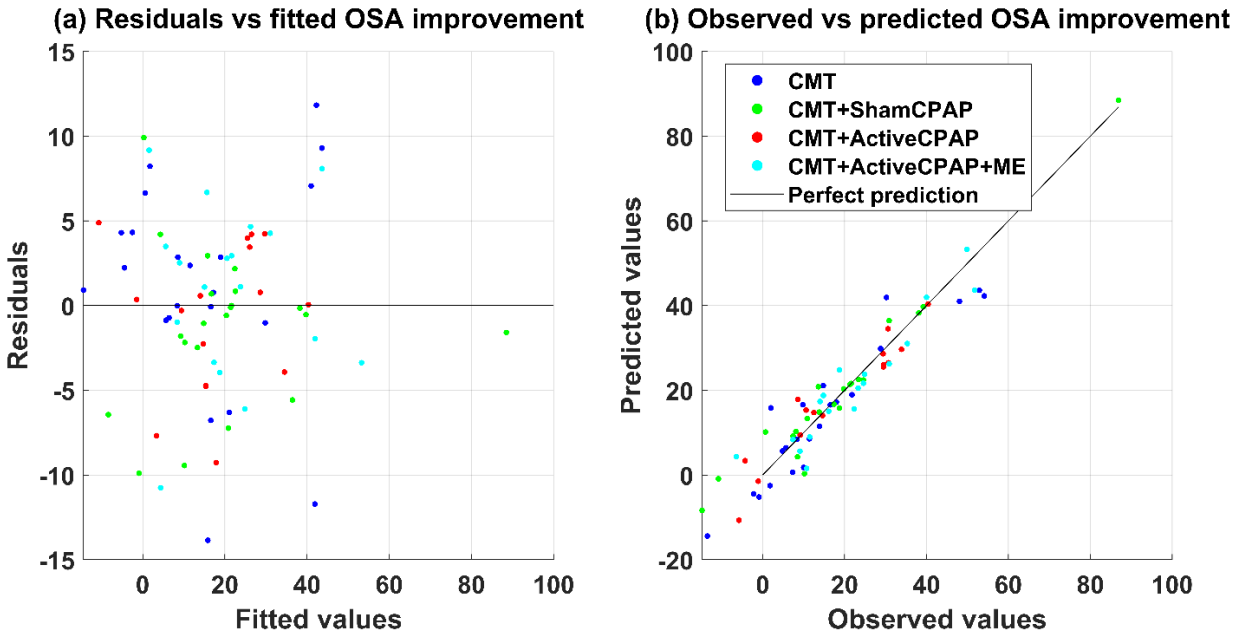

Figure 9-5 Diagnostic plots for assessing the multiple linear regression model fit with the OSA improvement outcome. Panel (a) depicts the residuals versus fitted values of OSA improvement, aiding in identifying any evident patterns or deviations from homoscedasticity. Panel (b) showcases the observed versus predicted values of OSA improvement,

9.4 Discussion

The primary objective of this study was to evaluate the effect of different treatment interventions on OSA improvement over a 12-month period. Key findings as demonstrated in Figure 9-1, Figure 9-2, and Figure 9-3, revealed discernible variations in sleep-related parameters and OSA improvement across different treatment arms. Specifically, treatment arms CMT+ActiveCPAP and CMT+ActiveCPAP+ME exhibited significant improvements in AHI and sleep efficiency compared to the control groups (CMT and CMT+ShamCPAP). The observed trends in sleep parameters and cardiovascular profiles across different treatment arms suggest a potential synergy between CPAP therapy and lifestyle modifications (CMT+ActiveCPAP+ME). These findings are consistent with previous research which posited that combining CPAP with other treatment modalities could yield enhanced therapeutic benefits in managing OSA [339]). Furthermore, the differential improvements in OSA across treatment arms, depicted through the frequency histogram in Figure 9-3, resonate with the assertion that individualized treatment plans could be pivotal in effectively managing OSA [340]. Moreover, the limited effect of certain variables like blood fibrin activity contradicted earlier studies [340], suggesting a need for further investigation into the multifaceted mechanisms underlying OSA improvement across diverse patient cohorts.

The in-depth assessment of the model's performance afforded critical insights into its predictive accuracy and the relevance of various predictive factors on OSA improvement. The R-squared value of 0.9072 signified that a substantial portion of the variance in OSA improvement could be explained by the model, indicating a high level of predictive accuracy. This high R^2 value not only underscores the model's capability but also provides a foundation upon which clinicians can understand the quantitative relationships between the predictors and OSA improvement. The

RMSE value of 11.45 further validated the model's precision, showing a reasonable level of error in predictions. This precise prediction is crucial in a clinical setting as it can aid healthcare providers in designing more effective treatment plans tailored to individual patient characteristics and needs. Moreover, the color-coded diagnostic plots illustrated in Figure 9-5 provided a clear visual validation of the model's performance across different treatment arms. The plots allowed for an easy evaluation of the model's residuals and predictive performance, showcasing its reliability and versatility in accommodating diverse treatment protocols. Such visual diagnostics are not only instrumental in ensuring the model's robustness but also enhance its interpretability for clinicians. The clear demarcation between treatment arms enabled a straightforward comparison, emphasizing the model's utility in evaluating and comparing the efficacy of different treatment protocols on OSA improvement.

The limitations of this study and the suggested future directions is paramount to understanding potential implications of the findings. One of the primary limitations was the restrictive demographic and clinical characteristic range of the participants, which may hinder the generalizability of the results to broader populations. A more diverse participant pool in future studies might unveil additional insights into the varying impacts of treatment on individuals with different demographic and clinical backgrounds. Moreover, the observational nature of the study could introduce confounding variables that may have influenced the outcomes. Although the employed statistical models attempted to control for known confounders, the possibility of residual confounding remains. Future studies employing randomized controlled trial designs could provide more robust evidence regarding causality and the effectiveness of different treatment protocols. The integration of advanced statistical techniques or machine learning algorithms in subsequent studies could potentially enhance predictive accuracy and provide a deeper understanding of the

complex relationships between the variables. The utilization of a larger dataset and the inclusion of additional predictive variables could also contribute to developing more comprehensive models that are capable of providing more nuanced predictions. Furthermore, as this study primarily focused on short-term OSA improvement, the long-term effects of different treatment protocols remain largely unexplored. Future research should endeavor to explore the longitudinal impacts of treatment, which could be instrumental in informing long-term clinical management strategies for OSA patients.

9.5 Conclusion

This study, focused on the adaptive therapeutic interventions for obstructive sleep apnea, unveils a potential pathway towards personalized treatment regimes, significantly impacting patient outcomes over time. The employment of robust statistical methods has illuminated insightful correlations between treatment modalities and varied OSA severity levels, showcasing the comparative efficacies of different treatment arms. The longitudinal analysis employing multiple linear regression and linear mixed-effects models establishes a solid groundwork for evaluating adaptive treatment regimes' long-term efficacy and safety. The findings underline the critical necessity for personalized treatment approaches in managing OSA, substantiated by the diverse patient responses to various treatment arms. The investigation into dynamical interactions between therapeutic interventions and patient outcomes highlights the potential of system control principles in enhancing OSA management. By adjusting treatment parameters dynamically in response to patient-specific requirements and disease progression, a significant stride towards more effective OSA management is achieved.

Chapter 10: Translational Research

In the complex landscape of disease diagnosis, the fusion of advanced technologies and domain-informed methodologies has the potential to revolutionize how we approach pressing health challenges. This chapter pivots from the theoretical models to the realm of real-world application by highlighting 2 translational research works, showcasing the impact of leveraging sensor-based data-driven modeling in contemporary healthcare. They include: (1) *Real-time Monitoring and Diagnosis of COVID-19 Using Magnetic Respiratory Sensing Technology and Machine Learning*, and (2) *Multifractality in Surface Potential for Cancer Diagnosis* [130]. Both these pioneering studies, detailed further in this chapter, underscore the potential of marrying technology with domain-specific insights in reshaping the future of disease diagnosis.

10.1 Real-Time Monitoring and Diagnosis of Covid-19 Using Magnetic Respiratory Sensing Technology and Machine Learning

The COVID-19 pandemic has posed an urgent need for developing reliable, noninvasive, contactless, portable, and cost-effective diagnostic tools that enable effective public health responses. Here, we create a novel platform for real-time tracking and diagnosis of COVID-19 and other respiratory-associated diseases by integrating an advanced magnetic respiratory sensing technology (MRST) with machine learning (ML). MRST can precisely measure and track breathing patterns and respiratory rates in real-time and under various circumstances using three distinct breath testing protocols: normal breath, breath-holding, and deep breath. Breath data collected on COVID-19 and healthy subjects using this monitor were used to train and validate our ML models. To ensure the robustness and reliability of our diagnostic system, we evaluated

various ML algorithms, such as support vector machines, random forest, ensemble models, and deep learning models, for their ability to diagnose COVID-19. This multi-model approach allows for a comprehensive performance comparison and provides the flexibility to deploy the most suitable model based on different healthcare scenarios and computational resources, balancing diagnostic accuracy with model interpretability. Various ML algorithms, such as support vector machines, random forest, and deep learning models, have been evaluated for their ability to diagnose COVID-19. The results obtained highlight the excellent capability of our diagnostic system in identifying respiratory abnormalities of patients infected by COVID-19, with greater than 90% accuracy. This newly developed sensor technology can be easily deployed in healthcare facilities and community settings for onsite and remote patient monitoring, which would significantly improve the overall healthcare system, and facilitate more effective public health measures to curb the spread of COVID-19 and its variants.

10.1.1 Introduction

Accurate and timely assessment of respiratory patterns plays a critical role in diagnosing and managing respiratory diseases, including coronavirus (COVID-19) and its variants [341]. Although the gold standard for COVID-19 diagnosis relies on PCR-based methods [342], these approaches are inherently limited by time-consuming procedures, logistical constraints, and the lack of continuous monitoring capabilities. Traditional methods for monitoring respiratory activities, such as spirometry, plethysmography, and impedance pneumography, are often invasive and inapplicable to continuous monitoring [343, 344]. These methods are also not desirable for large-scale deployment in community settings, which is essential in managing the global COVID-19 pandemic. Recent advances in noninvasive respiratory monitoring technologies, such as respiratory inductance plethysmography (RIP) [345], electrical impedance tomography (EIT)

[346], and magnetic respiratory sensing technology (MRST) [347, 348], have the potential to overcome these challenges and provide novel platforms for diagnosis, monitoring, and management of COVID-19 [349-351]. However, RIP calibration can be complex and user-dependent, which possibly causes inconsistent measurements. It is also susceptible to motion artifacts and may not accurately measure tidal volume or minute ventilation in all patients. Furthermore, the RIP system can be uncomfortable to wear for extended periods, making it less suited for continuous long-term monitoring. Regarding EIT technology, its main limitations are the requirement of expertise to use and interpret. It also suffers from limited spatial resolution making it difficult to precisely localize changes within the lungs and potential inaccuracies. MRST, however, holds the potential to overcome these limitations.

Unlike RIP and EIT, MRST is highly non-invasive and measures changes in the magnetic field due to respiratory movements without direct skin contact. The technology can deliver high-resolution, real-time data, providing intricate details of respiratory patterns for continuous monitoring [347, 348]. Moreover, the magnetic nature of the sensor makes it resistant to motion artifacts, which enhances its reliability in varied conditions. MRST can also be deployed in a user-friendly wearable format broadening its applicability and user convenience. Hence, MRST provides a more effective solution to many of the technical and practical challenges presented by RIP and EIT. In our previous studies, we have presented innovative advances towards the deployment of MRST for health monitoring [347, 348]. In the first study [347], we introduced a contactless magneto-LC resonance technology, a form of MRST, for real-time respiratory motion monitoring without any physical contact marking a significant step in the field. Further building on this, we proposed a magnetic respiratory sensor dedicated to human healthcare applications [348] paving the way for more personalized and effective monitoring solutions.

Respiratory patterns are crucial health indicators, with abnormalities often signaling disease [352]. This is particularly true for COVID-19 patients, who present signs such as elevated respiratory rate, reduced tidal volume, and irregular breathing rhythms [353-355]. Our research builds on these findings, leveraging MRST and machine learning (ML) [356] to track disease progression and possibly enable early diagnosis. MRST, with its high sensitivity in detecting respiratory movements, combined with ML's capabilities in analyzing large, complex datasets, offers a powerful tool for disease monitoring. Specifically, ML's predictive modeling and classification capabilities have shown promise in pattern recognition, notably in respiratory disease diagnostics and monitoring [124, 126, 357, 358]. Expanding on this concept, Phan et al. utilized ML in their innovative diagnostic device, which is designed to identify COVID-19 patients and determine infection severity [359]. This application illustrates the potential of ML in guiding treatment regimens under medical supervision.

Researchers have utilized ML algorithms to diagnose COVID-19 using diverse data types, including chest X-rays, CT scans, and electronic health records (EHR) [360-362]. These studies have demonstrated ML's promise in diagnosing COVID-19, even achieving comparable or superior performance to human experts. The successful application of ML extends to respiratory data for diagnosing and predicting the severity of diseases such as asthma [363], COPD [364], obstructive sleep apnea [124, 358], and pneumonia [365], further highlighting its feasibility and accuracy in identifying disease-specific features. Additionally, several relevant works have contributed to the development and application of ML in respiratory disease management, particularly COVID-19. Novel ML models predict respiratory failure in critically ill patients [366] and the risk of COVID-19 infection based on respiratory rate changes [367]. Automated monitoring of respiratory biomarkers and vital signs in home and clinical settings has been

explored [368], along with automatic COVID-19 diagnosis using respiratory sound data [369]. Non-invasive methods for determining respiratory rate from photoplethysmogram and electrocardiogram signals have also been developed [370]. Recognizing these advancements, it becomes clear that incorporating ML with RMST holds significant potential for revolutionizing real-time monitoring and diagnosis of respiratory diseases, including COVID-19. Therefore, this research aims to further explore and expand the potential of MRST coupled with ML for real-time monitoring and diagnosis of COVID-19.

10.1.2 Methodologies

The overview of the real-time monitoring and diagnosis system for COVID-19 using MRST and ML is summarized in Figure 10-1 below. Figure 10-1 provides a comprehensive overview of our study's design and the proposed COVID-19 monitoring and diagnosis system. It starts with the magnetic respiratory monitoring system (part a), which uses a Hall effect sensor to detect changes in the magnetic field due to respiratory movements. This setup ensures a non-invasive and accurate tracking of an array of respiratory patterns. The study progresses to the breath testing protocol (part b) used during data collection. This protocol consists of three types of breaths, namely, normal breath, breath holding, and deep breath. Incorporating these diverse types of breaths guarantees that a wide variety of respiratory behaviors are considered, providing a rich data set for further analysis. The acquired respiratory data are subsequently processed using specialized algorithms for signal processing and feature extraction (part c). These computational methods help to discern subtle yet diagnostically significant patterns within the collected data. Finally, these extracted features serve as input for the ML models (part d) that have been trained to diagnose COVID-19 based on these specific respiratory features.

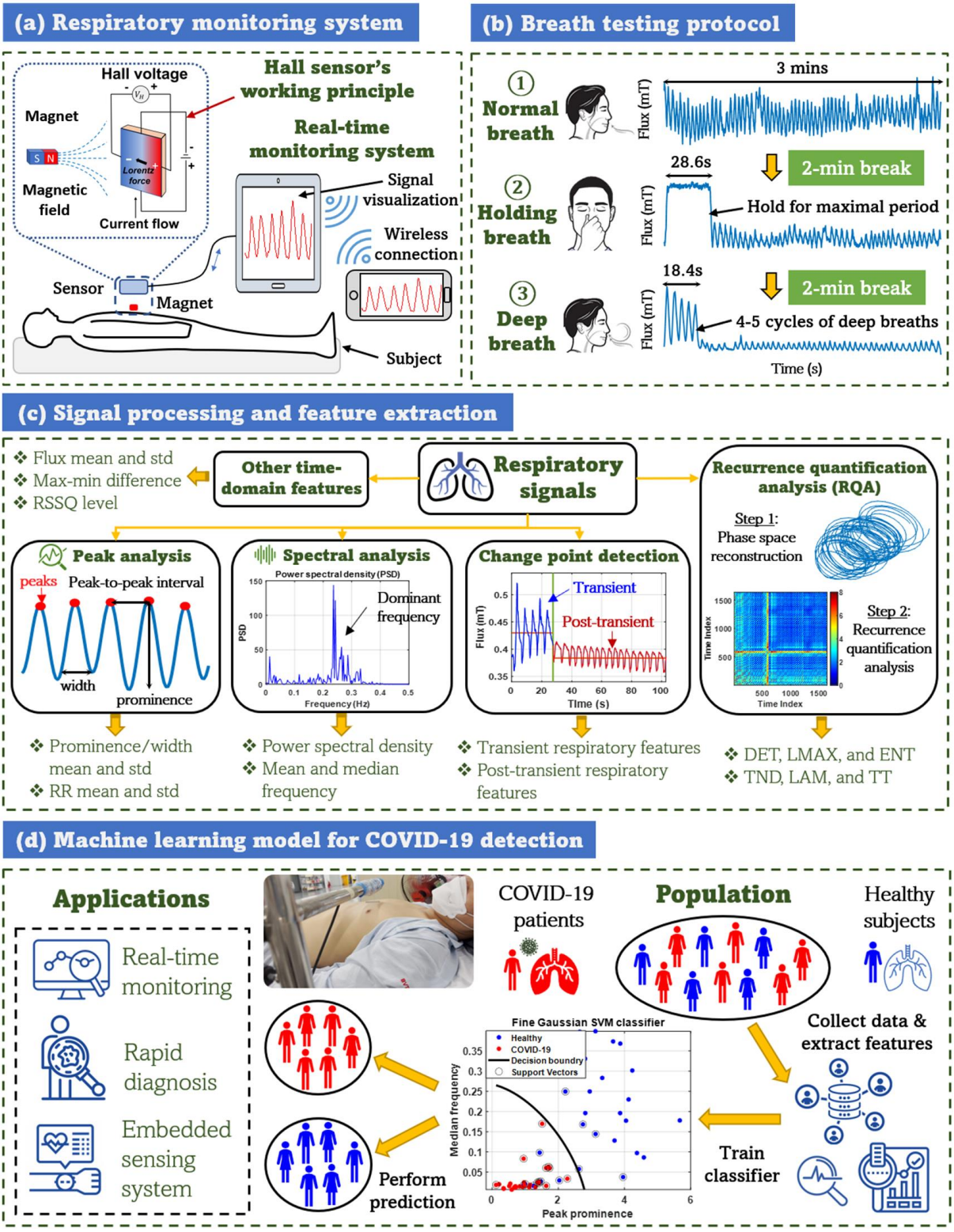

Figure 10-1 Overview of the study design and the proposed COVID-19 monitoring and diagnosis system. Parts (a) and (b) were derived from the following work [347, 348]

10.1.3 Results and Discussion

Our study involved a comprehensive collection of respiratory signal data from a total of 70 participants (33 COVID-19 patients and 37 healthy individuals). A more detailed summary of the participant characteristics can be found in Table 10-1.

Table 10-1 Characteristics of patients in the dataset

	COVID-19 patients	**Healthy subjects**
Participants, *n*	33	37
Age, *mean (std), years*	46.88 (13.64)	40.91 (16.88)
Gender		
Male, *n (%)*	14 (42.42)	13 (35.14)
Female, *n (%)*	19 (57.58)	24 (64.86)
BMI, *mean (std), kg/m^2*	22.93 (2.99)	22.03 (3.32)
Hospitalization days, *mean (std), days*	5.91 (4.83)	
Temperature, *mean (std), ℃*	37.05 (0.29)	
Diastolic blood pressure, *mean (std), mmHg*	80.87 (9.85)	
Systolic blood pressure, *mean (std), mmHg*	136.23 (24.55)	
COVID-19 symptoms		
Difficult breathing, *n, (%)*	16 (48.48)	
Cough, *n (%)*	20 (60.61)	
Fever, *n (%)*	15 (45.45)	
Fatigue, *n (%)*	9 (27.27)	
Muscle aches, *n (%)*	6 (18.18)	
Loss of taste, *n (%)*	3 (9.09)	
Sore throat, *n (%)*	3 (9.09)	
Running nose, *n (%)*	2 (6.06)	

Next, we present a comprehensive feature extraction analysis from the collected respiratory signal data as shown in Figure 10-2, which highlights a significant distinction in the respiratory patterns between healthy subjects and COVID-19 patients.

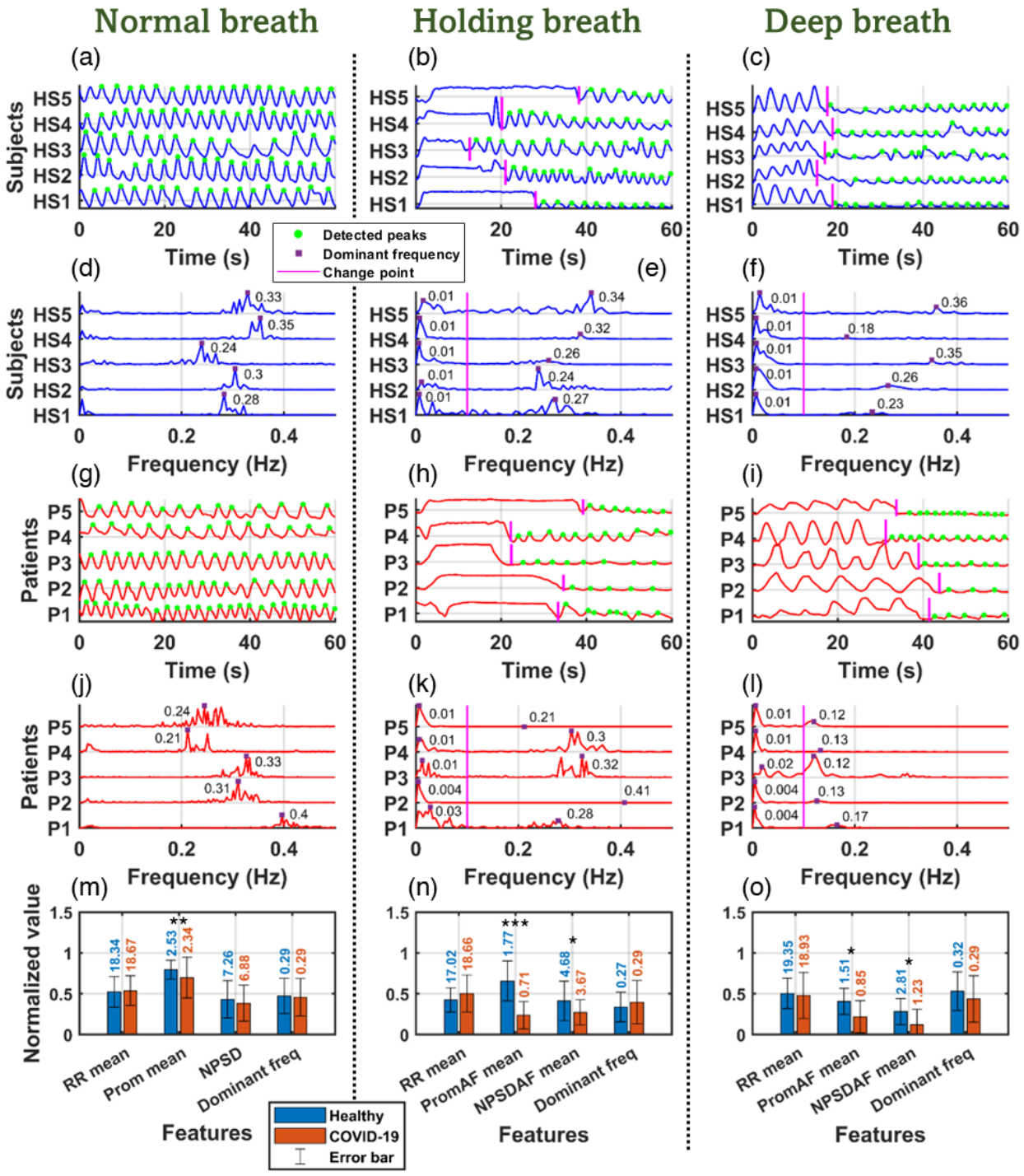

Figure 10-2 Analysis and feature extraction of respiratory signals for healthy subjects and COVID-19 patients. The significant differences in respiratory features between the two groups were tested using the two-sample t-test with confidence level $\alpha = 0.05$ and significance codes: $p < 0.001$ '***', $p < 0.01$ '**', $p < 0.05$ '*'

We analyzed four representative time-domain and frequency-domain features including the mean of the respiration rate (RR), mean prominence (Prom), normalized power spectral density (NPSD), and dominant frequency (Freq). The calculated mean values of these features were compared for both groups under each of the three breathing conditions. As depicted in the bar charts in panels 2m-2o, a significant contrast is observed in these features between the healthy and COVID-19 subjects. We performed a two-sample t-test to compare the differences in the respiratory features (RR, Prom, NPSD, Freq) between healthy subjects and COVID-19 patients across three breathing conditions: normal, holding, and deep breath with significant level $\alpha = 0.05$. According to the results for normal breathing, we observed significant differences in the prominence feature (Prom) between the two groups ($p = 0.0076$). For the other features including respiration rate (RR), normalized power spectral density (NPSD), and dominant frequency (Freq), the differences were not statistically significant ($p > 0.05$). For the holding breath condition, prominent differences were observed in the Prom ($p < 0.001$) and NPSD ($p = 0.0107$) features between the two groups. No statistically significant differences were found for RR and Freq features ($p > 0.05$). Finally, regarding deep breathing, we found significant differences in the Prom ($p = 0.0123$) and NPSD ($p = 0.0265$) features. Building on this, we employed recurrence quantification analysis (RQA), a non-linear analysis technique, to capture the dynamic patterns of the respiratory signals (see Figure 10-3).

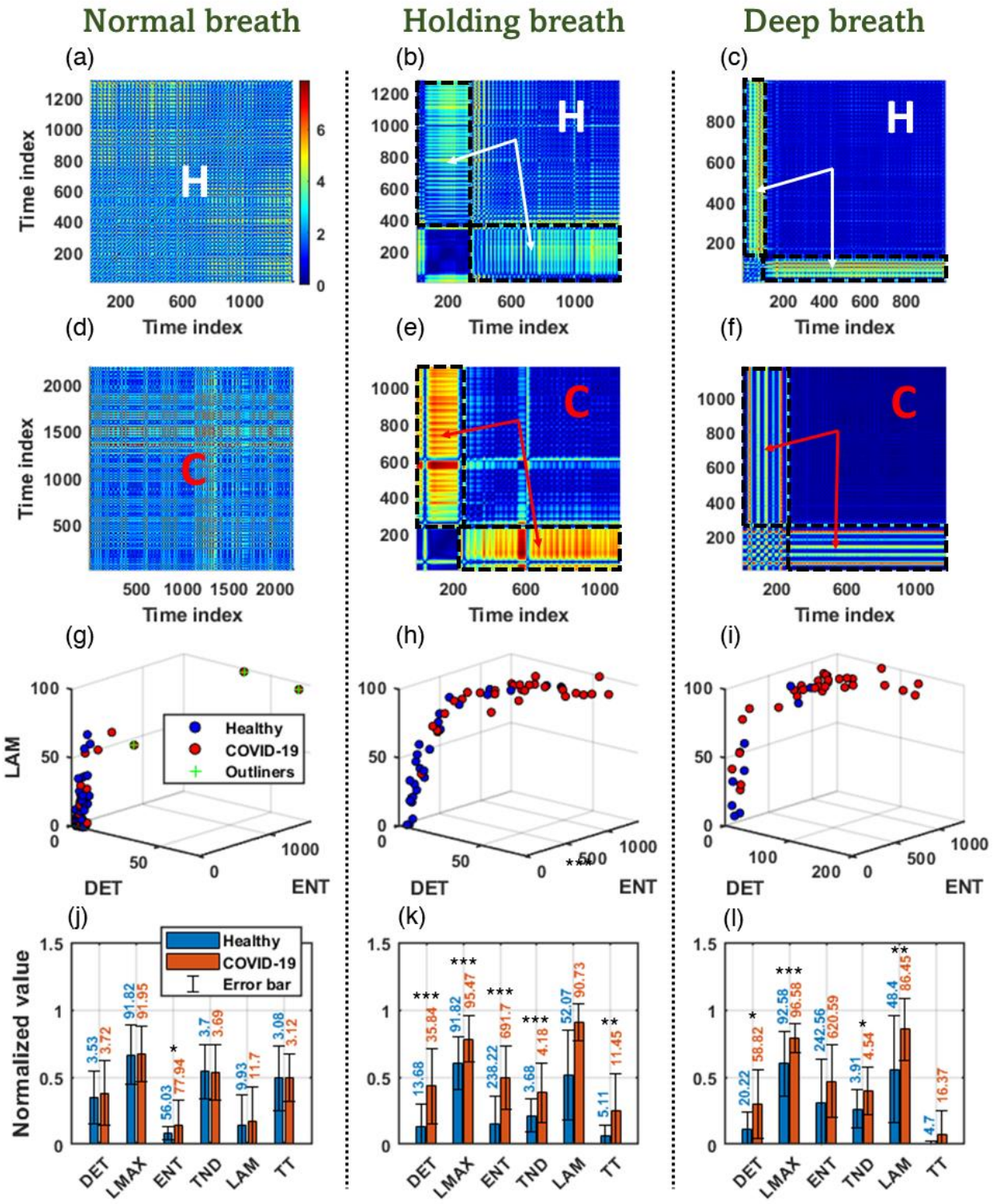

Figure 10-3 Analysis and feature extraction of respiratory signals for healthy subjects and COVID-19 patients using recurrence quantification analysis (RQA).

The RQA results showcased in Figure 10-3 highlight the distinctive recurrence plots for the two groups under the three different breathing conditions (panels (a)-(f)). Specifically, these plots visually demonstrate how certain regions—termed "fingerprint" regions—of the recurrence plots distinctly capture the complex respiratory dynamics associated with the COVID-19 patients, thus differentiating them from the healthy subjects. These "fingerprint" regions are characterized by 3 key RQA features: Determinism (DET), Entropy (ENT), and Laminarity (LAM). The 3D scatter plots of these features for the two groups (panels (g)-(i)) reveal clear differentiated clusters for holding breath and deep breath tests, thus indicating that these RQA features have substantial discriminatory power. However, A high degree of overlapping data points from normal breathing test was observed between the healthy and COVID-19 patients. While the disease COVID-19 does cause changes in respiratory function, these changes may not significantly affect the normal relaxed breathing state to a level where it creates separate clusters in the feature space.

As with our previous respiratory features, we used the two-sample t-test to compare the Recurrence Quantification Analysis (RQA) [371] features (DET, LMAX, ENT, TND, LAM, TT) between healthy subjects and COVID-19 patients across three breathing conditions. However, it is important to note that not all features exhibit significant differences in every breathing condition, once again demonstrating the intricate impact of COVID-19 on respiratory dynamics. The next step is to examine how these features contribute to the predictive performance of our ML models. Following the extraction and analysis of various features from the respiratory signals as detailed in the previous section, we proceeded to the feature selection phase to concentrate on the most significant attributes and reduce the dimensionality of our data. This process is comprehensively illustrated in Figure 10-4, showing the results for each of the three breathing tests: normal, holding, and deep breaths.

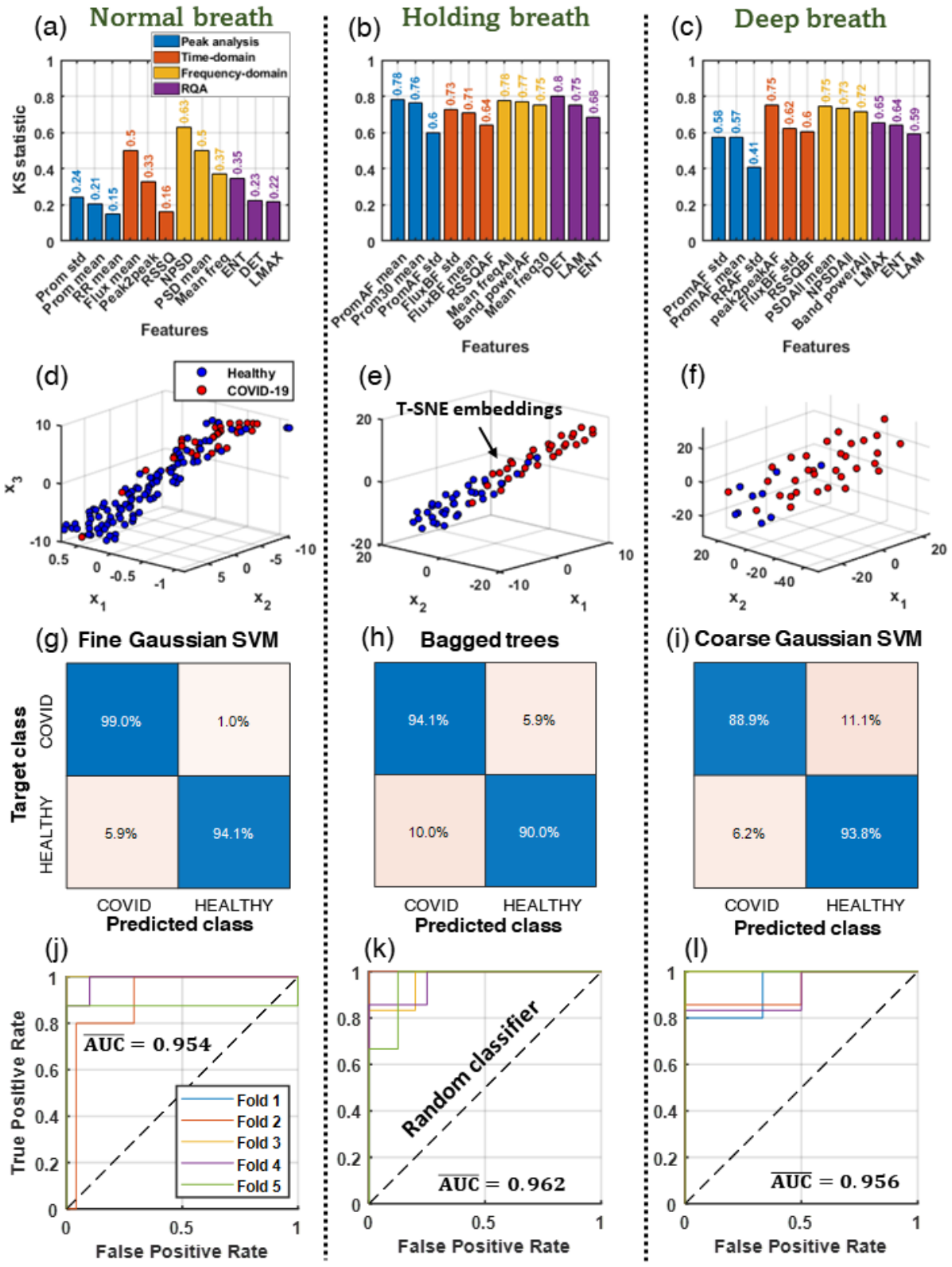

Figure 10-4 Feature selection, visualization, and performance evaluation of the ML model for COVID-19 diagnosis

We employed the Kolmogorov-Smirnov (KS) statistics (panels (a)-(c)) to rank features across the four feature groups we worked with: time-domain, frequency-domain, peak analysis, and recurrence quantification analysis (RQA). For the normal breath test, the most significant features from each group were Flux mean, NPSD, Prom std, and ENT. The holding breath test highlighted Flux BF std, Mean freqAll, Prom AF mean, and ENT as the most discriminative features. The deep breath test revealed peak2peakAF, PSDAll mean, Prom AF std, and LMAX as the most indicative features. This crucial step allowed us to streamline our focus to features that could meaningfully distinguish between healthy subjects and COVID-19 patients, echoing the findings of our initial feature extraction and analysis phase. The high-dimensional feature space was visualized using manifold learning with the t-SNE method (panels (d)-(f)). These three-dimensional plots effectively highlight the separation between healthy subjects and COVID-19 patients in the transformed feature space, reinforcing the discrimination power of the selected features. Following feature selection, ML learning models were trained and evaluated for their performance in classifying COVID-19 cases and healthy subjects. The confusion matrices (panels (g)-(i)) display the classification results for each breathing test, demonstrating high accuracy in discriminating between the two groups. The confusion matrices provide a comprehensive overview of the true positive, false positive, true negative, and false negative rates, which are essential metrics for understanding the model's performance. To further validate the robustness and diagnostic capability of our ML models, 5-fold cross-validation was performed and receiver operating characteristic (ROC) curves were plotted (panels (j)-(l)). The area under the curve (AUC) was reported as a quantitative measure of the models' classification performance. Particularly, for normal breathing, the best classifier was the Fine Gaussian SVM model [372], which achieved a sensitivity and specificity of 99% and 94.1% respectively, and an average ROC

curve area ($\overline{AUC}$) of 0.954 across 5-fold cross-validation. For holding breath, a Bagged Trees model [373] appeared to be the most proficient model with a slightly lower sensitivity of 94.1%, and specificity of 90%, and the $\overline{AUC}$ value was 0.962. Lastly, for deep breath, the Coarse Gaussian SVM model [372] obtained the best results, with a sensitivity of 99%, a specificity of 94.1%, and an $\overline{AUC}$ value of 0.956. These consistent findings across diverse breathing tests and models affirm the robustness of our feature selection and the efficacy of the resultant models in distinguishing between healthy subjects and COVID-19 patients.

The causal analysis was performed to further understand the link between respiratory patterns and the presence of COVID-19 in patients. A matching method was applied, which categorized patients into "treated" (those diagnosed with COVID-19) and "control" (healthy individuals) groups. Age, gender, and body mass index (BMI) were considered as confounders that could potentially influence both the respiratory patterns and the COVID-19 status. The comparison results between the unmatched and matched groups of healthy individuals and COVID-19 patients were summarized in Table 10-2. The standardized mean difference (SMD) in Table 10-2 suggests a significant reduction in the mean differences of age, gender distribution, and BMI between the healthy and COVID-19 groups post-matching, indicating that the matching process was successful in creating comparable groups.

Table 10-2 Pre-matching and post-matching comparison

	UNMATCHED			**MATCHED**		
	Healthy	**COVID-19**	**SMD***	**Healthy**	**COVID-19**	**SMD**
Participants, *n*	37	33		33	33	
Age, *mean (std)*	40.91 (16.88)	46.88 (13.64)	0.398	46.26 (10.84)	46.88 (13.64)	0.034
Male *n (%)*	13 (35.14)	14 (42.42)	0.262	16 (48.48)	14 (42.42)	< 0.001
BMI, *mean (std)*	22.03 (3.32)	22.93 (2.99)	0.293	23.47 (3.07)	22.93 (2.99)	0.031

*SMD = Standardized Mean Difference

The impact of COVID-19 on respiratory patterns, as assessed by our causal analysis, is illustrated in Figure 10-5. Panels (a)-(b) present the normalized values of six selected respiratory features for both the healthy and COVID-19 groups following the application of the matching method. These plots allow us to visually examine the distribution of the chosen features for each group and any apparent shift in these distributions that may indicate an effect of COVID-19. In panels (c)-(d), we transition from feature distributions to the quantification of the impact of COVID-19 on these features, as captured by the Average Causal Effect Percentages (ACEPs).

The primary purpose of this causal analysis is to quantitatively assess the impact of COVID-19 on specific respiratory patterns and to ascertain whether certain respiratory features can serve as distinguishable markers to differentiate between COVID-19 patients and healthy individuals based on their respiratory data. This is conducted with the aim of identifying potential pathophysiological changes in respiratory function associated with COVID-19. Our findings, as depicted in Figure 10-5, clearly illuminate the profound impact that COVID-19 can have on respiratory patterns, as evident from the high significance levels of the features. However, the nature of this impact is multifaceted and varies between different features and test conditions, highlighting the intricate nature of COVID-19's influence on respiratory patterns.

Specifically, for the normal breath test, as displayed in panel (c), the features Prom std, Flux mean, NPSD, and ENT demonstrated a very high significance level ($p < 0.001$), strongly supporting the observed causal effects of COVID-19. The alterations ranged from a minor decrease of -0.29% for LMAX, which was not statistically significant ($p > 0.05$), up to a substantial increase of 241.41% for ENT ($p < 0.01$), suggesting profound potential modifications in some respiratory patterns due to COVID-19. Moreover, the feature DET also indicated a significant causal effect with a 93.6% increase ($p < 0.05$), although with a lower degree of confidence. The holding breath

test results, represented in panel (d), demonstrated similar patterns with variations in significance. All tested features, Prom AF mean, Flux BF mean, Mean freq All, DET, LAM, and ENT, showed very high significance levels ($p < 0.001$), except for DET, which had a slightly higher p-value ($p < 0.01$). The effects ranged from a substantial decrease of -74.46% for Mean freq All to an increase of 109.39% for LAM.

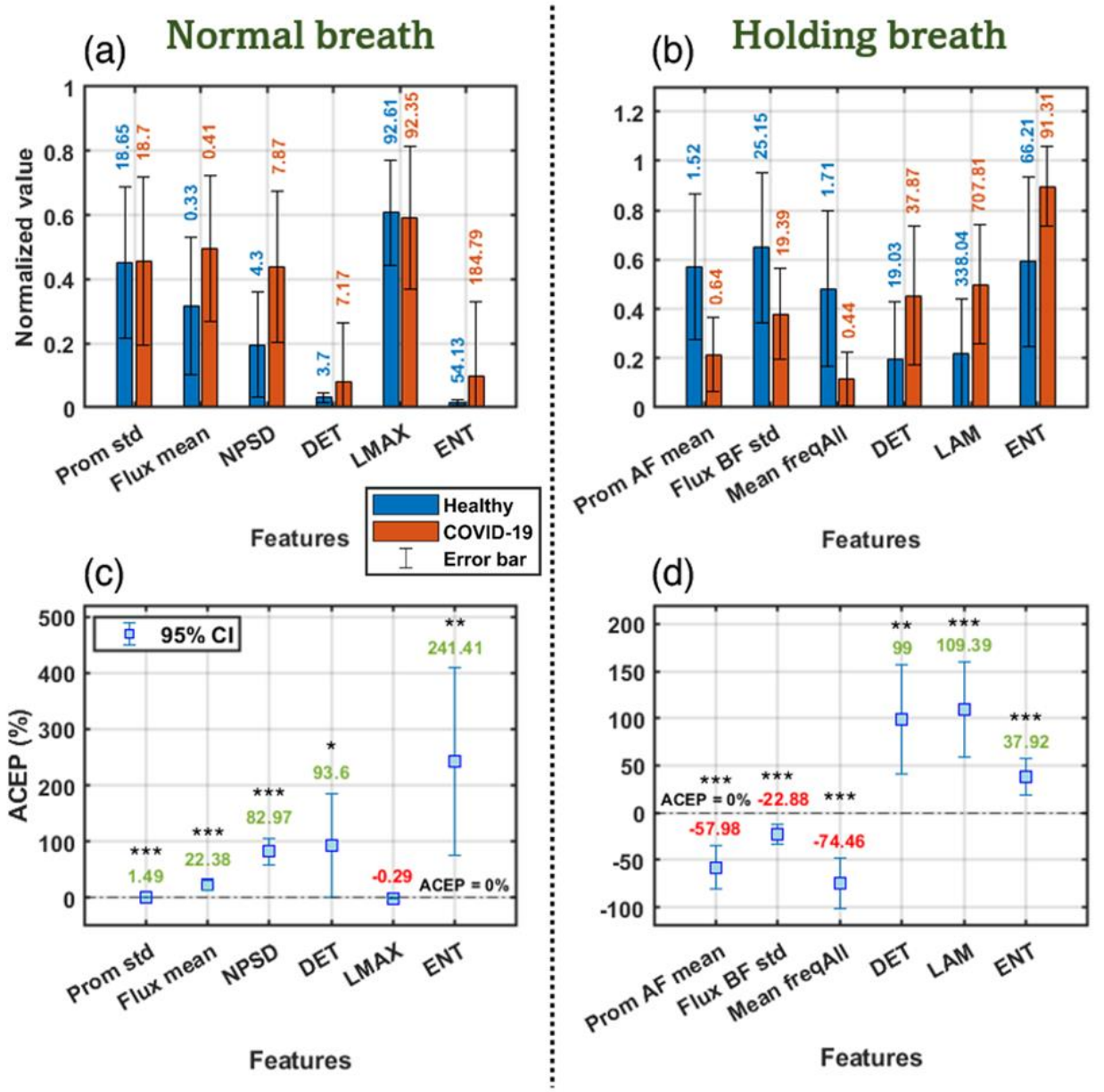

Figure 10-5 Causal analysis results illustrate the impact of COVID-19 on the respiratory patterns.

10.2 Multifractality in Surface Potential for Cancer Diagnosis [4]

Recent advances in high-resolution biomedical imaging have improved cancer diagnosis, focusing on morphological, electrical, and biochemical properties of cells and tissues, scaling from cell clusters down to the molecular level. Multiscale imaging revealed high complexity that requires advanced data processing methods of multifractal analysis. We performed label-free multiscale imaging of surface potential variations in human ovarian cancer cells using Kelvin probe force microscopy (KPFM). An improvement in the differentiation between nonmalignant and cancerous cells by multifractal analysis using adaptive versus median threshold for image binarization was demonstrated. The results reveal the multifractality of cancer cells as a new biomarker for cancer diagnosis.

10.2.1 Introduction

Ovarian cancer is one of the most common types of cancer among women worldwide [374, 375]. Morbidity and mortality of cancer are substantially decreased with early detection. Cytological screening tests have decreased mortality. However, these methods have insufficient sensitivity and are time-consuming in both analysis and training of professionals with subjective manual diagnosis. More accurate tests may substantially decrease the cost and patient inconvenience. Tumorigenesis is a complex process with an uncontrolled growth of cells that ignore apoptotic signals triggered by cell cycle dysregulation and modulate cell survival pathway signaling. This process involves remodeling of the extracellular matrix, accompanied by morphological and electrochemical changes in the plasma membrane. Nanoscale imaging

[4] This section was published in The Journal of Physical Chemistry B 2023, 127, 31, pp. 6867–6877. Permission is included in Appendix C.

techniques investigate these changes with a high spatial resolution to better understand tumorigenic mechanisms.

The plasma membrane resting potential was shown to undergo abnormal depolarization in cancer cells [376, 377]. Various mechanisms of membrane potential regulation have been investigated that involve cell signaling pathways mediated by the disrupted activities of ion channels, pumps, and transporters. The potential difference between tumor and paratumor was found for several types of cancer, and the resulting depolarization was correlated with metastasis [378]. The membrane potential has been identified as an important electrostatic marker that reflects the changes in cellular activities.

The common methods of membrane potential measurements based on electrodes and voltage-sensitive dyes have a lack of imaging and a limited spatial resolution, respectively. KPFM is a nanoscale electrostatic force imaging technique based on the contact potential difference (CPD) between a scanning probe tip and sample [379], which has been less commonly used for cell imaging. KPFM has a high spatial resolution of 10-50 nm [379], which is determined by the size of the tip apex and by the lift height. It was previously used in a variety of biomedical applications such as mapping the surface potential of biomolecules [380-382], including DNA [383, 384], proteins [385, 386], and plasma membrane of cells [387, 388], revealing biomolecular interactions at the single-molecule level [380, 389-391].

Nanoscale morphological measurements by atomic force microscopy (AFM) have previously been used for cancer detection [391-393]. AFM provides direct imaging of cell surface morphology with nanoscale resolution. Physical properties such as cell stiffness, adhesion, and elasticity were used to identify cancerous tissue [394, 395]. However, in some cases AFM morphological imaging cannot differentiate between normal and cancer cells, while adhesion maps

showed differences in fractality [396]. Fractal [397-402] and multifractal [403, 404] analyses were previously used for cancer diagnosis. Fractal geometry was used to describe the morphology of cancer cells and tissues by a single parameter, the fractal dimension, as a diagnostic biomarker [405, 406]. The change in fractal dimension or self-similar organization of surface morphology by malignant transformation can be quantified. Fractal dimension is suitable for the characterization of monofractal objects that have the same scaling exponent at different scales. However, a more complex organization (*e.g.*, cellular membrane) exhibits different fractal exponents at different scaling ranges resulting in several interwoven fractal sets, which are better described by the multifractal formalism [407, 408]. Fractal and multifractal analyses significantly improved the diagnostic efficiency of AFM imaging for cancer detection. However, the interpretation of complex morphologies was limited due to the lack of corresponding molecular information. KPFM is a nanoscale imaging technique based on molecular bioelectricity that provides deeper insights.

In this work, we performed the fractal and multifractal analysis of the morphological (AFM) and electrostatic (KPFM) images of the ovarian cancer cells. The high spatial resolution allows for probing a broad range of scales, covering more than three orders of magnitude, from < 10 nm to tens of micrometers. We used the box-counting method to determine the fractal dimensions with significant variations at different scaling ranges. We used the multifractal analysis for a more precise characterization of the scaling behavior, which showed a significant difference between the surface potential of the nonmalignant and cancer cells. We showed an improved efficiency of KPFM compared to AFM multifractality for cancer detection.

10.2.2 Methodologies

Figure 10-6 shows the typical examples of the optical (panels (a)-(b)), AFM (panels (c)-(d)) and KPFM (panels (e)-(f)) images of the SHT290 and ES-2 cells. The cancer detection

procedure involved the following steps. In step 1, the simultaneous AFM/KPFM image sampling was performed by scanning 3×3 μm^2 areas selected on the cytoplasmic and nucleus parts of the cells with 512×512 pixel density as described above (panels (i)). After normalization, in step 2, the image binarization was performed using either the adaptive threshold or median methods (panels (j)). In step 3, either the fractal or multifractal analysis was performed (panels (k)) that delivered parameters for the statistical analysis.

To convert 2D gray-scale AFM/KPFM images to binary images, we used two image binarization methods: adaptive and median thresholding. The adaptive image thresholding technique, i.e. the Bradley's method,[409] binarizes the gray-scale image using a locally adaptive threshold, estimated for each pixel utilizing the local mean intensity around the neighborhood of the pixel. The adaptive method uses a neighborhood size of ~$1/8^{th}$ of the image size (64 pixels). If the current pixel value is less than the computed threshold, then it is set to black (i.e., value 0), otherwise, it is set to white (i.e., value 1). The median thresholding image binarization uses the median value of all pixels as a hard threshold and sets the pixels whose values are larger than the median to black and to white otherwise.

The binarization-based box-counting method is simple and computationally efficient, which is particularly important when analyzing large datasets or multiple cell lines, as it reduces the processing time and computational resources required. The box-counting method has been widely used in previous studies to calculate the fractal parameters of biological samples, including cell analysis and cancer detection. Several studies in the field of cell analysis and cancer detection utilized image binarization for calculating the fractal dimension [397-402] and multifractal parameters [403, 404]. Fractal dimension is a measure of the space-filling capacity of a fractal object relative to its embedding space [410].

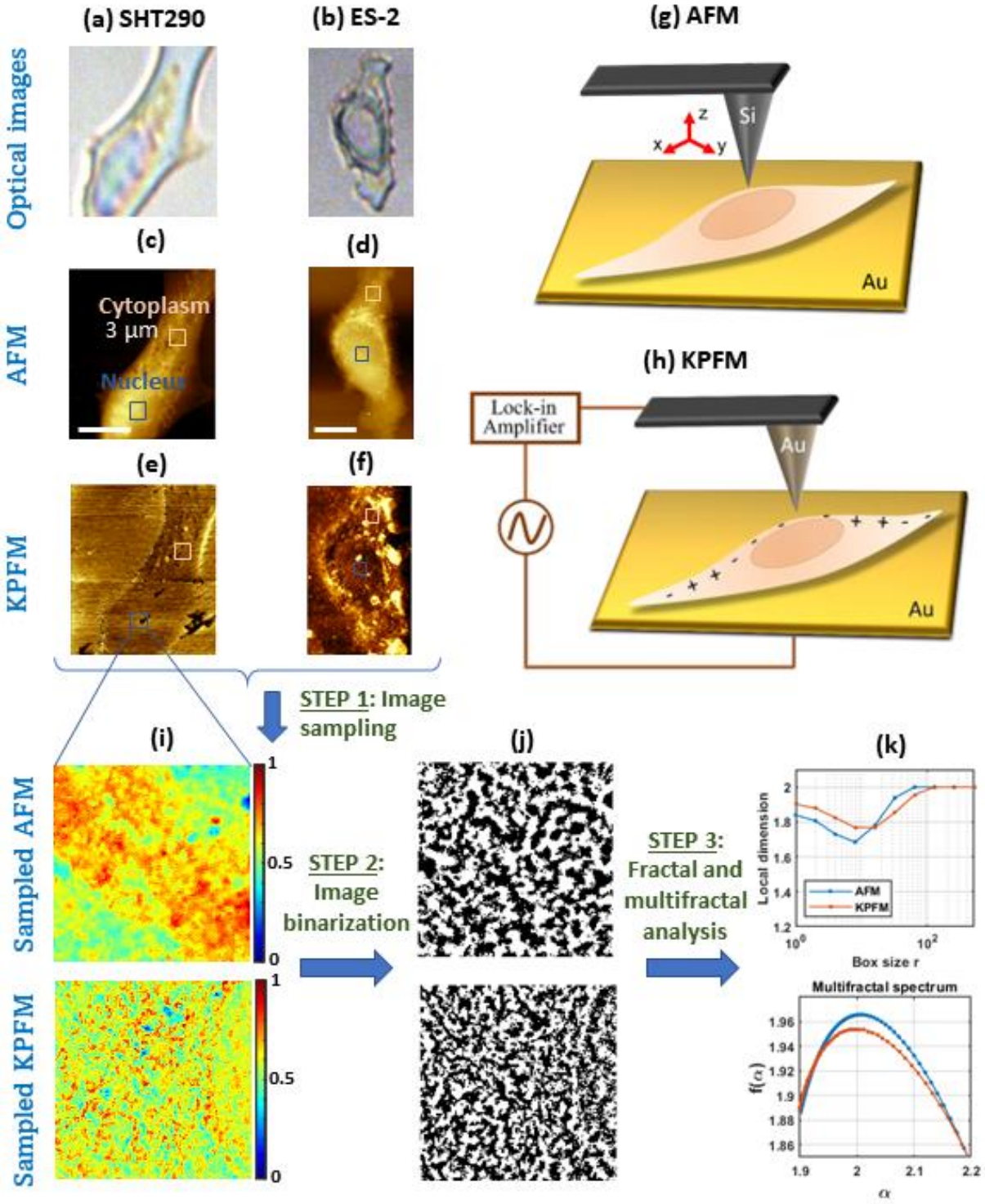

Figure 10-6 Illustration of the fractal and multifractal analysis procedure applied to AFM and KPFM images of nonmalignant (SHT290) and cancer (ES-2) cells. Optical (a,b), AFM (c,d), and KPFM (e,f) images. AFM (g) and KPFM (h) experimental schematic diagrams. (i-k) Three-step data analysis. Scale bars in (c), (d) are 10 μm

10.2.3 Results

Typical representative examples of the AFM/KPFM images of the SHT290 and ES-2 cells and their corresponding binarized images, local fractal dimensions, and multifractal spectra using the adaptive and median value thresholding methods are shown in Figure 10-7.

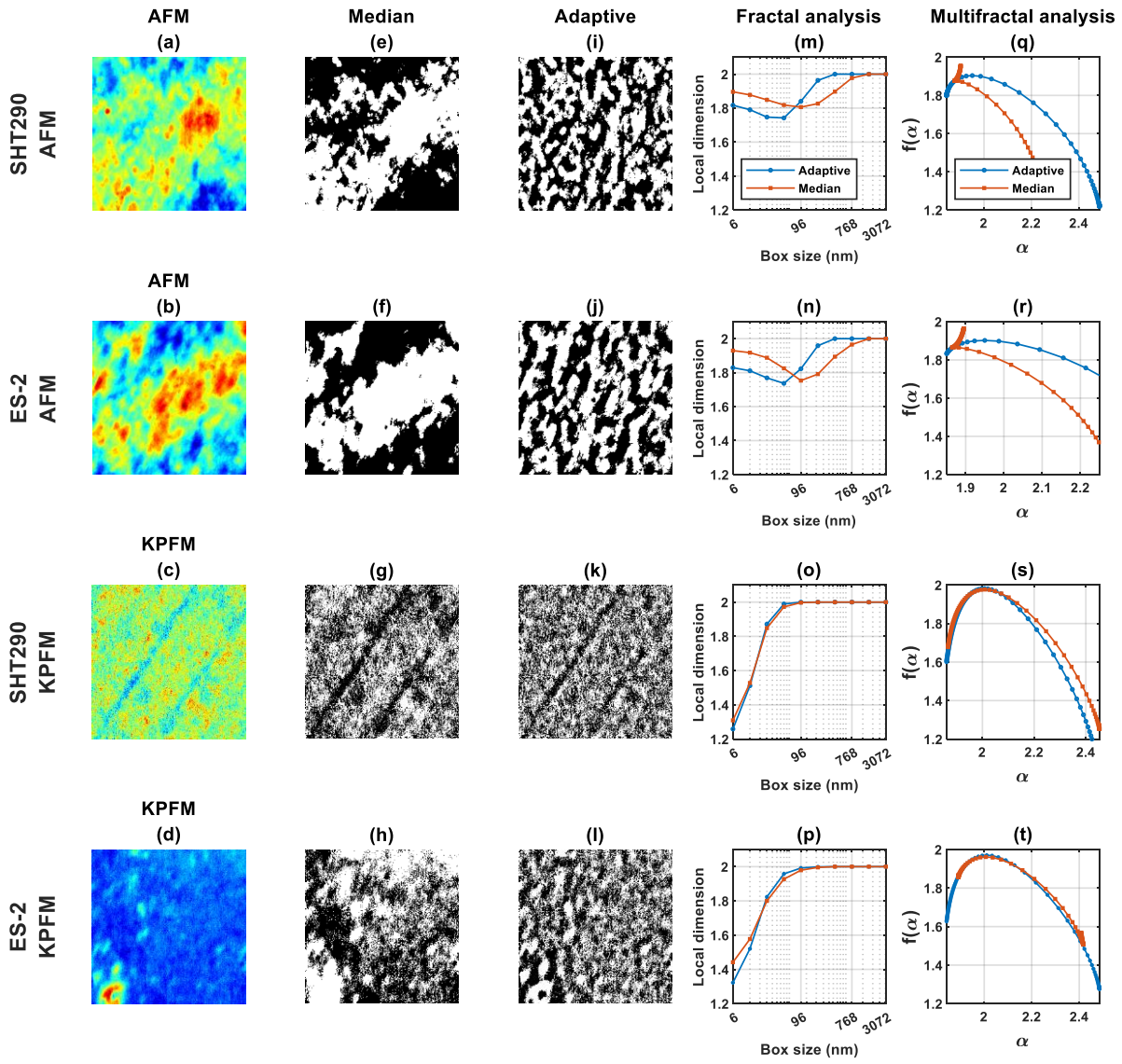

Figure 10-7 Typical representative examples of the AFM (a, b) and KPFM (c, d) images of SHT290 and ES-2 cells and their corresponding binarized images (e - l), local fractal dimensions (m - p), and multifractal spectra (q - t) using the adaptive and median value thresholding methods

10.2.3.1 Fractal Analysis

First, we present the results of fractal analysis of AFM and KPFM images using the box-counting method with adaptive thresholding. Figure 10-8 shows the dependence of the local fractal dimension D_f as a function of the box size r that was obtained from the slope of the tangent of $N(r)$ at each value of r estimated from the box-counting algorithm ($D_f = -d \ln N(r) / d \ln r$) [411] using adaptive and median thresholding methods.

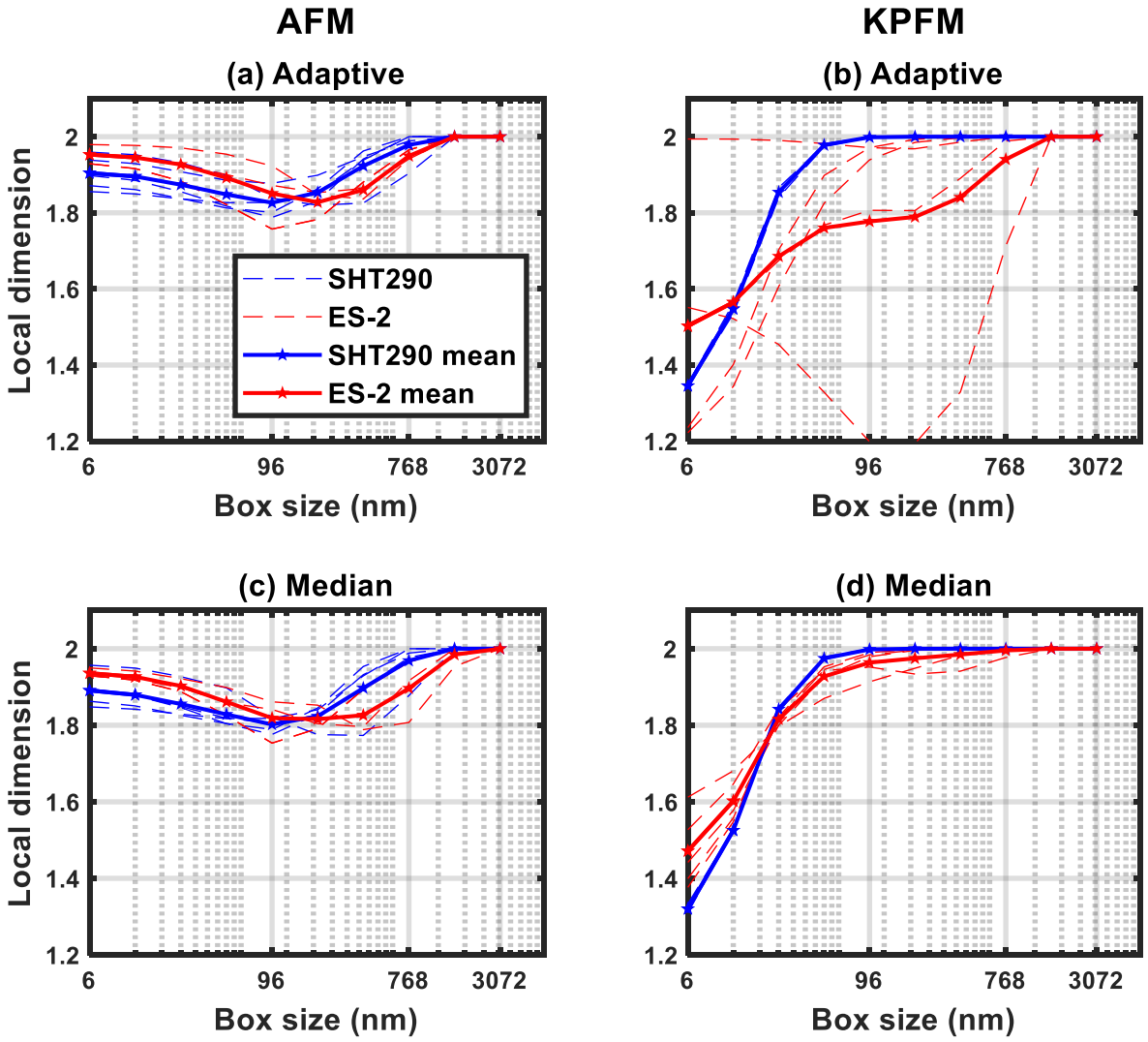

Figure 10-8 Fractal analysis of AFM and KPFM images using the box-counting method with adaptive and median thresholding. Dependence of the local fractal dimension D_f as a function of the box size for individual cells (thin dashed lines) and mean data (thick solid lines)

10.2.3.2 Multifractal Analysis

Next, we performed multifractal analysis of the same AFM and KPFM images that were used for the fractal analysis above. Figure 10-9 shows the Rényi spectra D_q, multifractal spectra $f(\alpha)$, and singularity width $\Delta\alpha$ obtained using the adaptive and median methods. Thick solid lines show the averages over all areas of the cells. Thin dashed lines show individual areas. The Rényi spectra show significant differences between the nonmalignant and cancer cells at D_1 and D_2 values (vertical dashed lines) in KPFM (panel (d)) compared to AFM (panel (a)) images. In these plots, positive q values accentuate denser regions, and negative q accentuate the less dense regions. The median method did not give satisfactory results for AFM images (panel (g)). However, it showed satisfactory results for the KPFM images (panel (j)), confirming the conclusion from the fractal analysis that surface potential is less sensitive than topography to random particles.

The multifractal spectra in Figure 10-9 provide direct information about the multifractality of AFM and KPFM images. The concave shape of the spectra indicates multifractality, which is quantified by the width $\Delta\alpha$. The wider spectra with the larger $\Delta\alpha$ correspond to higher multifractality. Multifractal analysis of the AFM and KPFM images showed qualitatively different results. While no significant difference was observed in the AFM spectra (panel (b)), there was a significant difference in the width $\Delta\alpha$ of ES-2 cells (red lines) having larger $\Delta\alpha$ than SHT290 (blue lines) as shown in panel (e). AFM spectra of both ES-2 and SHT290 cells showed small cell-to-cell variations in the whole α range in panel (b), while KPFM spectra showed larger variations for ES-2 compared to SHT290 at large α values (panel (e)).

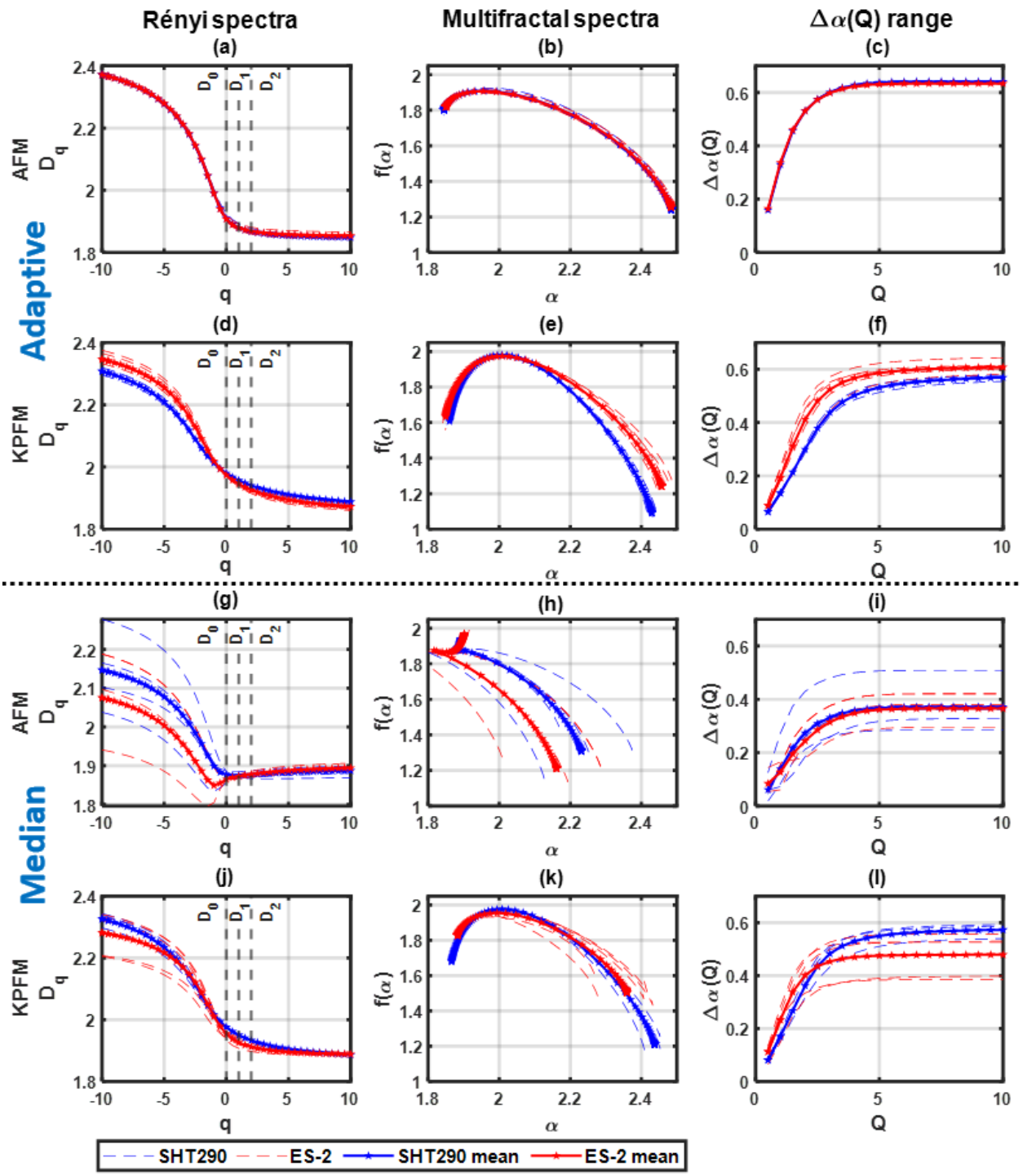

Figure 10-9 Rényi spectra, multifractal spectra, and singularity exponent range obtained from multifractal analysis of adaptive and median AFM/KPFM images of SHT290 and ES-2 cells for individual areas (dashed lines) and averages (solid lines). Vertical dashed lines mark the D_0, D_1 and D_2 values

Figure 10-10 shows the comparison of the multifractal parameters D_0, D_1, D_2, and $\Delta\alpha(4)$ from the cytoplasm, nucleus, and combined regions using the adaptive (adapt) and median (med) methods.

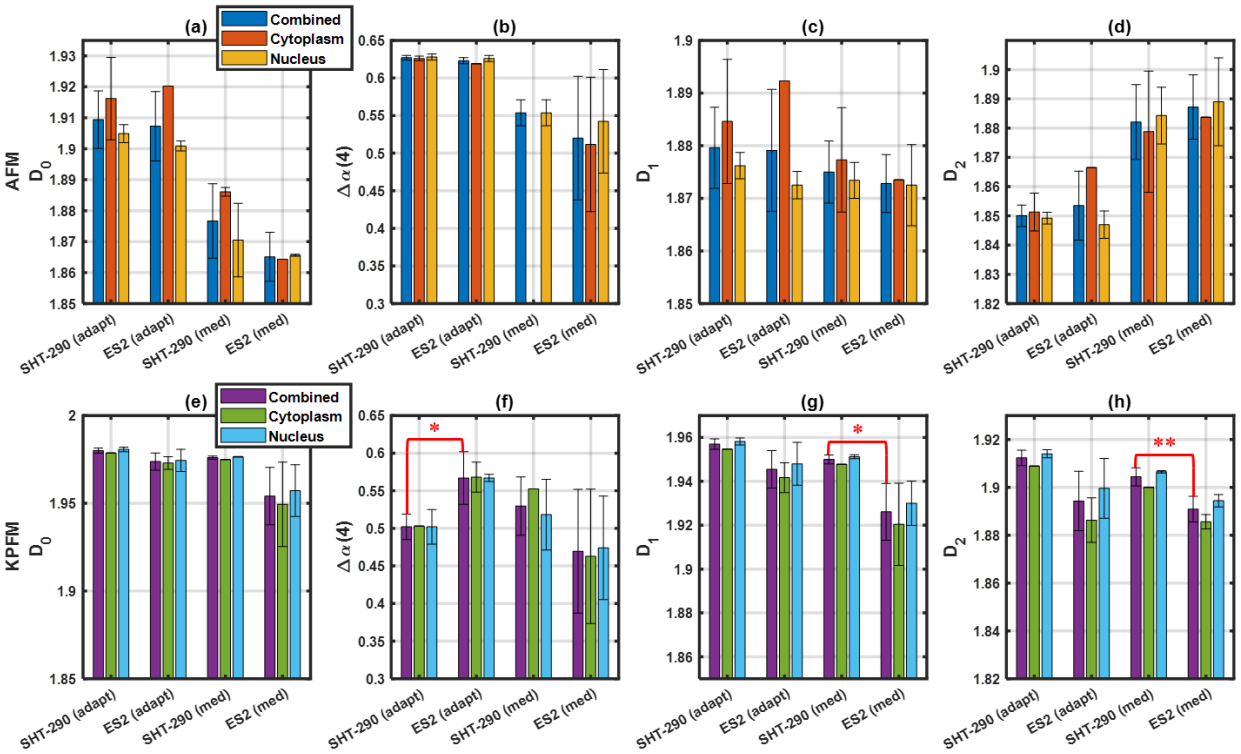

Figure 10-10 Comparison of the multifractal parameters D_0, D_1, D_2, and $\Delta\alpha(4)$ from the combined and separate cytoplasm and nucleus regions using adaptive (adapt) and median (med) methods

10.2.4 Discussion

The cell surface potential in our KPFM images is obtained from the CPD signals that are equal to the difference between the surface potential of the cell surface and the surface potential of the Au tip of the scanning probe [378, 387, 388]. Since the cells were grown on the atomically-flat Au substrates, we removed the contribution of the substrates to the cell surface potential by subtracting the CPD signal of the substrate from the CPD signal of the cells. Finally, in this work we do not consider the absolute values of the surface potential but, rather, its spatial fluctuations

with respect to the average value that determine the multifractality as a measure of the surface potential “roughness”. These spatial fluctuations are solely due to the spatial variations of the cell surface potential since the substate contribution was subtracted.

The observed differences between the morphological and surface potential measurements can be explained by the molecular structural and electrostatic changes of the plasma membrane. The morphological AFM and electrostatic KPFM are complementary imaging techniques that reflect different molecular mechanisms of tumorigenesis, such as the expression of membrane surface proteins, activity of ion channels and cytoskeletal reorganization. In the case of ovarian cancer cells (*i.e.*, nonmalignant-immortalized SHT290 and tumorigenic ES-2), KPFM provides significant differences in multifractality, while AFM does not. These observations agree with the molecular model of the ovarian cancer based on the overexpression of certain proteins such as the protein kinase C (PKC) family [412, 413]. PKC activation by Ca^{2+} may reflect the change in the surface potential, although binding of PKC to the inner side of the plasma membrane does not affect the membrane outer surface morphology [413]. The previous study indicated an overexpression of PKC proteins in ES-2 cells compared to SHT290 cells [413], utilizing Ca^{2+} in a complex signaling cascade involved in cancer progression [414]. Although the comparison of the SHT290 and ES-2 is not a standard cancer model, the previous work established the differences between the surfaces of the SHT290 and ES-2 cells with relevance to cancer progression by investigating the mechanism of cancer treatment by the inhibition of the PKC protein expression [413]. Using this model allows us to correlate the changes in the multifractality of the surface potential with the expression of PKC proteins that are different in these cell lines. These inner membrane proteins are not expected to influence the cell surface morphology but can influence the surface potential. These expectations were confirmed in the presented results.

Previous studies reported a depolarization of the surface potential of cancer cells and tissues [377, 378]. Although ES-2 cells exhibited a larger depolarization compared to SHT290, there was a larger variance among the cancer cells compared to their nonmalignant counterparts. The SHT290 and ES-2 cells were cultured in different growth media as described above that may have a possible influence on the cell surface, including cell morphology, adhesion, and surface potential [415]. Different media compositions provide varying amounts of nutrients, growth factors, and other essential components for cell growth and maintenance that can influence cell metabolism, membrane composition, and overall cell behavior [416]. We used the same growth media that were previously used for the comparison of the SHT290 and ES-2 cells [413].

The comparison between the nucleus and cytoplasm areas did not show any significant differences in both AFM and KPFM signals, indicating that the cell migration mechanisms of cytoskeletal reorganization do not contribute to the observed multifractality of the surface potential. For example, Ca^{2+} flickering was previously found to be predominant in lamellipodia at migrating cell edges [417]. High calcium microdomains were observed that could contribute to the spatial organization of the surface potential and polarity between the leading and trailing edges. However, our study included both cell edges and showed no significant differences, ruling out the calcium-based migration mechanism.

The main result of our work, that KPFM multifractality can distinguish between the nonmalignant and cancer cells but AFM multifractality cannot, may be due to the effect of KPFM, multifractality or both. We showed that it is a synergistic effect to both KPFM and multifractality by blurring the AFM images using a Gaussian filter and performing the multifractality hypothesis testing (not shown). We did not observe any significant differences in the multifractal parameters between SHT290 and ES-2 cells, and we conclude that the observed main effect is not due to the

spatial resolution difference between AFM and KPFM. Also, the results showed that the main parameter that distinguishes the nonmalignant and cancer cells was the width of the multifractality spectrum $\Delta\alpha(4)$) of KPFM images and not the other parameters such as the dimensions of KPFM or any AFM parameters. This confirms that multifractality of KPFM is the relevant biomarker based on the synergistic effect of both KPFM and multifractal analysis.

Note that the electrostatic properties of the cells are modified by the fixation procedure during sample preparation. However, although the fixation process can affect the biochemistry of the cells, it does not eliminate the differences in the surface potential between the nonmalignant and cancer cells. While the fixation process may have an impact on the electrostatic properties of the cells, it is still possible to distinguish between the nonmalignant and cancer cells based on the preserved differences in the surface potential. The surface potential of cells is due to the plasma membrane proteins, Na, K, Ca and other ions, phospholipids, and surface water molecules. Some of these are expected to change by the fixation process. However, there is still a ~ 5 – 10 nm surface water layer from the humidity in air. Additionally, KPFM measurements taken in air are a common practice for many studies investigating biological samples, as it allows for a stable and controlled environment for the measurements. For example, previous studies of isolated biomolecules in air and dried fixed cells in air using KPFM showed the CPD signals of dried biomaterials are close to the values obtained in liquid [388, 418].

10.3 Conclusion

Translational research stands at the nexus between fundamental research and patient care, endeavoring to streamline the path from bench to bedside. As underscored in Chapter 10, the integration of cutting-edge technology and domain-informed, sensor-based, data-driven modeling

holds the promise to redefine the trajectory of healthcare and its capacity to address pressing challenges. The showcased studies aptly capture the spirit of this potential:

- *The first study is Real-time Monitoring and Diagnosis of COVID-19 Using MRST and Machine Learning*. The dire necessity birthed during the COVID-19 pandemic brought to the fore the limitations of current diagnostic systems. However, it also ushered in an era of innovation, as observed in our exploration. Combining MRST's precision in recording respiratory metrics with machine learning's analytical might, we birthed a diagnostic tool that's non-invasive, reliable, and critically timely. Its real-world applicability is profound, especially in the context of swift and informed decision-making during pandemic scenarios.
- *The second study is Multifractality in Surface Potential for Cancer Diagnosis*. Cancer, one of humanity's oldest adversaries, requires a nuanced and multi-faceted approach for its early detection and treatment. Through our groundbreaking work with KPFM and multifractal analysis, we not only introduced a potential new biomarker for cancer detection but also highlighted the transformative possibilities that emerge when traditional diagnostics are augmented with advanced technologies.

These investigations collectively spotlight the essence of translational research: pioneering solutions that hold tangible promise for immediate real-world application.

Chapter 11: Conclusions and Future Directions

The journey embarked upon in this dissertation sought to understand, elucidate, and ultimately improve methodologies and applications within the domain of complex system modeling and analysis. At its onset, the fundamental objectives were identified, not merely as academic exercises but as pressing requirements to tackle real-world challenges, particularly in the sectors of healthcare and industry. These objectives were translated into research questions, and various methodologies were adopted, tested, and refined to address them. This chapter serves a twofold purpose. First, it acts as a bridge, succinctly connecting the core themes, results, and insights explored in the preceding chapters, ensuring a holistic understanding of the research's trajectory. The intention is to provide a cohesive summary that encapsulates the essence of the research's depth and breadth. Secondly, this chapter endeavors to gaze forward, pointing towards the horizons that beckon for further exploration. The dynamism of the fields we've delved into guarantees that today's conclusions could be tomorrow's starting points. Thus, by assessing both the accomplishments and the avenues yet to be treaded, this chapter sets the stage for an integrative conclusion and a glimpse into potential future endeavors.

11.1 Key Conclusions

Over the course of this dissertation, we traversed a multi-dimensional landscape, integrating methodologies, theories, and applications to extract meaningful insights. Herein, we summarize some of the pivotal conclusions:

- *The first is complex system modeling and pathogenesis dynamics*. In Chapter 4, the work centered around probabilistic domain-knowledge modeling to predict acute-onset

dynamics. We conclusively demonstrated that our methodology holds significant advantages in terms of accuracy and computational efficiency over traditional models. Integrating domain-knowledge into probabilistic models helps in assimilating past knowledge while being adaptive to new data, leading to more precise forecasting of disease onsets.

- *The second is understanding corrosion growth in infrastructure*. Chapter 5 provided insights into the latent variables influencing corrosion in oil and gas pipelines. It became evident that applying physics-informed models allows for a richer understanding of underlying processes, thus enhancing predictive accuracy. This understanding is crucial, not just academically, but also from an industrial perspective, where early detection and mitigation of corrosion can save vast amounts of resources and prevent catastrophic failures.
- *The third is intermittent dynamics and sleep apnea*. The foray into the intricacies of obstructive sleep apnea in Chapter 6 emphasized the value of noise-robust spectral analysis. We concluded that traditional methods might not always capture the nuances of intermittent dynamics effectively. The proposed Koopman Spectral Analysis emerged as a more robust method, allowing for better insights into pathophysiological processes, particularly in noisy environments.
- *The fourth is turbulence in intracranial aneurysms*. Our exploration in Chapter 7 revolved around the critical issue of detecting transitions to turbulence in intracranial aneurysms. The conclusion was clear: optimized dynamic mode decomposition provides a more accurate and earlier detection than conventional methods. Such timely detection is pivotal in medical scenarios, potentially averting severe health implications.

- *The fifth is sampling strategies and system robustness*. Chapter 8's insights on multi-scale complex systems reaffirmed the value of adaptive strategies. We concluded that reinforcement learning models, when suitably trained, can autonomously determine optimal data sampling strategies, thereby enhancing the robustness and efficiency of system models, especially in noisy settings.
- *The sixth is sleep disorders and cardiovascular outcomes*. Our venture into therapeutic interventions in Chapter 9 led to the conclusion that systems control theory, combined with longitudinal data analysis, offers a refined understanding of the interplay between sleep-disordered breathing and cardiovascular outcomes. The analytical plans provided concrete pathways for unraveling the complexities of this relationship.
- *The last is translational research impacts*. Finally, Chapter 10 underscored the power of cutting-edge technology in real-world disease diagnosis scenarios. The magnetic respiratory sensing technology and machine learning's synergy showcased that advanced, non-invasive diagnostic tools have a pivotal role in modern healthcare, especially in pandemic scenarios. On a parallel note, the potential of multifractality as a novel biomarker in cancer diagnosis represents a transformative step forward.

Collectively, these conclusions not only validate the methodologies and approaches adopted throughout the dissertation but also underscore the vast potential they hold for real-world applications.

11.2 Future Directions

The research journey undertaken in this dissertation not only establishes foundational methodologies and insights but also illuminates paths for future exploration. As we reflect on the results and contributions, several avenues of future research become evident:

- *The first is enhanced system modeling*. While Chapter 4 delved into probabilistic domain-knowledge modeling, the approach can be extended to accommodate even more complex systems. The framework can be augmented with real-time adaptive mechanisms to ensure models stay current as systems evolve. The potential of combining this with other emerging techniques, such as neural symbolic integration, can be explored for a more holistic modeling approach.
- *The second is smart infrastructure maintenance*. Building upon the insights from Chapter 5 regarding corrosion growth, there's an opportunity to develop predictive maintenance tools that anticipate structural vulnerabilities in oil and gas pipelines. These tools can leverage real-time monitoring combined with advanced analytics to proactively mitigate risks, leading to more efficient and safer infrastructure management.
- *The third is personalized healthcare insights*. The methodologies from Chapters 6 and 7 concerning sleep apnea analysis and aneurysm detection can be further fine-tuned. Incorporating wearable health technology data can result in a comprehensive, personalized patient analysis, enhancing diagnostic precision and tailoring treatments to individual health profiles.
- *The fourth is scalable reinforcement learning frameworks*. Chapter 8's reinforcement learning approach can be expanded for larger, more intricate systems. There's potential to integrate the method with other machine learning paradigms, exploring hybrid models capable of handling greater complexity and achieving even more accurate system representations.
- *The fifth is advanced diagnostic platforms*. Following Chapter 10's work on disease diagnosis, the integration of advanced sensing technologies with other modalities like

infrared or ultrasonic techniques can be examined. Such multimodal diagnostic platforms can offer richer data sets and potentially higher diagnostic accuracy.

- *The last is cross-disciplinary collaborations*. Finally, the methodologies and findings of this dissertation beckon collaborations across different scientific and engineering domains. By marrying the strengths of diverse fields, we can propel our understanding of complex systems and drive even more impactful innovations.

In essence, while this dissertation provides valuable contributions, it also underscores the ever-evolving nature of research. Each chapter's insights inspire new questions and potential pathways, ensuring the journey of exploration and discovery remains an ongoing endeavor.

11.3 Closing Remarks

As we draw this dissertation to a close, it's essential to acknowledge that the endpoint of one research journey often signals the beginning of many others. The investigations, findings, and methodologies detailed within these pages are not merely conclusions but stepping stones, laying a foundational framework for future inquiries and endeavors. The path of scientific exploration is inherently iterative, each discovery opening doors to a myriad of new questions, each challenge surmounted giving rise to more sophisticated problems. This is the beauty and complexity of research, a dynamic interplay of knowledge acquisition and persistent curiosity. The insights gathered from this dissertation offer both a culmination of years of dedicated work and a blueprint for future explorations. While we've delved deep into system dynamics, novel methodologies, and their potential real-world applications, the vast realm of what remains unknown is awe-inspiring. However, it is this very unknown that fuels the passion for discovery. It beckons researchers to look beyond the present, to imagine possibilities, and to push the boundaries of understanding further than ever before.

References

[1] D. Laney, "3D data management: Controlling data volume, velocity and variety," *META group research note,* vol. 6, no. 70, p. 1, 2001.

[2] C. Cortes and V. Vapnik, "Support-vector networks," *Machine learning,* vol. 20, pp. 273-297, 1995.

[3] J. R. Quinlan, "Induction of decision trees," *Machine learning,* vol. 1, pp. 81-106, 1986.

[4] L. Breiman, "Random forests," *Machine learning,* vol. 45, pp. 5-32, 2001.

[5] D. E. Rumelhart, G. E. Hinton, and R. J. Williams, "Learning representations by back-propagating errors," *nature,* vol. 323, no. 6088, pp. 533-536, 1986.

[6] Y. LeCun, Y. Bengio, and G. Hinton, "Deep learning," *nature,* vol. 521, no. 7553, pp. 436-444, 2015.

[7] A. Krizhevsky, I. Sutskever, and G. E. Hinton, "ImageNet classification with deep convolutional neural networks," *Communications of the ACM,* vol. 60, no. 6, pp. 84-90, 2017.

[8] S. Hochreiter and J. Schmidhuber, "Long short-term memory," *Neural computation,* vol. 9, no. 8, pp. 1735-1780, 1997.

[9] T. Mikolov, I. Sutskever, K. Chen, G. S. Corrado, and J. Dean, "Distributed representations of words and phrases and their compositionality," *Advances in neural information processing systems,* vol. 26, 2013.

[10] F. Doshi-Velez and B. Kim, "Towards a rigorous science of interpretable machine learning," *arXiv preprint arXiv:1702.08608,* 2017.

[11] S. Barocas and A. D. Selbst, "Big data's disparate impact," *California law review*, pp. 671-732, 2016.

[12] D. Castelvecchi, "Can we open the black box of AI?," *Nature News*, vol. 538, no. 7623, p. 20, 2016.

[13] M. T. Ribeiro, S. Singh, and C. Guestrin, "" Why should i trust you?" Explaining the predictions of any classifier," in *Proceedings of the 22nd ACM SIGKDD international conference on knowledge discovery and data mining*, 2016, pp. 1135-1144.

[14] S. M. Lundberg and S.-I. Lee, "A unified approach to interpreting model predictions," *Advances in neural information processing systems*, vol. 30, 2017.

[15] C. Rudin, "Stop explaining black box machine learning models for high stakes decisions and use interpretable models instead," *Nature machine intelligence*, vol. 1, no. 5, pp. 206-215, 2019.

[16] J. Pearl, "Bayesian networks," 2011.

[17] A. Krizhevsky, I. Sutskever, and G. E. Hinton, "Imagenet classification with deep convolutional neural networks," *Advances in neural information processing systems*, vol. 25, 2012.

[18] D. Koller and N. Friedman, *Probabilistic graphical models: principles and techniques*. MIT press, 2009.

[19] H. Poon and P. Domingos, "Joint unsupervised coreference resolution with Markov logic," in *Proceedings of the 2008 conference on empirical methods in natural language processing*, 2008, pp. 650-659.

[20] J. Wu, C. Zhang, T. Xue, B. Freeman, and J. Tenenbaum, "Learning a probabilistic latent space of object shapes via 3d generative-adversarial modeling," *Advances in neural information processing systems,* vol. 29, 2016.

[21] M. Raissi, P. Perdikaris, and G. E. Karniadakis, "Physics-informed neural networks: A deep learning framework for solving forward and inverse problems involving nonlinear partial differential equations," *Journal of Computational physics,* vol. 378, pp. 686-707, 2019.

[22] J. Zscheischler *et al.*, "A typology of compound weather and climate events," *Nature reviews earth & environment,* vol. 1, no. 7, pp. 333-347, 2020.

[23] N. Rebout, J.-C. Lone, A. De Marco, R. Cozzolino, A. Lemasson, and B. Thierry, "Measuring complexity in organisms and organizations," *Royal Society Open Science,* vol. 8, no. 3, p. 200895, 2021.

[24] T. Kerola, R. Kettunen, and T. Nieminen, "The complex interplay of cardiovascular system and cognition: how to predict dementia in the elderly?," *International journal of cardiology,* vol. 150, no. 2, pp. 123-129, 2011.

[25] C. P. Wheeler-Jones, "Cell signalling in the cardiovascular system: an overview," *Heart,* vol. 91, no. 10, pp. 1366-1374, 2005.

[26] Q. K. Telesford, S. L. Simpson, J. H. Burdette, S. Hayasaka, and P. J. Laurienti, "The brain as a complex system: using network science as a tool for understanding the brain," *Brain connectivity,* vol. 1, no. 4, pp. 295-308, 2011.

[27] D. S. Bassett and M. S. Gazzaniga, "Understanding complexity in the human brain," *Trends in cognitive sciences,* vol. 15, no. 5, pp. 200-209, 2011.

[28] S. Mei, X. Zhang, and M. Cao, *Power grid complexity*. Springer Science & Business Media, 2011.

[29] W. Jifeng, L. Huapu, and P. Hu, "System dynamics model of urban transportation system and its application," *Journal of Transportation Systems engineering and information technology*, vol. 8, no. 3, pp. 83-89, 2008.

[30] N. Johnson, *Simply complexity: A clear guide to complexity theory*. Simon and Schuster, 2009.

[31] J. H. Holland, "Complex adaptive systems," *Daedalus*, vol. 121, no. 1, pp. 17-30, 1992.

[32] J. Ladyman, J. Lambert, and K. Wiesner, "What is a complex system?," *European Journal for Philosophy of Science*, vol. 3, pp. 33-67, 2013.

[33] R. Marion and M. Uhl-Bien, "Leadership in complex organizations," *The leadership quarterly*, vol. 12, no. 4, pp. 389-418, 2001.

[34] L. Parrott and H. Lange, "An introduction to complexity science," *Managing forests as complex adaptive systems: building resilience to the challenge of global change. Routledge, New York, New York, USA*, pp. 17-32, 2013.

[35] G. C. Gallopín, "Linkages between vulnerability, resilience, and adaptive capacity," *Global environmental change*, vol. 16, no. 3, pp. 293-303, 2006.

[36] Z.-K. Zhang, C. Liu, X.-X. Zhan, X. Lu, C.-X. Zhang, and Y.-C. Zhang, "Dynamics of information diffusion and its applications on complex networks," *Physics Reports*, vol. 651, pp. 1-34, 2016.

[37] R. A. Kelly *et al.*, "Selecting among five common modelling approaches for integrated environmental assessment and management," *Environmental modelling & software*, vol. 47, pp. 159-181, 2013.

[38] Y. Bar-Yam, "When systems engineering fails-toward complex systems engineering," in *SMC'03 Conference Proceedings. 2003 IEEE International Conference on Systems, Man and Cybernetics. Conference Theme-System Security and Assurance (Cat. No. 03CH37483)*, 2003, vol. 2: IEEE, pp. 2021-2028.

[39] M. Mitchell, *Complexity: A guided tour*. Oxford university press, 2009.

[40] K. Kaneko and I. Tsuda, "Chaotic itinerancy," *Chaos: An Interdisciplinary Journal of Nonlinear Science,* vol. 13, no. 3, pp. 926-936, 2003.

[41] S. M. Rinaldi, J. P. Peerenboom, and T. K. Kelly, "Identifying, understanding, and analyzing critical infrastructure interdependencies," *IEEE control systems magazine,* vol. 21, no. 6, pp. 11-25, 2001.

[42] D. J. Wilkinson, "Stochastic modelling for quantitative description of heterogeneous biological systems," *Nature Reviews Genetics,* vol. 10, no. 2, pp. 122-133, 2009.

[43] G. I. Schuëller and H. Pradlwarter, "Uncertain linear systems in dynamics: Retrospective and recent developments by stochastic approaches," *Engineering Structures,* vol. 31, no. 11, pp. 2507-2517, 2009.

[44] D. Bishara, Y. Xie, W. K. Liu, and S. Li, "A state-of-the-art review on machine learning-based multiscale modeling, simulation, homogenization and design of materials," *Archives of computational methods in engineering,* vol. 30, no. 1, pp. 191-222, 2023.

[45] J. H. Miller and S. E. Page, *Complex adaptive systems: an introduction to computational models of social life: an introduction to computational models of social life*. Princeton university press, 2009.

[46] L. Tesfatsion, "Agent-based computational economics: A constructive approach to economic theory," *Handbook of computational economics,* vol. 2, pp. 831-880, 2006.

[47] P. W. Anderson, "More Is Different: Broken symmetry and the nature of the hierarchical structure of science," *Science,* vol. 177, no. 4047, pp. 393-396, 1972.

[48] J. P. Crutchfield, "The calculi of emergence: computation, dynamics and induction," *Physica D: Nonlinear Phenomena,* vol. 75, no. 1-3, pp. 11-54, 1994.

[49] K. Mainzer, *Thinking in complexity: The computational dynamics of matter, mind, and mankind*. Springer, 2004.

[50] S. H. Strogatz, *Nonlinear dynamics and chaos with student solutions manual: With applications to physics, biology, chemistry, and engineering*. CRC press, 2018.

[51] A. Hastings *et al.*, "Transient phenomena in ecology," *Science,* vol. 361, no. 6406, p. eaat6412, 2018.

[52] F. Lorenzelli, *The essence of chaos*. CRC Press, 2014.

[53] A. N. Pisarchik and U. Feudel, "Control of multistability," *Physics Reports,* vol. 540, no. 4, pp. 167-218, 2014.

[54] W. S. Parker, "Predicting weather and climate: Uncertainty, ensembles and probability," *Studies in history and philosophy of science part B: Studies in History and Philosophy of Modern Physics,* vol. 41, no. 3, pp. 263-272, 2010.

[55] E. N. Lorenz, "Atmospheric predictability as revealed by naturally occurring analogues," *Journal of Atmospheric Sciences,* vol. 26, no. 4, pp. 636-646, 1969.

[56] J. Troccaz, G. Dagnino, and G.-Z. Yang, "Frontiers of medical robotics: from concept to systems to clinical translation," *Annual review of biomedical engineering,* vol. 21, pp. 193-218, 2019.

[57] R. Sharma, D. Singh, P. Gaur, and D. Joshi, "Intelligent automated drug administration and therapy: Future of healthcare," *Drug Delivery and Translational Research,* pp. 1-25, 2021.

[58] B. Engquist and O. Runborg, "Computational high frequency wave propagation," *Acta numerica*, vol. 12, pp. 181-266, 2003.

[59] P. J. Hunter and T. K. Borg, "Integration from proteins to organs: the Physiome Project," *Nature reviews Molecular cell biology*, vol. 4, no. 3, pp. 237-243, 2003.

[60] Y. Efendiev and T. Y. Hou, *Multiscale finite element methods: theory and applications*. Springer Science & Business Media, 2009.

[61] E. Weinan, B. Engquist, X. Li, W. Ren, and E. Vanden-Eijnden, "Heterogeneous multiscale methods: a review," *Communications in computational physics*, vol. 2, no. 3, pp. 367-450, 2007.

[62] M. Rybak *et al.*, "Therapeutic monitoring of vancomycin in adult patients: a consensus review of the American Society of Health-System Pharmacists, the Infectious Diseases Society of America, and the Society of Infectious Diseases Pharmacists," *American Journal of Health-System Pharmacy*, vol. 66, no. 1, pp. 82-98, 2009.

[63] A. Lavin *et al.*, "Simulation intelligence: Towards a new generation of scientific methods," *arXiv preprint arXiv:2112.03235*, 2021.

[64] A. Karpatne *et al.*, "Theory-guided data science: A new paradigm for scientific discovery from data," *IEEE Transactions on knowledge and data engineering*, vol. 29, no. 10, pp. 2318-2331, 2017.

[65] H. Redner, *The ends of science: an essay in scientific authority*. Routledge, 2019.

[66] M. A. Ahmad, C. Eckert, and A. Teredesai, "Interpretable machine learning in healthcare," in *Proceedings of the 2018 ACM international conference on bioinformatics, computational biology, and health informatics*, 2018, pp. 559-560.

[67] J. Pearl and D. Mackenzie, *The book of why: the new science of cause and effect*. Basic books, 2018.

[68] S. Zhang, L. Yao, A. Sun, and Y. Tay, "Deep learning based recommender system: A survey and new perspectives," *ACM computing surveys (CSUR)*, vol. 52, no. 1, pp. 1-38, 2019.

[69] R. Kohavi and G. H. John, "Wrappers for feature subset selection," *Artificial intelligence*, vol. 97, no. 1-2, pp. 273-324, 1997.

[70] D. Bertsimas and J. Dunn, "Optimal classification trees," *Machine Learning*, vol. 106, pp. 1039-1082, 2017.

[71] I. Guyon and A. Elisseeff, "An introduction to variable and feature selection," *Journal of machine learning research*, vol. 3, no. Mar, pp. 1157-1182, 2003.

[72] D. Heckerman, "A tutorial on learning with Bayesian networks," *Innovations in Bayesian networks: Theory and applications*, pp. 33-82, 2008.

[73] S. Li, Q. Zhao, C. Zhang, and Y. Zou, "Deep Discriminative Causal Domain Generalization," *Information Sciences*, p. 119335, 2023.

[74] B. Rezaeianjouybari and Y. Shang, "Deep learning for prognostics and health management: State of the art, challenges, and opportunities," *Measurement*, vol. 163, p. 107929, 2020.

[75] M. T. Ribeiro, S. Singh, and C. Guestrin, "Model-agnostic interpretability of machine learning," *arXiv preprint arXiv:1606.05386*, 2016.

[76] A. Holzinger, C. Biemann, C. S. Pattichis, and D. B. Kell, "What do we need to build explainable AI systems for the medical domain?," *arXiv preprint arXiv:1712.09923*, 2017.

[77] W.-L. Chiang, X. Liu, S. Si, Y. Li, S. Bengio, and C.-J. Hsieh, "Cluster-gcn: An efficient algorithm for training deep and large graph convolutional networks," in *Proceedings of the 25th ACM SIGKDD international conference on knowledge discovery & data mining*, 2019, pp. 257-266.

[78] B. Chakraborty and S. A. Murphy, "Dynamic treatment regimes," *Annual review of statistics and its application,* vol. 1, pp. 447-464, 2014.

[79] I. Goodfellow, Y. Bengio, and A. Courville, *Deep learning*. MIT press, 2016.

[80] A. Rajkomar, J. Dean, and I. Kohane, "Machine learning in medicine," *New England Journal of Medicine,* vol. 380, no. 14, pp. 1347-1358, 2019.

[81] M. E. Taylor and P. Stone, "Transfer learning for reinforcement learning domains: A survey," *Journal of Machine Learning Research,* vol. 10, no. 7, 2009.

[82] D. P. Kingma and J. Ba, "Adam: A method for stochastic optimization," *arXiv preprint arXiv:1412.6980,* 2014.

[83] D. Hassabis, D. Kumaran, C. Summerfield, and M. Botvinick, "Neuroscience-inspired artificial intelligence," *Neuron,* vol. 95, no. 2, pp. 245-258, 2017.

[84] C. M. Bishop and N. M. Nasrabadi, *Pattern recognition and machine learning* (no. 4). Springer, 2006.

[85] H. Poincaré, "Sur le problème des trois corps et les équations de la dynamique," *Acta mathematica,* vol. 13, no. 1, pp. A3-A270, 1890.

[86] U. Frisch, *Turbulence: the legacy of AN Kolmogorov*. Cambridge university press, 1995.

[87] H. Kitano, "Computational systems biology," *Nature,* vol. 420, no. 6912, pp. 206-210, 2002.

[88] E. N. Lorenz, "Deterministic nonperiodic flow," *Journal of atmospheric sciences*, vol. 20, no. 2, pp. 130-141, 1963.

[89] M. Tegmark, "Importance of quantum decoherence in brain processes," *Physical review E*, vol. 61, no. 4, p. 4194, 2000.

[90] S. A. Levin, "The problem of pattern and scale in ecology: the Robert H. MacArthur award lecture," *Ecology*, vol. 73, no. 6, pp. 1943-1967, 1992.

[91] G. Schöner and J. S. Kelso, "Dynamic pattern generation in behavioral and neural systems," *Science*, vol. 239, no. 4847, pp. 1513-1520, 1988.

[92] P. Sterling, "Allostasis: a model of predictive regulation," *Physiology & behavior*, vol. 106, no. 1, pp. 5-15, 2012.

[93] A. Snigirev, I. Snigireva, V. Kohn, S. Kuznetsov, and I. Schelokov, "On the possibilities of x-ray phase contrast microimaging by coherent high-energy synchrotron radiation," *Review of scientific instruments*, vol. 66, no. 12, pp. 5486-5492, 1995.

[94] S. H. Strogatz, "Norbert Wiener's brain waves," in *Frontiers in mathematical biology*: Springer, 1994, pp. 122-138.

[95] M. Scheffer, *Critical transitions in nature and society*. Princeton University Press, 2020.

[96] R. FitzHugh, "Impulses and physiological states in theoretical models of nerve membrane," *Biophysical journal*, vol. 1, no. 6, pp. 445-466, 1961.

[97] J. Q. Broughton, F. F. Abraham, N. Bernstein, and E. Kaxiras, "Concurrent coupling of length scales: methodology and application," *Physical review B*, vol. 60, no. 4, p. 2391, 1999.

[98] I. Daubechies, *Ten lectures on wavelets*. SIAM, 1992.

[99] B. J. West, B. Deering, and W. D. Deering, *The lure of modern science: Fractal thinking*. World Scientific, 1995.

[100] M. Maeda, H. Hamada, A. Tsuda, K. Kaneko, and Y. Fukunaga, "High rate of TTV infection in multitransfused patients with pediatric malignancy and hematological disorders," *American journal of hematology*, vol. 65, no. 1, pp. 41-44, 2000.

[101] J. C. Phillips *et al.*, "Scalable molecular dynamics on CPU and GPU architectures with NAMD," *The Journal of chemical physics*, vol. 153, no. 4, 2020.

[102] M. Grieves and J. Vickers, "Digital twin: Mitigating unpredictable, undesirable emergent behavior in complex systems," *Transdisciplinary perspectives on complex systems: New findings and approaches*, pp. 85-113, 2017.

[103] D. S. Novikov, V. G. Kiselev, and S. N. Jespersen, "On modeling," *Magnetic resonance in medicine*, vol. 79, no. 6, pp. 3172-3193, 2018.

[104] G. Carleo *et al.*, "Machine learning and the physical sciences," *Reviews of Modern Physics*, vol. 91, no. 4, p. 045002, 2019.

[105] I. Foster, Y. Zhao, I. Raicu, and S. Lu, "Cloud computing and grid computing 360-degree compared," in *2008 grid computing environments workshop*, 2008: Ieee, pp. 1-10.

[106] H. Kaul and Y. Ventikos, "Investigating biocomplexity through the agent-based paradigm," *Briefings in Bioinformatics*, vol. 16, no. 1, pp. 137-152, 2015.

[107] J. Weiss, "A tutorial on the proper orthogonal decomposition," in *AIAA aviation 2019 forum*, 2019, p. 3333.

[108] C. Hijón, P. Español, E. Vanden-Eijnden, and R. Delgado-Buscalioni, "Mori–Zwanzig formalism as a practical computational tool," *Faraday discussions*, vol. 144, pp. 301-322, 2010.

[109] L. Magni and R. Scattolini, *Advanced and multivariable control*. Società Editrice Esculapio, 2023.

[110] N. Wiener, "Cybernetics," *Scientific American,* vol. 179, no. 5, pp. 14-19, 1948.

[111] R. E. Kalman, "A new approach to linear filtering and prediction problems," 1960.

[112] S. S. Sastry and A. Isidori, "Adaptive control of linearizable systems," *IEEE Transactions on Automatic Control,* vol. 34, no. 11, pp. 1123-1131, 1989.

[113] A. Mirzaee and K. Salahshoor, "Fault diagnosis and accommodation of nonlinear systems based on multiple-model adaptive unscented Kalman filter and switched MPC and H-infinity loop-shaping controller," *Journal of Process Control,* vol. 22, no. 3, pp. 626-634, 2012.

[114] C. J. Tomlin and M. R. Greenstreet, *Hybrid Systems: Computation and Control: 5th International Workshop, HSCC 2002, Stanford, CA, USA, March 25-27, 2002, Proceedings*. Springer Science & Business Media, 2002.

[115] A. Afram and F. Janabi-Sharifi, "Theory and applications of HVAC control systems–A review of model predictive control (MPC)," *Building and Environment,* vol. 72, pp. 343-355, 2014.

[116] S. J. Qin and T. A. Badgwell, "A survey of industrial model predictive control technology," *Control engineering practice,* vol. 11, no. 7, pp. 733-764, 2003.

[117] F. Borrelli, A. Bemporad, and M. Morari, *Predictive control for linear and hybrid systems*. Cambridge University Press, 2017.

[118] J. Kober, J. A. Bagnell, and J. Peters, "Reinforcement learning in robotics: A survey," *The International Journal of Robotics Research,* vol. 32, no. 11, pp. 1238-1274, 2013.

[119] D. Silver *et al.*, "Mastering the game of go without human knowledge," *nature,* vol. 550, no. 7676, pp. 354-359, 2017.

[120] J. P. Hespanha, P. Naghshtabrizi, and Y. Xu, "A survey of recent results in networked control systems," *Proceedings of the IEEE,* vol. 95, no. 1, pp. 138-162, 2007.

[121] N. S. V. Lund, A. K. V. Falk, M. Borup, H. Madsen, and P. Steen Mikkelsen, "Model predictive control of urban drainage systems: A review and perspective towards smart real-time water management," *Critical Reviews in Environmental Science and Technology,* vol. 48, no. 3, pp. 279-339, 2018.

[122] A. D. Association, "Standards of medical care in diabetes—2019 abridged for primary care providers," *Clinical diabetes: a publication of the American Diabetes Association,* vol. 37, no. 1, p. 11, 2019.

[123] T. Bezemer *et al.*, "A human (e) factor in clinical decision support systems," *Journal of medical Internet research,* vol. 21, no. 3, p. e11732, 2019.

[124] P. K. Huynh, A. Setty, H. Phan, and T. Q. Le, "Probabilistic domain-knowledge modeling of disorder pathogenesis for dynamics forecasting of acute onset," *Artificial Intelligence in Medicine,* vol. 115, p. 102056, 2021.

[125] P. K. Huynh, A. A. Alqarni, O. P. Yadav, and T. Q. Le, "A Physics-informed Latent Variables of Corrosion Growth in Oil and Gas Pipelines," in *2023 Annual Reliability and Maintainability Symposium (RAMS)*, 2023: IEEE, pp. 1-7.

[126] P. K. Huynh, A. R. Setty, Q. M. Tran, O. P. Yadav, N. Yodo, and T. Q. Le, "A domain-knowledge modeling of hospital-acquired infection risk in Healthcare personnel from retrospective observational data: A case study for COVID-19," *Plos one,* vol. 17, no. 11, p. e0272919, 2022.

[127] P. K. Huynh, A. R. Setty, T. B. Le, and T. Q. Le, "A noise-robust Koopman spectral analysis of an intermittent dynamics method for complex systems: a case study in pathophysiological processes of obstructive sleep apnea," *IISE Transactions on Healthcare Systems Engineering,* vol. 13, no. 2, pp. 101-116, 2023.

[128] S. L. Brunton, B. W. Brunton, J. L. Proctor, E. Kaiser, and J. N. Kutz, "Chaos as an intermittently forced linear system," *Nature communications,* vol. 8, no. 1, p. 19, 2017.

[129] A. Wynn, D. Pearson, B. Ganapathisubramani, and P. J. Goulart, "Optimal mode decomposition for unsteady flows," *Journal of Fluid Mechanics,* vol. 733, pp. 473-503, 2013.

[130] P. K. Huynh, D. Nguyen, G. Binder, S. Ambardar, T. Q. Le, and D. V. Voronine, "Multifractality in Surface Potential for Cancer Diagnosis," *arXiv preprint arXiv:2304.10085,* 2023.

[131] C. R. Turner, A. Fuggetta, L. Lavazza, and A. L. Wolf, "A conceptual basis for feature engineering," *Journal of Systems and Software,* vol. 49, no. 1, pp. 3-15, 1999.

[132] Y. Huang, H. Liu, L. Zuo, and A. Tao, "Key genes and co-expression modules involved in asthma pathogenesis," *PeerJ,* vol. 8, p. e8456, 2020.

[133] X. Yu, S. Lai, H. Chen, and M. Chen, "Protein–protein interaction network with machine learning models and multiomics data reveal potential neurodegenerative disease-related proteins," *Human Molecular Genetics,* vol. 29, no. 8, pp. 1378-1387, 2020.

[134] J. K. Das, G. Tradigo, P. Veltri, P. H. Guzzi, and S. Roy, "Data Science in Unveiling COVID-19 Pathogenesis and Diagnosis: Evolutionary Origin to Drug Repurposing," 2020.

[135] Z. Han, B. Wei, S. Leung, I. B. Nachum, D. Laidley, and S. Li, "Automated pathogenesis-based diagnosis of lumbar neural foraminal stenosis via deep multiscale multitask learning," *Neuroinformatics,* vol. 16, no. 3-4, pp. 325-337, 2018.

[136] A. Kourliouros, I. Savelieva, A. Kiotsekoglou, M. Jahangiri, and J. Camm, "Current concepts in the pathogenesis of atrial fibrillation," *American heart journal,* vol. 157, no. 2, pp. 243-252, 2009.

[137] R. O. Bahado-Singh *et al.*, "Precision cardiovascular medicine: artificial intelligence and epigenetics for the pathogenesis and prediction of coarctation in neonates," *The Journal of Maternal-Fetal & Neonatal Medicine,* pp. 1-8, 2020.

[138] J. Bouaud *et al.*, "Implementation of an ontological reasoning to support the guideline-based management of primary breast cancer patients in the DESIREE project," *Artificial Intelligence in Medicine,* vol. 108, p. 101922, 2020.

[139] R. R. Smullyan, *First-order logic*. Springer Science & Business Media, 2012.

[140] S. Pokharel, G. Zuccon, X. Li, C. P. Utomo, and Y. Li, "Temporal Tree Representation for Similarity Computation between Medical Patients," *Artificial Intelligence in Medicine,* p. 101900, 2020.

[141] E. H. Shortliffe and J. J. Cimino, *Biomedical informatics*. Springer, 2006.

[142] M. Vilardell *et al.*, "Missing data imputation and synthetic data simulation through modeling graphical probabilistic dependencies between variables (ModGraProDep): An application to breast cancer survival," *Artificial Intelligence in Medicine,* vol. 107, p. 101875, 2020.

[143] S. McLachlan, K. Dube, G. A. Hitman, N. Fenton, and E. Kyrimi, "Bayesian Networks in Healthcare: Distribution by Medical Condition," *Artificial Intelligence in Medicine*, p. 101912, 2020.

[144] E. Shortliffe, *Computer-based medical consultations: MYCIN*. Elsevier, 2012.

[145] R. R. Makkar *et al.*, "Intracoronary cardiosphere-derived cells for heart regeneration after myocardial infarction (CADUCEUS): a prospective, randomised phase 1 trial," vol. 379, no. 9819, pp. 895-904, 2012.

[146] R. A. Miller, H. E. Pople Jr, and J. D. J. N. E. J. o. M. Myers, "Internist-I, an experimental computer-based diagnostic consultant for general internal medicine," vol. 307, no. 8, pp. 468-476, 1982.

[147] J. D. Hamilton, *Time series analysis*. Princeton university press Princeton, NJ, 1994.

[148] F. Jelinek, *Statistical methods for speech recognition*. MIT press, 1997.

[149] D. Ron, Y. Singer, and N. J. M. l. Tishby, "The power of amnesia: Learning probabilistic automata with variable memory length," vol. 25, no. 2-3, pp. 117-149, 1996.

[150] A. K. McCallum and D. Ballard, "Reinforcement learning with selective perception and hidden state," University of Rochester. Dept. of Computer Science, 1996.

[151] Z. Wu *et al.*, "Coarse-to-fine classification for diabetic retinopathy grading using convolutional neural network," *Artificial Intelligence in Medicine*, vol. 108, p. 101936, 2020.

[152] J. Feng, S.-W. Zhang, L. Chen, and A. s. D. N. Initiative, "Identification of Alzheimer's disease based on wavelet transformation energy feature of the structural MRI image and NN classifier," *Artificial Intelligence in Medicine*, vol. 108, p. 101940, 2020.

[153] C. Meek, D. M. Chickering, and D. Heckerman, "Autoregressive tree models for time-series analysis," in *Proceedings of the 2002 SIAM International Conference on Data Mining*, 2002: SIAM, pp. 229-244.

[154] M. Aoki, *State space modeling of time series*. Springer Science & Business Media, 2013.

[155] A. C. Harvey, *Forecasting, structural time series models and the Kalman filter*. Cambridge university press, 1990.

[156] M. West and J. Harrison, *Bayesian forecasting and dynamic models*. Springer Science & Business Media, 2006.

[157] J. Durbin and S. J. Koopman, *Time series analysis by state space methods*. Oxford university press, 2012.

[158] D. Koller, N. Friedman, and F. Bach, *Probabilistic graphical models: principles and techniques*. MIT press, 2009.

[159] M. W. Libbrecht and W. S. Noble, "Machine learning applications in genetics and genomics," *Nature Reviews Genetics*, vol. 16, no. 6, pp. 321-332, 2015.

[160] S. Huang, N. Cai, P. P. Pacheco, S. Narrandes, Y. Wang, and W. Xu, "Applications of support vector machine (SVM) learning in cancer genomics," *Cancer Genomics-Proteomics*, vol. 15, no. 1, pp. 41-51, 2018.

[161] C. Parmar, P. Grossmann, D. Rietveld, M. M. Rietbergen, P. Lambin, and H. J. Aerts, "Radiomic machine-learning classifiers for prognostic biomarkers of head and neck cancer," *Frontiers in oncology*, vol. 5, p. 272, 2015.

[162] D. Vitanovski *et al.*, "Personalized learning-based segmentation of thoracic aorta and main branches for diagnosis and treatment planning," in *2012 9th IEEE International Symposium on Biomedical Imaging (ISBI)*, 2012: IEEE, pp. 836-839.

[163] R. Alizadehsani, M. Abdar, S. M. J. Jalali, M. Roshanzamir, A. Khosravi, and S. Nahavandi, "Comparing the Performance of Feature Selection Algorithms for Wart Treatment Selection," in *Proceedings of The International Workshop on Future Technology*, 2019, pp. 6-18.

[164] R. Ross, "The pathogenesis of atherosclerosis—an update," *New England Journal of Medicine*, vol. 314, no. 8, pp. 488-500, 1986.

[165] K. F. van der Sluijs, T. van der Poll, R. Lutter, N. P. Juffermans, and M. J. J. C. c. Schultz, "Bench-to-bedside review: bacterial pneumonia with influenza-pathogenesis and clinical implications," vol. 14, no. 2, p. 219, 2010.

[166] K. J. Rothman, S. Greenland, and T. L. Lash, *Modern epidemiology*. Wolters Kluwer Health/Lippincott Williams & Wilkins Philadelphia, 2008.

[167] S. Srinivas, "A generalization of the noisy-or model," in *Proceedings of the Ninth International Conference on Uncertainty in Artificial Intelligence*, 1993: Morgan Kaufmann Publishers Inc., pp. 208-215.

[168] J. Heijman, J.-B. Guichard, D. Dobrev, and S. Nattel, "Translational challenges in atrial fibrillation," *Circulation research*, vol. 122, no. 5, pp. 752-773, 2018.

[169] S. R. Eddy, "Profile hidden Markov models," *Bioinformatics (Oxford, England)*, vol. 14, no. 9, pp. 755-763, 1998.

[170] K. Murphy and Y. Weiss, "The factored frontier algorithm for approximate inference in DBNs," in *Proceedings of the Seventeenth Conference on Uncertainty in Artificial Intelligence*, 2001: Morgan Kaufmann Publishers Inc., pp. 378-385.

[171] C. K. Carter and R. Kohn, "On Gibbs sampling for state space models," *Biometrika*, vol. 81, no. 3, pp. 541-553, 1994.

[172] G. Moody, A. Goldberger, S. McClennen, and S. Swiryn, "Predicting the onset of paroxysmal atrial fibrillation: The Computers in Cardiology Challenge," in *Computers in Cardiology*, 2001, vol. 28: IEEE, pp. 113-116.

[173] G. B. Moody and R. G. Mark, "The MIT-BIH arrhythmia database on CD-ROM and software for use with it," in *Proceedings Computers in Cardiology*, 1990: IEEE, pp. 185-188.

[174] K. Murphy, "The bayes net toolbox for matlab," *Computing Science and Statistics*, vol. 33, no. 2, pp. 1024-1034, 2001.

[175] N. M. Punjabi, "The epidemiology of adult obstructive sleep apnea," *Proceedings of the American Thoracic Society*, vol. 5, no. 2, pp. 136-143, 2008.

[176] D. J. Eckert and A. Malhotra, "Pathophysiology of adult obstructive sleep apnea," *Proceedings of the American thoracic society*, vol. 5, no. 2, pp. 144-153, 2008.

[177] A. Malhotra and D. P. White, "Obstructive sleep apnoea," *The Lancet*, vol. 360, no. 9328, pp. 237-245, 2002.

[178] J. Pan and W. J. Tompkins, "A real-time QRS detection algorithm," *IEEE Transactions on Biomedical Engineering*, no. 3, pp. 230-236, 1985.

[179] P. S. Hamilton and W. J. Tompkins, "Quantitative investigation of QRS detection rules using the MIT/BIH arrhythmia database," *IEEE Transactions on Biomedical Engineering*, no. 12, pp. 1157-1165, 1986.

[180] X. Wu, Y. Zheng, C.-H. Chu, and Z. He, "Extracting Deep Features from Short ECG Signals for Early Atrial Fibrillation Detection," *Artificial Intelligence in Medicine*, p. 101896, 2020.

[181] T. Thong, J. McNames, M. Aboy, and B. Goldstein, "Prediction of paroxysmal atrial fibrillation by analysis of atrial premature complexes," *IEEE Transactions on Biomedical Engineering*, vol. 51, no. 4, pp. 561-569, 2004.

[182] Y. Bengio and P. Frasconi, "An input output HMM architecture," in *Advances in neural information processing systems*, 1995, pp. 427-434.

[183] K. P. Murphy, "A variational approximation for Bayesian networks with discrete and continuous latent variables," in *Proceedings of the Fifteenth Conference on Uncertainty in Artificial Intelligence*, 1999: Morgan Kaufmann Publishers Inc., pp. 457-466.

[184] F. Scarselli, M. Gori, A. C. Tsoi, M. Hagenbuchner, and G. Monfardini, "The graph neural network model," *IEEE Transactions on Neural Networks*, vol. 20, no. 1, pp. 61-80, 2008.

[185] H. A. Kishawy and H. A. Gabbar, "Review of pipeline integrity management practices," *International Journal of Pressure Vessels and Piping*, vol. 87, no. 7, pp. 373-380, 2010.

[186] C. Leygraf and M. Philippe, "Atmospheric Corrosion in Corrosion Mechanisms in Theory and Practice," ed: New York, Hong Kong, Marcel Dekker, 1995.

[187] R. Nyborg, "Overview of CO2 corrosion models for wells and pipelines," in *CORROSION 2002*, 2002: OnePetro.

[188] S. Zhang, W. Zhou, and H. Qin, "Inverse Gaussian process-based corrosion growth model for energy pipelines considering the sizing error in inspection data," *Corrosion Science*, vol. 73, pp. 309-320, 2013.

[189] R. Heidary, S. A. Gabriel, M. Modarres, K. M. Groth, and N. Vahdati, "A review of data-driven oil and gas pipeline pitting corrosion growth models applicable for prognostic and health management," *International Journal of Prognostics and Health Management*, vol. 9, no. 1, 2018.

[190] A. Valor, F. Caleyo, L. Alfonso, J. Velázquez, and J. Hallen, "Markov chain models for the stochastic modeling of pitting corrosion," *Mathematical Problems in Engineering*, vol. 2013, 2013.

[191] M. Al-Amin, W. Zhou, S. Zhang, S. Kariyawasam, and H. Wang, "Hierarchical Bayesian corrosion growth model based on in-line inspection data," *Journal of Pressure Vessel Technology*, vol. 136, no. 4, 2014.

[192] C. I. Ossai, "A data-driven machine learning approach for corrosion risk assessment—a comparative study," *Big Data and Cognitive Computing*, vol. 3, no. 2, p. 28, 2019.

[193] S. Peng, Z. Zhang, E. Liu, W. Liu, and W. Qiao, "A new hybrid algorithm model for prediction of internal corrosion rate of multiphase pipeline," *Journal of Natural Gas Science and Engineering*, vol. 85, p. 103716, 2021.

[194] M. E. A. B. Seghier, B. Keshtegar, K. F. Tee, T. Zayed, R. Abbassi, and N. T. Trung, "Prediction of maximum pitting corrosion depth in oil and gas pipelines," *Engineering Failure Analysis*, vol. 112, p. 104505, 2020.

[195] C. Wang, G. Ma, J. Li, Z. Dai, and J. Liu, "Prediction of corrosion rate of submarine oil and gas pipelines based on ia-svm model," in *IOP Conference Series: Earth and Environmental Science*, 2019, vol. 242, no. 2: IOP Publishing, p. 022023.

[196] B. Everett, *An introduction to latent variable models*. Springer Science & Business Media, 2013.

[197] P. Huynh, L. Irish, O. P. Yadav, A. Setty, and T. T. Q. Le, "Causal Inference in Longitudinal Studies Using Causal Bayesian Network with Latent Variables," in *2022 Annual Reliability and Maintainability Symposium (RAMS)*, 2022: IEEE, pp. 1-7.

[198] D. Kaplan, "An overview of Markov chain methods for the study of stage-sequential developmental processes," *Developmental psychology,* vol. 44, no. 2, p. 457, 2008.

[199] G. Kitagawa and W. Gersch, "Linear Gaussian state space modeling," in *Smoothness priors analysis of time series*: Springer, 1996, pp. 55-65.

[200] S. Fine, Y. Singer, and N. Tishby, "The hierarchical hidden Markov model: Analysis and applications," *Machine learning,* vol. 32, no. 1, pp. 41-62, 1998.

[201] Y. Bengio and P. Frasconi, "Input-output HMMs for sequence processing," *IEEE Transactions on Neural Networks,* vol. 7, no. 5, pp. 1231-1249, 1996.

[202] S. Roweis, "Constrained hidden Markov models," *Advances in neural information processing systems,* vol. 12, 1999.

[203] G. E. Hinton, "Variational learning for switching state-space models," *Graphical Models: Foundations of Neural Computation,* p. 315, 2001.

[204] Z. Ghahramani and M. Jordan, "Factorial hidden Markov models," *Advances in Neural Information Processing Systems,* vol. 8, 1995.

[205] Z. Ghahramani, "Learning dynamic Bayesian networks," *International School on Neural Networks, Initiated by IIASS and EMFCSC,* pp. 168-197, 1997.

[206] C. Sutton and A. McCallum, "An introduction to conditional random fields," *Foundations and Trends® in Machine Learning,* vol. 4, no. 4, pp. 267-373, 2012.

[207] J. M. Ottino, "Engineering complex systems," *Nature,* vol. 427, no. 6973, pp. 399-399, 2004.

[208] J. D. Sterman, "System dynamics modeling: tools for learning in a complex world," *California management review,* vol. 43, no. 4, pp. 8-25, 2001.

[209] G. E. Karniadakis, I. G. Kevrekidis, L. Lu, P. Perdikaris, S. Wang, and L. Yang, "Physics-informed machine learning," *Nature Reviews Physics,* vol. 3, no. 6, pp. 422-440, 2021.

[210] L.-t. Hu and P. M. Bentler, "Fit indices in covariance structure modeling: Sensitivity to underparameterized model misspecification," *Psychological methods,* vol. 3, no. 4, p. 424, 1998.

[211] F. Murtagh and P. Contreras, "Algorithms for hierarchical clustering: an overview," *Wiley Interdisciplinary Reviews: Data Mining and Knowledge Discovery,* vol. 2, no. 1, pp. 86-97, 2012.

[212] H. Vanaei, A. Eslami, and A. Egbewande, "A review on pipeline corrosion, in-line inspection (ILI), and corrosion growth rate models," *International Journal of Pressure Vessels and Piping,* vol. 149, pp. 43-54, 2017.

[213] S. Hansun, "A new approach of moving average method in time series analysis," in *2013 conference on new media studies (CoNMedia)*, 2013: IEEE, pp. 1-4.

[214] E. Sorokin, G. Tempea, and T. Brabec, "Measurement of the root-mean-square width and the root-mean-square chirp in ultrafast optics," *JOSA B,* vol. 17, no. 1, pp. 146-150, 2000.

[215] C. Janiesch, P. Zschech, and K. Heinrich, "Machine learning and deep learning," *Electronic Markets,* vol. 31, no. 3, pp. 685-695, 2021.

[216] Y. He and A. Bilgic, "Iterative least squares method for global positioning system," *Advances in Radio Science,* vol. 9, no. C. 5-2, pp. 203-208, 2011.

[217] F. A. V. Bazán and A. T. Beck, "Stochastic process corrosion growth models for pipeline reliability," *Corrosion Science,* vol. 74, pp. 50-58, 2013.

[218] C. Plagemann, K. Kersting, and W. Burgard, "Nonstationary Gaussian process regression using point estimates of local smoothness," in *Joint European Conference on Machine Learning and Knowledge Discovery in Databases*, 2008: Springer, pp. 204-219.

[219] H. Kantz and T. Schreiber, *Nonlinear time series analysis*. Cambridge university press, 2004.

[220] C. Grebogi, E. Ott, F. Romeiras, and J. A. Yorke, "Critical exponents for crisis-induced intermittency," *Physical Review A*, vol. 36, no. 11, p. 5365, 1987.

[221] G. M. Zaslavsky and G. M. Zaslavskij, *Hamiltonian chaos and fractional dynamics*. Oxford University Press on Demand, 2005.

[222] H. Bessaih, E. Hausenblas, and P. A. Razafimandimby, "Strong solutions to stochastic hydrodynamical systems with multiplicative noise of jump type," *Nonlinear Differential Equations and Applications NoDEA*, vol. 22, no. 6, pp. 1661-1697, 2015.

[223] A. E. Hramov, A. A. Koronovskii, and M. K. Kurovskaya, "Intermittent behavior near the synchronization threshold in system with fluctuating control parameter," *EPL (Europhysics Letters)*, vol. 105, no. 5, p. 50003, 2014.

[224] Y. Contoyiannis, F. Diakonos, and A. Malakis, "Intermittent dynamics of critical fluctuations," *Physical review letters*, vol. 89, no. 3, p. 035701, 2002.

[225] F. Takens, "Detecting strange attractors in turbulence," in *Dynamical systems and turbulence, Warwick 1980*: Springer, 1981, pp. 366-381.

[226] H. Ye *et al.*, "Equation-free mechanistic ecosystem forecasting using empirical dynamic modeling," *Proceedings of the National Academy of Sciences*, vol. 112, no. 13, pp. E1569-E1576, 2015.

[227] G. Sugihara *et al.*, "Detecting causality in complex ecosystems," *science,* vol. 338, no. 6106, pp. 496-500, 2012.

[228] H. D. Abarbanel, R. Brown, J. J. Sidorowich, and L. S. Tsimring, "The analysis of observed chaotic data in physical systems," *Reviews of modern physics,* vol. 65, no. 4, p. 1331, 1993.

[229] J.-N. Juang and R. S. Pappa, "An eigensystem realization algorithm for modal parameter identification and model reduction," *Journal of guidance, control, and dynamics,* vol. 8, no. 5, pp. 620-627, 1985.

[230] W. W. Wei, "Time series analysis," in *The Oxford Handbook of Quantitative Methods in Psychology: Vol. 2*, 2006.

[231] D. Giannakis and A. J. Majda, "Nonlinear Laplacian spectral analysis for time series with intermittency and low-frequency variability," *Proceedings of the National Academy of Sciences,* vol. 109, no. 7, pp. 2222-2227, 2012.

[232] S. L. Brunton, B. W. Brunton, J. L. Proctor, E. Kaiser, and J. N. Kutz, "Chaos as an intermittently forced linear system," *Nature communications,* vol. 8, no. 1, pp. 1-9, 2017.

[233] D. Giannakis, "Data-driven spectral decomposition and forecasting of ergodic dynamical systems," *Applied and Computational Harmonic Analysis,* vol. 47, no. 2, pp. 338-396, 2019.

[234] S. L. Brunton, J. L. Proctor, and J. N. Kutz, "Discovering governing equations from data by sparse identification of nonlinear dynamical systems," *Proceedings of the national academy of sciences,* vol. 113, no. 15, pp. 3932-3937, 2016.

[235] A. J. Majda and Y. Lee, "Conceptual dynamical models for turbulence," *Proceedings of the National Academy of Sciences,* vol. 111, no. 18, pp. 6548-6553, 2014.

[236] A. J. Majda and J. Harlim, "Physics constrained nonlinear regression models for time series," *Nonlinearity,* vol. 26, no. 1, p. 201, 2012.

[237] A. Oppenheim, G. Wornell, S. Isabelle, and K. Cuomo, "Proceedings of the International Conference on Acoustics, Speech, and Signal Processing," 1992.

[238] J. M. Lilly, "Element analysis: a wavelet-based method for analysing time-localized events in noisy time series," *Proceedings of the Royal Society A: Mathematical, Physical and Engineering Sciences,* vol. 473, no. 2200, p. 20160776, 2017.

[239] B. O. Koopman, "Hamiltonian systems and transformation in Hilbert space," *Proceedings of the national academy of sciences of the united states of america,* vol. 17, no. 5, p. 315, 1931.

[240] J. H. Tu, "Dynamic mode decomposition: Theory and applications," Princeton University, 2013.

[241] M. O. Williams, I. G. Kevrekidis, and C. W. Rowley, "A data–driven approximation of the koopman operator: Extending dynamic mode decomposition," *Journal of Nonlinear Science,* vol. 25, no. 6, pp. 1307-1346, 2015.

[242] S. L. Brunton, B. W. Brunton, J. L. Proctor, and J. N. Kutz, "Koopman invariant subspaces and finite linear representations of nonlinear dynamical systems for control," *PloS one,* vol. 11, no. 2, p. e0150171, 2016.

[243] E. B. Rozenbaum, S. Ganeshan, and V. Galitski, "Lyapunov exponent and out-of-time-ordered correlator's growth rate in a chaotic system," *Physical review letters,* vol. 118, no. 8, p. 086801, 2017.

[244] I. Mezić, "Spectral properties of dynamical systems, model reduction and decompositions," *Nonlinear Dynamics,* vol. 41, no. 1, pp. 309-325, 2005.

[245] D. L. Donoho and M. Gavish, "The optimal hard threshold for singular values is 4/√ 3," vol. 4, ed: Citeseer, 2013.

[246] T. Penzel, G. B. Moody, R. G. Mark, A. L. Goldberger, and J. H. Peter, "The apnea-ECG database," in *Computers in Cardiology 2000. Vol. 27 (Cat. 00CH37163)*, 2000: IEEE, pp. 255-258.

[247] X. Wu, Y. Zheng, C.-H. Chu, and Z. He, "Extracting deep features from short ECG signals for early atrial fibrillation detection," *Artificial Intelligence in Medicine,* vol. 109, p. 101896, 2020.

[248] M. Vollmer, "HRVTool–an open-source matlab toolbox for analyzing heart rate variability," in *2019 Computing in Cardiology (CinC)*, 2019: IEEE, pp. Page 1-Page 4.

[249] L. Pecchia, R. Castaldo, L. Montesinos, and P. Melillo, "Are ultra-short heart rate variability features good surrogates of short-term ones? State-of-the-art review and recommendations," *Healthcare technology letters,* vol. 5, no. 3, pp. 94-100, 2018.

[250] T. Q. Le, C. Cheng, A. Sangasoongsong, W. Wongdhamma, and S. T. Bukkapatnam, "Wireless wearable multisensory suite and real-time prediction of obstructive sleep apnea episodes," *IEEE journal of translational engineering in health and medicine,* vol. 1, pp. 2700109-2700109, 2013.

[251] K. P. Champion, S. L. Brunton, and J. N. Kutz, "Discovery of nonlinear multiscale systems: Sampling strategies and embeddings," *SIAM Journal on Applied Dynamical Systems,* vol. 18, no. 1, pp. 312-333, 2019.

[252] J. L. Brisman, J. K. Song, and D. W. Newell, "Cerebral aneurysms," *New England journal of medicine,* vol. 355, no. 9, pp. 928-939, 2006.

[253] A. A. Saeyeldin *et al.*, "Thoracic aortic aneurysm: unlocking the “silent killer” secrets," *General thoracic and cardiovascular surgery,* vol. 67, pp. 1-11, 2019.

[254] M. H. Vlak, A. Algra, R. Brandenburg, and G. J. Rinkel, "Prevalence of unruptured intracranial aneurysms, with emphasis on sex, age, comorbidity, country, and time period: a systematic review and meta-analysis," *The Lancet Neurology,* vol. 10, no. 7, pp. 626-636, 2011.

[255] D. J. Nieuwkamp, L. E. Setz, A. Algra, F. H. Linn, N. K. de Rooij, and G. J. Rinkel, "Changes in case fatality of aneurysmal subarachnoid haemorrhage over time, according to age, sex, and region: a meta-analysis," *The Lancet Neurology,* vol. 8, no. 7, pp. 635-642, 2009.

[256] D. O. Wiebers, "Unruptured intracranial aneurysms: natural history, clinical outcome, and risks of surgical and endovascular treatment," *The Lancet,* vol. 362, no. 9378, pp. 103-110, 2003.

[257] T. Rustagi, E. M. Uy, M. Rai, S. Kannan, and P. Senatus, "Intracranial hemorrhage from undetected aneurysmal rupture complicating transphenoidal pituitary adenoma resection," *Connecticut Medicine,* vol. 75, no. 7, 2011.

[258] J. W. Thompson *et al.*, "In vivo cerebral aneurysm models," *Neurosurgical focus,* vol. 47, no. 1, p. E20, 2019.

[259] X. Chen *et al.*, "Meta-analysis of computed tomography angiography versus magnetic resonance angiography for intracranial aneurysm," *Medicine,* vol. 97, no. 20, 2018.

[260] J. D. Burns, J. Huston III, K. F. Layton, D. G. Piepgras, and R. D. Brown Jr, "Intracranial aneurysm enlargement on serial magnetic resonance angiography: frequency and risk factors," *Stroke,* vol. 40, no. 2, pp. 406-411, 2009.

[261] L. Lu *et al.*, "Digital subtraction CT angiography for detection of intracranial aneurysms: comparison with three-dimensional digital subtraction angiography," *Radiology*, vol. 262, no. 2, pp. 605-612, 2012.

[262] Y. Zhang *et al.*, "Hemodynamic analysis of intracranial aneurysms with daughter blebs," *European neurology*, vol. 66, no. 6, pp. 359-367, 2011.

[263] L. Boussel *et al.*, "Aneurysm growth occurs at region of low wall shear stress: patient-specific correlation of hemodynamics and growth in a longitudinal study," *Stroke*, vol. 39, no. 11, pp. 2997-3002, 2008.

[264] H. G. Morales *et al.*, "How do coil configuration and packing density influence intra-aneurysmal hemodynamics?," *American Journal of Neuroradiology*, vol. 32, no. 10, pp. 1935-1941, 2011.

[265] J. Cebral *et al.*, "Aneurysm rupture following treatment with flow-diverting stents: computational hemodynamics analysis of treatment," *American journal of neuroradiology*, vol. 32, no. 1, pp. 27-33, 2011.

[266] T. B. Le, "Dynamic modes of inflow jet in brain aneurysms," *Journal of Biomechanics*, vol. 116, p. 110238, 2021.

[267] P. Yu and V. Durgesh, "Application of Dynamic Mode Decomposition to Study Temporal Flow Behavior in a Saccular Aneurysm," *Journal of Biomechanical Engineering*, vol. 144, no. 5, p. 051002, 2022.

[268] M. R. Jovanović, P. J. Schmid, and J. W. Nichols, "Sparsity-promoting dynamic mode decomposition," *Physics of Fluids*, vol. 26, no. 2, 2014.

[269] B. R. Noack, "From snapshots to modal expansions–bridging low residuals and pure frequencies," *Journal of Fluid Mechanics*, vol. 802, pp. 1-4, 2016.

[270] T. Askham and J. N. Kutz, "Variable projection methods for an optimized dynamic mode decomposition," *SIAM Journal on Applied Dynamical Systems,* vol. 17, no. 1, pp. 380-416, 2018.

[271] K. Valen-Sendstad and D. A. Steinman, "Mind the gap: impact of computational fluid dynamics solution strategy on prediction of intracranial aneurysm hemodynamics and rupture status indicators," *American Journal of Neuroradiology,* vol. 35, no. 3, pp. 536-543, 2014.

[272] R. Schmidt and K. Singh, "Meshmixer: an interface for rapid mesh composition," in *ACM SIGGRAPH 2010 Talks,* 2010, pp. 1-1.

[273] U. Ayachit, *The paraview guide: a parallel visualization application*. Kitware, Inc., 2015.

[274] T. B. Le and L. Akerkouch, "On the Modal Analysis of Blood Flow Dynamics in Brain Aneurysms," in *Frontiers in Biomedical Devices,* 2020, vol. 83549: American Society of Mechanical Engineers, p. V001T07A008.

[275] T. B. Le, T. Nguyen, P. Huynh, and T. Q. Le, "SURROGATE MODELS OF BLOOD FLOW DYNAMICS IN BRAIN ANEURYSMS USING DYNAMIC MODE DECOMPOSITION," in *Frontiers in Biomedical Devices*, 2023, vol. 86731: American Society of Mechanical Engineers, p. V001T02A006.

[276] M. Haji Mohammadi, F. Sotiropoulos, and J. Brinkerhoff, "Moving least squares reconstruction for sharp interface immersed boundary methods," *International Journal for Numerical Methods in Fluids,* vol. 90, no. 2, pp. 57-80, 2019.

[277] P. Yu and V. Durgesh, "Modal Decomposition Techniques: Application in Coherent Structures for a Saccular Aneurysm Model," *Fluids,* vol. 7, no. 5, p. 165, 2022.

[278] J. O. Dada and P. Mendes, "Multi-scale modelling and simulation in systems biology," *Integrative Biology,* vol. 3, no. 2, pp. 86-96, 2011.

[279] D. E. Kirschner, C. A. Hunt, S. Marino, M. Fallahi-Sichani, and J. J. Linderman, "Tuneable resolution as a systems biology approach for multi-scale, multi-compartment computational models," *Wiley Interdisciplinary Reviews: Systems Biology and Medicine,* vol. 6, no. 4, pp. 289-309, 2014.

[280] C. Johansen and I. Tien, "Probabilistic multi-scale modeling of interdependencies between critical infrastructure systems for resilience," *Sustainable and Resilient Infrastructure,* vol. 3, no. 1, pp. 1-15, 2018.

[281] S. Thacker, R. Pant, and J. W. Hall, "System-of-systems formulation and disruption analysis for multi-scale critical national infrastructures," *Reliability Engineering & System Safety,* vol. 167, pp. 30-41, 2017.

[282] A. Abdulle, E. Weinan, B. Engquist, and E. Vanden-Eijnden, "The heterogeneous multiscale method," *Acta Numerica,* vol. 21, pp. 1-87, 2012.

[283] B. Engquist, X. Li, W. Ren, and E. Vanden-Eijnden, "Heterogeneous multiscale methods: a review," *Communications in Computational Physics,* vol. 2, no. 3, pp. 367-450, 2007.

[284] I. G. Kevrekidis, C. W. Gear, J. M. Hyman, P. G. Kevrekidis, O. Runborg, and C. Theodoropoulos, "Equation-free, coarse-grained multiscale computation: enabling microscopic simulators to perform system-level analysis," *Commun. Math. Sci,* vol. 1, no. 4, pp. 715-762, 2003.

[285] E. Weinan, *Principles of multiscale modeling*. Cambridge University Press, 2011.

[286] G. Froyland, G. A. Gottwald, and A. Hammerlindl, "A computational method to extract macroscopic variables and their dynamics in multiscale systems," *SIAM Journal on Applied Dynamical Systems,* vol. 13, no. 4, pp. 1816-1846, 2014.

[287] G. Froyland, G. A. Gottwald, and A. Hammerlindl, "A trajectory-free framework for analysing multiscale systems," *Physica D: Nonlinear Phenomena,* vol. 328, pp. 34-43, 2016.

[288] J. N. Kutz, X. Fu, and S. L. Brunton, "Multiresolution dynamic mode decomposition," *SIAM Journal on Applied Dynamical Systems,* vol. 15, no. 2, pp. 713-735, 2016.

[289] Y. Liu, J. N. Kutz, and S. L. Brunton, "Hierarchical deep learning of multiscale differential equation time-steppers," *Philosophical Transactions of the Royal Society A,* vol. 380, no. 2229, p. 20210200, 2022.

[290] O. Sen, S. Davis, G. Jacobs, and H. Udaykumar, "Evaluation of convergence behavior of metamodeling techniques for bridging scales in multi-scale multimaterial simulation," *Journal of Computational Physics,* vol. 294, pp. 585-604, 2015.

[291] J. Hasenauer, N. Jagiella, S. Hross, and F. J. Theis, "Data-driven modelling of biological multi-scale processes," *Journal of Coupled Systems and Multiscale Dynamics,* vol. 3, no. 2, pp. 101-121, 2015.

[292] S. Zhang, P. Zhu, P. D. Arendt, and W. Chen, "Extended objective-oriented sequential sampling method for robust design of complex systems against design uncertainty," in *International Design Engineering Technical Conferences and Computers and Information in Engineering Conference,* 2012, vol. 45011: American Society of Mechanical Engineers, pp. 1237-1246.

[293] J. Qiu, W. Ji, H.-K. Lam, and M. Wang, "Fuzzy-Affine-Model-Based Sampled-Data Filtering Design for Stochastic Nonlinear Systems," *IEEE transactions on fuzzy systems,* vol. 29, no. 11, pp. 3360-3373, 2020.

[294] L. Ljung, *System identification*. Springer, 1998.

[295] B. Azhagusundari and A. S. Thanamani, "Feature selection based on information gain," *International Journal of Innovative Technology and Exploring Engineering (IJITEE),* vol. 2, no. 2, pp. 18-21, 2013.

[296] G. Franceschini and S. Macchietto, "Model-based design of experiments for parameter precision: State of the art," *Chemical Engineering Science,* vol. 63, no. 19, pp. 4846-4872, 2008.

[297] V. Venkatasubramanian, R. Rengaswamy, K. Yin, and S. N. Kavuri, "A review of process fault detection and diagnosis: Part I: Quantitative model-based methods," *Computers & chemical engineering,* vol. 27, no. 3, pp. 293-311, 2003.

[298] S. G. Hyberts, H. Arthanari, and G. Wagner, "Applications of non-uniform sampling and processing," *Novel sampling approaches in higher dimensional NMR,* pp. 125-148, 2012.

[299] B. Settles, "Active learning," *Synthesis lectures on artificial intelligence and machine learning,* vol. 6, no. 1, pp. 1-114, 2012.

[300] B. Smucker, M. Krzywinski, and N. Altman, "Optimal experimental design," *Nat. Methods,* vol. 15, no. 8, pp. 559-560, 2018.

[301] J. Snoek, H. Larochelle, and R. P. Adams, "Practical bayesian optimization of machine learning algorithms," *Advances in neural information processing systems,* vol. 25, 2012.

[302] Y. Wu, M. Rosca, and T. Lillicrap, "Deep compressed sensing," in *International Conference on Machine Learning*, 2019: PMLR, pp. 6850-6860.

[303] S. Ji, Y. Xue, and L. Carin, "Bayesian compressive sensing," *IEEE Transactions on signal processing*, vol. 56, no. 6, pp. 2346-2356, 2008.

[304] Y. Sui, "Weighted l1 minimization techniques for compressed sensing and their applications," 2020.

[305] J. A. Tropp and A. C. Gilbert, "Signal recovery from random measurements via orthogonal matching pursuit," *IEEE Transactions on information theory*, vol. 53, no. 12, pp. 4655-4666, 2007.

[306] M. E. Tipping, "Sparse Bayesian learning and the relevance vector machine," *Journal of machine learning research*, vol. 1, no. Jun, pp. 211-244, 2001.

[307] M. Elad, *Sparse and redundant representations: from theory to applications in signal and image processing* (no. 1). Springer, 2010.

[308] S. D. Babacan, M. Luessi, R. Molina, and A. K. Katsaggelos, "Sparse Bayesian methods for low-rank matrix estimation," *IEEE Transactions on Signal Processing*, vol. 60, no. 8, pp. 3964-3977, 2012.

[309] R. S. Sutton and A. G. Barto, *Reinforcement learning: An introduction*. MIT press, 2018.

[310] F. Garcia and E. Rachelson, "Markov decision processes," *Markov Decision Processes in Artificial Intelligence*, pp. 1-38, 2013.

[311] S. Fujimoto, H. Hoof, and D. Meger, "Addressing function approximation error in actor-critic methods," in *International conference on machine learning*, 2018: PMLR, pp. 1587-1596.

[312] S. Conde, I. Fekete, and J. N. Shadid, "Embedded error estimation and adaptive step-size control for optimal explicit strong stability preserving Runge--Kutta methods," *arXiv preprint arXiv:1806.08693*, 2018.

[313] P. M. Djuric *et al.*, "Particle filtering," *IEEE signal processing magazine,* vol. 20, no. 5, pp. 19-38, 2003.

[314] K. Xia *et al.*, "A digital twin to train deep reinforcement learning agent for smart manufacturing plants: Environment, interfaces and intelligence," *Journal of Manufacturing Systems,* vol. 58, pp. 210-230, 2021.

[315] J. Karki, "Active low-pass filter design," *Texas Instruments application report,* 2000.

[316] J. Zhang, "An explicit fourth-order compact finite difference scheme for three-dimensional convection–diffusion equation," *Communications in numerical methods in engineering,* vol. 14, no. 3, pp. 209-218, 1998.

[317] R. Chartrand, "Numerical differentiation of noisy, nonsmooth data," *International Scholarly Research Notices,* vol. 2011, 2011.

[318] A. K. Cline, C. B. Moler, G. W. Stewart, and J. H. Wilkinson, "An estimate for the condition number of a matrix," *SIAM Journal on Numerical Analysis,* vol. 16, no. 2, pp. 368-375, 1979.

[319] S. Srinivasa, "A review on multivariate mutual information," *Univ. of Notre Dame, Notre Dame, Indiana,* vol. 2, no. 1, 2005.

[320] J. Jeon, W. Kim, W. Jung, and Y. Sung, "Maser: Multi-agent reinforcement learning with subgoals generated from experience replay buffer," in *International Conference on Machine Learning*, 2022: PMLR, pp. 10041-10052.

[321] T. Haarnoja, A. Zhou, P. Abbeel, and S. Levine, "Soft actor-critic: Off-policy maximum entropy deep reinforcement learning with a stochastic actor," in *International conference on machine learning*, 2018: PMLR, pp. 1861-1870.

[322] T. Q. Le, S. T. Bukkapatnam, B. A. Benjamin, B. A. Wilkins, and R. Komanduri, "Topology and random-walk network representation of cardiac dynamics for localization of myocardial infarction," *IEEE Transactions on Biomedical Engineering*, vol. 60, no. 8, pp. 2325-2331, 2013.

[323] P. E. Peppard, T. Young, J. H. Barnet, M. Palta, E. W. Hagen, and K. M. Hla, "Increased prevalence of sleep-disordered breathing in adults," *American journal of epidemiology*, vol. 177, no. 9, pp. 1006-1014, 2013.

[324] L. F. Drager, S. M. Togeiro, V. Y. Polotsky, and G. Lorenzi-Filho, "Obstructive sleep apnea: a cardiometabolic risk in obesity and the metabolic syndrome," *Journal of the American College of Cardiology*, vol. 62, no. 7, pp. 569-576, 2013.

[325] S. Javaheri *et al.*, "Sleep apnea: types, mechanisms, and clinical cardiovascular consequences," *Journal of the American College of Cardiology*, vol. 69, no. 7, pp. 841-858, 2017.

[326] D. J. Gottlieb *et al.*, "Prospective study of obstructive sleep apnea and incident coronary heart disease and heart failure: the sleep heart health study," *Circulation*, vol. 122, no. 4, pp. 352-360, 2010.

[327] K. J. Åström and B. Wittenmark, *Adaptive control*. Courier Corporation, 2013.

[328] A. R. Schwartz, S. P. Patil, A. M. Laffan, V. Polotsky, H. Schneider, and P. L. Smith, "Obesity and obstructive sleep apnea: pathogenic mechanisms and therapeutic approaches," *Proceedings of the American Thoracic Society*, vol. 5, no. 2, pp. 185-192, 2008.

[329] J. M. Marin, S. J. Carrizo, E. Vicente, and A. G. Agusti, "Long-term cardiovascular outcomes in men with obstructive sleep apnoea-hypopnoea with or without treatment with continuous positive airway pressure: an observational study," *The Lancet,* vol. 365, no. 9464, pp. 1046-1053, 2005.

[330] W. J. Randerath *et al.*, "Non-CPAP therapies in obstructive sleep apnoea," ed: Eur Respiratory Soc, 2011.

[331] J. Sun, S. Xu, Y. Liu, and H. Zhang, "Combination therapy-based adaptive control for organism using medicine dosage regulation mechanism," in *Adaptive Dynamic Programming: For Chemotherapy Drug Delivery*: Springer, 2023, pp. 93-113.

[332] H. Fröhlich *et al.*, "From hype to reality: data science enabling personalized medicine," *BMC medicine,* vol. 16, no. 1, pp. 1-15, 2018.

[333] J. A. Mindell and J. A. Owens, *A clinical guide to pediatric sleep: diagnosis and management of sleep problems*. Lippincott Williams & Wilkins, 2015.

[334] N. T. Ayas, S. Pittman, M. MacDonald, and D. P. White, "Assessment of a wrist-worn device in the detection of obstructive sleep apnea," *Sleep medicine,* vol. 4, no. 5, pp. 435-442, 2003.

[335] M. Younes, M. Ostrowski, W. Thompson, C. Leslie, and W. Shewchuk, "Chemical control stability in patients with obstructive sleep apnea," *American journal of respiratory and critical care medicine,* vol. 163, no. 5, pp. 1181-1190, 2001.

[336] M. Morrell *et al.*, "Changes in brain morphology in patients with obstructive sleep apnoea," *Thorax,* vol. 65, no. 10, pp. 908-914, 2010.

[337] O. Mesarwi, J. Polak, J. Jun, and V. Y. Polotsky, "Sleep disorders and the development of insulin resistance and obesity," *Endocrinology and Metabolism Clinics,* vol. 42, no. 3, pp. 617-634, 2013.

[338] E. I. Schwarz, M. A. Puhan, C. Schlatzer, J. R. Stradling, and M. Kohler, "Effect of CPAP therapy on endothelial function in obstructive sleep apnoea: a systematic review and meta-analysis," *Respirology,* vol. 20, no. 6, pp. 889-895, 2015.

[339] M. Georgoulis *et al.,* "A weight-loss Mediterranean diet/lifestyle intervention ameliorates inflammation and oxidative stress in patients with obstructive sleep apnea: Results of the "MIMOSA" randomized clinical trial," *European journal of nutrition,* vol. 60, pp. 3799-3810, 2021.

[340] D. J. Gottlieb and N. M. Punjabi, "Diagnosis and management of obstructive sleep apnea: a review," *Jama,* vol. 323, no. 14, pp. 1389-1400, 2020.

[341] N. Zhu *et al.,* "A novel coronavirus from patients with pneumonia in China, 2019," *New England journal of medicine,* 2020.

[342] V. M. Corman *et al.,* "Detection of 2019 novel coronavirus (2019-nCoV) by real-time RT-PCR," *Eurosurveillance,* vol. 25, no. 3, p. 2000045, 2020.

[343] E. C. Goligher *et al.,* "Evolution of diaphragm thickness during mechanical ventilation. Impact of inspiratory effort," *American journal of respiratory and critical care medicine,* vol. 192, no. 9, pp. 1080-1088, 2015.

[344] M. J. Tobin, "Basing respiratory management of COVID-19 on physiological principles," vol. 201, ed: American Thoracic Society, 2020, pp. 1319-1320.

[345] G. K. Wolf and J. H. Arnold, "Noninvasive assessment of lung volume: respiratory inductance plethysmography and electrical impedance tomography," *Critical care medicine,* vol. 33, no. 3, pp. S163-S169, 2005.

[346] B. H. Brown, "Electrical impedance tomography (EIT): a review," *Journal of medical engineering & technology,* vol. 27, no. 3, pp. 97-108, 2003.

[347] O. Thiabgoh, T. Eggers, and M.-H. Phan, "A new contactless magneto-LC resonance technology for real-time respiratory motion monitoring," *Sensors and Actuators A: Physical,* vol. 265, pp. 120-126, 2017.

[348] K. Y. Hwang *et al.,* "A novel magnetic respiratory sensor for human healthcare," *Applied Sciences,* vol. 11, no. 8, p. 3585, 2021.

[349] R. T. Brouillette, A. S. Morrow, D. E. Weese-Mayer, and C. E. Hunt, "Comparison of respiratory inductive plethysmography and thoracic impedance for apnea monitoring," *The Journal of pediatrics,* vol. 111, no. 3, pp. 377-383, 1987.

[350] I. Frerichs *et al.,* "Chest electrical impedance tomography examination, data analysis, terminology, clinical use and recommendations: consensus statement of the TRanslational EIT developmeNt stuDy group," *Thorax,* vol. 72, no. 1, pp. 83-93, 2017.

[351] V. O. Jimenez *et al.,* "Magnetoimpedance Biosensors and Real-Time Healthcare Monitors: Progress, Opportunities, and Challenges," *Biosensors,* vol. 12, no. 7, p. 517, 2022.

[352] S. C. Buttery, M. Zysman, S. A. Vikjord, N. S. Hopkinson, C. Jenkins, and L. E. Vanfleteren, "Contemporary perspectives in COPD: patient burden, the role of gender and trajectories of multimorbidity," *Respirology,* vol. 26, no. 5, pp. 419-441, 2021.

[353] J. Xie *et al.,* "Association between hypoxemia and mortality in patients with COVID-19," in *Mayo Clinic Proceedings*, 2020, vol. 95, no. 6: Elsevier, pp. 1138-1147.

[354] Y. Liu *et al.*, "Viral dynamics in mild and severe cases of COVID-19," *The Lancet infectious diseases,* vol. 20, no. 6, pp. 656-657, 2020.

[355] W. Ottestad and S. Søvik, "COVID-19 patients with respiratory failure: what can we learn from aviation medicine?," *British journal of anaesthesia,* vol. 125, no. 3, pp. e280-e281, 2020.

[356] K. Shailaja, B. Seetharamulu, and M. Jabbar, "Machine learning in healthcare: A review," in *2018 Second international conference on electronics, communication and aerospace technology (ICECA)*, 2018: IEEE, pp. 910-914.

[357] P. Rajpurkar *et al.*, "Deep learning for chest radiograph diagnosis: A retrospective comparison of the CheXNeXt algorithm to practicing radiologists," *PLoS medicine,* vol. 15, no. 11, p. e1002686, 2018.

[358] T. Q. Le and S. T. Bukkapatnam, "Nonlinear dynamics forecasting of obstructive sleep apnea onsets," *PloS one,* vol. 11, no. 11, p. e0164406, 2016.

[359] K. Y. H. M.H. Phan, V. Ortiz Jimenez, and B. Muchharla, "Real-Time Monitoring of Coronavirus Progress using Magnetic Sensing and Machine Learning," United States Patent Appl. 17 /331,761, 2021. [Online]. Available: https://patents.google.com/patent/US20210369137A1/en

[360] I. D. Apostolopoulos and T. A. Mpesiana, "Covid-19: automatic detection from x-ray images utilizing transfer learning with convolutional neural networks," *Physical and engineering sciences in medicine,* vol. 43, pp. 635-640, 2020.

[361] T. Ozturk, M. Talo, E. A. Yildirim, U. B. Baloglu, O. Yildirim, and U. R. Acharya, "Automated detection of COVID-19 cases using deep neural networks with X-ray images," *Computers in biology and medicine,* vol. 121, p. 103792, 2020.

[362] L. Yan *et al.*, "Prediction of criticality in patients with severe Covid-19 infection using three clinical features: a machine learning-based prognostic model with clinical data in Wuhan," *MedRxiv,* p. 2020.02. 27.20028027, 2020.

[363] A. Kaplan *et al.*, "Artificial intelligence/machine learning in respiratory medicine and potential role in asthma and COPD diagnosis," *The Journal of Allergy and Clinical Immunology: In Practice,* vol. 9, no. 6, pp. 2255-2261, 2021.

[364] K. R. Mahmudah, B. Purnama, F. Indriani, and K. Satou, "Machine Learning Algorithms for Predicting Chronic Obstructive Pulmonary Disease from Gene Expression Data with Class Imbalance," in *BIOINFORMATICS*, 2021, pp. 148-153.

[365] K. Swetha, M. Niranjanamurthy, M. Amulya, and Y. Manu, "Prediction of pneumonia using big data, deep learning and machine learning techniques," in *2021 6th International Conference on Communication and Electronics Systems (ICCES)*, 2021: IEEE, pp. 1697-1700.

[366] I. Bendavid *et al.*, "A novel machine learning model to predict respiratory failure and invasive mechanical ventilation in critically ill patients suffering from COVID-19," *Scientific Reports,* vol. 12, no. 1, p. 10573, 2022.

[367] D. J. Miller *et al.*, "Analyzing changes in respiratory rate to predict the risk of COVID-19 infection," *PloS one,* vol. 15, no. 12, p. e0243693, 2020.

[368] X. Ni *et al.*, "Automated, multiparametric monitoring of respiratory biomarkers and vital signs in clinical and home settings for COVID-19 patients," *Proceedings of the National Academy of Sciences,* vol. 118, no. 19, p. e2026610118, 2021.

[369] K. K. Lella and A. Pja, "Automatic diagnosis of COVID-19 disease using deep convolutional neural network with multi-feature channel from respiratory sound data: cough, voice, and breath," *Alexandria Engineering Journal,* vol. 61, no. 2, pp. 1319-1334, 2022.

[370] S. Baker, W. Xiang, and I. Atkinson, "Determining respiratory rate from photoplethysmogram and electrocardiogram signals using respiratory quality indices and neural networks," *Plos one,* vol. 16, no. 4, p. e0249843, 2021.

[371] C. L. Webber Jr and J. P. Zbilut, "Recurrence quantification analysis of nonlinear dynamical systems," *Tutorials in contemporary nonlinear methods for the behavioral sciences,* vol. 94, no. 2005, pp. 26-94, 2005.

[372] K. Soman, R. Loganathan, and V. Ajay, *Machine learning with SVM and other kernel methods*. PHI Learning Pvt. Ltd., 2009.

[373] C. D. Sutton, "Classification and regression trees, bagging, and boosting," *Handbook of statistics,* vol. 24, pp. 303-329, 2005.

[374] S. Pecorelli, G. Favalli, L. Zigliani, and F. Odicino, "Cancer in women," *International Journal of Gynecology & Obstetrics,* vol. 82, no. 3, pp. 369-379, 2003.

[375] Z. Momenimovahed, A. Tiznobaik, S. Taheri, and H. Salehiniya, "Ovarian cancer in the world: epidemiology and risk factors," *International journal of women's health,* pp. 287-299, 2019.

[376] B. Chernet and M. Levin, "Endogenous voltage potentials and the microenvironment: bioelectric signals that reveal, induce and normalize cancer," *Journal of clinical & experimental oncology,* 2013.

[377] M. Yang and W. J. Brackenbury, "Membrane potential and cancer progression," *Frontiers in physiology,* vol. 4, p. 185, 2013.

[378] H. Zhao *et al.,* "Electrostatic potential difference between tumor and paratumor regulates cancer stem cell behavior and prognose tumor spread," *Bioengineering & Translational Medicine,* p. e10399, 2022.

[379] W. Melitz, J. Shen, A. C. Kummel, and S. Lee, "Kelvin probe force microscopy and its application," *Surface science reports,* vol. 66, no. 1, pp. 1-27, 2011.

[380] J. Park *et al.,* "Single-molecule recognition of biomolecular interaction via Kelvin probe force microscopy," *ACS nano,* vol. 5, no. 9, pp. 6981-6990, 2011.

[381] G. Lee *et al.,* "Mapping the surface charge distribution of amyloid fibril," *Applied Physics Letters,* vol. 101, no. 4, p. 043703, 2012.

[382] W. Lee *et al.,* "Characterization of the regrowth behavior of amyloid-like fragmented fibrils decomposed by ultrasonic treatment," *RSC Advances,* vol. 4, no. 100, pp. 56561-56566, 2014.

[383] C. Leung, D. Maradan, A. Kramer, S. Howorka, P. Mesquida, and B. W. Hoogenboom, "Improved Kelvin probe force microscopy for imaging individual DNA molecules on insulating surfaces," *Applied Physics Letters,* vol. 97, no. 20, p. 203703, 2010.

[384] D. N. Richards *et al.,* "DNA immobilization on GaP (100) investigated by kelvin probe force microscopy," *The Journal of Physical Chemistry C,* vol. 114, no. 36, pp. 15486-15490, 2010.

[385] H. Lee, W. Lee, J. H. Lee, and D. S. Yoon, "Surface potential analysis of nanoscale biomaterials and devices using kelvin probe force microscopy," *Journal of Nanomaterials,* vol. 2016, 2016.

[386] P. Gao and Y. Cai, "Label-free detection of the aptamer binding on protein patterns using Kelvin probe force microscopy (KPFM)," *Analytical and bioanalytical chemistry,* vol. 394, no. 1, pp. 207-214, 2009.

[387] C.-C. Tsai, H.-H. Hung, C.-P. Liu, Y.-T. Chen, and C.-Y. Pan, "Changes in plasma membrane surface potential of PC12 cells as measured by Kelvin probe force microscopy," *PLoS One,* vol. 7, no. 4, p. e33849, 2012.

[388] W. Zhao, W. Cui, S. Xu, L.-Z. Cheong, D. Wang, and C. Shen, "Direct study of the electrical properties of PC12 cells and hippocampal neurons by EFM and KPFM," *Nanoscale Advances,* vol. 1, no. 2, pp. 537-545, 2019.

[389] H. Lee *et al.*, "Kelvin probe force microscopy of DNA-capped nanoparticles for single-nucleotide polymorphism detection," *Nanoscale,* vol. 8, no. 28, pp. 13537-13544, 2016.

[390] K. Jang, J. Choi, C. Park, and S. Na, "Label-free and high-sensitive detection of Kirsten rat sarcoma viral oncogene homolog and epidermal growth factor receptor mutation using Kelvin probe force microscopy," *Biosensors and Bioelectronics,* vol. 87, pp. 222-228, 2017.

[391] T. Kwon, S. Gunasekaran, and K. Eom, "Atomic force microscopy-based cancer diagnosis by detecting cancer-specific biomolecules and cells," *Biochimica et Biophysica Acta (BBA)-Reviews on Cancer,* vol. 1871, no. 2, pp. 367-378, 2019.

[392] J. Zemła, J. Danilkiewicz, B. Orzechowska, J. Pabijan, S. Seweryn, and M. Lekka, "Atomic force microscopy as a tool for assessing the cellular elasticity and adhesiveness to identify cancer cells and tissues," in *Seminars in cell & developmental biology*, 2018, vol. 73: Elsevier, pp. 115-124.

[393] X. Deng *et al.*, "Application of atomic force microscopy in cancer research," *Journal of nanobiotechnology,* vol. 16, no. 1, pp. 1-15, 2018.

[394] L. Bemmerlein *et al.*, "Decoding Single Cell Morphology in Osteotropic Breast Cancer Cells for Dissecting Their Migratory, Molecular and Biophysical Heterogeneity," *Cancers,* vol. 14, no. 3, p. 603, 2022.

[395] S. E. Cross, Y.-S. Jin, J. Tondre, R. Wong, J. Rao, and J. K. Gimzewski, "AFM-based analysis of human metastatic cancer cells," *Nanotechnology,* vol. 19, no. 38, p. 384003, 2008.

[396] M. E. Dokukin, N. V. Guz, R. M. Gaikwad, C. D. Woodworth, and I. Sokolov, "Cell surface as a fractal: normal and cancerous cervical cells demonstrate different fractal behavior of surface adhesion maps at the nanoscale," *Physical review letters,* vol. 107, no. 2, p. 028101, 2011.

[397] E. Bakalis *et al.*, "Universal Markers Unveil Metastatic Cancerous Cross-Sections at Nanoscale," *Cancers,* vol. 14, no. 15, p. 3728, 2022.

[398] A. Mezheyeuski *et al.*, "Image analysis-derived metrics of histomorphological complexity predicts prognosis and treatment response in stage II-III colon cancer," *Scientific reports,* vol. 6, no. 1, pp. 1-9, 2016.

[399] F. E. Lennon *et al.*, "Lung cancer—a fractal viewpoint," *Nature reviews Clinical oncology,* vol. 12, no. 11, pp. 664-675, 2015.

[400] M. Bizzarri, A. Giuliani, A. Cucina, F. D'Anselmi, A. M. Soto, and C. Sonnenschein, "Fractal analysis in a systems biology approach to cancer," in *Seminars in cancer biology,* 2011, vol. 21, no. 3: Elsevier, pp. 175-182.

[401] P. Kestener, J. M. Lina, P. Saint-Jean, and A. Arneodo, "Wavelet-based multifractal formalism to assist in diagnosis in digitized mammograms," *Image Analysis & Stereology,* vol. 20, no. 3, pp. 169-174, 2001.

[402] N. V. Guz, M. E. Dokukin, C. D. Woodworth, A. Cardin, and I. Sokolov, "Towards early detection of cervical cancer: Fractal dimension of AFM images of human cervical epithelial cells at different stages of progression to cancer," *Nanomedicine: Nanotechnology, Biology and Medicine,* vol. 11, no. 7, pp. 1667-1675, 2015.

[403] R. Lopes and N. Betrouni, "Fractal and multifractal analysis: a review," *Medical image analysis,* vol. 13, no. 4, pp. 634-649, 2009.

[404] J. d. D. H. Velázquez, S. Mejía-Rosales, and A. G. Goicochea, "Fractal properties of biophysical models of pericellular brushes can be used to differentiate between cancerous and normal cervical epithelial cells," *Colloids and Surfaces B: Biointerfaces,* vol. 170, pp. 572-577, 2018.

[405] R. Sedivy and R. M. Mader, "Fractals, chaos, and cancer: do they coincide?," *Cancer investigation,* vol. 15, no. 6, pp. 601-607, 1997.

[406] J. W. Baish and R. K. Jain, "Fractals and cancer," *Cancer research,* vol. 60, no. 14, pp. 3683-3688, 2000.

[407] B. B. Mandelbrot, *Multifractals and 1/f noise: Wild self-affinity in physics (1963–1976)*. Springer, 2013.

[408] Q. Cheng, "Multifractality and spatial statistics," *Computers & Geosciences,* vol. 25, no. 9, pp. 949-961, 1999.

[409] D. Bradley and G. Roth, "Adaptive thresholding using the integral image," *Journal of graphics tools,* vol. 12, no. 2, pp. 13-21, 2007.

[410] B. B. Mandelbrot, *The fractal geometry of nature*. WH freeman New York, 1982.

[411] Y. Liu *et al.*, "An improved differential box-counting method to estimate fractal dimensions of gray-level images," *Journal of visual communication and Image Representation,* vol. 25, no. 5, pp. 1102-1111, 2014.

[412] E. M. Griner and M. G. Kazanietz, "Protein kinase C and other diacylglycerol effectors in cancer," *Nature Reviews Cancer,* vol. 7, no. 4, pp. 281-294, 2007.

[413] T. Smalley, R. Metcalf, R. Patel, S. A. Islam, R. R. Bommareddy, and M. Acevedo-Duncan, "The atypical protein kinase c small molecule inhibitor ζ-stat, and its effects on invasion through decreases in pkc-ζ protein expression," *Frontiers in Oncology*, vol. 10, p. 209, 2020.

[414] S. Kouba *et al.*, "Lipid metabolism and Calcium signaling in epithelial ovarian cancer," *Cell calcium,* vol. 81, pp. 38-50, 2019.

[415] A. J. Keung, S. Kumar, and D. V. Schaffer, "Presentation counts: microenvironmental regulation of stem cells by biophysical and material cues," *Annual review of cell and developmental biology,* vol. 26, pp. 533-556, 2010.

[416] M. J. Dalby, N. Gadegaard, and R. O. Oreffo, "Harnessing nanotopography and integrin–matrix interactions to influence stem cell fate," *Nature materials,* vol. 13, no. 6, pp. 558-569, 2014.

[417] C. Wei, X. Wang, M. Chen, K. Ouyang, L.-S. Song, and H. Cheng, "Calcium flickers steer cell migration," *Nature,* vol. 457, no. 7231, pp. 901-905, 2009.

[418] A. K. Sinensky and A. M. Belcher, "Label-free and high-resolution protein/DNA nanoarray analysis using Kelvin probe force microscopy," *Nature nanotechnology,* vol. 2, no. 10, pp. 653-659, 2007.

Appendix A: Supplementary File of Probabilistic Domain-Knowledge Modeling

Derivation of Equation 4.6 in Chapter 4 is as follows:

We start with the equation of updating the pathogenetic states $PM_i^{(t+1)}$ given observations $o_i^{(1:t+1)}$. By Bayes rule, we yielded:

$$P\left(PM_i^{(t+1)}\middle|o_i^{(1:t+1)}\right) \propto P\left(o_i^{(t+1)}|PM_i^{(t+1)}\right)P\left(PM_i^{(t+1)}\middle|o_i^{(1:t)}\right)$$

To compute one-step ahead prediction $P\left(PM_i^{(t+1)}\middle|o_i^{(1:t)}\right)$, we need to marginalize out $PM_i^{(t)}$:

$$P\left(PM_i^{(t+1)}\middle|o_i^{(1:t)}\right) = \sum_{PM_i^{(t)}} P\left(PM_i^{(t+1)}\middle|PM_i^{(t)}\right)P\left(PM_i^{(t)}\middle|o_i^{(t)}\right)$$

As stated, the state-observation model was used with the inclusion of two components: a state transition model $P\left(PM_i^{(t+1)}\middle|PM_i^{(t)}\right)$ and an observation model $P\left(PM_i^{(t)}\middle|O_i^{(t)}\right)$. So, the parameters of those two distributions were learned from the training data. Now, we extend to multiple-step ahead prediction $P\left(PM_i^{(t+h)}\middle|o_i^{(1:t)}\right)$, where $h \geq 0$ is the forecasting horizon. Again, $P\left(PM_i^{(t+h)}\middle|o_i^{(1:t)}\right)$ was computed by marginalizing out PM_i at from t to $t+h-1$:

$$P\left(PM_i^{(t+h)}\middle|o_i^{(1:t)}\right) = \sum_{PM_i^{(t:t+h-1)}} P\left(PM_i^{(t)}, PM_i^{(t+1)}, \dots, PM_i^{(t+h)}|o_i^{(1:t)}\right)$$

$$= \sum_{PM_i^{(t:t+h-1)}} P\left(PM_i^{(t:t+h)}|o_i^{(1:t)}\right)$$

Equation above showed that the computation of $P\left(PM_i^{(t+h)}\middle|o_i^{(1:t)}\right)$ requires the computation of $P\left(PM_i^{(t+\delta)}\middle|o_i^{(1:t)}\right)$, where $0 \le \delta \le t+h$, by Bayes rule, we have:

$$P\left(PM_i^{(t+\delta)}\middle|o_i^{(1:t)}\right) = \sum_{PM_i^{(t:t+\delta-1)}} P\left(PM_i^{(t:t+\delta)}|o_i^{(1:t)}\right)$$

$$= \sum_{PM_i^{(t+\delta-1)}} P\left(PM_i^{(t+\delta)}|PM_i^{(t+\delta-1)}, o_i^{(1:t)}\right)P\left(PM_i^{(t+\delta-1)}|o_i^{(1:t)}\right)$$

To illustrate the above equation, we first compute $P\left(PM_i^{(t+2)}\middle|o_i^{(1:t)}\right)$ from $P\left(PM_i^{(t+1)}\middle|o_i^{(1:t)}\right)$:

$$P\left(PM_i^{(t+2)}\middle|o_i^{(1:t)}\right) = \sum_{PM_i^{(t:t+1)}} P\left(PM_i^{(t+2)}|PM_i^{(t+1)}, o_i^{(1:t)}\right)P\left(PM_i^{(t+1)}|o_i^{(1:t)}\right)$$

$$= \sum_{PM_i^{(t:t+1)}} P\left(PM_i^{(t+2)}|PM_i^{(t+1)}, o_i^{(1:t)}\right) \sum_{PM_i^{(t)}} P\left(PM_i^{(t+1)}\middle|PM_i^{(t)}\right)P\left(PM_i^{(t)}\middle|o_i^{(t)}\right)$$

After this step, we can estimate the distribution $P\left(PM_i^{(t+2)}\middle|o_i^{(1:t)}\right)$, for $\delta = 3$, we yield:

$$P\left(PM_i^{(t+3)}\middle|o_i^{(1:t)}\right) = \sum_{PM_i^{(t:t+2)}} P\left(PM_i^{(t:t+2)}|o_i^{(1:t)}\right)$$

$$= \sum_{PM_i^{(t:t+2)}} P\left(PM_i^{(t+3)}|PM_i^{(t+2)}, o_i^{(1:t)}\right)P\left(PM_i^{(t+2)}|o_i^{(1:t)}\right)$$

$$= \sum_{PM_i^{(t:t+2)}} P\left(PM_i^{(t+3)}|PM_i^{(t+2)}, o_i^{(1:t)}\right) \sum_{PM_i^{(t:t+1)}} \sum_{PM_i^{(t)}} P\left(PM_i^{(t+2)}|PM_i^{(t+1)}, o_i^{(1:t)}\right) P\left(PM_i^{(t+1)}\middle|PM_i^{(t)}\right)P\left(PM_i^{(t)}\middle|o_i^{(t)}\right) \quad (1)$$

For larger $\delta \ge 3$, the same principle would be applied. Hence, we have:

$$P\left(PM_i^{(t+\delta)}|o_i^{(1:t)}\right) = \sum_{PM_i^{(t:t+\delta-1)}} P\left(PM_i^{(t+\delta)}|PM_i^{(t+\delta-1)}, o_i^{(1:t)}\right) P\left(PM_i^{(t+\delta-1)}|o_i^{(1:t)}\right)$$

$$\prod_{\delta=1}^{h} P\left(PM_i^{(t+\delta)}|o_i^{(1:t)}\right) = P\left(PM_i^{(t:t+\delta)}|o_i^{(1:t)}\right) \quad (2)$$

$$\sum_{PM_i^{(t:t+h-1)}} P\left(PM_i^{(t:t+\delta)}|o_i^{(1:t)}\right) = P\left(PM_i^{(t+h)}\middle|o_i^{(1:t)}\right) \quad (3)$$

From (1), (2), and (3), we yielded:

$$P\left(PM_i^{(t+h)}\middle|o_i^{(1:t)}\right) = \sum_{PM_i^{(t:t+h-1)}} \prod_{\delta=1}^{h} \sum_{PM_i^{(t+\delta-1)}} P\left(PM_i^{(t+\delta)}|PM_i^{(t+\delta-1)}, o_i^{(1:t)}\right) P\left(PM_i^{(t+\delta-1)}|o_i^{(1:t)}\right) \blacksquare$$

Table A-1 Detailed descriptions of 10 variables in the static Bayesian network of OSA case study including their abbreviations, value set, CPD specifications, and underlying assumptions

	Variables	Value set	Probability distribution
RISK FACTORS	**Age group ($\boldsymbol{AG}$)**	$Val(\boldsymbol{AG}) = \{1,2,3\}$ • 1 = Young adult • 2 = Adult and middle-aged • 3 = Senior	$\boldsymbol{AG} = \begin{cases} 1\ if\ 18 \le Age \le 25 \\ 2\ if\ 26 \le Age \le 60 \\ 3 \quad if\ Age > 60 \end{cases}$ $P(\boldsymbol{AG}=1) = 0.15, P(\boldsymbol{AG}=2) = 0.55, P(\boldsymbol{AG}=3) = 0.3.$
	Gender ($\boldsymbol{G}$)	$Val(\boldsymbol{G}) = \{1,2\}$ • 1 = Female • 2 = Male	$P(\boldsymbol{G}=1) = P(\boldsymbol{G}=2) = 0.5$
	Obesity ($\boldsymbol{OB}$)	$Val(\boldsymbol{OB}) = \{1,2,3\}$ • 1 = Overweight • 2 = Obesity • 3 = Morbid Obesity	$\boldsymbol{OB} = \begin{cases} 1\ if\ 25 \le \boldsymbol{BMI} \le 30 \\ 2\ if\ 30 < \boldsymbol{BMI} \le 40 \\ 3 \quad if\ \boldsymbol{BMI} > 40 \end{cases}$ $P(\boldsymbol{OB}=1) = 0.25, P(\boldsymbol{OB}=2) = 0.45, P(\boldsymbol{OB}=3) = 0.3.$
	OSA severity ($\boldsymbol{OS}$)	$Val(\boldsymbol{OS}) = \{1,2,3\}$ • 1 = Mild • 2 = Moderate • 3 = Severe	$\boldsymbol{OS} = \begin{cases} 1\ if\ 6 \le \boldsymbol{AHI} \le 20 \\ 2\ if\ 21 \le \boldsymbol{AHI} \le 40 \\ 3 \quad if\ \boldsymbol{AHI} > 40 \end{cases}$ where $\boldsymbol{AHI}$ is Apnea-Hypopnea Index $P(\boldsymbol{OB}=1) = 0.25, P(\boldsymbol{OB}=2) = 0.45, P(\boldsymbol{OB}=3) = 0.3.$

Table A-1 (Continued)

STRUCTURAL ABNORMALITIES	**Tissue enlargement ($\boldsymbol{TE}$)**	$\boldsymbol{Val(TE) = \{1, 2\}}$ • 1 = Absent • 2 = Present	$\boldsymbol{TE|(G = 0)} = \begin{cases} \boldsymbol{0\ if\ NC < 15\ in} \\ \boldsymbol{1\ \ if\ otherwise} \end{cases}$ $\boldsymbol{TE|(G = 1)} = \begin{cases} \boldsymbol{0\ if\ NC < 17\ in} \\ \boldsymbol{1\ \ if\ otherwise} \end{cases}$ where $\boldsymbol{NC}$ is neck circumference $\boldsymbol{P(OB = 1) = 0.25, P(OB = 2) = 0.45, P(OB = 3) = 0.3.}$
	Craniofacial abnormality ($\boldsymbol{CA}$)	$Val(\boldsymbol{PCSA}) = \{1,2\}$ • 1 = Absent • 2 = Present	Determined by physical examination or X-ray images. $P(\boldsymbol{CA} = 1) = 0.3, P(\boldsymbol{CA} = 2) = 0.7$
	Pharyngeal cross-sectional area ($\boldsymbol{PCSA}$)	$Val(\boldsymbol{PCSA}) = \{1,2,3\}$ • 1 = Slightly small • 2 = Moderately small • 3 = Severely small	A tabular CPD was specified for the conditional distribution: $P(\boldsymbol{PCSA} = a_1 \boldsymbol{|TE} = a_2, \boldsymbol{CA} = a_3)$ An assignment tuple (a_1, a_2, a_3) corresponded to one entry in the table. Totally, there are $3 \times 2 \times 2 = 12$ values.
FUNCTIONAL ABNORMALITIES	**Defective UA reflexes ($\boldsymbol{DUAR}$)**	$Val(\boldsymbol{DUAR}) = \{1,2\}$ • 1 = Absent • 2 = Present	A tabular CPD was specified as: $P(\boldsymbol{DUAR} = a_1 \boldsymbol{|OS} = a_2)$ Totally, there are $3 \times 2 = 6$ values.
	Functional residual capacity ($\boldsymbol{FRC}$)	$Val(\boldsymbol{FRC}) = \{1,2\}$ • 1 = Normal • 2 = Abnormal	A tabular CPD was des: $P(\boldsymbol{FRC} = a_1 \boldsymbol{|OB} = a_2)$ Totally, there are $3 \times 2 = 6$ entries.
	UA Collapsibility ($\boldsymbol{UAC}$)	$Val(\boldsymbol{UAC}) = \{1,2,3\}$ • 1 = Mild • 2 = Moderate • 3 = Severe	A tabular CPD was specified for the conditional distribution: $P(\boldsymbol{UAC} = a_1 \boldsymbol{|OS} = a_2, \boldsymbol{AG} = a_3)$ There are $3 \times 3 \times 2 = 18$ parameters.

Table A-2 Detailed descriptions of variables in PAF PPGM model including their abbreviations, value set, CPD specifications, and underlying assumptions

Random variables	Value set	Conditional probability distribution (CPD)
SUBSTRATE (*S or ExoIn*)	$Val(\boldsymbol{S}) = \{1,2,3\}$ • 1 = Mildly vulnerable • 2 = Moderately vulnerable • 3 = Severely vulnerable	We discretized the substrate as follows: $$\boldsymbol{S} = \begin{cases} 1 & if\ Z < -1 \\ 2\ if & -1 \le Z \le 1 \\ 3 & if\ Z > 1 \end{cases}$$ where Z is the z-score of log ($\lambda_{extrasystole}$) of a certain patient, in which $\lambda_{extrasystole}$ is the number of PAC beats in 30-min ECG record.
PAC TYPE (PAC)	$Val(\boldsymbol{PAC}) = \{0,1,2,3,4,5,6\}$ • 0 = Normal • 1 = Bigeminy • 2 = Trigeminy • 3 = Quadrigeminy • 4 = Couplet • 5 = Triplet • 6 = Isolated	The observations of PAC type were derived from PAC detection algorithm output. Predictive time-slice transition model: $$P\left(\boldsymbol{PAC}^{(t+1)} = j \middle| \boldsymbol{PAC}^{(t)} = i\right) = \boldsymbol{A}(i,j)$$ Where $\boldsymbol{A}(i,j)$ is the Markov transition matrix estimated by $\frac{\#times\ state\ i \to state\ j}{\#total\ transitions}$, $i,j = 0,1,\ldots,6$.
ACCUMULATION LEVEL (AL)	$Val(\boldsymbol{AL}) = [0,\infty)$	Predictive time-slice transition model: $$\boldsymbol{AL}^{(t+1)} \mid \boldsymbol{AL}^{(t)} \sim \mathcal{N}\left(\exp\left(w_{\widehat{\boldsymbol{PAC}}^{(t+1)}}\right) \cdot \boldsymbol{AL}^{(t)}, \sigma^2_{\boldsymbol{AL}}\right)$$ where $w_{\widehat{\boldsymbol{PAC}}^{(t+1)}}$ is the weight corresponding to predicted PAC type at time $t+1$. The weights were calculated by the relative frequency of the PAC types multiplied with a constant.
ECTOPIC ACTIVITY (E)	$Val(\boldsymbol{E}) = \{0,1\}$ • 0 = Absent • 1 = Present	Initial distribution: $P\left(\boldsymbol{E}^{(0)} = 1\right) = 1$, which assumed that ectopic activity was not present at initial. Within time slice t: $$P\left(\boldsymbol{E}^{(t)} = 1 \middle| \boldsymbol{AL}^{(t)} = \zeta\right) = \frac{1}{1 + e^{-r(\zeta_0 - \zeta)}}$$ $$P\left(\boldsymbol{E}^{(t)} = 1 \middle| \boldsymbol{AL}^{(t)} = \zeta\right) = 1 - \frac{1}{1 + e^{-r(\zeta_0 - \zeta)}}$$ where $\boldsymbol{w_i} = \{w_0, w_1\}$ are the weights of Sigmoid function, ζ_0 is the time-average accumulation level and r is the steepness of the sigmoid. The parameters $\boldsymbol{w_i}$ and r were estimated using Iterative Reweighted Least Squares technique.

Table A-2 (Continued)

<table>
<tr>
<td>REENTRY ($\boldsymbol{R}$)</td>
<td>$Val(\boldsymbol{R}) = \{0,1\}$
• 0 = Absent
• 1 = Present</td>
<td>Tabular CPD is given as follows:
<table>
<tr><td>Conditioning values</td><td>$\boldsymbol{R^{(t)}} = 0$</td><td>$\boldsymbol{R^{(t)}} = 1$</td></tr>
<tr><td>$\boldsymbol{E^{(t)}} = 0$</td><td>θ_{R00}</td><td>$1 - \theta_{R00}$</td></tr>
<tr><td>$\boldsymbol{E^{(t)}} = 1$</td><td>θ_{R01}</td><td>$1 - \theta_{R01}$</td></tr>
</table>
where $\theta_{R00} = P(\boldsymbol{R^{(t)}} = 0|\boldsymbol{E^{(t)}} = 0)$ and $\theta_{R01} = P\left(\boldsymbol{R^{(t)}} = 0\middle|\boldsymbol{E^{(t)}} = 1\right)$ are parameters of the CPD.</td>
</tr>
<tr>
<td>LEAK ($\boldsymbol{L}$)</td>
<td>$Val(\boldsymbol{L}) = \{0,1\}$.
• 0 = Absent
• 1 = Present</td>
<td>Temporally constant assignment of $\boldsymbol{L^{(t)}}$ ($t \leq 0 \leq T$):
$$\boldsymbol{L^{(t)}} = \rho_0$$
where T is the number of time slices, and ρ_0 is the occurrence probability of all the other unmodeled causes that can turn the onset on.</td>
</tr>
<tr>
<td>ECTOPIC ACTIVITY FILTER ($\boldsymbol{Z_E}$)</td>
<td>$Val(\boldsymbol{Z_E}) = \{0,1\}$.
• 0 = Absent
• 1 = Present</td>
<td>$$\boldsymbol{P}\left(\boldsymbol{Z_E^{(t)}}\middle|\boldsymbol{E^{(t)}}\right) = \begin{cases} 0 \ if \ \boldsymbol{E^{(t)}} = 0 \\ \rho_1 \ if \ \boldsymbol{E^{(t)}} = 1 \end{cases}$$
where ρ_1 is the probability that ectopic activity mechanism can itself cause the onset.</td>
</tr>
<tr>
<td>REENTRY FILTER ($\boldsymbol{Z_R}$)</td>
<td>$Val(\boldsymbol{Z_R}) = \{0,1\}$.
• 0 = Absent
• 1 = Present</td>
<td>$$\boldsymbol{P}\left(\boldsymbol{Z_R^{(t)}}\middle|\boldsymbol{R^{(t)}}\right) = \begin{cases} 0 \ if \ \boldsymbol{R^{(t)}} = 0 \\ p_2 \ if \ \boldsymbol{R^{(t)}} = 1 \end{cases}$$
where ρ_2 is the probability that reentry mechanism can itself lead to the onset.</td>
</tr>
<tr>
<td>ONSET</td>
<td>$Val(\boldsymbol{Onset}) = \{0,1\}$.
• 0 = Absent
• 1 = Present</td>
<td>The parent set of $\boldsymbol{Onset}$: $Pa_{\boldsymbol{Onset^{(t)}}} = \{\boldsymbol{L}, \boldsymbol{R}, \boldsymbol{E}\}$
The probability that none of the mechanisms triggers the onset:
$$\boldsymbol{P}\left(\boldsymbol{Onset^{(t)}} = 0\middle|\boldsymbol{Z_R^{(t)}}, \boldsymbol{Z_E^{(t)}}, \boldsymbol{L^{(t)}}\right) = (1 - \rho_0) \prod_{i=1:Pa_{\boldsymbol{Onset^{(t)}}}=\boldsymbol{1}}^{2} 1 - \rho_i$$
Probability that the onset is present:
$$\boldsymbol{P}\left(\boldsymbol{Onset^{(t)}} = 1\middle|\boldsymbol{Z_R^{(t)}}, \boldsymbol{Z_E^{(t)}}, \boldsymbol{L^{(t)}}\right) = 1 - \boldsymbol{P}\left(\boldsymbol{Onset^{(t)}} = 0\middle|\boldsymbol{L^{(t)}}, \boldsymbol{R^{(t)}}, \boldsymbol{E^{(t)}}\right)$$</td>
</tr>
</table>

Appendix B: Supplementary File of Reinforcement Learning Optimal Sampling Study

Algorithm B-1: Randomized brute-force search for SINDy optimal sampling policy in noisy multi-scale complex systems

Input: number of simulations M, $\boldsymbol{\mathcal{A}}, \boldsymbol{S}, \boldsymbol{\eta_u}, \boldsymbol{\eta_v}, T_s^{init}, \varepsilon_{tol}, \boldsymbol{x}_0, \boldsymbol{\Xi}^*, \max_{iter}, \boldsymbol{\Theta}, \lambda_\kappa, \lambda_\mathbf{I}$, and λ_t

Output: optimal sampling policy π_B^* using randomized brute-force search

Sample initial data $\boldsymbol{D}_t = \{\boldsymbol{x}^{(k)}\}_{k=1}^{n_{\boldsymbol{D}_t}}$ starting at $\boldsymbol{x}_0$ with $T_s^{init}, \boldsymbol{f}(\boldsymbol{u}), \boldsymbol{g}(\boldsymbol{v})$, where $\boldsymbol{x} = [\boldsymbol{u}^T \quad \boldsymbol{v}^T]$

Introduce Gaussian noise to $\boldsymbol{x}(t)$ and $\dot{\boldsymbol{x}}(t)$ with the noise levels $\boldsymbol{\eta_u}, \boldsymbol{\eta_v}$:

$$\widetilde{\boldsymbol{x}}(t) \longleftarrow \boldsymbol{x}(t) + \boldsymbol{\varepsilon_u}, \qquad \widetilde{\dot{\boldsymbol{x}}}(t) \longleftarrow \boldsymbol{f}\big(\boldsymbol{x}(t)\big) + \boldsymbol{\varepsilon_v}, \qquad \boldsymbol{\varepsilon_u} \sim \mathcal{N}(\boldsymbol{0}, \boldsymbol{\eta_u^T I}_n), \qquad \boldsymbol{\varepsilon_v} \sim \mathcal{N}(\boldsymbol{0}, \boldsymbol{\eta_v^T I}_l)$$

Estimate $\widehat{\boldsymbol{\Xi}}_t$ and $\varepsilon_{SINDy,t}$ from $\widetilde{\boldsymbol{x}}(t), \widetilde{\dot{\boldsymbol{x}}}(t)$ using the SINDy algorithm: $\varepsilon_{SINDy,t} \longleftarrow \left\|\widehat{\boldsymbol{\Xi}}_t - \boldsymbol{\Xi}^*\right\|_F^2$

for $i \in \{1, \dots, M\}$ **do**

- Initialize loss function for π_i: $\mathcal{L}(\pi_i) \longleftarrow 0$
- **while** $(\varepsilon_{SINDy,t} < \varepsilon_{tol})$ and $(n_{iter} < \max_{iter})$ **do**
  - $n_{iter} \longleftarrow n_{iter} + 1$
  - Randomly select action $a_t \in \boldsymbol{\mathcal{A}} \sim \text{Multinomial}(n = 1, p_i = 1/3)$ at current state $\boldsymbol{s}$
  - Update T_s according to the action a_t, $t \longleftarrow t + T_s$
  - Update sampling period T_s according to the action a_t
  - Sample new $\widetilde{\boldsymbol{x}}(t)$ and $\widetilde{\dot{\boldsymbol{x}}}(t)$ from the noisy multi-scale system and append them to $\boldsymbol{D}_t$
  - Estimate new $\widehat{\boldsymbol{\Xi}}_t$ and $\varepsilon_{SINDy,t}$ using SINDy algorithm.
  - Calculate states $\kappa\big(\boldsymbol{\Theta}(\boldsymbol{D}_t)\big)$, $tr((\boldsymbol{\Theta}(\boldsymbol{D}_t)^T\boldsymbol{\Theta}(\boldsymbol{D}_t))^{-1})$, and $\mathrm{I}(\boldsymbol{D}_t)$
  - Update current state: $\boldsymbol{s}' \longleftarrow \boldsymbol{s}$
  - Calculate intermediate reward r_t using Equation (3.7)
  - Update loss function: $\mathcal{L}(\pi_i) = \mathcal{L}(\pi_i) - r_t$
- **end**

end

Find the best π_i among M simulated policies: $\pi_B^* \longleftarrow \underset{\pi_i}{\text{argmin}}\, \mathcal{L}(\pi_i), i = 1, \dots M$

Return π_B^*

Algorithm B-2: Greedy sampling for SINDy optimal sampling policy in noisy multi-scale complex systems

Input: $\boldsymbol{\mathcal{A}, S}$, search range Δ_s, $\boldsymbol{\eta_u}$, $\boldsymbol{\eta_v}$, T_s^{init}, ε_{tol}, $\boldsymbol{x}_0$, $\boldsymbol{\Xi}^*$, $\max_{iter}$, and $\boldsymbol{\Theta}$

Output: optimal sampling policy π_G^* using greedy sampling

Sample initial data $\boldsymbol{D}_t = \left\{\boldsymbol{x}^{(k)}\right\}_{k=1}^{n_{\boldsymbol{D}_t}}$ starting at $\boldsymbol{x}_0$ with T_s^{init}, $\boldsymbol{f}(\boldsymbol{u})$, $\boldsymbol{g}(\boldsymbol{v})$, where $\boldsymbol{x} = [\boldsymbol{u}^T \quad \boldsymbol{v}^T]$

Introduce Gaussian noise to $\boldsymbol{x}(t)$ and $\dot{\boldsymbol{x}}(t)$ with noise levels $\boldsymbol{\eta_u}$, $\boldsymbol{\eta_v}$:

$$\widetilde{\boldsymbol{x}}(t) \longleftarrow \boldsymbol{x}(t) + \boldsymbol{\varepsilon_u}, \qquad \widetilde{\dot{\boldsymbol{x}}}(t) \longleftarrow \boldsymbol{f}\big(\boldsymbol{x}(t)\big) + \boldsymbol{\varepsilon_v}, \qquad \boldsymbol{\varepsilon_u} \sim \mathcal{N}(\boldsymbol{0}, \boldsymbol{\eta_u^T I}_n), \qquad \boldsymbol{\varepsilon_v} \sim \mathcal{N}(\boldsymbol{0}, \boldsymbol{\eta_v^T I}_l)$$

Estimate $\widehat{\boldsymbol{\Xi}}_t$ and $\varepsilon_{SINDy,t}$ from $\widetilde{\boldsymbol{x}}(t), \widetilde{\dot{\boldsymbol{x}}}(t)$ using SINDy algorithm: $\varepsilon_{SINDy,t} \longleftarrow \left\|\widehat{\boldsymbol{\Xi}}_t - \boldsymbol{\Xi}^*\right\|_F^2$

while $(\varepsilon_{SINDy,t} < \varepsilon_{tol})$ and $(n_{iter} < \max_{iter})$ **do**

- Define optimality-criteria function $\Phi(\boldsymbol{D}_t)$:
- A-optimality: $\Phi(\cdot) = tr(\mathbf{I})$, D-optimality: $\Phi(\cdot) = tr(\mathbf{I})$, and E-optimality: $\Phi(\cdot) = \lambda_{min}(\boldsymbol{I})$
- Sample best "new" data within search range Δ_s with optimality-criteria $\Phi(\cdot)$:
- $\boldsymbol{x}^{(k+1)} \longleftarrow \boldsymbol{x}(\tau^*), \dot{\boldsymbol{x}}^{(k+1)} \longleftarrow \dot{\boldsymbol{x}}(\tau^*)$, where $\tau^* = \underset{\tau \in [t, t+\Delta_s]}{\operatorname{argmax}}\, \Phi(\boldsymbol{D}_t')$ and $\boldsymbol{D}_t' = \left\{\boldsymbol{x}^{(1)}, \dots, \boldsymbol{x}^{(k)}, \widetilde{\boldsymbol{x}}(\tau)\right\}$
- Update T_s according to optimal τ^*, $t \longleftarrow t + \tau^*$

Estimate new $\widehat{\boldsymbol{\Xi}}_t$ and $\varepsilon_{SINDy,t}$ using SINDy algorithm

end

Obtain optimal sampling policy π_G^*

Appendix C: Copyright Permissions

The permission below is for the use of material in Chapter 4.

CCC RightsLink | Sign in/Register

Probabilistic domain-knowledge modeling of disorder pathogenesis for dynamics forecasting of acute onset

Author: Phat K. Huynh,Arveity Setty,Hao Phan,Trung Q. Le

Publication: Artificial Intelligence in Medicine

Publisher: Elsevier

Date: May 2021

Journal Author Rights

Please note that, as the author of this Elsevier article, you retain the right to include it in a thesis or dissertation, provided it is not published commercially. Permission is not required, but please ensure that you reference the journal as the original source. For more information on this and on your other retained rights, please visit: https://www.elsevier.com/about/our-business/policies/copyright#Author-rights

BACK CLOSE WINDOW

The permission below is for the use of material in Chapter 5.

CCC RightsLink | Sign in/Register

IEEE Requesting permission to reuse content from an IEEE publication

A Physics-informed Latent Variables of Corrosion Growth in Oil and Gas Pipelines

Conference Proceedings: 2023 Annual Reliability and Maintainability Symposium (RAMS)

Author: Phat K. Huynh

Publisher: IEEE

Date: 23 January 2023

Thesis / Dissertation Reuse

The IEEE does not require individuals working on a thesis to obtain a formal reuse license, however, you may print out this statement to be used as a permission grant:

The permission below is for the use of material in Chapter 6.

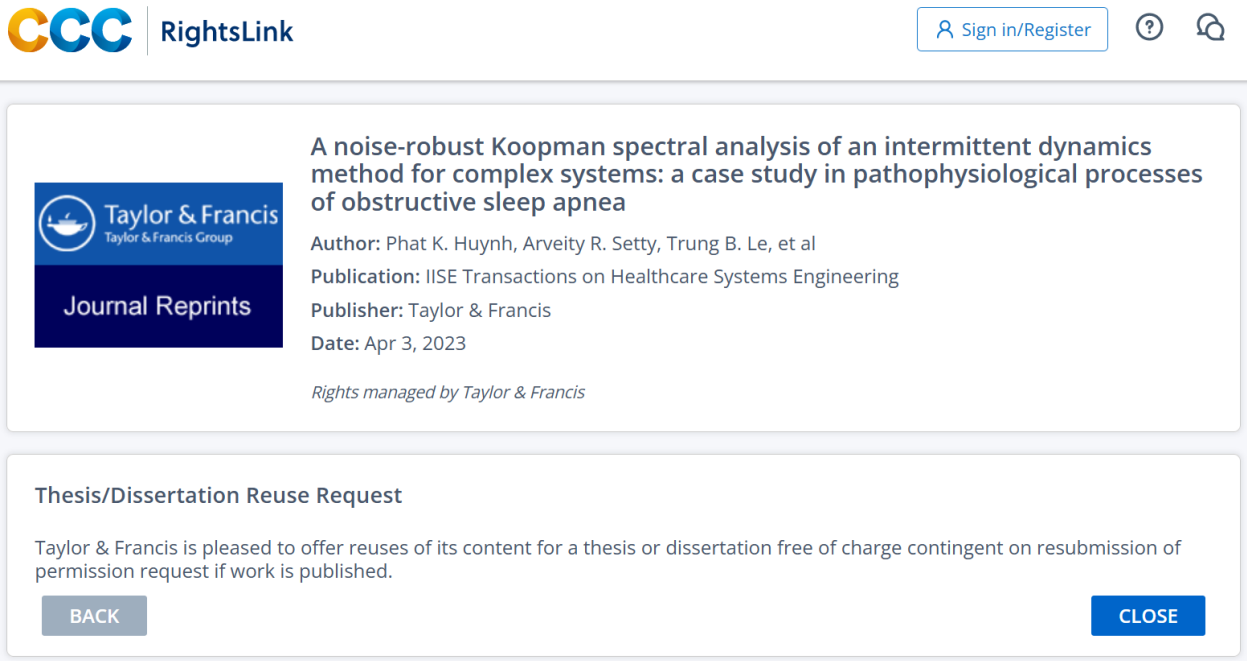

RightsLink

Sign in/Register

Taylor & Francis
Taylor & Francis Group
Journal Reprints

A noise-robust Koopman spectral analysis of an intermittent dynamics method for complex systems: a case study in pathophysiological processes of obstructive sleep apnea

Author: Phat K. Huynh, Arveity R. Setty, Trung B. Le, et al

Publication: IISE Transactions on Healthcare Systems Engineering

Publisher: Taylor & Francis

Date: Apr 3, 2023

Rights managed by Taylor & Francis

Thesis/Dissertation Reuse Request

Taylor & Francis is pleased to offer reuses of its content for a thesis or dissertation free of charge contingent on resubmission of permission request if work is published.

BACK

CLOSE

The permission below is for the use of material in Section 10.2 – Chapter 10.

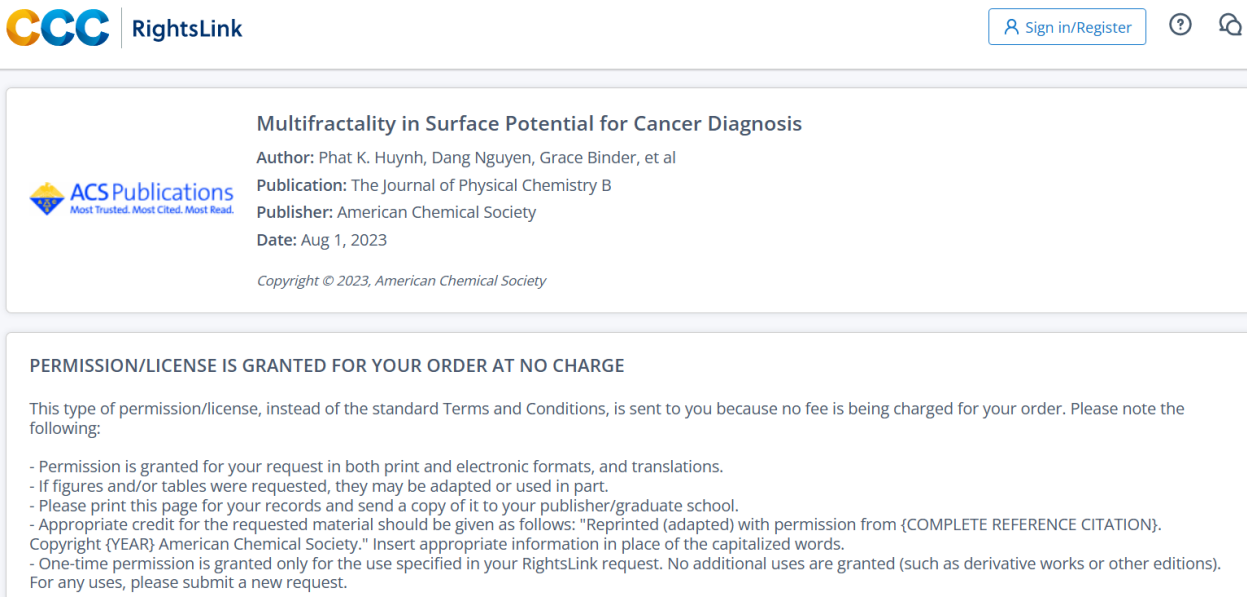

RightsLink

Sign in/Register

ACS Publications
Most Trusted. Most Cited. Most Read.

Multifractality in Surface Potential for Cancer Diagnosis

Author: Phat K. Huynh, Dang Nguyen, Grace Binder, et al

Publication: The Journal of Physical Chemistry B

Publisher: American Chemical Society

Date: Aug 1, 2023

Copyright © 2023, American Chemical Society

PERMISSION/LICENSE IS GRANTED FOR YOUR ORDER AT NO CHARGE

This type of permission/license, instead of the standard Terms and Conditions, is sent to you because no fee is being charged for your order. Please note the following:

- Permission is granted for your request in both print and electronic formats, and translations.
- If figures and/or tables were requested, they may be adapted or used in part.
- Please print this page for your records and send a copy of it to your publisher/graduate school.
- Appropriate credit for the requested material should be given as follows: "Reprinted (adapted) with permission from {COMPLETE REFERENCE CITATION}. Copyright {YEAR} American Chemical Society." Insert appropriate information in place of the capitalized words.
- One-time permission is granted only for the use specified in your RightsLink request. No additional uses are granted (such as derivative works or other editions). For any uses, please submit a new request.

About the Author

Phat Kim Huynh is currently a PhD candidate in the Industrial and Management Systems Engineering Department at the University of South Florida with a strong foundation in industrial engineering and biomedical applications. Earning a B.S. in Biomedical Engineering from the International University - VNU-HCM in Vietnam, he transitioned to the U.S. where they pursued both a Ph.D. in Industrial and Manufacturing Engineering and an M.S. in Industrial Engineering and Management from North Dakota State University. Afterwards, he transferred to and completed his PhD program at the University of South Florida, focusing on the integration of domain-specific knowledge into machine learning and modeling nonlinear dynamics in complex systems. His main interdisciplinary research interests are: (1) domain-informed sensor-based data-driven modeling for complex systems, (2) smart sensor-based AI Systems for health monitoring and analytics, and (3) adaptive stochastic and robust control strategies for multi-scale interconnected systems. His work has been published in prestigious high-impact journals such as IISE Transactions, AI in Medicine, IISE Transactions on Healthcare Systems, and Plos One.